



**DEVELOPMENT OF CARBON COMPOSITE NANOMATERIALS-  
BASED SENSORS AND BIOSENSORS FOR FOOD,  
ENVIRONMENTAL, AND CLINICAL APPLICATIONS**

**PREEYANUT BUTMEE**

**A THESIS SUBMITTED IN PARTIAL FULFILLMENT OF THE  
REQUIREMENTS FOR THE DEGREE OF DOCTOR OF PHILOSOPHY  
MAJOR IN CHEMISTRY  
FACULTY OF SCIENCE  
UBON RATCHATHANI UNIVERSITY  
ACADEMIC YEAR 2020  
COPYRIGHT OF UBON RATCHATHANI UNIVERSITY**



**UBON RATCHATHANI UNIVERSITY**  
**THESIS APPROVAL**  
**DOCTOR OF PHILOSOPHY**  
**IN CHEMISTRY FACULTY OF SCIENCE**

**TITLE** DEVELOPMENT OF CARBON COMPOSITE NANOMATERIALS-  
BASED SENSORS AND BIOSENSORS FOR FOOD, ENVIRONMENTAL,  
AND CLINICAL APPLICATIONS

**AUTHOR** MISS PREEYANUT BUTMEE

**EXAMINATION COMMITTEE**

DR. GAMOLWAN TUMCHARERN	CHAIRPERSON
ASSOC. PROF. DR. ANCHALEE SAMPHAO	MEMBER
ASST. PROF. DR. KITTIYA WONGKHAN	MEMBER
DR. PRANORM SAEJUENG	MEMBER
ASST. PROF. DR. PURIM JARUJAMRUS	MEMBER

**ADVISOR**

*Anchalee S.*  
.....  
(ASSOC. PROF. DR. ANCHALEE SAMPHAO)

*Charida Pukahuta*  
.....  
(ASST. PROF. DR. CHARIDA PUKAHUTA)  
DEAN, FACULTY OF SCIENCE

*A. Pongrat*  
.....  
(ASSOC. PROF. DR. ARIYAPORN PONGRAT)  
VICE PRESIDENT FOR ACADEMIC AFFAIRS

**COPYRIGHT OF UBON RATCHATHANI UNIVERSITY**  
**ACADEMIC YEAR 2020**

## ACKNOWLEDGEMENTS

I would like to express the deepest appreciation to my advisor, Assoc. Prof. Dr. Anchalee Samphao, for her helpful advices, patience, motivation, and excellent support throughout my Ph.D. study. I am also deeply thanks to Dr. Gamolwan Tumcharern from National Nanotechnology Center (NANOTEC), my co-advisor and thesis committee chairman, for her guidance, dedication, kindly supports of my Ph.D. study and the researches. Her guidance has been an important driving force to help me overcome the frustrations and failures encountered in the researches. I would not be able to complete this thesis without their support. My grateful thanks go to Asst. Prof. Dr. Kittiya Wongkhan, Dr. Pranorm Saejueng and Asst. Prof. Dr. Purim Jarujamrus for being a committee of my thesis defense and invaluable discussions.

I would like to express my sincere appreciation to Prof. Gerald Thouand from University of Nantes, France, for giving me an opportunity to do 5 months short research at the CNRS GEPEA laboratory, Technological Institute of the University of Nantes, France and for his kind advices on biological sciences. Acknowledgements are extended to Prof. Kurt Kalcher from University of Graz, Austria for helps, valuable suggestions and comments on electrochemistry. Special thanks would extend to Department of chemistry, Faculty of science, Ubon Ratchathani University, the scientific equipment center of Ubon Ratchathani University, National Nanotechnology Center (NANOTEC), and National Science and Technology Development Agency (NSTDA) for supporting all the equipment and instruments where this thesis carried out. I gratefully acknowledge scholarship support from the Thailand Graduate Institute of Science and Technology (TGIST) and Nantes University. Moreover, I am profoundly thankful to the research group under my advisor (AS-GROUP) and responsive nanomaterials research team (RNM) for their friendship, help and support.

Finally, my deepest and most sincere appreciation goes to my family for their constant encouragement, unconditional support and endless love.

Preeyanut Butmee

Researcher

### บทคัดย่อ

เรื่อง	: การพัฒนาเซนเซอร์และไบโอเซนเซอร์โดยใช้วัสดุผสมคาร์บอนขนาดนาโนสำหรับประยุกต์ใช้ทางด้านอาหาร สิ่งแวดล้อม และคลินิก
ชื่อผู้วิจัย	: ปรียานุช บุตรมี
ชื่อปริญญา	: วิทยาศาสตร์ดุขภักดิ์บัณฑิต
สาขาวิชา	: เคมี
อาจารย์ที่ปรึกษา	: รองศาสตราจารย์ ดร. อัญชลี สำเภา
คำสำคัญ	: เซนเซอร์, ไบโอเซนเซอร์, วัสดุนาโน, เทคนิคทางเคมีไฟฟ้า, เทคนิคพื้นผิวขยายสัญญาณรามาน

วิทยานิพนธ์นี้นำเสนอการออกแบบและพัฒนาเซนเซอร์สองชนิดและไบโอเซนเซอร์สองชนิดสำหรับประยุกต์ใช้ทางด้านอาหาร สิ่งแวดล้อม และคลินิก โดยอาศัยคุณสมบัติของวัสดุผสมคาร์บอนขนาดนาโน ตรวจสอบด้วยเทคนิคทางเคมีไฟฟ้าและเทคนิคพื้นผิวขยายสัญญาณรามาน

ในงานส่วนแรก เซนเซอร์ตรวจสอบด้วยเทคนิคทางเคมีไฟฟ้าถูกสร้างขึ้นสำหรับประยุกต์ใช้ทางด้านอาหาร โดยปรับปรุงขั้วไฟฟ้ากลาสซีคาร์บอนพอสต์ด้วยกราฟีนนาโนเพลตเลตที่ถูกทำฟังก์ชันกับของเหลวไอออนิก ประยุกต์ใช้สำหรับตรวจสอบสารบิสฟีนอลเอ ด้วยเทคนิคดิฟเฟอเรนเชียลพัลล์โวลแทมเมทรี ผลการศึกษาพบว่า เซนเซอร์ให้ช่วงความเป็นเส้นตรงในการตรวจสอบสารบิสฟีนอลเอที่ 0.02-5.0 ไมโครโมลาร์ ขีดจำกัดต่ำสุดในการตรวจสอบเท่ากับ 6.4 นาโนโมลาร์ ประยุกต์ใช้ตรวจสอบปริมาณสารบิสฟีนอลเอในตัวอย่างน้ำดื่มและขวดน้ำพลาสติกที่ใช้บรรจุดื่ม ผลการวิเคราะห์มีความถูกต้องสูงและให้ผลสอดคล้องกับเทคนิคมาตรฐานโครมาโทกราฟีของเหลวสมรรถนะสูง

ในส่วนที่สอง ไบโอเซนเซอร์ตรวจสอบด้วยเทคนิคทางเคมีไฟฟ้าถูกพัฒนาขึ้นสำหรับประยุกต์ใช้ทางคลินิก โดยใช้แอนติบอดีเป็นชั้นจذبสำหรับตรวจสอบ ซึ่งถูกตรึงเข้ากับอนุภาคคอร์เชลล์  $\text{Fe}_3\text{O}_4@Au$  ขนาดนาโน บนผิวหน้าขั้วไฟฟ้าพิมพ์สกรีนคาร์บอนที่ปรับปรุงด้วยแมงกานีสไดออกไซด์ เกาะติดแผ่นกราฟีนนาโนเพลตเลต ประยุกต์ใช้สำหรับตรวจสอบสารบ่งชี้มะเร็ง ด้วยเทคนิคลิเนียร์สวீปโวลแทมเมทรี และเทคนิคอิเล็กโทรเคมีคัล อิมพีแดนซ์สเปกโทรสโกปี ในสารละลายมาตรฐานโพแทสเซียมเฮกซะไซยาโนเฟอร์เรต เข้มข้น 5 มิลลิโมลาร์ โดยสัญญาณการตรวจสอบที่เปลี่ยนแปลงไปในสถานะที่มีและไม่มีสารบ่งชี้มะเร็งจะสัมพันธ์โดยตรงกับความเข้มข้นของสารบ่งชี้มะเร็ง ผลการศึกษาพบว่า ไบโอเซนเซอร์ให้ช่วงความเป็นเส้นตรงที่ 0.001-100 นาโนกรัมต่อมิลลิลิตร ขีดจำกัดในการตรวจสอบเท่ากับ 0.1 และ 0.3 พิโคกรัมต่อมิลลิลิตร สำหรับเทคนิคลิเนียร์สวี่ฟ โวลแทมเมทรี และเทคนิคอิเล็กโทรเคมีคัล อิมพีแดนซ์สเปกโทรสโกปี ตามลำดับ ประยุกต์ใช้สำหรับตรวจสอบปริมาณ



#### IV

สารบ่งชี้มะเร็งในเซรัมมนุษย์ พบว่าผลการวิเคราะห์สอดคล้องกับเทคนิคการวัดการเรืองแสงโดยอาศัยปฏิกิริยาทางเคมีไฟฟ้าและแอนติบอดี

ส่วนที่สามเกี่ยวข้องกับการพัฒนาไบโอเซนเซอร์ตรวจวัดด้วยเทคนิคทางเคมีไฟฟ้า สำหรับประยุกต์ใช้ทางด้านสิ่งแวดล้อม โดยใช้ขั้วไฟฟ้าพิมพ์สกรีนคาร์บอนที่ปรับปรุงด้วยรีดิวซ์กราฟีนออกไซด์และอนุภาคซิลเวอร์ขนาดนาโน ประยุกต์ใช้สำหรับตรวจวัดสารกำจัดศัตรูพืชชนิดไกลโฟเสต โดยอาศัยหลักการยับยั้งการทำงานของเอนไซม์เอซิดฟอสฟาเทส ด้วยเทคนิคโครโนแอมเพโรเมทรี เมื่อมีสารไกลโฟเสต สัญญาณการวิเคราะห์ลดลงเนื่องจากไกลโฟเสตยับยั้งการทำงานของเอนไซม์ ดังนั้นสัญญาณที่ลดลงจึงสอดคล้องกับความเข้มข้นของสารไกลโฟเสต จากการศึกษาพบว่าไบโอเซนเซอร์ให้ช่วงความเป็นเส้นตรงสองช่วง ได้แก่ 0.05-0.5 มิลลิกรัมต่อลิตร และ 0.5-22.0 มิลลิกรัมต่อลิตร ขีดจำกัดในการตรวจวัดเท่ากับ 16 ไมโครกรัมต่อลิตร ประยุกต์ใช้สำหรับตรวจหาปริมาณของไกลโฟเสตในตัวอย่างน้ำและดิน พบว่าผลการวิเคราะห์ให้ความถูกต้องสูงและสอดคล้องกับเทคนิคมาตรฐานโครมาโทกราฟีของเหลวสมรรถนะสูง

ในส่วนสุดท้าย วิธีวิเคราะห์สารไกลโฟเสตยังถูกออกแบบโดยใช้เทคนิคพื้นผิวขยายสัญญาณรามาน สำหรับประยุกต์ใช้ทางด้านสิ่งแวดล้อม โดยใช้ไททาเนียมออกไซด์นาโนทิวป์ที่เกาะติดด้วยอนุภาคซิลเวอร์ขนาดนาโนและคลุมด้วยรีดิวซ์กราฟีนออกไซด์ สร้างเป็นเซนเซอร์ตรวจวัด จากการศึกษา พบว่าเซนเซอร์ที่สร้างขึ้นมีความไวในการตรวจวัดสัญญาณรามานที่สูง โดยให้ประสิทธิภาพในการขยายสัญญาณมากถึง  $7.1 \times 10^3$  สามารถประยุกต์ใช้เซนเซอร์สำหรับตรวจวัดสารไกลโฟเสตได้ในช่วง 0.1-100 มิลลิกรัมต่อลิตร ด้วยขีดจำกัดในการตรวจวัดเท่ากับ 0.05 มิลลิกรัมต่อลิตร ผลการตรวจวิเคราะห์สารไกลโฟเสตในตัวอย่างน้ำและดินจากธรรมชาติที่ได้จากเซนเซอร์ที่พัฒนาขึ้นสอดคล้องกับเทคนิคมาตรฐานโครมาโทกราฟีของเหลวสมรรถนะสูง

การพัฒนางานวิจัยทางด้านเซนเซอร์และไบโอเซนเซอร์นี้ประสบผลสำเร็จ เซนเซอร์และไบโอเซนเซอร์ที่พัฒนาสามารถตรวจวัดสารได้จริง มีราคาถูก ตรวจวัดสารได้ง่ายขึ้น การตรวจวิเคราะห์ได้รวดเร็ว นอกจากนี้องค์ความรู้ที่เกิดขึ้นสามารถนำไปต่อยอดไม่เพียงแต่ในด้านการวิจัย ยังรวมไปถึงการต่อยอดในเชิงพาณิชย์ในอนาคตข้างหน้าได้

## ABSTRACT

TITLE : DEVELOPMENT OF CARBON COMPOSITE  
NANOMATERIALS-BASED SENSORS AND  
BIOSENSORS FOR FOOD, ENVIRONMENTAL, AND  
CLINICAL APPLICATIONS

AUTHOR : PREEYANUT BUTEE

DEGREE : DOCTOR OF SCIENCE

MAJOR : CHEMISTRY

ADVISOR : ASSOC. PROF. ANCHALEE SAMPHAO, Ph.D.

KEYWORDS : SENSOR, BIOSENSOR, NANOMATERIALS,  
ELECTROCHEMICAL METHOD, SURFACE ENHANCED  
RAMAN SPECTROSCOPY

For this thesis, two sensors and two biosensors were designed based on carbon composite nanomaterials using electrochemical methods and surface enhanced Raman spectroscopy as detection methods for food, environmental, and clinical applications.

In the first section, an electrochemical sensor for food applications was fabricated based on a glassy carbon paste electrode (GCPE) modified with graphene nanoplatelets (GNP) functionalized with ionic liquid (IL). The sensor was applied for the detection of bisphenol A (BPA) and performed by differential pulse voltammetry (DPV). Under optimum conditions, the proposed sensor exhibited a linear range for BPA determination from 0.02-5.0  $\mu\text{M}$  with a detection limit (LOD) of 6.4 nM. The GCPE/GNP-IL sensor was successfully applied to the determination of BPA in drinking water and plastic drinking water bottles. The results demonstrated a high degree of accuracy and are in agreement with high-performance liquid chromatography (HPLC).

In the second section, an electrochemical biosensor for clinical applications was designed based on CEA antibody (anti-CEA) anchored with core shell  $\text{Fe}_3\text{O}_4@\text{Au}$  nanoparticles which were immobilized on a screen-printed carbon electrode (SPCE) modified with manganese dioxide laid out on graphene nanoplatelets (GNP- $\text{MnO}_2$ ). A biosensor was applied for label-free detection of carcinoembryonic antigens (CEA), which was monitored by linear sweep voltammetry (LSV) and electrochemical

impedance spectroscopy (EIS). The difference in signal response owing to redox reactions of  $\text{Fe}(\text{CN})_6^{3-/4-}$  before and after a direct binding of CEA to a fixed amount of anti-CEA on the electrode surface was regarded as the biosensor response corresponding directly to the CEA concentration. Under optimized conditions, the biosensor exhibited a linear range of 0.001-100 ng/mL with the LOD of 0.10 pg/mL (LSV) and 0.30 pg/mL (EIS). The applicability of the biosensor was verified by determination of CEA in human serums compared to electrochemiluminescence immunoassay.

In the third section, an electrochemical biosensor for environmental applications was constructed based on SPCE modified with reduced graphene oxide (rGO) and silver nanoparticles (AgNPs). The biosensor was applied for indirect detection of glyphosate herbicide, which relied on the inhibition of acid phosphatase enzymes (ACP) immobilized on the SPCE/rGO-AgNPs surface. In the presence of glyphosate, the current signal was decreased, owing to the enzymatic reaction of ACP to its substrate. The signal was measured by chronoamperometry and quantitative measurements proportional to the glyphosate concentration. The biosensor exhibited two linear ranges from 0.05 to 0.5 mg/L and 0.5 to 22.0 mg/L, and the LOD of 16  $\mu\text{g/L}$  were obtained. The proposed biosensor was successfully applied for the determination of glyphosate in water and soil samples, and the results were in full accordance with the HPLC method.

In the last section, the analytical method for detection of glyphosate in environmental samples was also designed based on surface-enhanced Raman spectroscopy (SERS). A vertical heterostructure composed of titanium dioxide nanotube arrays ( $\text{TiO}_2$  NTs), AgNPs and rGO was constructed and served as a SERS-based sensor. Under optimum conditions, the  $\text{TiO}_2$  NTs/AgNPs-rGO surface exhibited high SERS activity, which provided analytical enhancement factors (AEF) as high as  $7.1 \times 10^8$ . The modified SERS sensor was successfully applied to glyphosate detection ranging from 0.1 to 100 mg/L and the LOD as 0.05 mg/L. The practical applications of glyphosate determination in environmental waters and soils were investigated and the results are in great accord with those obtained by the HPLC method.

The research is successful in developing sensors and biosensors. The sensors and biosensors developed are analytical devices employed as low-cost platforms for simple use and rapid detection. In addition, the new knowledge obtained will increase not only in the research field but also for commercial use in the future.

## CONTENTS

	PAGES
<b>ACKNOWLEDGEMENT</b>	<b>I</b>
<b>THAI ABSTRACT</b>	<b>III</b>
<b>ENGLISH ABSTRACT</b>	<b>V</b>
<b>CONTENTS</b>	<b>VII</b>
<b>LIST OF TABLES</b>	<b>IX</b>
<b>LIST OF FIGURES</b>	<b>XIII</b>
<b>LIST OF ABBRIVATIONS</b>	<b>XXIII</b>
<b>CHAPTER 1 INTRODUCTION</b>	
1.1 Importance and source of research	1
1.2 Objective	3
1.3 Scope of research	4
<b>CHAPTER 2 THEORETICALS AND REVIEWS</b>	
2.1 Sensor and biosensor	7
2.2 Recognition by antibody	8
2.3 Recognition by enzyme	17
2.4 Electrochemical method	26
2.5 Raman spectroscopy	36
2.6 Nanomaterials	43
2.7 Characterization techniques	46
2.8 Standard methods	50
2.9 Toxic substances and cancer biomarker	52
2.10 Literature reviews	55
<b>CHAPTER 3 EXPERIMENTAL</b>	
3.1 Instruments and equipment	77
3.2 Chemicals and reagents	79
3.3 Carbon composite nanomaterials-based sensor: electrochemical sensor for bisphenol A detection	83

**CONTENTS (CONTINUED)**

	<b>PAGES</b>
3.4 Carbon composite nanomaterials-based biosensor: electrochemical biosensor for detection of CEA biomarker	89
3.5 Carbon composite nanomaterials-based biosensor: electrochemical enzymatic biosensor for glyphosate detection	98
3.6 Carbon composite nanomaterials-based sensor: SERS for glyphosate detection	108
<b>CHAPTER 4 RESULTS AND DISCUSSION</b>	
4.1 Carbon composite Nanomaterials-based sensor: electrochemical sensor for bisphenol A detection	119
4.2 Carbon composite nanomaterials-based biosensor: electrochemical biosensor for CEA detection	137
4.3 Carbon composite nanomaterials-based biosensor: electrochemical biosensor for glyphosate detection	157
4.4 Carbon composite nanomaterials-based sensor: SERS-based sensor for detection of glyphosate	183
<b>CHAPTER 5 CONCLUSIONS</b>	<b>225</b>
<b>REFERENCES</b>	<b>235</b>
<b>APPENDICES</b>	
A EXPERIMENTAL DETAILS	271
B THE RESULTS OF ANALYSIS	277
C CALCULATION PART	327
D PUBLICATIONS AND PRESENTATIONS	333
<b>CURRICURUM VITAE</b>	<b>339</b>

## LIST OF TABLES

TABLE	PAGES
2.1 The common classes of antigens	11
2.2 Enzyme categories and their biochemical properties	18
2.3 Type of reversible enzyme inhibitors	24
2.4 Various electrochemical sensors for determination of BPA	57
2.5 Various electrochemical biosensors for determination of CEA	61
2.6 Various electrochemical biosensors and sensors for determination of glyphosate	65
2.7 Various kinds of nanomaterials used as a SERS substrate	71
3.1 Instruments	77
3.2 Equipment	78
3.3 List of chemicals and reagents	79
4.1 Determination of BPA in plastic products and in water in contact with them by the sensor and HPLC ( $n=3$ )	136
4.2 Detection of CEA in diluted human serum samples by the electrochemical biosensor in comparison with ECL immunoassay	156
4.3 Determination of glyphosate in environmental waters and soils by the biosensor and UHPLC ( $n=3$ )	182
4.4 Comparison of EF, repeatability, reproducibility, and stability between the TiO <sub>2</sub> NTs/AgNPs-rGO and commercial substrates	218
4.5 Determination of glyphosate in environmental waters and soils by the SERS-based sensor and UHPLC ( $n=3$ )	223
5.1 Conditions for GCPE/GNP-IL construction and DPV measurement	225
5.2 Analytical performance of the sensor for BPA detection	226
5.3 Electrochemical sensing assays for the determination of BPA	226
5.4 Optimum conditions for biosensor construction and CEA analysis	228
5.5 Analytical performance of the biosensor for CEA analysis	228
5.6 Electrochemical biosensing immunoassays for the determination of CEA	229

## LIST OF TABLES (CONTINUED)

TABLE	PAGES
5.7 Optimum conditions of enzymatic biosensor for glyphosate detection	230
5.8 Analytical performance of the biosensor for glyphosate detection	230
5.9 Electrochemical methods for the determination of glyphosate	231
5.10 Conditions for SERS measurement and SERS substrate construction	232
5.11 Analytical performance of the TiO <sub>2</sub> NTs/AgNPs-rGO	232
5.12 Comparison of analytical performance of different SERS sensor	233
5.13 Comparison of glyphosate detection from different SERS sensor	233
B.1 The current of GCPE/GNP-IL on the amount of IL	279
B.2 The current of GCPE/GNP-IL on the amount of GNP-IL	280
B.3 The peak current and peak potential of GCPE/GNP-IL on pH solution	280
B.4 The current of GCPE/GNP-IL on the pulse potential	280
B.5 The current of GCPE/GNP-IL on the step potential	281
B.6 The current of GCPE/GNP-IL on the scan rate	281
B.7 The current of different modified electrodes on BPA determination	282
B.8 The current response on the detection of 0.02 $\mu$ M BPA	282
B.9 The response for repeatability and reproducibility study	283
B.10 The response for the GCPE/GNP-IL on its stability	283
B.11 The response for the GCPE/GNP-IL on its selectivity (n=3)	284
B.12 The linear regression for BPA determination by the GCPE/GNP-IL using standard addition method and concentration of BPA found in the samples	285
B.13 The peak area, retention time, and concentration of BPA found in the samples using external calibration method	288
B.14 The response of the biosensor on the amount of GNP (n=3)	292
B.15 The response of the biosensor on the amount of MnO <sub>2</sub> (n=3)	292

### LIST OF TABLES (CONTINUED)

TABLE		PAGES
B.16	The response of the biosensor on concentration of antibody	292
B.17	The response of the biosensor on the pH solution (n=3)	293
B.18	The response of biosensor on the temperature (n=3)	293
B.19	The response of the biosensor on the incubation time (n=3)	294
B.20	The response of the biosensor on the reaction time (n=3)	294
B.21	The LSV and EIS response on CEA determination	295
B.22	The LSV and EIS response on the detection of blank	295
B.23	The response of biosensor on repeatability and reproducibility	297
B.24	The response of the biosensor on stability	297
B.25	The response of the biosensor on selectivity	297
B.26	The EIS and LSV response of SPCE/GNP-MnO <sub>2</sub> /Fe <sub>3</sub> O <sub>4</sub> @ Au biosensor for CEA determination in diluted serum samples	298
B.27	The current of SPCE/rGO-AgNPs/ACP on the potential apply	300
B.28	The current of SPCE/rGO-AgNPs/ACP on the amount of rGO	301
B.29	The current of SPCE/rGO-AgNPs/ACP on amount of AgNPs	301
B.30	The current of SPCE/rGO-AgNPs/ACP on amount of enzyme	301
B.31	The current of enzymatic biosensor on substrate concentration	302
B.32	The current of SPCE/rGO-AgNPs/ACP on pH value	302
B.33	The current of SPCE/rGO-AgNPs/ACP on enzyme kinetics	303
B.34	The current of SPCE/rGO-AgNPs/ACP on glyphosate determination	304
B.35	The current response on the detection of 0.05 mg/L glyphosate	305
B.36	The response of enzymatic biosensor on reproducibility study	306
B.37	The response for the SPCE/rGO-AgNPs/ACP on its stability	306
B.38	The response for the SPCE/rGO-AgNPs/ACP on its selectivity	306
B.39	The linear regression for glyphosate detection by the SPCE/rGO-AgNPs/ACP using standard addition method and concentration of glyphosate found in the samples	307



## LIST OF TABLES (CONTINUED)

TABLE	PAGES
B.40      The peak area, retention time, and concentration of glyphosate found in the samples using external calibration method	311
B.41      Raman intensity on laser excitation wavelength	314
B.42      Raman intensity of TiO <sub>2</sub> NTs/AgNPs-rGO on objective lens	314
B.43      Raman intensity of TiO <sub>2</sub> NTs/AgNPs-rGO on acquisition time	314
B.44      Raman intensity of the TiO <sub>2</sub> NTs/AgNPs-rGO on accumulation	315
B.45      Raman intensity of the TiO <sub>2</sub> NTs/AgNPs on anodic potential	315
B.46      Raman intensity of the TiO <sub>2</sub> NTs/AgNPs on anodic time	315
B.47      Raman intensity of the TiO <sub>2</sub> NTs/AgNPs on AgNPs thickness	316
B.48      Raman intensity of the TiO <sub>2</sub> NTs/AgNPs-rGO on GO concentration	316
B.49      Raman intensity of the substrate on deposition cycles	317
B.50      Raman intensity of the different substrates	317
B.51      Raman intensity of the substrate on MB determination	317
B.52      Raman intensity of 0.1 M MB on Ti sheet and 1 nM MB on the TiO <sub>2</sub> NTs/AgNPs-rGO substrate	319
B.53      Raman intensity of TiO <sub>2</sub> NTs/AgNPs-rGO substrate on repeatability and reproducibility study	319
B.54      Raman intensity of the TiO <sub>2</sub> NTs/AgNPs-rGO and TiO <sub>2</sub> NTs/AgNPs substrates on stability	319
B.55      Raman intensity of the TiO <sub>2</sub> NTs/AgNPs-rGO on recyclability	320
B.56      Raman intensity of the Si wafer, TiO <sub>2</sub> NTs/AgNPs-rGO, and commercial SERS substrates	321
B.57      Raman intensity of SERS sensor on glyphosate determination	321
B.58      Raman intensity on the detection of background signal	321
B.59      Raman intensity of the TiO <sub>2</sub> NTs/AgNPs-rGO on its selectivity	322
B.60      The linear regression for glyphosate determination by the TiO <sub>2</sub> NTs/AgNPs-rGO SERS sensor using standard addition method and concentration of glyphosate found in the samples	323

## LIST OF FIGURES

FIGURE	PAGES
1.1 Overview of the research	3
2.1 General model of (A) sensor and (B) biosensor	8
2.2 Structural diagrams representing antibody molecule	9
2.3 The antigenic determinant (or epitope) on antigen molecule	10
2.4 Specific interaction of an antibody with a complement antigen	12
2.5 Binding interactions between antigen and antibody	13
2.6 Concentration ratio of antibody to antigen	14
2.7 Basic steps involved in attaching antibodies on a glass surface	15
2.8 Labeled immunoassay based on uncompetitive detection	16
2.9 Induced-fit model of enzyme catalysis	17
2.10 Scheme of enzymatic biosensor for (A) substrate detection and (B) inhibitor detection	19
2.11 A plot of enzyme kinetics according to the (A) Michaelis- Menten equation and (B) Lineweaver-Burk plot	23
2.12 Diagram of (A) normal binding of enzyme with its substrate and (B) reversible enzyme inhibition	24
2.13 Sign conventions used in nowadays	27
2.14 Basic three-electrodes electrochemical system	28
2.15 Preparation process of glassy carbon paste electrode	29
2.16 A design of a portable screen-printed carbon electrode	30
2.17 (A) The waveform of potential applied and (B) voltammogram of a single electron oxidation-reduction in cyclic voltammetry	31
2.18 (A) The potential waveform and (B) voltammogram of LSV	31
2.19 (A) A profile of applied potential and (B) the signal in DPV	32
2.20 Schematic diagram of electrode reaction processes involved in stirred solution. Arrows indicated the direction of oxidizing species (ox) moving into the electrode and reduced to reducing species (red) which move out to the bulk solution	33
2.21 Scheme of the impedance presentation in the complex plane	35

## LIST OF FIGURES (CONTINUED)

FIGURE	PAGES
2.22 (A) Nyquist diagram and (B) its equivalent circuit	35
2.23 A simple schematic diagram of the Raman effect	36
2.24 Jablonski diagram of energy states for Rayleigh, Stoke and anti-Stoke scattering	37
2.25 The infrared and Raman spectrum of biological buffer	38
2.26 Illustration of SERS mechanism	39
2.27 (A) Surface-plasmon polariton and (B) Localized surface plasmon resonance	41
2.28 (A) Typical SERS hot spots in nanostructures and (B) First, second and third generation SERS hotspots	42
2.29 Metallic nanoparticles functionalized with a variety of molecules	44
2.30 Typical cations and anions used for IL design	45
2.31 A graphical representation of incident X-rays diffracting from atoms within crystalline layers	46
2.32 Physical electronics XPS instruments	47
2.33 Energy-dispersive X-ray generation process	48
2.34 High performance liquid chromatography system	50
2.35 Progress of HPLC separation of a three-component mixture	51
2.36 Bisphenol A and its hormones structurally analogous	53
2.37 The chemical structure of glyphosate	55
2.38 Electrochemical detection of VEGF biomarker using the Avastin-MGO/Au biosensor	59
2.39 (A) The principle for OPs determination and (B) the reaction mechanism of AChE on acetylthiocholine chloride	62
2.40 Mechanism of reaction occurring at ALP/ZnO/GCE	64
2.41 Reduction (%) of Raman intensity of R6G at $1525\text{ cm}^{-1}$ detected on AgNPs (black square) and GO-AgNPs (red circle) substrates as a function of the storage time	67
2.42 SEM images of (A) TiO <sub>2</sub> NTs and (B) Ag-coated TiO <sub>2</sub> NTs	68

## LIST OF FIGURES (CONTINUED)

FIGURE	PAGES
2.43 FE-SEM micrographs of AgNPs-TiO <sub>2</sub> NRs	68
2.44 SEM images of TiO <sub>2</sub> NSs after Ag-sputtering for 10 second	69
2.45 (A) Raman spectra of Klarite and Ag-Cu-grid substrate for R6G detection and (B) An overlay of Raman spectra of the four test concentrations of glyphosate using the Ag-Cu-grid	72
2.46 (A) Representative concentration-depend SERS spectra of (a) 10 <sup>-3</sup> (b) 10 <sup>-4</sup> (c) 10 <sup>-5</sup> (d) 10 <sup>-6</sup> (e) 10 <sup>-7</sup> M ninhydrin-linked glyphosate and its corresponding standard curve	73
2.47 (A) The SERS spectra of different concentration of thiram on AuAg nanochains and (B) its corresponding standard curve	74
2.48 SERS spectrum of 1×10 <sup>2</sup> nM thiram (Curve I), the mixture of 1×10 <sup>2</sup> nM thiram and 5×10 <sup>3</sup> nM MP (Curve II), and 5×10 <sup>3</sup> nM MP (Curve III) on the Ag-NP@GN substrate	75
3.1 Schematic diagram of the electrochemical sensor preparation	85
3.2 Schematic diagram of electrochemical biosensor preparation	92
3.3 Schematic demonstration of the electrochemical biosensor for label-free detection of CEA	93
3.4 Schematic of electrochemical enzymatic biosensor preparation	101
3.5 Schematic demonstration of the electrochemical biosensor for indirect detection of glyphosate based on enzyme inhibition	102
3.6 Schematic of fabrication process for TiO <sub>2</sub> NTs/AgNPs-rGO	110
4.1 SEM of (A) GCPE and (B) GCPE/GNP-IL at the magnification of 3000x	120
4.2 (A) FTIR spectra of GNP, IL and GNP-IL (B) Chemical structure of 1-butyl-2,3-dimethylimidazolium tetrafluoroborate	121
4.3 (A) CV and (B) EIS of modified electrodes in 5 mM Fe(CN) <sub>6</sub> <sup>3-/4-</sup>	122
4.4 (A) DPV of the different modified electrodes in 2 μM BPA solution and (B) its corresponding results	124

## LIST OF FIGURES (CONTINUED)

FIGURE	PAGES
4.5 (A) CV at different scan rates on the GCPE/GNP-IL in 5 mM $\text{Fe}(\text{CN})_6^{3-/4-}$ and (B) its corresponding result; (C) CV in 1 $\mu\text{M}$ BPA at different scan rates and (D) its corresponding data	125
4.6 Effect of amount of (A) IL and (B) GNP-IL on BPA detection	126
4.7 (A) DPV of 1 $\mu\text{M}$ BPA in phosphate buffer solution with different pH values and (B) dependence of the peak potential and peak current on pH	127
4.8 Effect (A) pulse potential, (B) step potential, and (C) scan rate on the sensor response to 1 $\mu\text{M}$ BPA	129
4.9 (A) DPV of GCPE/GNP-IL for BPA detection under optimum conditions and (B) calibration plots obtained with different modified electrodes	130
4.10 Stability of the GCPE/GNP-IL on 1 $\mu\text{M}$ BPA detection	132
4.11 Effect of interferences on the response of the GCPE/GNP-IL	133
4.12 (A) DPV of the GCPE/GNP-IL for BPA determination in real samples by standard addition method and (B) its corresponding standard curve	134
4.13 (A) Chromatograms of BPA standards in the range from 0.05-200 mg/L and (B) calibration plots of peak area versus BPA concentration	135
4.14 XRD patterns (A) GNP, $\text{MnO}_2$ and GNP- $\text{MnO}_2$ composite; (B) AuNPs, $\text{Fe}_3\text{O}_4$ and core shell $\text{Fe}_3\text{O}_4@\text{Au}$ nanoparticles	138
4.15 FT-IR spectra of (A) GNP, $\text{MnO}_2$ and GNP- $\text{MnO}_2$ composite; (B) $\text{Fe}_3\text{O}_4$ , core shell $\text{Fe}_3\text{O}_4@\text{Au}$ and core shell $\text{Fe}_3\text{O}_4@\text{Au}$ -conjugated anti-CEA	139
4.16 SEM images of (A) SPCE and SPCE modified with (B) GNP, (C) $\text{MnO}_2$ , (D) GNP- $\text{MnO}_2$ , (E) $\text{Fe}_3\text{O}_4@\text{Au}$ , and (F) $\text{Fe}_3\text{O}_4@\text{Au}$ /anti-CEA	141

## LIST OF FIGURES (CONTINUED)

FIGURE	PAGES
4.17 (A) CV and (B) EIS of the different modified electrodes in 5 mM $\text{Fe}(\text{CN})_6^{3-/4-}$ solution	142
4.18 (A) CV and (B) current density dependence on square root of a scan rate on SPCE/GNP- $\text{MnO}_2/\text{Fe}_3\text{O}_4$ @Au in 5 mM $\text{Fe}(\text{CN})_6^{3-/4-}$	144
4.19 EIS responses on 5 mM $\text{Fe}(\text{CN})_6^{3-/4-}$ detection of different modified electrodes in absence (blank line) and presence (red line) of 10 ng/mL CEA	145
4.20 (A) LSV and (B) EIS response of different stages during the biosensor fabrication in 5 mM $\text{Fe}(\text{CN})_6^{3-/4-}$ and 10 ng/mL CEA	146
4.21 Amount of (A) GNP on the electrode surface and (B) $\text{MnO}_2$ deposited on GNP sheet toward 10 ng/mL CEA detected in 5 mM $\text{Fe}(\text{CN})_6^{3-/4-}$	147
4.22 Effect of antibody concentration on detection of 10 ng/mL CEA	148
4.23 Effect of (A) pH and (B) temperature on the detection of 10 ng/mL CEA	149
4.24 Effect of (A) incubation time and (B) reaction time on the detection of 10 ng/mL CEA	150
4.25 (A) LSV and (B) its calibration plot; (C) EIS response and (D) its calibration plot for CEA detection using 5 mM $\text{Fe}(\text{CN})_6^{3-/4-}$	152
4.26 Stability of the SPCE/GNP- $\text{MnO}_2/\text{Fe}_3\text{O}_4$ @Au biosensor obtained on 1 ng/mL CEA detection by (A) LSV and (B) EIS	154
4.27 Selectivity of the biosensor for (a) blank, (b) PSA, (c) HSA, (d) IgG, (e) BSA, (f) cholesterol, (g) glucose, (h) sucrose, (i) cysteine, (j) ascorbic acid, (k) uric acid (l) mixed interferences, and (m) CEA (500 ng/mL interferences and 1 ng/mL CEA)	155
4.28 XRD pattern of the different modified electrodes	158
4.29 Raman spectra of the different modified electrodes	159
4.30 EDS (A) spectrum and (B) mapping of the SPCE/rGO-AgNPs	160

## LIST OF FIGURES (CONTINUED)

FIGURE	PAGES
4.31 SEM of (A) SPCE, (B) SPCE/rGO, (C) SPCE/AgNPs, and (D) SPCE/rGO-AgNPs at a magnification of 10,000x	162
4.32 (A) CV and (B) EIS of the different modified electrodes in 1 mM $\text{Fe}(\text{CN})_6^{3-/4-}$ solution	163
4.33 (A) CV of different modified electrodes in buffer solution with and without of 5 mg/L phenol and (B) its corresponding results	165
4.34 (A) CV at different scan rates on the SPCE/rGO-AgNPs in 1 mM $\text{Fe}(\text{CN})_6^{3-/4-}$ and (B) its corresponding result; (C) CV at different scan rates in 5 mg/L phenol and (D) its corresponding data	166
4.35 CV of the SPCE/rGO-AgNPs/ACP for determination of inhibition effect of glyphosate on ACP activity	167
4.36 Effect of operating potential on the detection of 0.2 mg/mL glyphosate	168
4.37 Effect of amount of (A) rGO and (B) AgNPs deposited on the SPCE on the detection of 0.2 mg/mL glyphosate	169
4.38 Effect of (A) ACP loading and (B) concentration of disodium phenyl phosphate on the detection of 0.2 mg/mL glyphosate	170
4.39 Effect of pH value on the detection of 0.2 mg/mL glyphosate	172
4.40 Amperometric response of SPCE/rGO-AgNPs/ACP to successive injections of 50-500 mg/L disodium phenyl phosphate in acetate buffer (pH 7.0) in the (A) absence and (B) presence of 1 mg/L glyphosate, and (C) its corresponding Lineweaver Burk plots	173
4.41 (A) The overall structure of ACP from red kidney bean (PDB entry 4KBP) (B) Phenyl phosphate docked and (C) Glyphosate docked	174
4.42 (A) Amperometric response of the SPCE/rGO-AgNPs/ACP for detection of glyphosate under optimum conditions and (B) its calibration plots	176
4.43 Stability of the SPCE/rGO-AgNPs/ACP on glyphosate detection	177

## LIST OF FIGURES (CONTINUED)

FIGURE	PAGES
4.44 Effect of interferences on the response of the SPCE/rGO-AgNPs/ACP	178
4.45 (A) Amperometric response of SPCE/rGO-AgNPs/ACP for glyphosate determination in real samples by standard addition method and (B) its corresponding standard curve	180
4.46 (A) Chromatograms of glyphosate standards in the range from 0.1-10 mg/L and (B) its calibration plots	181
4.47 UV-visible absorption spectra of different nanomaterials	185
4.48 EIS in a 5 mM $\text{Fe}(\text{CN})_6^{3-/4-}$ solution of Ti, $\text{TiO}_2$ NTs, $\text{TiO}_2$ NTs/rGO, $\text{TiO}_2$ NTs/AgNPs, and $\text{TiO}_2$ NTs/AgNPs-rGO	186
4.49 XRD spectra of different nanomaterials	188
4.50 Raman spectra of different nanomaterials	189
4.51 XPS of (A) $\text{TiO}_2$ NTs/AgNPs-rGO and high resolution XPS analysis of (B) Ti 2p (C) O 1s (D) Ag 3d and (E) C 1s components	190
4.52 EDS spectrum of $\text{TiO}_2$ NTs/AgNPs-rGO	191
4.53 Raman spectra and chemical structure of methylene blue	192
4.54 The influences of laser excitation wavelengths on the detection of (A) 1 mM MB and (B) 1 nM MB	194
4.55 SEM images of the (A) top surface and (B) cross-sectional microstructure of the $\text{TiO}_2$ NTs as a function of anodic voltage and a fixed time of 30 min	197
4.56 SERS response on the detection of 1 nM MB of the $\text{TiO}_2$ NTs prepared at different voltages and covered with 5 nm AgNPs (black line) and the effect of the anodic voltage on tube diameter (red line) and length (blue line)	199
4.57 SEM images of the (A) top surface and (B) cross-sectional microstructure of the $\text{TiO}_2$ NTs as a function of anodic time and a fixed voltage of 30 V	200



## LIST OF FIGURES (CONTINUED)

FIGURE	PAGES
4.58 SERS response on the detection of 1 nM MB of the TiO <sub>2</sub> NTs prepared at different anodic times and covered with 5 nm AgNPs (black line) and the effect of the anodic time on tube diameter (red line) and length (blue line)	202
4.59 AFM image and the thickness of AgNPs deposited on a Si substrate	203
4.60 SEM images of TiO <sub>2</sub> NTs covered with different thickness of Ag	204
4.61 SERS response of the TiO <sub>2</sub> NTs/AgNPs on 1 nM MB detection	205
4.62 Effects of (A) GO concentration and (B) electrodeposition cycles for rGO deposition on the detection of 1 nM MB	206
4.63 SEM of the TiO <sub>2</sub> NTs/AgNPs-rGO prepared at different electrochemical deposition cycles	207
4.64 SERS responses of different substrates on 1 mM MB detection	209
4.65 (A) SERS spectra of MB with different concentrations on the TiO <sub>2</sub> NTs/AgNPs-rGO and (B) its corresponding calibration curve	210
4.66 (A) SERS spectra of 1 mM MB collected from twenty different positions on the same TiO <sub>2</sub> NTs/AgNPs-rGO substrate and (B) SERS intensity at 1624 cm <sup>-1</sup> band obtained from ten different substrates	211
4.67 (A) Stability of the TiO <sub>2</sub> NTs/AgNPs and TiO <sub>2</sub> NTs/AgNPs-rGO and (B) long-term stability of the TiO <sub>2</sub> NTs/AgNPs-rGO on 1 mM MB detection	213
4.68 (A) SERS spectra of MB (1 mM) on the TiO <sub>2</sub> NTs/AgNPs-rGO and (B) SEM images of the TiO <sub>2</sub> NTs/AgNPs-rGO surface before and after Xenon arc lamp irradiation by repeating for 3 cycles	214
4.69 (A) Diagrams of electron and hole transfer in TiO <sub>2</sub> NTs/AgNPs-rGO and (B) its reaction mechanisms; (C) possible degradation mechanism of MB under visible light irradiation	215

## LIST OF FIGURES (CONTINUED)

FIGURE	PAGES
4.70 (A) SERS spectra of glyphosate with different concentrations and (B) its corresponding calibration curve	220
4.71 Effect of interferences on response of the TiO <sub>2</sub> NTs/AgNPs-rGO	221
A.1 (A) Electrode composition and (B) electrode surface	273
A.2 (A) Potentiostat/Galvanostat and (B) three-electrode system	273
A.3 Screen printed carbon electrode	274
A.4 Electrode holder for fixing of the screen-printed carbon electrode	274
A.5 (A) SERS substrate, (B) Raman analysis part, and (C) instrumentation	274
A.6 (A) Xenon arc lamp equipped with a solar simulator and (B) the set-up of SERS substrate for recyclable study	275
B.1 Current responses on the GCPE/GNP-IL measured by DPV in 0.1 M phosphate buffer solution containing 1 $\mu$ M BPA solution	279
B.2 (A) LSV and (B) EIS responses of the SPCE/GNP-MnO <sub>2</sub> /Fe <sub>3</sub> O <sub>4</sub> @Au biosensor toward 10 ng/mL CEA detected in phosphate buffer solution containing 5 mM Fe(CN) <sub>6</sub> <sup>3-/4-</sup>	291
B.3 Amperometric responses on the SPCE/rGO-AgNPs/ACP at potential of 0.4 V in 0.1 M acetate buffer solution containing 20 g/L disodium phenyl phosphate and 0.2 mg/L glyphosate	300

## LIST OF ABBRIVATIONS

ABBRIATION	FULL WORD
A	Area of electrode/substrate
ACP	Acid phosphatase
AEF	Analytical enhancement factor
Ag-Ab	Antigen-antibody complex
Ag/AgCl	Silver-silver chloride reference electrode
AgNPs	Silver nanoparticles
anti-CEA	Antibody of carcinoembryonic antigen
a.u.	Absorbance unit
AuNPs	Gold nanoparticles
BE	Binding energy
BPA	Bisphenol A
BSA	Bovine serum albumin
C	Concentration
C <sub>0</sub>	Initial concentration
°C	Degree Celsius
CB	Conduction band
CE	Counter electrode
CEA	Carcinoembryonic antigen
CM	Chemical enhancement mechanism
cm <sup>-1</sup>	Wavenumber
cm <sup>2</sup>	Square centimeter
CNBF	4-chloro-3 5-dinitrobenzotrifluoride
C <sub>NRS</sub>	Concentration of analyte on normal substrate
CPS	Intensity in counts per second
C <sub>SERS</sub>	Concentration of analyte on SERS substrate
CV	Cyclic voltammetry
D <sub>0</sub>	Diffusion coefficient
DC	Direct current

## LIST OF ABBRIVATIONS (CONTINUED)

ABBREVIATION	FULL WORD
DPV	differential pulse voltammetry
E	Enzyme
$e^-$	Electron
EDS	Energy dispersive spectroscopy
EIS	Electrochemical impedance spectroscopy
ELISA	Enzyme-linked immunosorbent assay
EM	Electromagnetic field enhancement mechanism
$\Delta E_p$	Peak-to-peak separation
$E_{pa}$	Anodic peak potential
$E_{pc}$	Cathodic peak potential
$E_{pulse}$	Pulse potential
ES	Enzyme-substrate complex
$E_{step}$	Step potential
eV	Electron volt
$F_{ab}$	Antigen binding site fragments
FAO	United Nations Food and Agricultural Organization
$F_c$	Crystallizable fragments
$Fe(CN)_6^{3-/4-}$	Hexacyanoferrate solution
$Fe_3O_4$	Magnetite
$Fe_3O_4@Au$	Core shell magnetic-gold nanoparticles
FTIR	Fourier transform infrared spectroscopy
g	gram
$g.L^{-1}$	Gram per liter
GA	Glutaraldehyde
GCPE	glassy carbon paste electrode
GNP	graphene nanoplatelets
GO	Graphene oxide
$h^+$	Holes

## LIST OF ABBRIVATIONS (CONTINUED)

ABBREVIATION	FULL WORD
HPLC	high performance liquid chromatography
$h\nu$	Photon energy
I	Current
$I_0$	Peak current before inhibition
$I_1$	Peak current after inhibition
$\Delta I$	Different in peak current before and after presence of analyte
IL	Ionic liquid
$I_{\max}$	Maximum current
$I_{\text{NRS}}$	Raman intensity on normal substrate
$I_{\text{pa}}$	Anodic peak current
$I_{\text{pc}}$	Cathodic peak current
IR	Infrared spectroscopy
$I_{\text{SERS}}$	Raman intensity on SERS substrate
IUPAC	International Union of Pure and Applied Chemistry
$J_p$	Peak current density
$k\Omega$	Kilo ohm
$k_a$	Association rate constant
$k_d$	Dissociation rate constant
$K_{\text{eq}}$	Equilibrium constant
$K_m$	Michaelis-Menten constant
LOD	Limit of detection
LOQ	Limit of quantification
LSPR	Localized surface plasmon resonance
LSV	Linear sweep voltammetry
M	Molar
$\text{mA}\cdot\text{cm}^{-2}$	Milliampere per Square centimeter
mAU	Intensity of absorbance

## LIST OF ABBRIVATIONS (CONTINUED)

ABBREVATION	FULL WORD
MB	Methylene blue
mM	Millimolar
MnO <sub>2</sub>	Manganese dioxide
mg.cm <sup>-2</sup>	Milligram per Square centimeter
mg.kg <sup>-1</sup>	Milligram per kilogram
mg.L <sup>-1</sup>	Milligram per liter
mg.mL <sup>-1</sup>	Milligram per milliliter
MRLs	Maximum residue levels
mV	Millivolt
mV.pH <sup>-1</sup>	Millivolt per pH
mV.s <sup>-1</sup>	Millivolt per second
n	Number of electron
n.d.	Not detectable
ng.mL <sup>-1</sup>	Nanogram per milliliter
nm	Nanometer
nM	Nanomolar
O	Oxidant
P	Product
R	Reductant
r <sup>2</sup>	Correlation coefficient
R <sub>ct</sub>	Charge transfer resistance
ΔR <sub>ct</sub>	Different in charge transfer resistance before and after presence of analyte
RE	Reference electrode
rGO	Reduced graphene oxide
RSD	Relative standard deviation
S	Substrate
SD	Standard deviation

## LIST OF ABBRIVATIONS (CONTINUED)

ABBRIATION	FULL WORD
SEM	Scanning electron microscope
SERS	Surface enhanced Raman spectroscopy
SPCE	Screen-printed carbon electrode
SPR	Surface plasma resonance
t	Time
T	Temperature
TiO <sub>2</sub> NTs	Titanium dioxide nanotube arrays
UHPLC	Ultra-high performance liquid chromatography
μA	Microampere
μA.cm <sup>-2</sup>	Microampere per square centimeter
μg	Microgram
μg.cm <sup>-2</sup>	Microgram per square centimeter
μg.mL <sup>-1</sup>	Microgram per milliliter
μm	Micrometer
μM	Micromolar
V	volt
VB	Valence band
V <sub>max</sub>	Maximum velocity
V.s <sup>-1</sup>	Volt per second
(V.s <sup>-1</sup> ) <sup>1/2</sup>	Square root of volt per second
WE	Working electrode
WHO	World Health Organization
XPS	X-ray photoelectron spectroscopy
XRD	X-ray diffraction spectroscopy
Z'	Real impedance part
Z''	Imaginary impedance part

# CHAPTER 1

## INTRODUCTION

### 1.1 Importance and source of research

Increasing attention has been focused on the development of effective tools for monitoring of toxic molecules contaminated in environments and foods to protect environmental pollutions and prevent serious threats to public health. Moreover, the developed methods should also be applied for real time measurements for health and clinical monitoring. Many analytical approaches have been proposed, including UV-visible spectrometry, fluorescence, chromatography, mass spectrometry, and atomic absorption spectrometry. These methods can be used to detect substances effectively, but also containing the drawbacks of requiring the enrichment and purification, expensive instrumentation, time-consuming process and need of professional operator. [1] Therefore, the development of novel sensitive detection techniques with faster, simpler, and less expensive methods continues to be a major challenge for rapid and sensitive detection of substances in various samples and matrices. Recently, the interest in using of sensors and biosensors has been increasing because they have the potential to complement or even replace the conventional analytical methods, particularly on-site detection due to their advantageous features, such as facile sample preparation, high sensitivity and selectivity, rapid response, instrument simplicity, convenient operation, miniaturization and portability, and reduction in cost per analysis. [2, 3]

Sensor and biosensor technologies represent an extremely wide field with a great impact not only in food and environmental quality control but also in clinical filed because they can be miniaturized into small devices and can provide analytical results within a few minutes, applicable for real-time analysis. [4] Sensor consists of two components including recognition system and transducer. The recognition layer is coupled to a transducer, which converts the interaction between analyte and interface of the sensor into a measurable analytical signal such as electric current and optical signal, depending on the type of transducer used. This statistic tool allows us to obtain



analyzable results with minimal manipulation. Biosensor is a subset of sensor in which the recognition system is based on biochemical elements or biological mechanisms, which play important roles in the analysis of specific compounds in biological assays.

Nowadays, electrochemistry and surface-enhanced Raman scattering (SERS) has emerged as the extremely promising detection method for construction of the sensors and biosensors. Electrochemical detection is one of the attractive methods because of fast response, low cost, easy preparation, instrument simplicity, high sensitivity, excellent selectivity, and real-time detection. It is a method that transforms electrochemical information into an analytically current signal. Several electrochemical (bio)sensors have been established with the detection limits of nano-, femto-molar or even lower range of concentrations that are suitable for trace analysis and early diagnostic applications. [5] Additionally, SERS have attracted much interest due to its properties of high sensitivity, chemical fingerprint, simple preparation, rapid and non-destructive analyses. Moreover, it can be applied for both qualitative and quantitative analysis. Raman spectroscopy is a molecular vibration spectroscopic technique, resulting from an inelastic scattering process which can provide information about the structural characteristics of a molecule. SERS is a technique where the normal Raman scattering of analytes is greatly enhanced by nanoscale rough metal surfaces. [6, 7] Therefore, electrochemical method and SERS become powerful analytical detection tools in recent years.

Nanotechnology has been considered as a technology of general use for modern tools development. The interactions between different materials in nanoscale ( $10^{-9}$  m) are able to generate new properties and a unique phenomenon can be occurred. [8] Because of this reason, nanomaterials have often been used in the modification of sensors and biosensors based on electrochemical and SERS analysis due to the surface area of materials greatly increase in the nanometer range, leading to improvement in electrical conductivity and electromagnetic enhancement. Several nanomaterials, such as carbon nanomaterials [9] metal nanoparticles [10] and metal oxide nanostructure [11] have demonstrated potential for the development of (bio)sensing systems that could be applied for trace analysis of compounds in various applications.

Therefore, this thesis mainly focused on the development of carbon composite nanomaterials-based sensors and biosensors for food, environmental and clinical applications using electrochemistry and SERS as the detection methods.

## 1.2 Objective

The objectives of this thesis are to develop two sensors and two biosensors, which are divided into 2 main-objectives according to the detection method and 4-sub objectives (Figure 1.1) as follow.

1.2.1 To develop electrochemical sensor and biosensors based on carbon composite nanomaterials

1.2.1.1 To construct electrochemical sensor based on graphene nanoplatelets and ionic liquid for the detection of bisphenol A

1.2.1.2 To construct electrochemical immunosensor based on graphene nanoplatelets, manganese dioxide, and core shell  $\text{Fe}_3\text{O}_4@\text{Au}$  nanoparticles for analysis of cancer biomarker

1.2.1.3 To establish electrochemical biosensor based on reduced graphene oxide and silver nanoparticles for the detection of glyphosate herbicide

1.2.2 To design SERS sensor-based carbon composite nanomaterials

1.2.2.1 To prepare SERS sensor based on titanium dioxide, reduced graphene oxide and silver nanoparticles for glyphosate herbicide detection

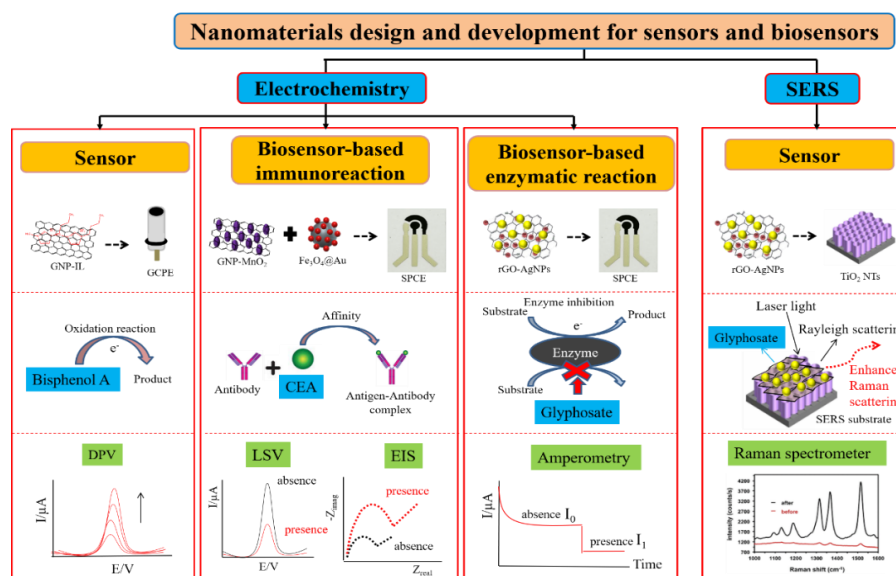


**Figure 1.1 Overview of the research**

### 1.3 Scope of research

Various scopes of this thesis are divided into 4 parts according to the sub-objectives as follows.

#### 1.3.1 Electrochemical sensor-based carbon composite nanomaterials

1.3.1.1 Fabrication of the electrochemical sensor based on a composite of graphene nanoplatelet (GNP) and 1-butyl-2, 3-dimethylimidazoliumtetrafluoro borate (ionic liquid, IL) as a modifier for glassy carbon paste electrode (GCPE)

1.3.1.2 Characterization of the sensor by scanning electron microscopy (SEM) and Fourier transform infrared spectroscopy (FTIR)

1.3.1.3 Characterization of the electrochemical behavior of the sensor by cyclic voltammetry (CV), electrochemical impedance spectroscopy (EIS), and differential pulse voltammetry (DPV)

1.3.1.4 Investigation of conditions for construction of the sensor and parameters affecting the detection of bisphenol A (BPA) using DPV, including amount of IL and GNP-IL composite, pH solution, and parameters for DPV measurement (such as pulse potential, step potential, and scan rate)

1.3.1.5 Investigation of analytical performances of the sensor for BPA detection using DPV, such as linear range, limit of detection and qualification, reproducibility and repeatability, stability, and selectivity

1.3.1.6 Study the applicability of the sensor for detection of BPA using DPV in real samples for food applications in comparison to high performance liquid chromatography (HPLC) as a standard method

#### 1.3.2 Electrochemical biosensor based on carbon composite nanomaterials and immunoreaction

1.3.2.1 Construction of the electrochemical biosensor based on immobilization of antibody conjugated core shell  $\text{Fe}_3\text{O}_4@\text{Au}$  nanoparticles on the surface on screen-printed carbon electrode (SPCE) modified with manganese dioxide ( $\text{MnO}_2$ ) deposited graphene nanoplatelet (GNP)

1.3.2.2 Characterization of the biosensor by scanning electron microscopy (SEM), X-ray diffraction spectroscopy (XRD), and Fourier transform infrared spectroscopy (FTIR)

1.3.2.3 Characterization of the electrochemical behavior of the biosensor by cyclic voltammetry (CV), electrochemical impedance spectroscopy (EIS), and linear sweep voltammetry (LSV)

1.3.2.4 Investigation of conditions for biosensor fabrication and parameters affecting the detection of carcinoembryonic antigen (CEA) using LSV and EIS, including amount of GNP and MnO<sub>2</sub>, antibody loading, pH solution, temperature, incubation time, and reaction time

1.3.2.5 Study of analytical performances of the biosensor for CEA analysis using LSV and EIS, such as linear range, limit of detection, reproducibility and repeatability, stability, and selectivity

1.3.2.6 Study the applicability of the biosensor for CEA analysis using LSV and EIS in human serum samples for clinical applications in comparison to electrochemiluminescence immunoassay (ECL) as a comparative method

1.3.3 Electrochemical biosensor based on carbon composite nanomaterials and enzymatic reaction

1.3.3.1 Fabrication of the electrochemical biosensor based on acid phosphatase enzyme (ACP) immobilized on a screen-printed carbon electrode (SPCE) modified with silver nanoparticles (AgNPs) and reduced graphene oxide (rGO)

1.3.3.2 Characterization of the biosensor by scanning electron microscopy (SEM), X-ray diffraction spectroscopy (XRD), Raman spectroscopy, and energy dispersive spectroscopy (EDS)

1.3.3.3 Characterization of the electrochemical behavior of the biosensor by cyclic voltammetry and electrochemical impedance spectroscopy

1.3.3.4 Investigation of biosensor construction conditions and parameters affecting the detection of glyphosate herbicide based on enzyme inhibition using chronoamperometry, including potential apply, amount of AgNPs and rGO, enzyme loading, concentration of enzyme substrate, and pH solution

1.3.3.5 Investigation of enzyme kinetic and inhibition mechanism of ACP on its substrate and glyphosate herbicide

1.3.3.6 Study interaction of ACP-substrate and ACP-glyphosate complexes by molecular docking

1.3.3.7 Study of analytical performances of the biosensor for glyphosate detection based on enzyme inhibition using chronoamperometry, such as linear range, limit of detection and quantification, reproducibility, stability, and selectivity

1.3.3.8 Study the applicability of the biosensor for glyphosate detection based on enzyme inhibition using chronoamperometry in real samples for environmental applications in comparison to ultra-high performance liquid chromatography (UHPLC)

#### 1.3.4 SERS sensor-based carbon composite nanomaterials

1.3.4.1 Fabrication of SERS substrate based on titanium dioxide nanotube ( $\text{TiO}_2$  NTs), silver nanoparticles (AgNPs) and reduced graphene oxide (rGO)

1.3.4.2 Characterization of the sensor by scanning electron microscopy (SEM), X-ray diffraction spectroscopy (XRD), Raman spectroscopy, energy dispersive spectroscopy (EDS), X-ray photoelectron spectroscopy (XPS), UV-visible spectroscopy, and electrochemical impedance spectroscopy (EIS)

1.3.4.3 Study parameters for Raman measurements such as laser excitation, objective lens, acquisition time, and number of accumulations

1.3.4.4 Investigation of conditions for SERS substrate fabrication such as voltage and time for anodization of  $\text{TiO}_2$  NTs, amount of AgNPs, and rGO thickness

1.3.4.5 Study of analytical performances of the sensor for detection of methylene blue (MB) as the probe molecule, including linear range, limit of detection, enhancement factor, reproducibility and repeatability, stability, and reusability

1.3.4.6 Study analytical performances of the sensor for glyphosate detection, such as linear range, limit of detection, and selectivity

1.3.4.7 Study the applicability of the sensor for glyphosate detection in real samples for environmental applications compared with ultra-high performance liquid chromatography (UHPLC)

## **CHAPTER 2**

### **THEORETICALS AND LITERATURE REVIEWS**

The aims of this thesis are the development of carbon composite nanomaterials-based sensors and biosensors using electrochemical method and surface enhanced Raman spectroscopy (SERS) as detection methods for determination of toxic substances in food and environment, and cancer biomarker for clinical applications. Therefore, the purpose of this chapter is to describe a general description and principle operation of sensor and biosensor, principle of electrochemical method and SERS as well as other techniques employed in this thesis. Besides, various types of nanomaterials used in this thesis and a brief literature reviews are fully presented in order to understand the fabrications, characterizations and benefits of related methods.

#### **2.1 Sensor and biosensor**

Sensor is a device that is capable of providing real-time analytical information about tested samples. It consists of two components, a recognition system and a transducer. The recognition system (or sensing element) can be a material that has certain recognition sites or be capable of interaction with analyte. When the analyte interacts in a more or less selective way with the sensing element, signal related with concentration is produced at a transducer, which provides signal processing to deduce and quantify a particular analyte. [12, 13]

Biosensor is a subset of sensor in which the recognition system is based on biochemical or biological mechanisms. Bio-recognition system play important roles in the analysis of specific compounds in biological assays. [12] Biological components usually used for construction of biosensor are enzymes, antibodies, cells, bacteria, DNAs/RNAs, and aptamers. Therefore, biosensor is called when the above-mentioned biological components are employed as a recognition system while sensor is called when non-biological elements are used. Figure 2.1 displays a general model of a sensor compared with biosensor.

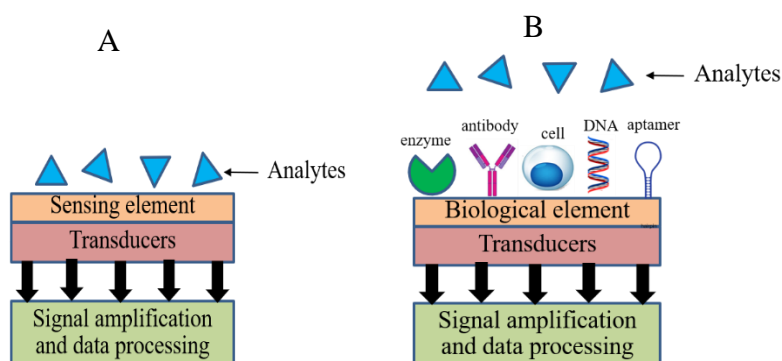


**Figure 2.1 General model of (A) sensor and (B) biosensor**

In this research, antibody and enzyme have been used as biological receptors for construction of the biosensor in order to improve the selectivity. The next sections describe the usability of antibody and enzyme as receptors for biosensor fabrications and the interaction mechanisms between antigen-antibody and enzyme-substrate.

## 2.2 Recognition by antibody

Biosensor in which the recognition system is based on antigen-antibody interaction is called immunosensor. The complement system between antigen and antibody is a common type of affinity interaction. Affinity interactions involve reversible multiple binding of two chemical species through ionic bonds, hydrogen bonds, hydrophobic interactions, and van der Waals interactions. [14] In addition, the affinity interaction is also involved complementary with respect to not only chemical reactivity but also shape. Generally, immunochemical reactions are used for diagnostic purposes in the clinical laboratory. Using specific antibody as recognition receptor, antigen can be identified. Conversely, using an antigen receptor, a specific antibody can be identified.

### 2.2.1 Antibody

Antibody [15] is glycoproteins produced by the immune system to identify and neutralize pathogen microorganisms such as bacteria and viruses. The part of the pathogen that interacts with the specific antibody is called antigen. Antibody is also called immunoglobulins (Ig). All immunoglobulins have a number of structural features in common. They possess two light polypeptides with an approximate molecular weight of 25 kDa per chain, and two heavy polypeptide chains of 50 kDa each. These four

chains are bound together on a single antibody molecule by disulfide bonds (S-S), forming a Y-shape structure with a central axis of symmetry (Figure 2.2).

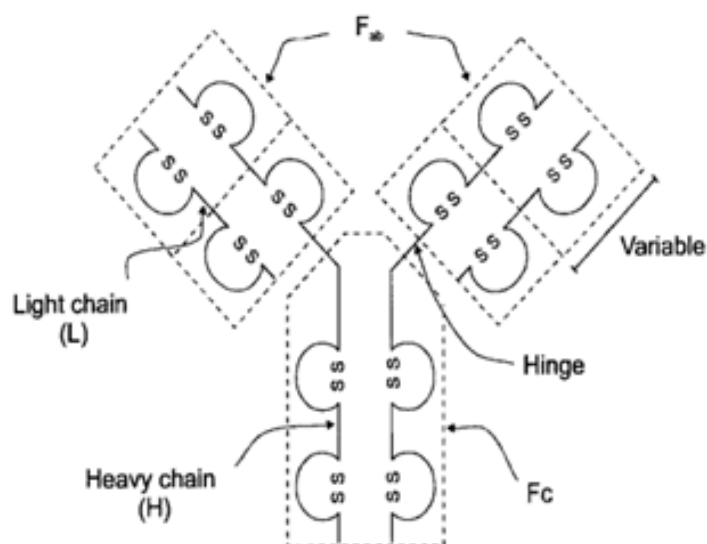


**Figure 2.2 Structural diagrams representing antibody molecule [15]**

Antibody molecule composes of constant and variable domains. Amino acid sequence, the constant domains, is similar in a specific class of antibody while the sequence in the variable domains is adapted for recognition of a specific antigen. The  $NH_2$ -terminal ends of the light polypeptide chains located the top of the Y-structure are called  $F_{ab}$  fragments. These fragments are the specific antigen-binding sites of the antibody. The  $COOH$ -terminal ends of the heavy polypeptide chains are called  $F_c$  fragments or crystallizable fragments, which determines the antibody class. Therefore, antibodies in different classes may have exactly the same antigen binding properties, but exhibit different functional properties. [16]

### 2.2.2 Antigen

Antigen is a molecule that is capable of binding selectively to antibody. The antigen-binding site of an antibody has a structure that allows a complementary fit with structural elements and functional groups on the antigen, forming a strong antibody-antigen complex. The portion of the antigen that interacts specifically with the antigen-binding site on the antibody is called antigenic determinant or epitope and the



complementary site on the antibody is called the paratope (Figure 2.3). The epitope has a size of about  $0.7 \times 1.2 \times 3.5$  nm, which are equivalent to about 5-7 amino acid residues.

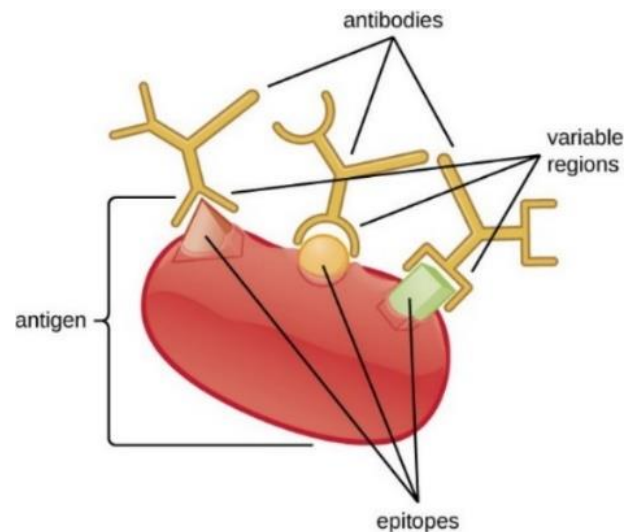


**Figure 2.3 The antigenic determinant (or epitope) on antigen molecule [17]**

Antigens can be classified according to the molecular weight into two types. One is hepten, which is a low molecular weight compounds of antigen ( $<1,000$  Da) that can only generate an immune response when they are chemically bound to a high molecular weight compound such as a carrier protein. Examples of haptens are hormones, drugs, allergens, and organic environment contaminants. Another is immunogen, which is antigen with high molecular weight ( $>1,000$  Da). In addition, antigens can be classified according to their binding characteristics of valency (meaning the total number of sites per antigen) and determinacy (meaning the number of different types of epitope sites per antigen). [17] There are four classes of antigens as listed in Table 2.1.

**Table 2.1 The common classes of antigens [17]**

Class	Epitope	Kind of epitope	Valency	Determinacy
1	Single epitope (Hapten)	A single epitope on antigen binds to antibody	Univalent	Uni-determinate
2	Two or more epitopes	Two or more epitopes of the same kind on antigen molecule	Multivalent	Uni-determinate
3	Many epitopes	Different kinds of epitopes but only one of each kind on one antigen molecule	Univalent	Multi-determinate
4	Many epitopes	Different kinds of epitopes and more than one of each kind per antigen molecule	Multivalent	Multi-determinate

### 2.2.3 Antigen-antibody interaction

Strength of antibody-antigen interaction is expressed by the association constant that indicates affinity of a paratope for a specific epitope as depicted in Figure 2.4. The reversible interaction between antigen and antibody can be formulated as expressed in Equation 2.1.



Where  $[\text{Ab}]$  is antibody concentration  
 $[\text{Ag}]$  is antigen concentration  
 $[\text{Ag-Ab}]$  is antigen-antibody complex

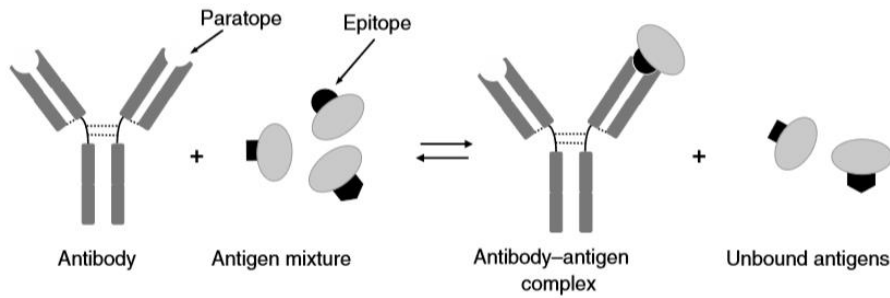


**Figure 2.4 Specific interaction of an antibody with a complement antigen [17]**

Generally, antigen-antibody association constant ( $k_a$ ) can range from  $10^5$ - $10^{12}$   $M^{-1}$ , but only systems with  $k_a > 10^8$  are useful for analytical purposes. The equilibrium association constant can be represented according to the law of mass action as Equation 2.2. A high affinity constant enables to design assays with the limit of detection down to  $10^{-9}$  to  $10^{-12}$  M.

$$K_{eq} = \frac{k_a}{k_d} = \frac{[Ag-Ab]}{[Ag][Ab]} \quad (2.2)$$

Where  $K_{eq}$  is equilibrium constant  
 $k_a$  is association rate constant  
 $k_d$  is dissociation rate constant

Binding interactions between antigen and antibody involve ionic bond, hydrogen bond, hydrophobic force, and van der Waals interaction as illustrated in Figure 2.5. First, the two partners are brought in close proximity and favorable positions by diffusion. When the epitope-paratope distance approaches some nanometers, electrostatic attraction becomes effective. Reducing in the distance between antigen and antibody also allows hydrogen bonds forming between relevant groups in each partner. At a very short distance, van der Waals interactions come into play. In addition, nonpolar groups can aggregate with each other in the aqueous environment by hydrophobic interactions. Consequently, antibody-antigen coupling possesses very high

selectivity due to the interplay of so many interactions combined with steric complementary with respect to shape and chemical reactivity.

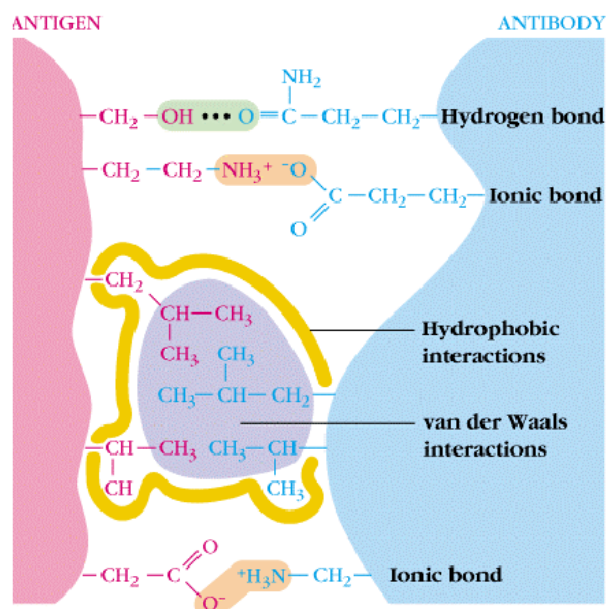


**Figure 2.5 Binding interactions between antigen and antibody [18]**

Even though the antibody-antigen binding has very high affinities, the reversal of antibody-antigen binding may be accomplished under extreme conditions. Therefore, parameters effecting antigen-antibody interactions should be understood and controlled.

#### 2.2.4 Factors affecting antigen-antibody interactions

The antigen-antibody interactions can be influenced by several factors such as antigen and antibody concentration, temperature, pH, and incubation time. [19, 20]

##### 2.2.4.1 Antigen and antibody concentration

Concentration ratio between antigen and antibody influences the antigen-antibody complexes because complex formation is related to the concentration of both antigen and antibody. As shown in Figure 2.6, the best result is reached when antibody molecules are bound to equal total amount of specific antigens, which is called the equivalence point. The rising part of curve is called antibody excess zone (Prozone), and the part of curve beyond equivalence point is called antigen excess zone (Postzone).

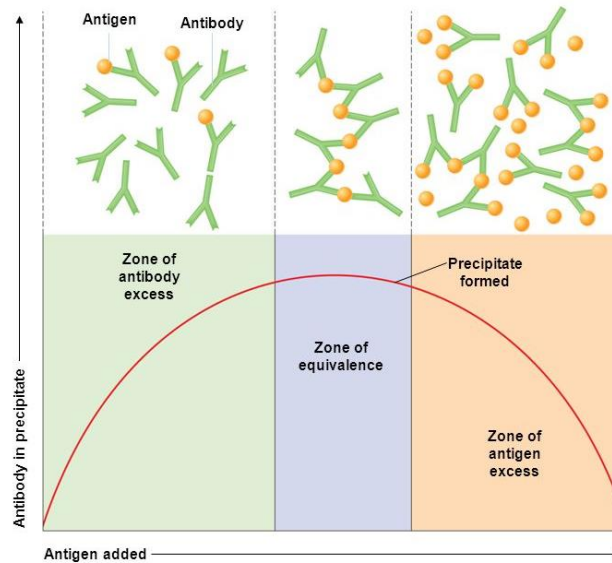


**Figure 2.6 Concentration ratio of antibody to antigen [21]**

#### 2.2.4.2 Temperature

Optimum temperature for antigen-antibody reaction depends on the chemical nature of the epitope, paratope, and bonding involved in their interaction. For example, hydrogen bond formation is more stable at lower temperature. Cold antibody can react well at 2°C to 10°C. Meanwhile, most antibodies react best with their corresponding antigens at 37°C. The antigen-antibody complexes can be dissociated at the temperature raising to about 56°C and they become denatured at temperatures in excess of 50°C.

#### 2.2.4.3 pH

Optimum pH presented in the equilibrium rate of antigen-antibody complex is in a range between 6.5 and 8.4. Below pH 6.5 and above pH 8.4, the antigen-antibody reaction is strongly inhibited because antibody may undergo conformational changes that can destroy the complementarity with the antigen.

#### 2.2.4.4 Incubation time

Reaction between antigen and antibody should be incubated for the optimum time. Too short on incubation period, antigen and antibody may not have sufficient time to form strong interaction. On the other hand, prolonged incubation may

cause dissociation of antigen-antibody complexes. Thus, the best balance of incubation time should be controlled.

### 2.2.5 Immunoassay

Immunoassay [22] is one of the efficient methodologies that demonstrate high selectivity based on complementary binding of antibodies for the recognition and quantitation of antigens. It constitutes an enormous group of assay techniques designed for selective quantitation of both low and high molecular weight species in complex biochemical media. Modern immunoassay methods mostly employ antibodies immobilized onto solid supports and antigen is the analyte. Antibodies can bind strongly and spontaneously to glass, some plastics, or microplates. [23] Figure 2.7 shows an example of a simple step for covalently attaching antibodies to a glass surface. First of all, a glass surface is derivatized with primary amines group ( $\text{-NH}_2$ ). These amines are subsequently reacted to the heterobifunctional crosslinker, resulting in a maleimide-activated surface able to react with sulfhydryl groups on antibodies.

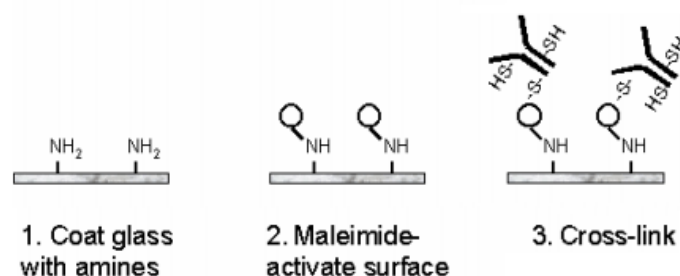


**Figure 2.7 Basic steps involved in attaching antibodies onto a glass surface [23]**

In general, immunoassays employ a variety of different formats for detection of antigens and two common formats popularly used in nowadays are labeled immunoassay and label-free immunoassay.

#### 2.2.5.1 Labeled immunoassay

The ideal label for immunoassay methods should be inexpensive, safe, and simple in preparation. Moreover, the labeled species should be stable and covalently link to antibodies or antigens at multiple sites, which enable the differentiation of the free and the bound forms without requiring a separation step. Enzyme [24] is currently the most widely used because it can provide multiple copies

of detectable species. The immunoassays employing enzymatic labels is named enzyme-linked immunosorbent assay (ELISA). In order to determine antigen, labeled immunoassay based on uncompetitive detection (or sandwich immunoassay) have been frequently performed. This method requires the use of matched antibody pairs (capture and detection antibodies) that are specific for a different epitope of the antigen to achieve accurate results. Firstly, capture antibodies are coated on the wall of glass microplate. The sample are then added, followed by enzyme-labeled detection antibodies, forming a sandwich that is retained on the solid surface as shown in Figure 2.8. The key advantage of a labeled immunoassay its high sensitivity, which is 2-5 times more sensitive than label-free immunoassay. This format also delivers high specificity because two antibodies are used to detect the antigen. Thus, sandwich labeled immunoassay is particularly suited to the analysis of complex samples.

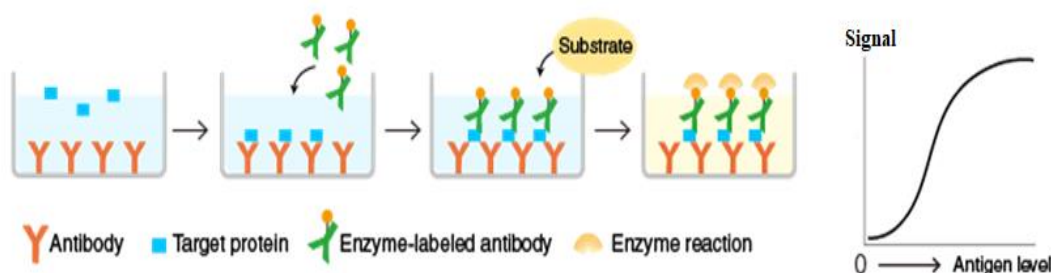


**Figure 2.8 Labeled immunoassay based on uncompetitive detection [25]**

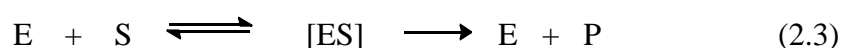
#### 2.2.5.2 Label-free immunoassay

This method is relied on directly detect the binding process between an unlabeled antibodies and antigens. Therefore, label-free immunoassay has been widely applied for various applications because of their simple preparation, more cost effectiveness, does not require an enzyme labels which limits their stability at room temperature, does not need a complicated labeling process. [26, 27] The binding process between an unlabeled antibodies and antigens could be measured by the detection of change in spectra, frequency, or resistance of a surface before and after antigens bind to it using surface plasma resonance (SPR), quartz crystal microbalance (QCM), electrochemical impedance spectroscopy (EIS), and so on. In order to determine

antigen, a fixed number of antibodies are used to coat a glass microplate. Then, samples containing unknown antigen are added, following standard blocking and washing steps. If there is a high concentration of antigen in the sample, a significant change in signal will be observed in comparison to a signal before presenting of sample. In contrast, if there is very little antigen in the sample, a little change in the signal output will be observed.

### 2.3 Recognition by enzyme

Enzyme is protein that functions as catalysts in chemical reactions occurring in living systems. Compound that can be converted by the catalytic action of enzyme is called enzyme substrate. The catalytic property is selective to a particular substrate or to a particular functional group of compounds. Recognition by enzymes is a dynamic process which involves three main steps. First, enzyme substrate is bound to the active site of the enzyme to form a substrate-enzyme complex. Then, the bound substrate undergoes a further chemical conversion. Finally, products are released and the active site of the enzyme returns to its initial state. The reaction between enzyme and its substrate can be represented in Equation 2.3 and Figure 2.9. This sequence is repeated with another substrate molecule as long as the substrate is still present.



Where	E	is	enzyme
	S	is	substrate
	ES	is	enzyme-substrate complex
	P	is	product

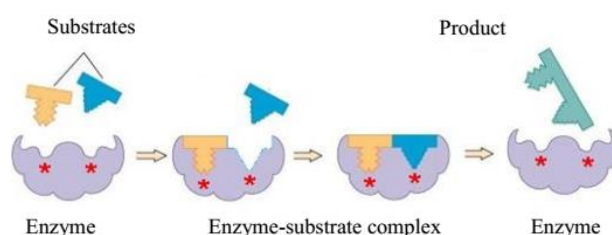


**Figure 2.9 Induced-fit model of enzyme catalysis [28]**



There are several types of enzymes used as receptor for biosensor fabrications. They are classified into six basic groups according to their function on a molecular level. These six types of enzymes; *oxidoreductases*, *transferases*, *hydrolases*, *lyases*, *isomerases*, and *ligases*, and their biological properties are described in Table 2.2.

**Table 2.2 Enzyme categories and their biochemical properties [28]**

Group	Biochemical properties
<i>Oxidoreductases</i>	Catalyze oxidation-reduction reactions where electrons are transferred from one molecule to another. Enzymes of this type are often called <i>oxidases</i> , <i>reductases</i> , and <i>dehydrogenases</i> .
<i>Transferases</i>	Catalyze group transfer reactions from one molecule (donor group) to another molecule (acceptor group). Example functional groups are phosphate, amino, methyl and glycosyl groups.
<i>Hydrolases</i>	Catalyze hydrolysis reactions by breaking single bonds through the addition of water. In general, larger molecules are broken down to smaller fragments by <i>hydrolases</i> .
<i>Lyases</i>	Catalyze elimination reactions where functional groups are added to break double bonds in molecules by the removal of functional groups.
<i>Isomerases</i>	Catalyze structural changes within a molecule, so that, isomeric forms are produced. These enzymes allow for structural or geometric changes but the molecule itself contains the same number.
<i>Ligases</i>	Catalyze condensation reactions to join molecules together with covalent bonds. It is used in catalysis where two substrates are ligated, formation of carbon-carbon, carbon-sulfide, carbon-nitrogen, and carbon-oxygen bonds

The enzymatic biosensors can be designed for the purpose of substrate determination which can be achieved by measuring the steady-state concentration of a product involved in the enzymatic process. In addition, enzymatic biosensor can be

utilized in the determination of inhibitors, which are chemical species that can affect the enzyme activity. Schematic diagram of biosensor for substrate detection and inhibitor detection is shown in Figure 2.10.

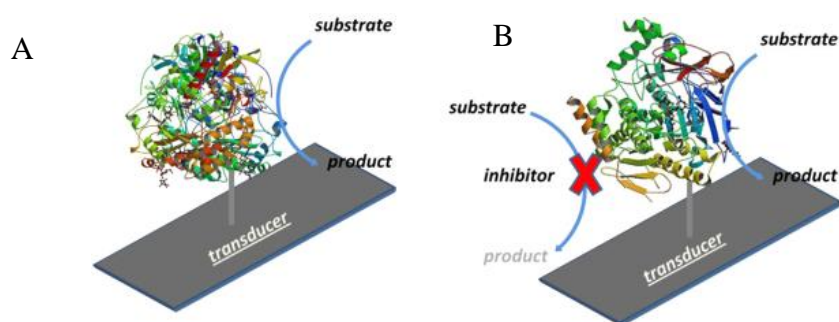


**Figure 2.10** Scheme of enzymatic biosensor for (A) substrate detection and (B) inhibitor detection [29]

### 2.3.1 Factors affecting enzyme activity

The stability and activity of an enzymatic biosensor depends on a number of physical and chemical parameters. Many factors such as temperature, pH, enzyme concentration, substrate concentration, activators and inhibitors are discussed as follow. [30, 31]

#### 2.3.1.1 Temperature

The reaction of enzyme catalysis is based on randomly colliding with its substrate molecules. When temperature increase, the rate of reaction initially increases because of more frequent random collisions between molecules per unit time. However, higher temperature may cause a change in shape of the active site due to bond breaking derived from increase of vibrational energy of enzyme. As a result, the active site is less complementary to the shape of their substrate. Eventually, the enzyme becomes denatured and the rate of reaction begins to decrease. Most enzymes in the human body have an optimum temperature around 37 °C.

#### 2.3.1.2 pH

Extreme change in pH can cause enzyme denature and permanent loss their function due to mismatch of electrostatic or hydrogen bond interaction in enzyme pocket. Most of the enzymes show optimum activity around neutral pH (6-8).

However, there are many exceptions like pepsin (pH of 1-2), acid phosphatase (pH of 4-5) and alkaline phosphatase (pH of 10-11).

#### 2.3.1.3 Enzyme concentration

Changing enzyme concentrations affect the reaction rate of an enzyme catalytic reaction. Rate of the reaction proportionately increase with concentration of enzyme because more frequent collide between enzyme and substrate is occurred at higher enzyme concentration.

#### 2.3.1.4 Substrate concentration

Increase of substrate concentrations gradually raises the rate of reaction within the limited range of substrate levels. More products are produced from reaction due to more substrate molecules collide with enzyme molecules. However, there is a limit of reaction rate after a certain concentration due to saturation at enzyme activity pocket.

#### 2.3.1.5 Activator

Activator is a chemical species that boost enzyme activity. They may be necessary for some kind of enzyme to possess catalytic activity. Additionally, they may increase the specific activity of an activated enzyme such as  $\text{Ca}^{2+}$  and  $\text{Mg}^{2+}$  binding phosphate-containing substrates. An initial rate of reaction can increase if concentrations of activator rise at saturated levels of substrates.

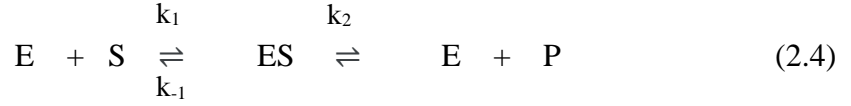
#### 2.3.1.6 Inhibitor

Inhibitor is a chemical species that reduce enzyme activity. It usually interacts with the enzyme resulting in forming enzyme-inhibitor complexes. When inhibitor is removed and enzyme activity is recovered, inhibition reaction is considered as reversible. On the other hand, inhibition is considered to be irreversible when the inhibitor causes a permanent loss of enzyme activity.

### 2.3.2 Enzyme kinetic

The reaction mechanisms of enzyme-substrate mostly refer to the Michaelis-Menten mechanism that is a representative feature of enzyme kinetics. [32, 33] This mechanism model assumes that the enzymatic reaction of free enzyme and its substrate, forming an enzyme-substrate (ES) complex followed by conversion to product, is reversible formation. The Michaelis-Menten mechanism can be formulated as a two-

step process (Equation 2.4), denoted by E, S, and P as enzyme, substrate, and product, respectively, and k symbols be assigned to relevant reaction rate constants.



The rate of reaction for generating the product is as Equation 2.5.

$$\text{rate} = \frac{d[P]}{dt} = k_2[ES] \quad (2.5)$$

Here, the rate of reaction becomes dependent on the ES complex. Therefore, all enzyme molecules are in the form of ES complex.

$$\text{Rate of [ES] formation: } \frac{d[ES]}{dt} = k_1[E][S] = k_1([E]_0 - [ES])[S] \quad (2.6)$$

$$\text{Rate of [ES] consumption: } -\frac{d[ES]}{dt} = k_{-1}[ES] + k_2[ES] \quad (2.7)$$

where  $[E]_0$  is the original concentration of enzyme. According to steady state approximation, the rate of formation (Equation 2.6) is equal to the rate of consumption (Equation 2.7) as can be seen in Equation 2.8.

$$k_1([E]_0 - [ES])[S] = k_{-1}[ES] + k_2[ES] \quad (2.8)$$

$$\text{Therefore, } [ES] = \frac{[E]_0[S]}{\frac{k_{-1} + k_2}{k_1} + [S]} = \frac{[E]_0[S]}{K_m + [S]} \quad (2.9)$$

Substituting Equation 2.9 into Equation 2.5, the final rate equation of product is obtained as Equation 2.10.

$$\frac{d[P]}{dt} = \frac{[k]_2[E]_0[S]}{K_m + [S]} \quad (2.10)$$

For high substrate concentrations, where  $[S] \gg K_m$ , Equation 2.10 simplifies to Equation 2.11.

$$\frac{d[P]}{dt} = \frac{[k]_2[E]_0[S]}{K_m + [S]} \approx \frac{[k]_2[E]_0[S]}{[S]} = k_2[E]_0 = V_{\max} \quad (2.11)$$

Substituting  $k_2[E]_0 = V_{\max}$  into Equation 2.10, the equation is known as the Michaelis-Menten equation (Equation 2.12).

$$\text{rate of reaction (v)} = \frac{V_{\max}[S]}{K_m + [S]} \quad (2.12)$$

It is assumed above that the substrate concentration is constant. Two kinetic constants in the Michaelis-Menten rate equation ( $K_m$  and  $V_{\max}$ ) are determined.

#### 2.3.2.1 Michaelis constant ( $K_m$ )

This constant describes the substrate concentration at which half the active sites of enzyme are occupied by substrate. Therefore,  $K_m$  value indicates the binding strength of the enzyme to its substrate. A high  $K_m$  value indicates that the enzyme binds the substrate weakly. Conversely, a low  $K_m$  value indicates a higher affinity for the substrate.

#### 2.3.2.2 Maximal velocity ( $V_{\max}$ )

This constant reflects how fast the enzyme can catalyze the reaction. The rate of enzymatic reaction increases with the increase of the substrate concentration up to a certain level ( $V_{\max}$ ). At this level, increase in substrate concentration does not cause any increase in reaction rate because no more enzyme is available for reacting with substrate.

These two constants play an important role. They are important to know in order to understand enzyme activity and to understand the effects of enzyme

inhibitors. The graphical evaluation of nonlinear plots from Michaelis-Menten equation is showed in Figure 2.11(A). However, there are some problems associated with evaluating enzyme kinetics using a nonlinear plot. This issue can be avoided and an accurate determination of  $K_m$  and  $V_{max}$  can be obtained by means of a linearized form, which is known as the Lineweaver-Burk equation (Equation 2.13). It is a inverse form of Michaelis-Menten equation (Equation 2.12). The graphical determination of  $K_m$  and  $V_{max}$  by Lineweaver-Burk plot is shown in Figure 2.11(B). This plot is commonly used for examining enzyme kinetics nowadays.

$$\frac{1}{v} = \frac{K_m + [S]}{V_{max}[S]} = \left(\frac{K_m}{V_{max}}\right)\left(\frac{1}{[S]}\right) + \frac{1}{V_{max}} \quad (2.13)$$

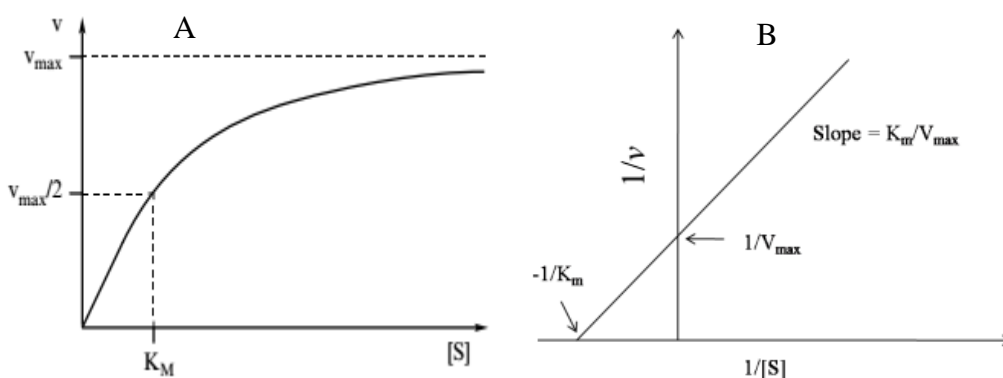


**Figure 2.11 A plot of enzyme kinetics according to the (A) Michaelis-Menten equation and (B) Lineweaver-Burk plot [34]**

### 2.3.3 Enzyme inhibition

Some compounds can bind to an enzyme molecule as an activator and thereby enhancement of enzyme activity. Meanwhile, some groups of compound acts as an inhibitor and thereby reducing enzyme activity. The detection based on enzyme inhibition allows the quantification of inhibitor concentration by standard assay methods, which is suitable for determination of substances that couldn't be directly detected based on enzyme catalysis. [35, 36] The inhibition of the enzyme can be either reversible or irreversible.

### 2.3.3.1 Reversible inhibition

Reversible inhibition involves a reversible reaction between inhibitor and enzyme. Inhibitor (I) may bind with enzyme in the free state (E) to form a binary (EI) complex as Equation 2.14. Meanwhile, inhibitor may also bind with a part of an enzyme-substrate (ES) to form a ternary (ESI) complex as Equation 2.15.



Reversible inhibition mechanism of the enzyme activity can further be classified into competitive, noncompetitive, and uncompetitive inhibition as shown in Figure 2.12. Details of each type of inhibitors are showed in Table 2.3.

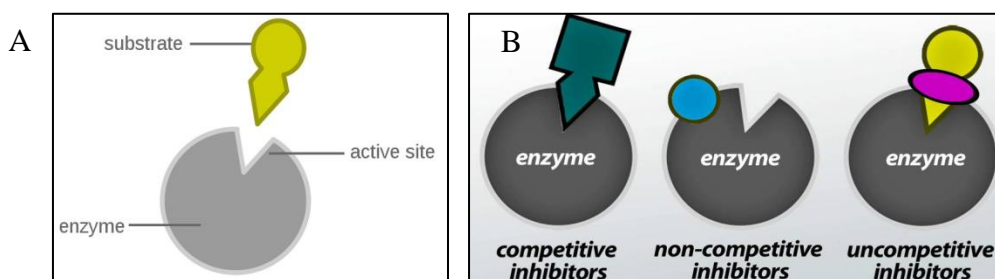


**Figure 2.12** Diagram of (A) normal binding of enzyme with its substrate and (B) reversible enzyme inhibition [36]

**Table 2.3** Type of reversible enzyme inhibitors [37]

Inhibitor type	Binding site on enzyme	Kinetic effect
Competitive inhibitor	<ul style="list-style-type: none"> <li>- Inhibitor competitively binds to active site of enzyme due to its close resemblance to substrate structure.</li> <li>- Inhibition can be reversed by increasing the concentration of substrate to a level where it out competes inhibitor.</li> </ul>	No change in $V_{\max}$ but $K_m$ increased

**Table 2.3 Type of reversible enzyme inhibitors (continued) [37]**

<b>Inhibitor type</b>	<b>Binding site on enzyme</b>	<b>Kinetic effect</b>
Noncompetitive inhibitor	<ul style="list-style-type: none"> <li>- Inhibitor binds to a site on enzyme which is totally different from active site.</li> <li>- This inhibition cannot be reversed by increasing the substrate concentration due to different binding site of inhibitor and substrate.</li> </ul>	No change in $K_m$ but $V_{max}$ decreased
Uncompetitive inhibitor	<ul style="list-style-type: none"> <li>- Inhibitor binds only to the ES complexes.</li> <li>- This ESI cannot form product due to conformational changes in enzyme.</li> </ul>	Both $V_{max}$ and $K_m$ decreased

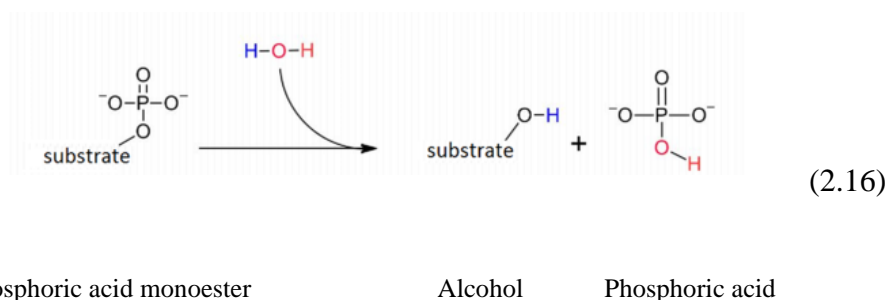
#### 2.3.3.2 Irreversible inhibition

Inhibitors strongly interact with enzymes in the irreversible process resulted in formation of a covalent bond between the enzyme active center and the inhibitor. This interaction led to a reduction of the active enzyme concentration and a destruction of the enzyme-substrate binding ability. In contrast to reversible inhibition, which is a fast and diffusion-controlled process, irreversible inhibition is a slow reaction that needs long incubation time to be completed. During this stage, enzyme activity decreases exponentially.

#### 2.3.4 Acid phosphatase

Acid phosphatase (ACP) [38, 39] is a family of enzymes widespread found in many animals and plant species. It is classified in a subcategory of *hydrolase*. In general, ACP is most effective in acidic environment. ACP catalyze the hydrolysis of a phosphoric acid monoester. Water is split in the reaction, with the -OH group attaching to the phosphate ion and the  $H^+$  protonating the hydroxyl group of the substrate. The net result of the reaction is the destruction of a phosphoric acid monoester and the creation of both alcohol and phosphoric acid as Equation 2.16.





ACP is a zinc-containing dimeric enzyme with molecular weight (MW) of 86,000 Da. Each monomer contains 429 amino acids with four cysteine residues linking two zinc atoms ( $\text{Zn}^{2+}$ ) and one magnesium atoms ( $\text{Mg}^{2+}$ ). The mechanism of ACP involves the geometric coordination of the substrate between the  $\text{Zn}^{2+}$  ions in the active sites, whereas the  $\text{Mg}^{2+}$  site doesn't appear to be close enough to directly partake in the hydrolysis mechanism. However,  $\text{Mg}^{2+}$  contributes to the shape of the electrostatic potential around the active center.

In this thesis, electrochemical method is one of the detection transducers for record the signal and its principle is explained in the next section.

## 2.4 Electrochemical method

Electrochemistry [40] is a method that is useful for qualitative and quantitative analysis of analytes via electrical parameters, such as current, potential, resistance, and impedance. An electrochemical reaction can be defined as a chemical reaction involving charge transfer of electrons through an interface between electrolyte solution and electrode surface. Electrons can be transferred from electrode to chemical specie in solution or released electrons from chemical substance can be taken up by electrode. This is generally given by Equation 2.17.



O and R denotes as oxidant and reductant, respectively.  $n$  represents number of electrons transferred over electrode interface. The electrical current flowing through an electrical system is carried by electrons and this current value can be positive or negative depending on the direction of electron transfer (from or to the electrode). For an

electrochemical data, positive potentials are directed to the right of the origin and anodic (oxidation) currents are taken as positive (directed upward from the origin), as showed in Figure 2.13. For electrochemical measurements, three electrodes are always necessary to realize and study an electron-transfer reaction which is explained in the next topic.

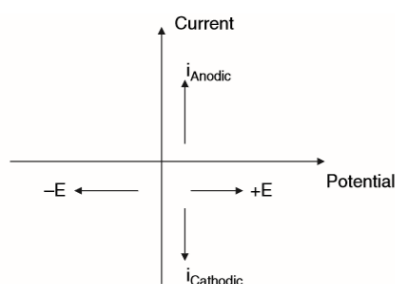


**Figure 2.13 Sign conventions used in nowadays [41]**

#### **2.4.1 Electrochemical system and electrode configuration**

A basic electrochemical cell always consists of three electrodes, including working electrode, reference electrode, and counter electrode. These electrodes are immersed in an electrolyte solution and connected to a direct current (DC) source, as shown in Figure 2.14. At the interface of the WE and electrolyte solution, the electrons are taken up by chemical substances and an equal number of electrons are taken up by the electrode. In this setup, a potential is applied over the WE and RE, while the current is flowing between the WE and CE.

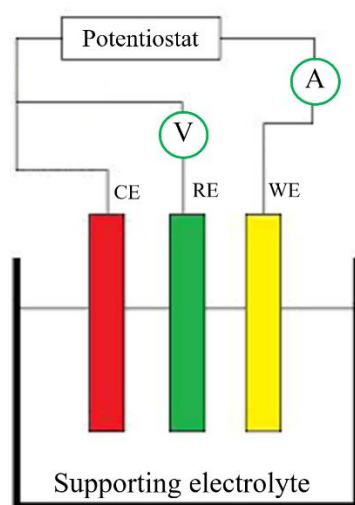


**Figure 2.14 Basic three-electrodes electrochemical system [42]**

#### 2.4.1.1 Reference electrode

The reference electrode (RE) is an electrode which has a stable and well-known electrode potential. It is used as a point of reference in the electrochemical cell for the potential control and measurement. The current flow through the RE is kept close to zero, which is achieved by using the CE to close the current circuit in the cell together. The RE normally used in nowadays is a silver-silver chloride electrode (Ag/AgCl) [43] with a reference potential of 0.222V versus the standard hydrogen electrode (SHE), an electrode selected as reference point having a potential of zero.

#### 2.4.1.2 Counter electrode

The counter electrode (CE), also known as auxiliary electrode (AE), is an electrode which is used to close the current circuit in the electrochemical cell and usually does not participate in the electrochemical reaction. Because the current is flowing between the WE and the CE, the total surface area of the CE must be higher than the area of the WE at least ten times greater. As a result, it will not be a limiting factor in the kinetics of the electrochemical process under investigation. In addition, the CE should be a good electrical conductor in order to allow high amount of current pass easily. Generally, platinum electrode is used in the field of electrochemical detection.

#### 2.4.1.3 Working electrode

The working electrode (WE) is the electrode in an electrochemical system on which the reaction of interest is occurring. It can be made of inert materials

such as gold, silver, platinum, glassy carbon, and so on. In this thesis, WE have been fabricated by using carbon materials because they can be adapted to various electrode configurations with great flexibility in sizes and shapes as well as their low cost, easy preparation, and renewal. Therefore, glassy carbon paste electrode and screen-printed carbon electrode were prepared to apply as the WE for construction of the electrochemical sensors and biosensors.

### 1) Glassy carbon paste electrode

Glassy carbon paste electrode (GCPE) is a mixture of glassy carbon materials and a liquid binder, such as mineral oil and paraffin oil, packed into electrode body as displayed in Figure 2.15. This electrode represents one of the most popular types of WE that offer simple laboratory preparation due to its inexpensive and sensitive, have unique surface characteristics, easy preparation with convenient modification, renewability in surface, wide potential window with low background signal, and suitable for various sensing of electrochemically active species. [44] Moreover, the selectivity and sensitivity of the GCPE can be improved by incorporating a selective agent and conducting materials in the glassy carbon paste. So that, design and synthesis of new modifiers to gain higher selectivity and sensitivity is a challenging requirement recently.

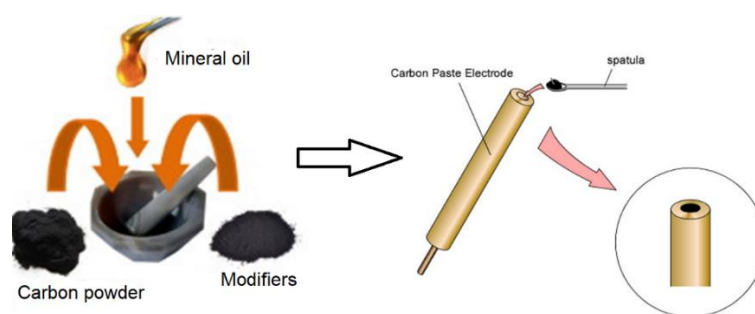


**Figure 2.15 Preparation process of glassy carbon paste electrode [45]**

### 2) Screen-printed carbon electrode

Screen-printed carbon electrodes (SPCE) has got widespread popularity among the various carbon-based electrodes due to its advantages such as simple fabrication, low cost, small size, disposability, portability, and easy mass-

production. [46] Moreover, the whole three-electrode system can be printed on the same substrate surface, which could be easily controlled and designed by a printing machine or homemade block screen as depicted in Figure 2.16. The RE providing stable and accurate potential can be made by printing of silver ink while the CE which allows charge to flow to the WE generally made by printing of carbon ink. At the same time, the WE is also produced by printing of carbon ink onto a same substrate. Moreover, the inks used for printing could be modified or added with some modifiers in order to improve electrochemical properties.

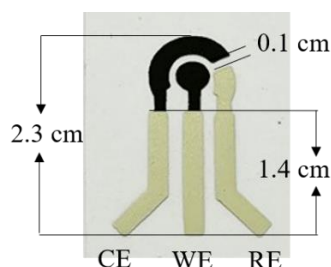


**Figure 2.16 A design of a portable screen-printed carbon electrode**

## 2.4.2 Electrochemical technique [41, 47, 48]

### 2.4.2.1 Cyclic voltammetry

Cyclic Voltammetry (CV) is a technique performed by cycling the potential and measuring the resulting current. In the forward scan of Figure 2.17(A), the potential is positively scanned starting from a lower potential (a) and ending at a greater potential (d). The potential extreme (d) is called the switching potential, which is the point where the voltage is sufficient to have caused an oxidation or reduction of an analyte. After that, the negatively reverse scan occurs from a higher potential (d) to a lower potential (g). The oxidation reaction occurs from (a) to (d) and a reduction reaction occurs from (d) to (g). This cycle can be repeated and the scan rate can be varied. Figure 2.17(B) shows a cyclic voltammogram resulting from a single electron reduction and oxidation. The resulting current occurred from positively scanned potential is called anodic current ( $i_{pa}$ ) and the corresponding peak potential occurs is called the anodic peak potential ( $E_{pa}$ ). After switching potential, the reduction process occurs via negatively scanned potential. This process presents in cathodic current ( $i_{pc}$ ) and cathodic

peak potential ( $E_{pc}$ ). In principle, the cyclic voltammogram is used to characterize potential oxidation or reduction of analytes.

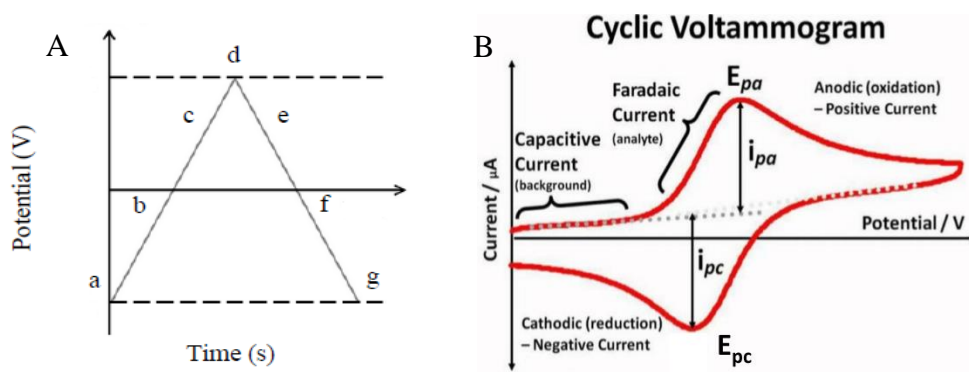


**Figure 2.17 (A) The waveform of potential applied and (B) voltammogram of a single electron oxidation-reduction in cyclic voltammetry [49]**

#### 2.4.2.2 Linear sweep voltammetry

Linear sweep voltammetry (LSV) is also known as fast direct-current voltammetry. The scan rates of 0.01-20 V/s are used, which is resulted in a peak-shaped current response. This method is identical to cyclic voltammetry, except that the potential is swept from a starting potential to an end potential without returning to the initial starting potential. However, a drawback of using fast scan rates is the increasing background current due to the capacitive charging effect of the electrical double layer. In LSV, the potential of the WE is ramped from an initial potential ( $V_1$ ) to a final potential ( $V_2$ ), as can be seen in Figure 2.18(A). Figure 2.18(B) shows a linear-sweep voltammogram depicted as a function of scan rate.

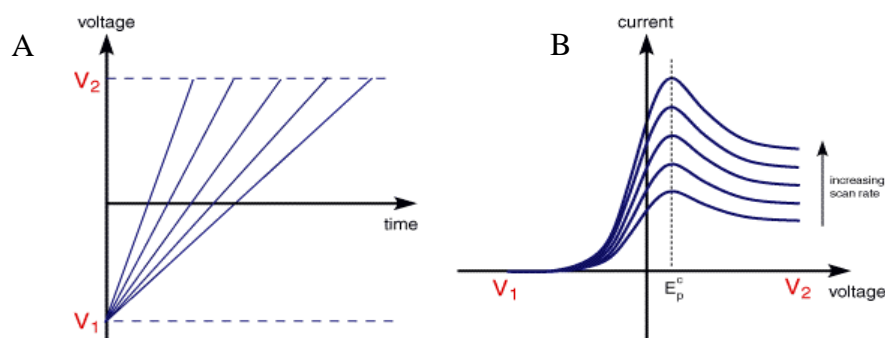


**Figure 2.18 (A) The potential waveform and (B) voltammogram of LSV [50]**

### 2.4.2.3 Differential pulse voltammetry

In differential pulse voltammetry (DPV), short pulses ( $t = 10\text{--}100$  ms) with limited amplitude ( $\Delta E = 1\text{--}100$  mV) are scanned linearly increasing, as showed in Figure 2.19(A). Practically, the current is measured before the application of a pulse ( $I_1$ ) and at the end of the pulse ( $I_2$ ). The resulting current is attributed to the difference in pulse potential ( $I_2 - I_1$ ) and the voltammogram of the pulse current is illustrated in Figure 2.19(B). A maximum in the difference between two pulse will be obtained at the highest point of the voltammogram. This point corresponds to the half-wave potential. Therefore, the peak potential in DPV is identical to characterize oxidation or reduction reaction of analyte.

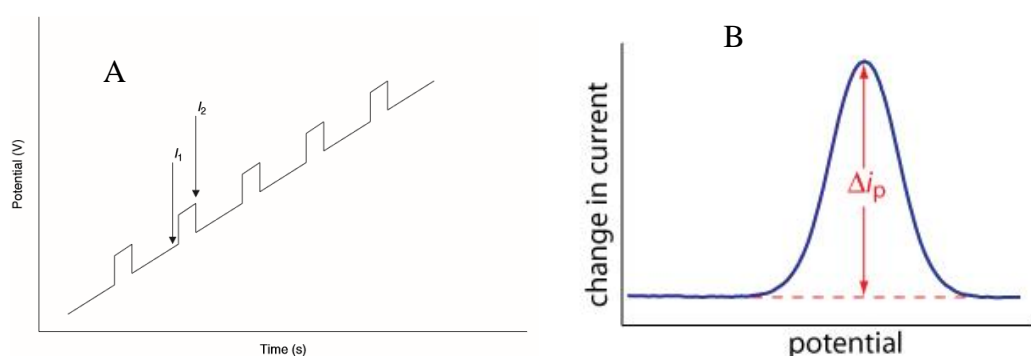


**Figure 2.19 (A) A profile of the applied potential and (B) the signal in DPV [41]**

### 2.4.2.4 Chronoamperometry

Chronoamperometry is a technique for measurement of the current that a fixed potential is applied on a WE. The oxidation or reduction reaction of electroactive substance resulted in electron transfer take place on the surface of WE. The reaction considers as a set of equilibrium involved in the diffusion of the reactant to the electrode and the diffusion of the product away from the electrode surface into the bulk of the solution under stirring condition (Figure 2.20). The resulting current has become effectively dependent of time as indicated by the Equation 2.18.

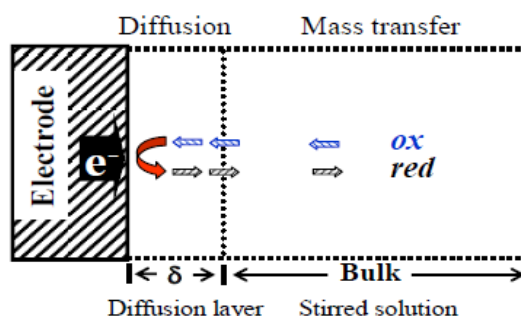


**Figure 2.20** Schematic diagram of electrode reaction processes involved in stirred solution. Arrows indicated the direction of oxidizing species (ox) moving into the electrode and reduced to reducing species (red) which move out to the bulk solution

$$I = nFAC \sqrt{\frac{D}{\pi t}} \quad (2.18)$$

Where	I	is	current (A)
	n	is	number of electrons
	A	is	area of electrode (cm <sup>2</sup> )
	C	is	concentration of solution (mol.L <sup>-1</sup> )
	D	is	diffusion coefficient (cm <sup>2</sup> .s <sup>-1</sup> )
	t	is	time (s)

#### 2.4.2.5 Electrochemical impedance spectroscopy

Electrochemical impedance spectroscopy (EIS) is a technique applied for investigation of external parameters that has an influence on the electrical conductivity of an electrochemical system. In particular, measurement of the impedance is useful in systems that cannot be studied with direct current methods. The principle of this technique is to apply an alternating signal of small amplitude (5-20 mV) to an electrode inserted into an electrolyte, the resulting current is obtained based on Ohm's law. The initial disturbance, which is a sinusoidal disturbance potential ( $\Delta E$ ), and the response of the electrode, which is sinusoidal current ( $\Delta I$ ), are compared by measuring



the phase shift ( $\phi$ ) of the current and voltage components from the applied signal. Therefore, the impedance, which is represented by  $Z$ , measures the relationship between  $\Delta E$  and  $\Delta I$ . The equation of Euler allows both signals to be written as complex e-powers (Equation 2.19 and 2.20).

$$E(t) = E_m e^{j(\omega t + \alpha)} \quad (2.19)$$

$$I(t) = I_m e^{j(\omega t + \beta)} \quad (2.20)$$

Where	$E(t)$	is	alternating potential
	$I(t)$	is	alternating current
	$E_m$	is	amplitude of potential (V)
	$I_m$	is	amplitude of signal (A)
	$\omega$	is	angle frequency $\omega=2\pi f$ (f in Hz)
	$t$	is	time
	$\alpha$ and $\beta$	is	phase

The impedance is defined as the ratio of the alternating potential and the alternating current signal as Equation 2.21.

$$Z(\omega) = \frac{E(t)}{I(t)} = \frac{E_m}{I_m} e^{j(\alpha - \beta)} = \frac{E_m}{I_m} e^{j\phi} = |Z| e^{j\phi} \quad (2.21)$$

This impedance can be presented as a vector in the complex plane with modulus  $|Z| = E_m/I_m$  and argument  $\phi = \alpha - \beta$ . The projection of the impedance vector at the axes results in resistance ( $Z'$ ) and reactance ( $Z''$ ), also called the real and imaginary part of the impedance, respectively (Figure 2.21 and Equation 2.22).

$$Z(\omega) = Z'(\omega) + jZ''(\omega) \quad (2.22)$$

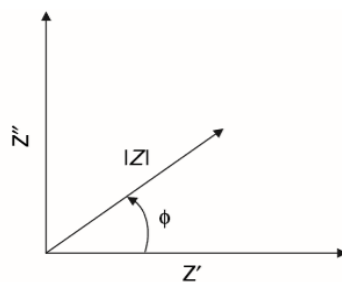


**Figure 2.21** Scheme of the impedance presentation in the complex plane [41]

The impedance of the three-electrode electrochemical cell is usually modeled with the electrical equivalent circuit corresponding to a Nyquist plot as showed in Figure 2.22. The electrochemical cell includes an electrical resistance of the electrolyte ( $R_s$ ), a double-layer capacitance at the interface between WE and electrolyte ( $C_{dl}$ ), a charge transfer resistance due to the redox reaction of a redox probe in electrolyte solution with the WE ( $R_{ct}$ ), and the Warburg impedance due to the diffusion process of reactants ( $Z_w$ ). In principle, the  $R_{ct}$  is the only circuit element that directly controls the electron transfer kinetics of the redox-probe during the reaction on the electrode surface, and it corresponds to the diameter of the semicircle. [51] Thus, a larger diameter of the semicircle means the higher resistance (lower conductance), while a smaller diameter of the semicircle corresponds the lower resistance (higher conductance).

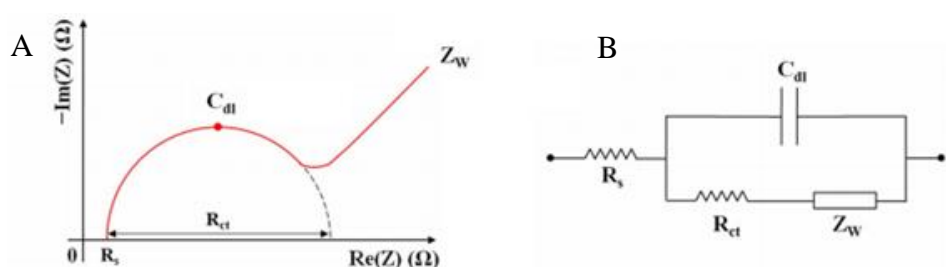


**Figure 2.22** (A) Nyquist diagram and (B) its equivalent circuit [41]

Furthermore, surface enhanced Raman spectroscopy (SERS) is also employed for the signal recorded in this thesis and its principle is explained in the next section.

## 2.5 Raman spectroscopy

Raman spectroscopy [52-54] is a spectroscopic technique used to observe vibrational, rotational, and other low-frequency modes in a system. It is commonly used in chemistry to provide a structural fingerprint in order to identify molecules. In addition, this technique has been applied frequently for both of qualitative and quantitative analysis. The principle relies on scattering of monochromatic light produced from a laser in the visible, near infrared, or near ultraviolet range. A sample is illuminated with a laser beam which interacts with the molecules of sample and originates a scattered light in all directions after its interaction, as can be seen in Figure 2.23. Majority of this scattered radiation that has a frequency equal to frequency of incident light is called Rayleigh scattering. While only a small fraction of scattered radiation having a frequency different from the incident light is called inelastic scattering. The shift in frequency from inelastic scattering gives information about the rotational or vibrational modes in the system, which is used to construct a Raman spectrum.

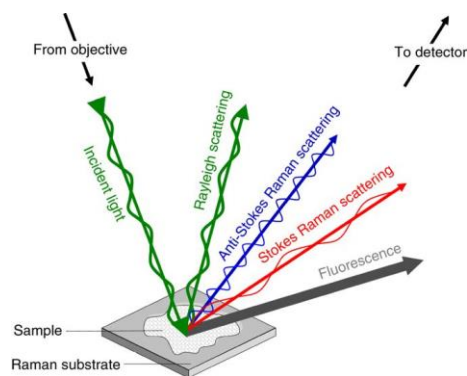


**Figure 2.23 A simple schematic diagram of the Raman effect [55]**

When the frequency of incident radiation is higher than frequency of scattered radiation, Stokes lines appear in Raman spectrum. But when the frequency of incident radiation is lower than frequency of scattered radiation, anti-Stokes lines appear in Raman spectrum. Figure 2.24 shows energy-level diagram involved in Rayleigh scattering and Raman scattering. Stokes shifted Raman bands involve the transitions from ground state at a lower energy vibrational levels to virtual state, while anti-Stokes bands involve the transitions from ground state at a higher energy vibrational levels to

virtual state. Therefore, Stokes bands are more intense than anti-Stokes bands because analyte molecules mostly locate at the lower energy levels and hence Stokes bands are used in conventional Raman spectroscopy. Meanwhile, anti-Stokes bands are measured with fluorescing samples because fluorescence causes interference with Stokes bands.

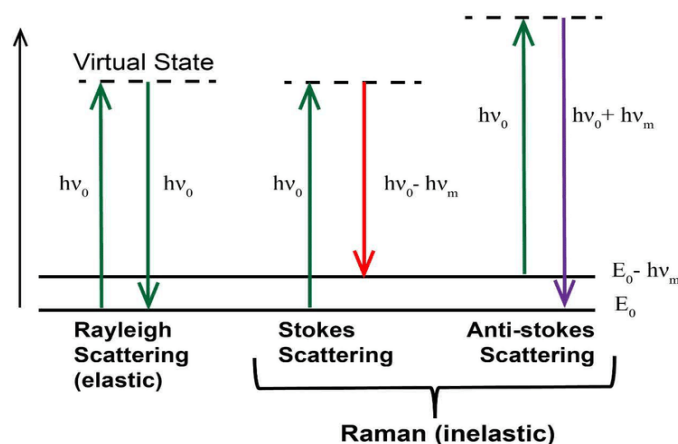


**Figure 2.24 Jablonski diagram of energy states for Rayleigh, Stoke and anti-Stoke scattering [56]**

Raman effect is based on the interaction between the electron cloud of a sample and the external electric field of the monochromatic light, which can create an induced dipole moment within the molecule based on its polarizability. The intensity of the Raman scattering is proportional to this polarizability change. Therefore, a change in polarizability during molecular vibration is an essential requirement to obtain Raman spectrum. In contrast to infrared (IR) spectroscopy, a complementary technique to Raman spectroscopy, it depends on a change in the dipole moment of a molecule. Raman spectroscopy measures relative frequencies from scatters radiation, but IR spectroscopy measures absolute frequencies from absorbs radiation. In general, the strong bands in the IR spectrum corresponds to weak bands in the Raman spectrum and vice versa. However, a big advantage of using Raman over IR is that the sample preparation is much easier and less time-consuming. In addition, Raman spectrum is significantly simpler than their IR counterparts (Figure 2.25). Moreover, Raman spectroscopy is the method of choice for studying aqueous solutions because IR spectroscopy relies on the absorbance or transmittance of infrared light and water is a strong absorber. These

advantageous features make Raman spectroscopy more suitable for various applications than IR spectroscopy.

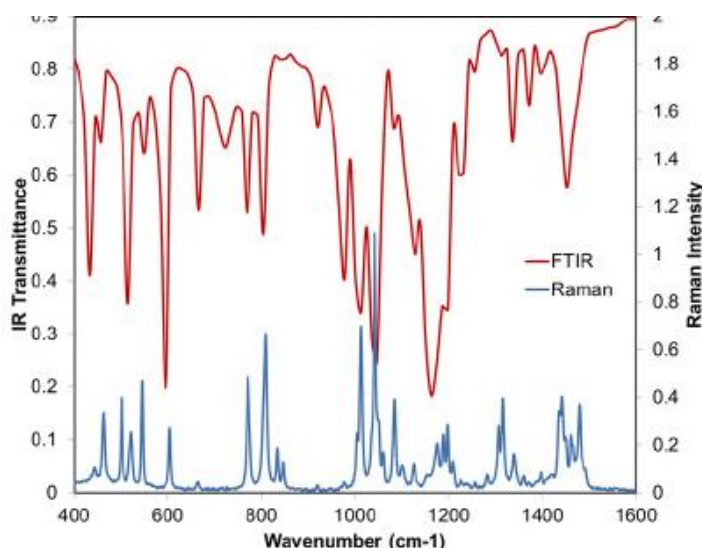


**Figure 2.25 The infrared and Raman spectrum of biological buffer [57]**

In Raman spectrum, the intensity of measured Raman scattering is plotted versus the Raman shift. The Raman shift is defined as difference between the measured frequency of scattered light and incident light. The Raman shift is given as change of the wavenumber ( $\text{cm}^{-1}$ ) which is inversely proportional to the wavelength. However, a classical Raman scattering produces only very weak signals which limits the application of Raman spectroscopy. Therefore, surface-enhanced Raman spectroscopy have been widely applied instead classical Raman spectroscopy. This technique employs the influence of small metal particles on the elementary process of Raman scattering and the Raman spectra are recorded with the same spectrometers as classical Raman spectroscopy.

### **2.5.1 Surface-enhanced Raman spectroscopy**

Surface enhanced Raman spectroscopy (SERS) is essentially combination of two technologies, namely Raman spectroscopy and nanotechnology. It has been emerged as one of the most promising analytical tools in recent years and it is particularly well suited for the detection of various chemical substances compared with other techniques due to its outstanding advantages. [58, 59] For instance, SERS can be

applied for not only quantitative analysis but also qualitative analysis because the spectra are related to the chemical structure of the target molecules, thus yielding fingerprint information that can be identified. However, a classical Raman spectroscopy is not applicable for sensitive detection due to the inherently weak Raman signals. Therefore, researchers discovered that Raman signals can be enhanced by  $10^4$ - $10^5$  if the target analyte is placed in close to a roughened noble metallic nanostructure as displayed in Figure 2.26.

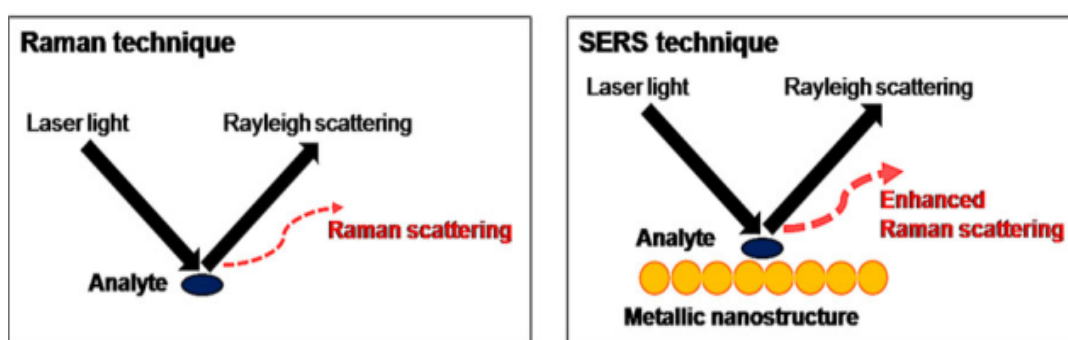


**Figure 2.26** Illustration of SERS mechanism [60]

The SERS enhancement factor (EF) is a key characteristic of the SERS effect. Two types of EFs calculation have been proposed with the aim to find a quantity enabling to compare experiments across different substrates and different conditions. The first one is comparison of intensities of the strongest band in SERS ( $I_{\text{SERS}}$ ) and conventional Raman spectrum ( $I_{\text{RS}}$ ) divided by numbers of molecular scatters participating on the substrate surface, which is performed at the same set-up experiment [61, 62] as depicted in Equation 2.23.

$$\text{EF} = \frac{I_{\text{SERS}} / N_{\text{SERS}}}{I_{\text{RS}} / N_{\text{RS}}} \quad (2.23)$$

Another EF calculation is the analytical enhancement factor (AEF). This calculation considers ratio of intensities of  $I_{\text{SERS}}$  and  $I_{\text{RS}}$  and molecular concentrations in analyzed solutions (Equation 2.24).

$$AEF = \frac{I_{SERS} / C_{SERS}}{I_{RS} / C_{RS}} \quad (2.24)$$

In principle, the SERS intensity of a free molecule depends on the induced dipole moment ( $P$ ) at the Raman-scattered frequency ( $\omega_R$ ) and position ( $r_m$ ). The induced dipole moment can be expressed as the product of the incident electric field strength ( $E$ ) and the molecular polarizability ( $\alpha$ ), as Equation 2.25. The polarizability reflects the modulation of the incident photons at frequency  $\omega_0$  and inelastic Raman photons at frequency  $\omega_R$ , while the electric field reflects the modulation of the incident photons at frequency  $\omega_0$  by the molecular vibration correlated with the position. [63]

$$P(\omega_R, r_m) = \alpha(\omega_R, \omega_0) E(\omega_0, r_m) \quad (2.25)$$

The interaction of the molecule with a rough metal surface must enhance either  $\alpha$  or  $E$ . Therefore, two possible mechanisms have been considered to explain the SERS effect. The first one involves enhancements in the electromagnetic field intensity as a result of plasmon resonance excitation, which is called electromagnetic enhancement mechanism. The another one is enhancement in polarizability due to chemical effects such as charge-transfer excited states, which is called chemical or molecular enhancement mechanism.

#### 2.5.1.1 Chemical enhancement mechanism

Chemical enhancement (CM) is attributed to the increase in the probability of a Raman transition when molecules are adsorbed onto roughened surfaces. [64] In this mechanism, the charge transfer mechanisms occur from the formation of charge transfer complexes between adsorbed analyte molecules and metal surface, where the excitation wavelength interacts with the charge transfer electronic states within the analyte and metal. Chemical enhancement can also contribute to the Raman polarizability of the free molecule or of the surface complex. The magnitudes of enhancement are highly specific to molecular states of the analyte molecules and also depends critically on the nature of the specific location or environment of the substrate surface. Normally, the contribution of chemical enhancement is  $10^2$ - $10^3$ .

### 2.5.1.2 Electromagnetic enhancement

Electromagnetic mechanism (EM) is based on enhancement of the electromagnetic field due to resonance excitations of electron oscillations at the roughened metal surface. When the wavelength of the incident electromagnetic field is close to the plasma wavelength of the metal, electron can be excited into an extended surface electronic state, which is called surface plasmon resonance. Surface plasmon is often separated into two categories as showed in Figure 2.27. Firstly, localized surface plasmons is the phenomenon in which the electrons coherently oscillate locally within and in the closed surface of a metallic nanostructure. Secondly, surface- plasmon polaritons is the phenomenon in which the coherent electron oscillation propagates as a longitudinal wave along the metal surface. [65]

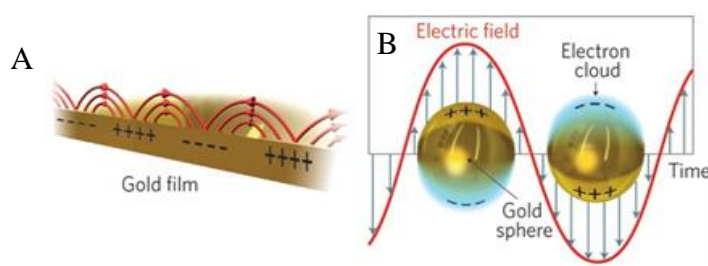


**Figure 2.27 (A) Surface plasmon polariton and (B) Localized surface plasmon resonance [66]**

The coupled state of the photon and localized surface plasmon resonance is accompanied by sharply enhanced amplitude of the electromagnetic field. Therefore, it can be concluded that EM is dominant for SERS contributed from the large electromagnetic field induced by the excitation of localized surface plasmon resonance. [67] Only the free electron like noble metals (Ag, Au, Cu) or the alkali metals are proper materials for surface-enhancing substrates, providing the EF up to  $10^5$ . Transition metals, such as Pt, Ru, Rh, Pd, Fe, Co, and Ni, are also applicable but they are generally less enhancing (EF value up to  $10^1$ - $10^4$ ). [68] However, the blooming of SERS in nowadays led to the development of nanostructures based on Au or Ag metals because they can greatly support surface plasmonic activity. [69] The EM field near a nanostructured material is often highly in the gap between Au or Ag nanoparticles,



which is called SERS hotspots. This space provides very intense the local EM field due to the strong EM coupling as can be seen in Figure 2.28(A). First-generation hotspots have been generated in assemblies of single nanoparticles with various shape designed such as nanosphere, nanorod, nanocube, nanostar, and so on. Second-generation SERS hotspots arise from coupled nanostructures with controllable inter-particle nanogaps. The SERS intensities from coupled plasmonic nanostructures are four orders of magnitude greater than using single nanostructures. [70] Even through second-generation hotspots produce very intense EM field, hybrid structures consisting of plasmonic nanostructures and other materials, such as silicon and semiconductor materials, have been proved as third-generation hotspots. This generation result from the hybridization of the EM field scattered from the plasmonic nanoparticles and the EM field reflected from the substrate material surfaces. The resulting EF depends crucially on the dielectric properties of the substrate materials, which can normally contribute enhancement of EM up to  $10^8$ . The generations of SERS hotspot are displayed in Figure 2.28(B).

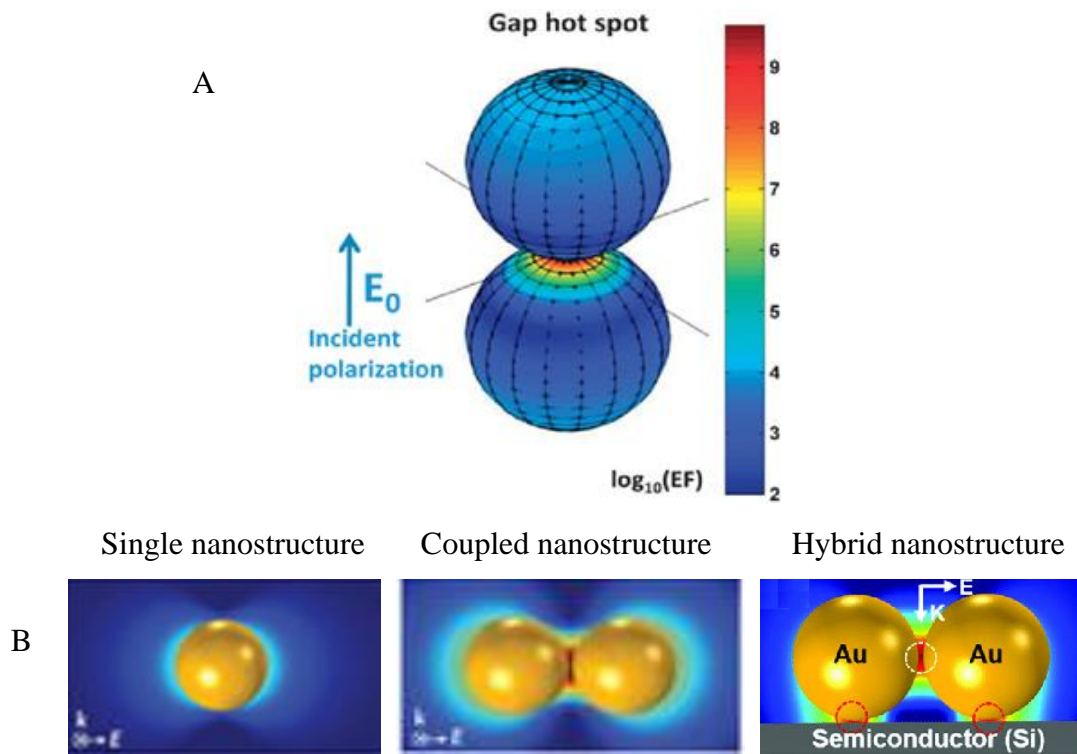


**Figure 2.28 (A) Typical SERS hot spots in nanostructures and (B) First, second and third generation SERS hotspots (continued) [70]**

For this reason, various nanomaterials have been incorporated in the fabrication of sensors and biosensors for any function and developing the potential application in a field of SERS as well as electrochemistry. The next sections explain nanomaterials employed in this thesis.

## **2.6 Nanomaterials**

Nanomaterials are materials manufactured at a very small scale. They are developed to exhibit novel characteristics compared to the same material without nanoscale features. Generally, materials with structure at the nanoscale have approximately size from 1 nm to 100 nm. Among nanomaterials available in nowadays, carbon nanomaterials, metal oxide nanomaterials, and metal nanoparticles, have been widely used for construction of sensors and biosensors. In this thesis, carbon nanomaterials, metal nanoparticles, metal oxide nanomaterials as well as ionic liquid are used for fabrication of sensors and biosensors in order to improve electrocatalytic activity and Raman enhancement mechanism. The property of these nanomaterials is explained in next part.

### **2.6.1 Carbon nanomaterials**

Graphene and their derivatives have gained much attention in the field of (bio)sensors developing, because of their specific physical and chemical features, large surface area, high thermal and electrical conductivity, high mechanical strength, and fast electron transfer rate. [71] Graphene is a two-dimensional material composed of carbon atoms positioned in a hexagonal lattice. A single layer of carbon atoms arranges in a honeycomb structure to form a single graphene sheet. Each carbon atom is covalently bonded to only three other carbon atoms, although they have the capability to bond to a fourth atom. As a result, there is more interaction with surrounding molecules, serving as a great material to improve the charge transfer ability for SERS and electrochemical applications.

### **2.6.2 Metal nanoparticles**

Metal nanoparticles have several exciting applications in different areas due to their unique physical and chemical properties include optical, electrical, thermal, catalytic, magnetic, and high electrical conductivity. [72] Among several classes of metal nanoparticles, silver nanoparticles (AgNPs) and gold nanoparticles (AuNPs) are

one of the most vital and fascinating nanomaterials that have been applied for the wide range of fields involved in chemical, physical and biomedical applications. In the field of electrochemical sensing, AgNPs and AuNPs represent a high conductivity, good biological compatibility, great electrocatalytic properties and high surface-to-volume ratio. Therefore, they have been widely used as an excellent nanoplatform for electrode modification. Moreover, the small size of AgNPs and AuNPs is suitable for further functionalization and convenient immobilization of various chemical and biochemical molecules, as showed in Figure 2.29. Besides, AgNPs and AuNPs exhibits a great surface plasmonic property that can improve electromagnetic enhancement mechanism in SERS system.

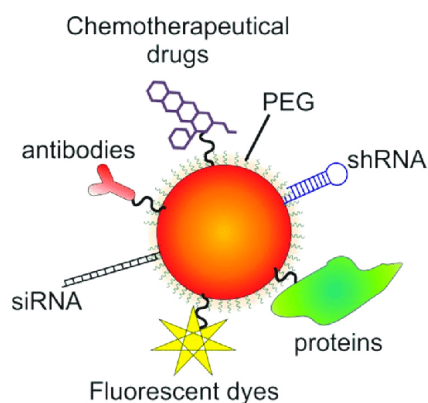


**Figure 2.29 Metallic nanoparticles functionalized with a variety of molecules [73]**

### 2.6.3 Metal oxide nanomaterials

Metal oxides play a very important role in many areas of chemistry, physics and materials science. The metal elements are able to form a large diversity of oxide compounds, resulting in changing surface properties leading to an increase/decrease in the band gap that influences the conductivity, optical property, and the chemical activity of the nanoparticles. [74] In addition, metal oxides can exhibit metallic, semiconductor or insulator character and can serve as electrocatalysts and photocatalysts that are a universally covering a wide variety of advanced research and emerging developments. Many kinds of metal oxides have been studied for the electrochemical detection and SERS, including NiO, ZnO, MnO<sub>2</sub>, Fe<sub>3</sub>O<sub>4</sub>, TiO<sub>2</sub>, and Co<sub>3</sub>O<sub>4</sub>. Nevertheless, the only drawback of metal oxides is not pretty good in electrical conductivity because of non-

conductive oxide. Therefore, the combination between conducting materials and metal oxide nanomaterials can simultaneously solve the problem of poor conductivity.

#### 2.6.4 Ionic liquid

Ionic liquid (IL) have been generally described as molten salts which are composed of asymmetric cations and anions. It exists in liquid state below 100°C and is flexible for the molecular structure design by easily varying the cations and anions. Figure 2.30 shows the most common cations and anions for IL design. IL has been applied in various electrochemical applications due to its outstanding properties such as thermal and chemical stability, negligible volatility, high ionic conductivity, and high dispersibility. [75] Moreover, it can be used as electrolytes and also can be used as the composite materials to modify the electrodes, which effectively immobilize the selective biomolecules onto the surface of the electrode.

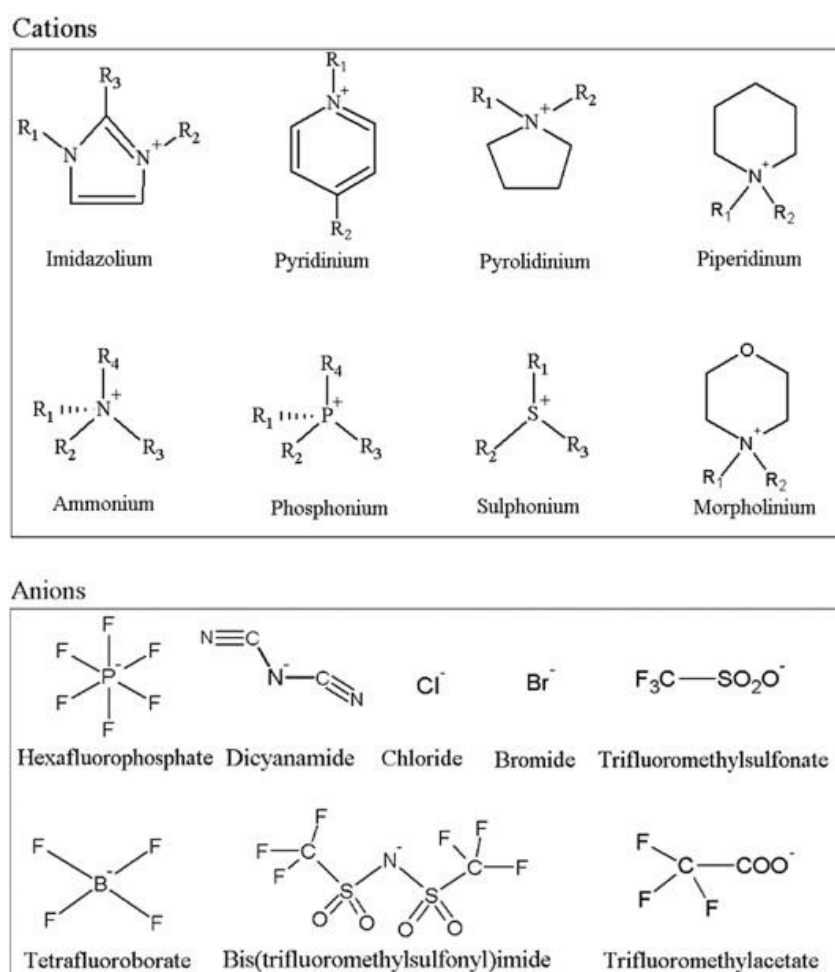


**Figure 2.30** Typical cations and anions used for IL design [76]

All of nanomaterials need to be characterized in order to prove that they are successfully synthesized. Therefore, the principle of characterization techniques are explained in the next section.

## 2.7 Characterization techniques

Characterization of nanomaterials is a crucial important in nanotechnology because the diversity of shapes and compositions as a consequence of difference in fabrication methods can be fulfilled understanding in physical and chemical characteristics of nanomaterials. The techniques used for characterization in this thesis are described below.

### 2.7.1 X-ray diffraction spectroscopy

X-ray diffraction spectroscopy (XRD) [77] is a technique primarily used for phase identification of a crystal structures and atomic spacing. This technique can provide information on unit cell dimensions because diffraction pattern in X-ray wavelengths is similar to the spacing of planes in a crystal lattice of crystalline materials. X-rays are generated in a cathode tube by heating a filament to produce electrons and then filtered to produce monochromatic radiation. The produced electrons are accelerated by applying a voltage and then bombarding the target material, resulting in characteristic X-ray spectra are produced according to Bragg's Law, as Equation 2.26 and Figure 2.31.

$$n\lambda = 2d \sin \theta \quad (2.26)$$

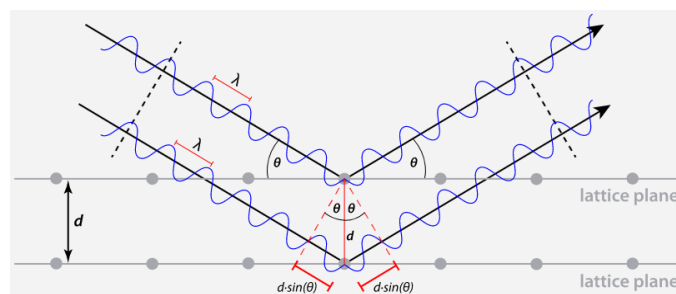


**Figure 2.31** A graphical representation of incident X-rays diffracting from atoms within crystalline layers [78]

In this equation,  $n$  is a positive integer,  $\lambda$  is the characteristic wavelength of the X-rays,  $d$  is the spacing between rows of atoms, and  $\theta$  is the angle of the X-ray beam with respect to these planes. This law relates the wavelength of electromagnetic radiation to the diffraction angle and the lattice spacing in a crystalline sample. The obtained diffracted X-rays spectra are detected by scanning the sample through a range of  $2\theta$  angles. All possible diffraction directions of the lattice are obtained which allows to identify the target sample because each material has a set of unique d-spacings. Typically, this is achieved by comparison of d-spacings with standard reference patterns.

### 2.7.2 X-ray photoelectron spectroscopy

X-ray photoelectron spectroscopy (XPS) [79, 80] is also known as electron spectroscopy for chemical analysis. This technique is the most widely used for surface analysis because it can be applied to a broad range of materials and provides chemical state information from the surface of the material. XPS is accomplished by exciting a samples surface with a monochromatic X-rays ( $h\nu$ ). When the energy of a monochromatic X-rays is higher than binding energy (BE) of electrons within the atoms, photogenerated electrode will be emitted from the sample surface (Figure 2.32). The emitted photoelectrons are then measured with an electron energy analyzer as kinetic energy (KE) based on the work of Ernest Rutherford (Equation 2.27), where  $e\Phi$  is a work function of electron energy analyzer. The binding energy of the emitted electrons can be determined and intensity of a photoelectron peak can be obtained.

$$KE = h\nu - BE - e\Phi \quad (2.32)$$

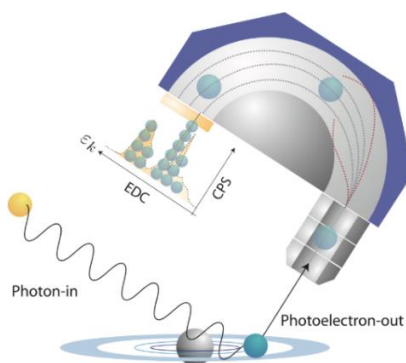


**Figure 2.32 Physical electronics XPS instruments [80]**

The XPS information provides about surface layers or thin film structures, which is important for many industrial and numerous applications, such as adhesion, electronic devices, packaging, surface treatments, and thin film coatings. Generally, the average depth of analysis for an XPS measurement is approximately 5 nm.

### 2.7.3 Energy-dispersive X-ray spectroscopy

Energy-dispersive X-ray spectroscopy (EDS or EDX) [81] is a standard method used for elemental analysis. Usually, the EDS is coupled with several microscope, including scanning electron microscope (SEM) and transmission electron microscope (TEM). When the sample is bombarded by the electron beam, electrons are ejected from the atoms of the sample surface, leading to electron vacancies are filled by electrons from a higher state as showed in Figure 2.33. The energy difference of this transition can be released in the form of X-ray, which is emitted to balance the energy difference between the two electrons states. The spectrum of X-ray energy versus counts is evaluated to identify the elemental compositions and type of elements that exist in the sample. The EDS can be analyzed individual points or map out the distribution of elements from the imaged area.

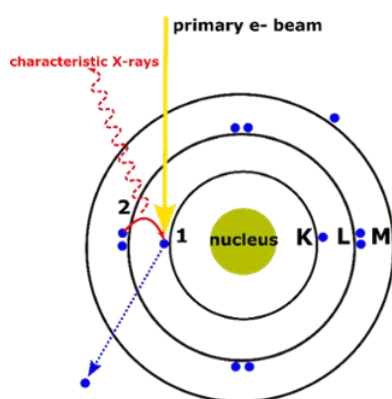


**Figure 2.33 Energy-dispersive X-ray generation process [81]**

### 2.7.4 Fourier-transform infrared spectroscopy

Fourier-transform infrared spectroscopy (FTIR) [82] is widely used to identify the structures of molecules based on characteristic absorption of infrared radiation. The range of infrared region is 12800 to 10  $\text{cm}^{-1}$  which can be divided into

near-infrared region ( $12800$  to  $4000\text{ cm}^{-1}$ ), mid-infrared region ( $4000$  to  $200\text{ cm}^{-1}$ ) and far-infrared region ( $50$  to  $1000\text{ cm}^{-1}$ ). However, the commonly used region for infrared absorption spectroscopy is  $4000$  to  $400\text{ cm}^{-1}$  because the absorption radiation of most organic compounds and inorganic ions is within this region. When sample molecules are exposed to infrared radiation, the specific wavelengths of radiation are selectively absorbed which causes the change of dipole moment of sample molecules. Consequently, the vibrational energy levels of sample molecules transfer from ground state to excited state. The absorption peak or transmittance percentage is determined by the vibrational energy gap which is plotted against the wavenumber ( $\text{cm}^{-1}$ ). The number of absorption peaks is related to the number of vibrational freedoms of the molecule while the intensity of absorption peaks is related to the change of dipole moment and the possibility of the transition of energy levels. Therefore, abundant structure information of a molecule can be analyzed by the infrared spectrum. Most molecules are infrared active except for several homonuclear diatomic molecules such as  $\text{O}_2$ ,  $\text{N}_2$  and  $\text{Cl}_2$  because of the zero dipole change in the vibration and rotation.

### **2.7.5 Scanning electron microscopy**

Scanning electron microscopy (SEM) [83] is a technique based on using a focused beam of high-energy electrons to create an image. Electrons are produced at the top of the column, accelerated down and passed through a combination of lenses and apertures to produce a focused beam of electrons which hits the surface of the sample. The sample is on a stage in the chamber area and the position of the electron beam on the sample is controlled by scan coils which allow the beam to be scanned over the surface of the sample. After the electrons interact with the sample, a number of signals are produced and then detected by appropriate detectors to form images. The obtained images can be used to obtain information about the surface morphology and chemical composition.

Additionally, standard methods are also performed in the part of real samples analysis to check accuracy and precision of the developed sensors and biosensors. The principle of standard methods used in this thesis are discussed in the next section.



## 2.8 Standard methods

### 2.8.1 High performance liquid chromatography

High performance liquid chromatography (HPLC) [84] is a form of column chromatography that pumps a sample mixture in a solvent (Mobile phase) at high pressure through a column with chromatographic packing material (Stationary phase). HPLC has the ability to separate and identify compounds that are present in sample at trace concentrations as low as parts per trillion. The components of a basic HPLC system are shown in the Figure 2.34. A reservoir holds the mobile phase. A high-pressure pump is a delivery system of mobile phase with a specified flow rate, typically milliliters per minute. An injector is able to introduce the sample into the continuously flowing mobile phase stream. The column contains the stationary phase needed to affect the separation. The material packed in the stationary phase should be a very small particle in order to gives a much greater surface area for interactions between the stationary phase and sample flowing past it. The detector records the signal, which is connected to the computer data station to generate the chromatogram on its display and to identify and quantitatively detect the concentration of analyte in sample. The mobile phase exits the detector and can be sent to waste.

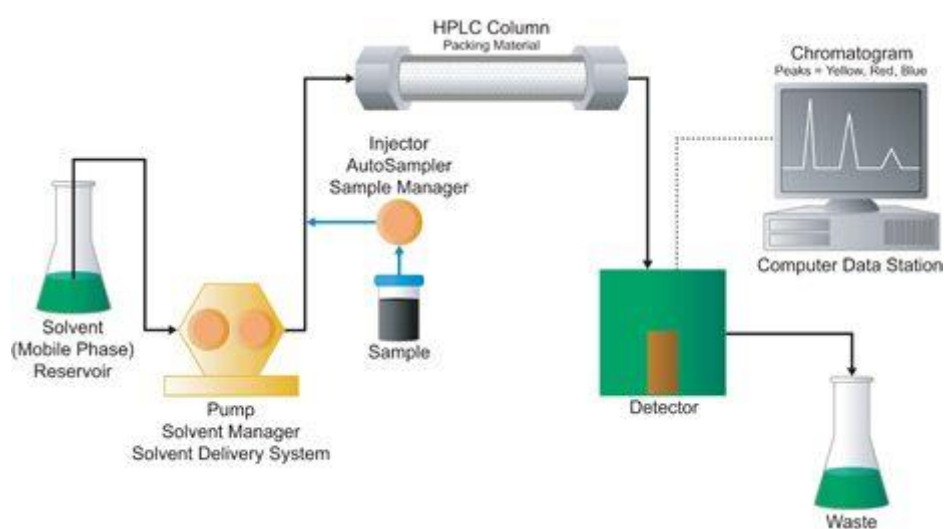


**Figure 2.34 High performance liquid chromatography system [85]**

When the sample enters the HPLC system, the sample is carried by a moving of mobile phase, flowing continuously and steadily past the stationary phase. The

individual components in sample are separated based on different speeds because there is a competition between the mobile phase and the stationary phase for attracting each of the analytes. As can be seen in Figure 2.35, the yellow analyte likes the mobile phase more than the other analytes, resulting in it moves at a *faster* speed. In contrast, the blue analyte likes the stationary phase because of stronger attraction with the packed particles, leading to significantly *slower* moving. In summary, analytes that have the weak interaction with the stationary phase will exit the column faster. As a result, a chromatogram is obtained, which is drawn on y-axis as signal intensity and x-axis as retention time. The position of each analytes in the chromatogram is varied depending on the interaction between the two phases due to polarities of the analytes.

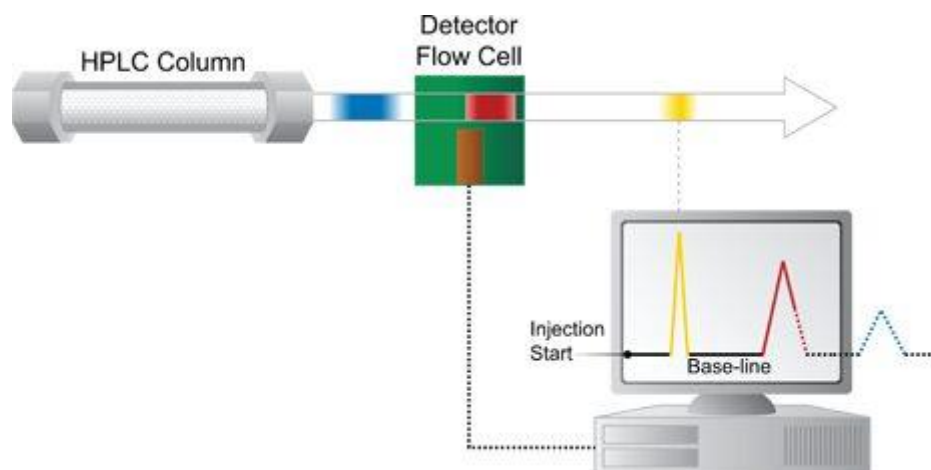


**Figure 2.35 Progress of HPLC separation of a three-component mixture [85]**

There are two types in HPLC depending on the polarity of the solvent and the stationary phase. The first one is normal phase HPLC. The column is filled with the polar material, such as silica particles, and the solvent is non-polar, for example hexane. Therefore, polar compounds in the sample mixture will stick longer to the polar silica while the non-polar compounds will pass more quickly through the column. Another type is reversed phase HPLC. In this case, the column size is the same but the silica is modified with long hydrocarbon chains, typically 18 carbon atoms, to make it non-polar. A polar solvent is used as mobile phase, for example a mixture of water and methanol. Polar molecules in the sample mixture will be a strong attraction with the polar mobile phase and will be being passed quickly through the column. In contrast, non-polar

compounds in the mixture will tend to form attractions with the non-polar stationary phase, leading to spending long time in the column. Commonly, reversed phase procedure is the mostly used form of HPLC.

### **2.8.2 Electrochemiluminescence**

Electrochemiluminescence (ECL) [86] is a kind of luminescence produced during electrochemical reactions. This technique represents a marriage between electrochemistry and luminescent spectroscopy. ECL is an energy relaxation process by optical emission of an excited molecule produced by an applied potential at an electrode surface. Intermediates are electrochemically generated on the electrode, resulting in electron transfer reactions of these electrogenerated species occurred and an electronically excited state is produced. These intermediates then emit light upon relaxation to a lower-level state and the wavelength of the emitted photon of light corresponds to the energy gap between these ground state and excited state. ECL is a highly sensitive and selective method because it is a combination of a spectrometric assay and an electrochemical assay, thus holding the advantages of both two methods. Besides, an excitation light is not used in ECL and the reaction is controlled by applying potential. Therefore, background fluorescence exhibits nearly zero. [87] Enhanced selectivity of ECL analysis is also achieved by variation of electrode potential to control electrogenerated species that are oxidized or reduced at the electrode surface and take part in ECL reaction.

In this thesis, nanomaterials-based sensors and biosensors are fabricated for determination of bisphenol A, glyphosate herbicide, and cancer biomarker. Therefore, properties and importance of these compounds are discussed in the next part.

## **2.9 Toxic substances and cancer biomarker**

### **2.9.1 Bisphenol A**

Bisphenol A (BPA) is scientifically known as 4,4'-(propane-2,2-diyl)diphenol. It is an organic monomer used in plastic additive synthesis, including polycarbonates (PC) and epoxy resins. A wide variety of food-storage or packaging materials are produced from PC, such as feeding bottles, water bottles and cans, as well as tableware and microwave ovenware. Moreover, epoxy resins are widely used as the internal coatings in food and beverage cans. Apart from food contact materials, it also

finds many applications such as production of currency notes, thermal printing paper, purchase-receipt paper, compact disks, adhesives, powder paints, and dental sealants. Potential contamination of BPA in food products can be enhanced by exposure to high temperatures, especially microwave heating. As a result, human can exposure to BPA via the contamination of food and beverages contained in both polycarbonate bottles and coated cans. [88] The structure of BPA is analogous to endocrine hormones, namely estradiol and diethylstilbestrol, due to the presence of phenol groups in their structure (Figure 2.36). Thus, BPA molecules disrupt the endocrine system by mimicking, antagonizing, or altering endogenous steroid levels through binding with estrogen receptors. Moreover, exposure to BPA is associated with cardiovascular diseases, obesity, carcinogenicity, neurotoxicity and developmental problems. [89] The exposure estimates for populations through food intake is generally in the range of 0.1-1.5  $\mu\text{g/kg}$  body weight/day.

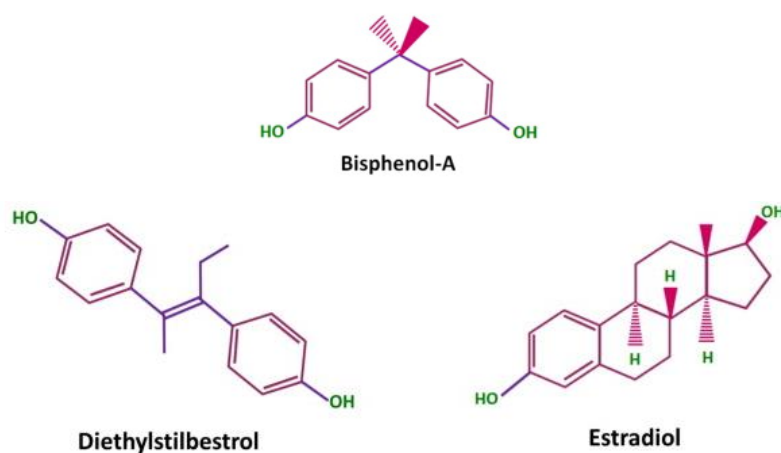


**Figure 2.36 Bisphenol A and its hormones structurally analogous [89]**

### 2.9.2 Cancer biomarker

There are over 200 types of cancers identified all over the world and more than 1500 deaths occurring each day. Cancer is a multistage disease and its progression is associated with genetic alterations which disturb the cellular signaling and result in tumorigenic transformation. The survival rate of cancer patients is still poor because of diagnosis at the late stage and poor prognosis of cancer. Typically, traditional diagnostic methods for cancers are primarily based on endoscopy, computed tomography, X-rays,

positron emission tomography, magnetic resonance imaging, and invasive tissue biopsies. Because of this reason, cancer biomarkers detection is emerging as one of the most promising strategies for early diagnostic of cancer. Cancer biomarkers are molecules which undergo prominent alterations during cancer. Thus, they are a molecular signature that can provide accurate information underlying the initiation of cancer. [90] Biomarkers may be nucleic acids, proteins, metabolites, isoenzymes or hormones. The presence of the specific biomarkers in a cell often indicates cancer development. Therefore, identification and detection of the specific biomarkers could help in early diagnosis and monitoring disease progression. Carcinoembryonic antigen (CEA) is one of the most important clinical cancer biomarkers associated with colon tumors, breast tumors, ovarian carcinoma, colorectal cancer and cystadenocarcinoma. [91] The normal concentration of CEA in serum is lower than 5.0 ng/mL for healthy human, while higher CEA concentration level is indicated the presence of cancer. [92]

### **2.9.3 Glyphosate herbicide**

Glyphosate, which is scientifically known as [N-(phosphonomethyl) glycine], is a kind of organophosphates herbicide with amine, carboxyl and phosphonate group (Figure 2.37). It is a broad-spectrum herbicide mostly used in agriculture globally. Glyphosate products are used primarily before and after planting of traditional agricultural crops. The world health organization (WHO) have classified the glyphosate herbicide as probably carcinogenic to humans in 2015 and the direct and indirect health effects of the large-scale use of glyphosate have increased worldwide in recent years. [93] Therefore, many authorities have suggested the maximum residue levels (MRLs) of this compound in water and agricultural products. The MRLs of glyphosate in most crops listed by the United Nations Food and Agricultural Organization is 0.1-5.0 mg/kg. The U.S. national primary have been set a maximum level of glyphosate in drinking water at 0.7 mg/L while the European Union limit has been set to 0.1 µg/L. [94]

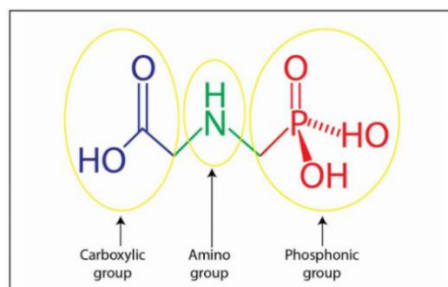


**Figure 2.37 The chemical structure of glyphosate**

## 2.10 Literature reviews

The literature reviews are divided into four parts according to sub-objectives of the thesis. The first part is electrochemical sensor for detection of bisphenol A. Secondly, electrochemical biosensor for cancer biomarker detection is discussed. Thirdly, electrochemical biosensor for determination of glyphosate herbicide based on enzyme inhibition is reviewed. And the last part is about the designment of SERS substrate and determination of herbicide based on SERS analysis.

### 2.10.1 Electrochemical detection of bisphenol A

Zhang and et al. [95] developed electrochemical sensor for determination of BPA based on arginine functionalized graphene (Arg-G) nanocomposite. Graphene was selected due to its high conductivity and electronic property. However, graphene tends to irreversible aggregation through *Van der Waals* forces, which limits its practical applications. To solve this problem, graphene was functionalized with arginine in order to facilitate the graphene dispersion. Due to arginine is a positively charged amino acid that can adsorb with graphene via electrostatic interaction. The electrochemical behaviors of BPA were investigated by differential pulse voltammetry (DPV) using Arg-G modified glassy carbon electrode (GCE). Under the optimized conditions, the oxidation peak current was proportional to BPA concentration in the range of 5 nM to 40  $\mu$ mol/L with the correlation coefficient of 0.9986 and the detection limit of 1.1 nM.

Wang et al. [96] fabricated carbon ionic liquid electrode (CILE) by using 1-ethyl-3-methylimidazolium tetrafluoroborate (ionic liquid) as binder and modifier. The CILE has been proved to be an efficient working electrode in the field of electroanalysis with the advantages such as high ionic conductivity and good electrocatalytic activity. Moreover, the CILE was further modified with a composite of

chitosan and graphene (CTS-GR) to enhance sensitivity and selectivity for electrochemical detection of BPA by DPV. Under the optimal conditions, a linear relationship between the oxidation peak current of BPA and its concentration was obtained in the range from 0.1-800.0  $\mu\text{M}$  with the limit of detection as 0.03  $\mu\text{M}$ .

Li and et al. [97] fabricated electrochemical sensor based on ordered mesoporous carbon CMK-3 modified nano-carbon ionic liquid paste electrode (CMK-3/nano-CILPE). Ordered mesoporous carbon was selected because it shows better performance on the adsorption of BPA. The charge transfer resistance of the modified electrode was significantly reduced because of using nano-graphite powders instead of graphite powders. Additionally, the nano-CILPE displayed lower background current and enhanced conductivity because of using ionic liquid as a binder. As a result, the prepared sensor showed good electrocatalytic activity to BPA due to large surface area and absorption capability of CMK-3 and high conductivity of ionic liquid. Under optimal conditions, the fabricated sensor displayed excellent electroactivity towards BPA using linear sweep voltammetry (LSV) and the linear range was obtained in a range from 0.2-150  $\mu\text{M}$  with a detection limit of 0.05  $\mu\text{M}$ .

Referring to the above reviews, BPA is an electroactive molecule due to phenolic groups but its direct electrochemical oxidation is sluggish. Therefore, graphene nanoplatelets (GNPs), a new class of graphene nanoparticles, are employed in this work in order to improve sensitivity of the sensor. However, GNPs tend to form irreversible agglomerates through strong  $\pi$ - $\pi$  restacking and *Van der waals* interactions. Hence the aggregation of GNPs is prevented by integration of ionic liquids (ILs) into functional graphene composites to not only increase their dispersibility but also improve their electrochemical performance. Moreover, glassy carbon paste electrodes (GCPEs), a kind of carbon composite-based electrode that combines the favorable electron transfer kinetics of glassy carbon with the advantages of composite paste electrodes, is also constructed in this work. Therefore, a simple electrochemical sensor for BPA is developed based on a composite of GNPs and 1-butyl-2,3-dimethylimidazolium tetrafluoroborate (IL) as a modifier for GCPE and the detection is performed by DPV. Moreover, the characteristics of various electrochemical sensors prepared with different kinds of nanomaterials as a sensing platform for detection of BPA in different samples are summarized in Table 2.4.

**Table 2.4 Various electrochemical sensors for determination of BPA**

Sensing platform	Electrode	Method	Linear range	LOD	Real samples	References
MWCNT	GCE	LSV	0.01-10.0 $\mu\text{M}$	5 nM	Food packages	[98]
MWCNT/CTAB	PGE	SWV	2-808 nM	134 pM	Water and baby bottles, baby teether	[99]
MWCNT/ZnO	CPE	SWV	0.002-700 $\mu\text{M}$	9 nM	Food samples	[100]
MWCNT/AuNPs	GCE	DPV	0.01-0.7 $\mu\text{M}$	4 nM	River water and mineral water	[101]
MWCNT/PDDA/AuPd	GCE	DPV	0.18-18 $\mu\text{M}$	60 nM	Tap water and milk	[102]
MWCNT/PtNPs/GN	GCE	DPV	0.06-10.0 $\mu\text{M}$	42 nM	Thermal printing papers	[103]
GN/PME	CPE	DPV	9 $\mu\text{M}$ -1 mM	10.5 nM	Tap water and waste water	[104]
GN/AuPd	GCE	DPV	0.05-10 $\mu\text{M}$	8 nM	Food packages	[105]
GN/NP-PtFe	GCE	DPV	0.2-96 $\mu\text{M}$	0.17 $\mu\text{M}$	Water samples	[106]
rGO/PLL/AgNPs	GCE	DPV	1-80 $\mu\text{M}$	0.54 $\mu\text{M}$	Drinking water	[107]
rGO/SiO <sub>2</sub> /AuNPs	GCE	DPV	0.03-120 $\mu\text{M}$	4 nM	Thermal paper samples	[108]
GO/carbon nanoparticles	SPCE	DPV	7.5-260 nM	1 nM	Water samples	[109]
SGrNF/AuNPs	GCE	LSV	0.08-250 $\mu\text{M}$	35 nM	Baby bottles	[110]
GNR/Au-Cu@BSA	GCE	SWV	0.01-70 $\mu\text{M}$	4 nM	Water and food storage container	[111]

MWCNT: multi-walled carbon nanotubes, CNT: carbon nanotubes, rGO: reduced graphene oxide, GN: graphene, GNR: graphene nanoribbons, SGrNF: stacked graphene nanofibers, NP-PtFe: nanoporous PtFe alloys, NPs: nanoparticles, PLL: poly-L-lysine, PDDA: poly (diallyldimethylammonium chloride), PME: poly(melamine), BSA: bovine serum albumin, CTAB: cetyltrimethylammonium bromide, GCE: glassy carbon electrode, PGE: pencil graphite electrode, SPCE: screen-printed carbon electrode, DPV: differential pulse voltammetry, SWV: square wave voltammograms, LOD: limit of detection



### 2.10.2 Electrochemical detection of cancer biomarker

Kumar and et al. [112] reported a fabrication of a paper based biosensor comprising of poly(3,4-ethylenedioxythiophene):poly(styrenesulfonate) (PEDOT:PSS) and reduced graphene oxide (rGO) composite. The observed significant increase in electrical conductivity was due to conformational rearrangement in the polymer and is due to strong non-covalent cooperative interaction between PEDOT and the cellulose molecules. Furthermore, incorporation of rGO into the conducting paper results in improved electrochemical performance and signal stability. This paper electrode is a promising alternative over the expensive conventional electrodes (gold and glassy carbon), that are known to have limited application in smart point-of-care (POC) devices. This low cost, flexible and environment friendly conducting paper-based biosensor utilized for carcinoembryonic antigen (CEA) based on electrochemical label-free immunoassay. The electrochemical studies were carried out using a conventional three-electrode cell with the electroactive paper as working electrode in phosphate buffer saline containing 5 mM  $[\text{Fe}(\text{CN})_6]^{3-/4-}$  as redox probe. Chronoamperometric signals were detected before and after presenting CEA and the difference in signal response is attributed to the formation of antigen–antibody complex causing significant rearrangement over the electrode surface. As a result, a reduction in amperometric current owing to redox reaction of  $[\text{Fe}(\text{CN})_6]^{3-/4-}$  was observed after presenting CEA. The biosensor revealed high sensitivity of  $25.8 \text{ mA} \cdot \text{ng}^{-1} \text{ mL cm}^{-2}$  in the physiological range of 1-10 ng/mL towards CEA detection.

Lin and et al. [113] proposed a reusable biosensor based on a magnetic graphene oxide (MGO)-modified Au electrode to detect vascular endothelial growth factor (VEGF) for cancer diagnosis. Avastin, an antibody of VEGF, was used as the specific biorecognition element and MGO was used as the carrier for Avastin loading. MGO was prepared through the in-situ generation and deposition of  $\text{Fe}_3\text{O}_4$  nanoparticles onto the surface of graphene oxide. The synergistic integration of these two nano-materials on the electrocatalytic behavior of different important electroactive compounds have been already proved and the studies demonstrate that the excellent electrocatalytic activity of MGO could be promising for the development of electrochemical biosensor. Moreover, the use of MGO enables rapid purification due to its magnetic properties, which prevents the loss of bioactivity and without requiring a

drying process. The Avastin-MGO solution can be drop-deposited onto the surface of the Au electrode. The electrochemical signal was measured by DPV to quantify the VEGF concentration based on label-free immunoassay in  $[\text{Fe}(\text{CN})_6]^{3-/4-}$  solution. The process of electrochemical detection by the Avastin-MGO-modified Au electrode is displayed in Figure 2.38.



**Figure 2.38** Electrochemical detection of VEGF biomarker using the Avastin-MGO/Au biosensor [113]

Pang and et al. [114] developed an enzyme-free electrochemical biosensor for microcystin-LR (MC-LR) detection using molybdenum disulfide ( $\text{MoS}_2$ ) nanosheets/gold nanoclusters (AuNCs) composite and Au core/Pt shell nanoparticles ( $\text{Au}@\text{PtNPs}$ ).  $\text{MoS}_2/\text{AuNCs}$  nanocomposite was used as a platform for immobilizing more antibody due to its large surface area and excellent biocompatibility.  $\text{MoS}_2$  was employed for fabrication of electrochemical biosensor due to their large surface area like 2D graphene. Meanwhile, AuNCs serves as an interface for immobilization of antibodies and improve electrical conductivity. This biosensor employed a sandwich immunoassay format where the capture antibody was immobilized on  $\text{MoS}_2/\text{AuNCs}$  composite surface and the detection antibody was labeled with  $\text{Au}@\text{PtNPs}$  as a non-enzymatic reporter.  $\text{Au}@\text{PtNPs}$  was chosen for the peroxidase mimics due to its high catalytic efficiency and good stability. The detection of MC-LR was based on the uncompetitive combination of MC-LR with  $\text{MoS}_2/\text{AuNCs}$  immobilized capture antibody and  $\text{Au}@\text{PtNPs}$  immobilized detected antibody to form a sandwich antibody-antigen-antibody immunocomplex. Thus, the concentration of the MC-LR is directly proportional to the electrochemical signal of the biosensor. Electrochemical measurements were carried out in phosphate buffer solution containing hydrogen peroxide and hydroquinone by DPV.

According to these reviews, label free immunoassay is employed as the biosensor format for the sensitive detection of CEA biomarker in this work because of their simple preparation, more cost effectiveness, does not need a complicated labeling process, and easy operation without using of secondary antibodies which could be directly measured the binding process of antibody-antigen interaction. A label free detection of CEA is designed based on CEA antibody (anti-CEA) anchored with core shell  $\text{Fe}_3\text{O}_4@\text{Au}$  nanoparticles, which are immobilized on a screen-printed carbon electrode modified with manganese dioxide decorating on graphene nanoplatelets (SPCE/GNP- $\text{MnO}_2$ ). GNP- $\text{MnO}_2$  are employed to improve the electrocatalytic activity and sensitivity of the biosensor due to the combination between GNP and  $\text{MnO}_2$  can simultaneously improve the electrocatalytic activity and substantially improve the dispersibility of GNP. Meanwhile, core shell  $\text{Fe}_3\text{O}_4@\text{Au}$  nanoparticles are chosen for immobilizing anti-CEA as an immune sensing platform. Because the magnetic properties of the  $\text{Fe}_3\text{O}_4$  could be handled easily on the sensing surface by an external magnetic field, whilst the Au possesses two functions: one binding with  $\text{Fe}_3\text{O}_4$  core and the other of directly and friendly interacting with antibodies. Additionally, the *screen-printed* electrode (SPCE) is employed as a working electrode for simple and facile way to fabricate the biosensor owing to its advantages such as simple fabrication, low cost, small size, disposability, portability, and easy mass-production, making it suitable for working with micro-volumes and for point of care analysis. The detection mechanism is based on the measurement of the peak current and charged transfer resistance owing to the redox reaction of  $[\text{Fe}(\text{CN})_6]^{3-/4-}$  using linear sweep voltammetry (LSV) and electrochemical impedance spectroscopy (EIS) as the detection techniques, respectively. Furthermore, the characteristics of numerous electrochemical biosensors prepared with different kinds of nanomaterials as a biosensing format for determination of CEA based on label-free immunoreaction are summarized in Table 2.5.

**Table 2.5 Various electrochemical biosensors for determination of CEA**

Sensing platform	Electrode	Method	Redox probe	Linear range	LOD	References
poly(3,4-ethylenedioxythiophene)/ AuNPs/Ab	GCE	DPV	Prussian blue	0.05-40 ng/mL	0.01 ng/mL	[115]
poly(carboxybetaine methacrylate)/ PANI/Ab	GCE	DPV	Polyaniline	10 fg/mL-0.1 ng/mL	3.05 fg/mL	[116]
poly(3,4ethylenedioxythiophene)/AuNPs/ GN	GCE	DPV	Fe(CN) <sub>6</sub> <sup>3-/4-</sup>	0.0004-40 ng/mL	0.1 pg/mL	[117]
Chitosan/Pd-Ir bimetallic NPs/Ab	GCE	EIS	H <sub>2</sub> O <sub>2</sub>	0.05-50 ng/mL	0.017 ng/mL	[118]
Methylene blue/GQDs/IL-nafion/Ab	GCE	DPV	Methylene blue	0.5 fg/mL-0.5 ng/mL	0.34 fg/mL	[119]
AuNPs/graphene/chitosan/Ab	GCE	CV	Fe(CN) <sub>6</sub> <sup>3-/4-</sup>	1 fg/mL -1 ng/mL	0.2 fg/mL	[120]
AuNPs/thionine/MoS <sub>2</sub> /Ab	GCE	SWV	Thionine	0.001-10 ng/mL	0.52 pg/mL	[121]
AuNPs/CNOs/SWCNTs/chitosan/Ab	GCE	SWV	Fe(CN) <sub>6</sub> <sup>3-/4-</sup>	100 fg/mL-400 ng/mL	100 fg/mL	[122]
TiO <sub>2</sub> microparticles/chitosan/ AuNPs/Ab	CPE	DPV	Fe(CN) <sub>6</sub> <sup>3-/4-</sup>	0.01-1 ng/mL and 1-20 ng/mL	0.01 ng/mL	[123]
GO/thionine/AuNPs/Ab	GCE	SWV	Thionine	0.1 fg/mL-1 µg/mL	0.05 fg/mL	[124]
rGO/Nile blue/AuNPs/Ab	GCE	DPV	Nile blue	0.001-40 ng/mL	0.45 pg/mL	[125]
Sulfonated GN/thionine/chitosan/ nanotubular mesoporous PdCu/Ab	GCE	CV	Thionine	0.01–12 ng/mL	4.86 pg/mL	[126]
Amino functional graphene/thionine/ AuNPs/Ab	Paper based SPCE	DPV	Thionine	0.05-500 ng/mL	0.01 ng/mL	[127]

NPs: nanoparticles, rGO: reduced graphene oxide, GO: graphene oxide, GN: graphene, MoS<sub>2</sub>: molybdenum disulfide, GQDs: quantum dot, IL: ionic liquid, PANI: polyaniline, CNOs: carbon nano-onions, SWCNTs: single-walled carbon nanotubes, Ab: antibody, HRP: horseradish peroxidase enzyme, CPE: carbon paste electrode, SPCE: screen-printed carbon electrode, DPV: differential pulse voltammetry, SWV: square wave voltammograms, CV: cyclic voltammetry, EIS: electrochemical impedance spectroscopy

### 2.10.3 Electrochemical detection of herbicide

Zhang and co-worker [128] developed a highly sensitive amperometric enzyme based-biosensor for determination of organophosphate pesticides (OPs) using conjugated polymer and nanocomposite of amine functionalized reduced graphene oxide ( $\text{NH}_2$ ) and silver nanoparticles (AgNPs). rGO was selected due to its favorable features in electrochemistry, while AgNPs can provide a suitable microenvironment to maintain the bioactivity of biomolecules and promote more efficient electron transfer between the immobilized biomolecules and the electrode substrates. For selective detection of OPs, acetylcholinesterase (AChE) was immobilized on the modified electrode surface as a biorecognition layer. The detection was performed based on inhibition of enzyme activity. The principle for OPs determination and the working mechanism is showed in Figure 2.39. The oxidation current of thiocholine product obtained from the enzymatic catalysis of AChE on acetylthiocholine chloride substrate upon a certain potential was monitored before and after presenting OPs by cyclic voltammetry (CV). The change of signal was calculated and taken as the sensing signal towards OPs.

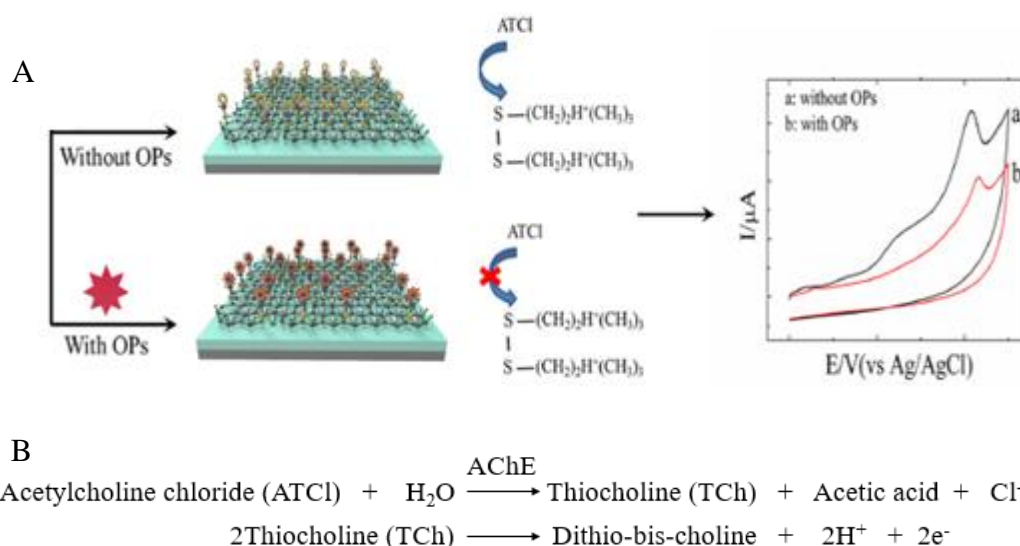


**Figure 2.39 (A) The principle for OPs determination and (B) reaction mechanism of AChE on acetylthiocholine chloride [128]**

Zhou and co-worker [129] fabricated AChE biosensor based on transition metal carbides ( $\text{Ti}_3\text{C}_2\text{T}_x$ ) nanosheets and chitosan (CS) for detecting OPs. CS- $\text{Ti}_3\text{C}_2\text{T}_x$  nanocomposites were used as enzyme immobilization support to construct highly performance biosensor because they could increase the effective surface area and provide biocompatible environment for AChE loading. Electrocatalytic behavior of the AChE biosensor towards its substrate, acetylthiocholine chloride, was determined by chronoamperometry at an applied potential of +0.655 V. Moreover, DPV was also employed for monitoring malathion, a typical organophosphorus pesticide, based on AChE inhibition. The inhibition of malathion was proportional to its concentration from  $1 \times 10^{-8}$  to  $1 \times 10^{-14}$  M with a detection limit of  $0.3 \times 10^{-14}$  M. The reproducibility of the biosensor was found to be 8.6% ( $n=5$ ), which confirmed an acceptable reproducibility of the AChE biosensor, and the biosensor still retained 85.39% of its initial current response after a 38-day storage period.

Pabbi and et al. [130] presented an electrochemical biosensor for the determination of OPs based on alkaline phosphatase enzyme (ALP) and flower shaped ZnO nanoparticles. The detection principle was based on the inhibition of ALP in presence of chlorpyrifos pesticide. In principle, ALP would dephosphorylate the phosphate monoester of substrate 2-phospho-L-ascorbic acid to release L-ascorbic acid (AA). The hydroxyl groups of AA would be oxidized on the glassy carbon electrode (GCE) modified ZnO and would convert to dehydroascorbate with the release of two electrons. A graphical representation of reaction mechanism occurring at ALP/ZnO/GCE is showed in Figure 2.40. The oxidation process of conversion of AA to dehydroascorbate was facilitated by evenly distributed electron holes present on the surface of ZnO nanoparticles. Electron holes help in the improvement of electron transfer kinetics, which increases sensitivity of the biosensor. Therefore, flower shape ZnO nanoparticles not only provide surface for adsorption of ALP but also increases electron-transfer kinetics and sensitivity of the biosensor. In the presence of pesticide, the ALP enzyme activity would inhibit and hence the current signal decreases. The decrease in signal is detected by CV and DPV. The developed biosensor could measure chlorpyrifos in the linear concentration range from  $10^{-6}$  M to  $10^{-1}$  M and  $10^{-9}$  M to  $10^{-3}$  M with negligible interference from triazophos, malathion, acephate and some metal ions.

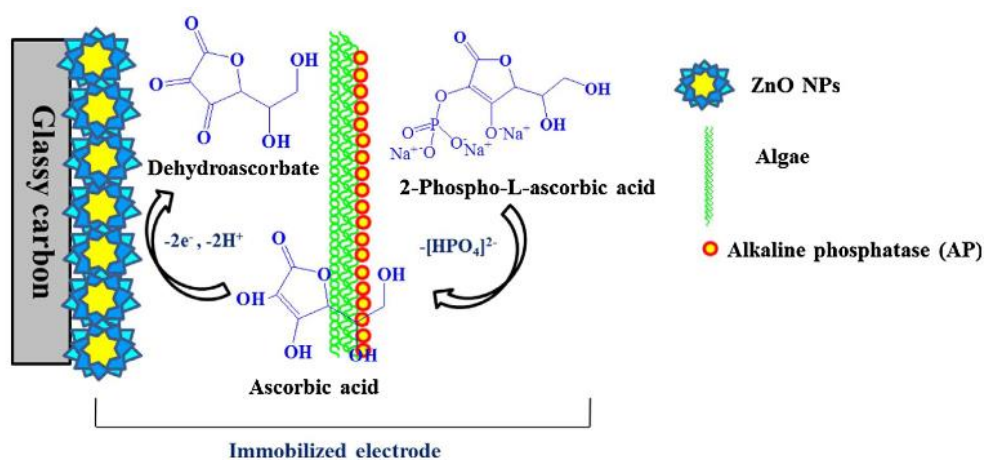


**Figure 2.40 Mechanism of reaction occurring at ALP/ZnO/GCE [130]**

In this work, an electrochemical biosensor-based enzymatic reaction is developed for indirect determination of glyphosate, one of the extensively used herbicides in agricultural situations worldwide, based on inhibition of acid phosphatase (ACP) activity. Generally, inhibition of AChE activity is the most popular method used for ultra-sensitive detection of OPs due to strong enzyme inhibition. However, the major drawbacks in utilization of AChE is that, several compounds are able to specifically inhibit this enzyme like organophosphorus, such as carbamate pesticides, aflatoxins, nerve agents and heavy metals. [29] To avoid this problem, ACP is selected as a biorecognition layer for enzymatic biosensor fabrication due to it selectively catalyze the hydrolysis of phosphate containing molecules. For biosensor preparation, the ACP are chemically immobilized on the surface of screen-printed carbon electrode (SPCE) modified with reduced graphene oxide and silver nanoparticles (rGO-AgNPs) via glutaraldehyde cross-linking. The current signal owing to the enzymatic reaction of ACP and its substrate, disodium phenyl phosphate, is measured by chronoamperometry. The decrease in signal owing to inhibition of ACP activity in the presence of glyphosate is quantitative proportional to glyphosate concentration. For comparison, the characteristics of electrochemical biosensors and sensors prepared with different kinds of nanomaterials and different type of recognition layer for determination of glyphosate are summarized in Table 2.6.

**Table 2.6 Various electrochemical biosensors and sensors for determination of glyphosate**

Sensing platform	Electrode	Recognition layer	Method	Linear range	LOD	References
PDMA doped with PSS	Au	HRP	CV	0.25-14.0 µg/L	1.70 µg/L	[131]
NiAl-LDH	Pt	-	Amperometry	0.15 µg/L-1.69 mg/L	0.16 µg/L	[132]
Nanoclay modified APTES-ODA/MWCNTs	CPE	Atemoya peroxidase	SWV	0.10-4.55 mg/L	30 µg/L	[133]
MWCNT-IL/CuO NPs	PEG	-	DPV	0.85 µg/L-0.19 mg/L	0.22 µg/L	[134]
Au NPs-MAC/MWCNTs	PEG	MIP	DPV	3.98-176.23 µg/L	0.35 µg/L	[94]
-	ITO	Cu-BTC MOF	DPV	0.17 ng/L-0.17 µg/L and 0.17 µg/L-1.7 mg/L	0.02 ng/L	[135]
Chitosan	Au microelectrode	MIP	EIS	0.31 ng/L-50 µg/L	0.001 ng/L	[136]
CuOx@mC	GCE	HKUST-1 MOF	DPV	0.17 pg/L-16.9 mg/L	0.13 pg/L	[137]

HRP: horseradish peroxidase, MIP: molecular imprinted polymer, PMDA: poly(2,5-dimethoxyani-line), PSS: poly(4-styrenesulfonic acid), LDH: layered double hydroxide, APTES: aminopropyltriethoxysilane, ODA: octadecylamine, MAC: N-methacryloyl-L-cysteine, Cu-BTC MOF: hierarchically porous Cu-BTC metal-organic frameworks, CuOx@mC: copper oxide@mesoporous carbon, CV: cyclic voltammetry, SWV: square-wave voltammetry, DPV: differential pulse voltammetry, EIS: electrochemical impedance spectroscopy, Au: gold, Pt: platinum, MWCNTs: multiwalled carbon nanotubes, IL: ionic liquid, CuO NPs: copper oxide nanoparticle, CPE: carbon paste electrode, PEG: pencil graphite electrode, ITO: indium tin oxide, GCE: glassy carbon electrode



#### 2.10.4 Nanomaterials-based sensors for SERS applications

Jiang and et al. [138] proposed graphene oxide-silver nanoparticle composites (GO-AgNPs) as a stable SERS sensing system. AgNPs is one of the widely used nanomaterials with plasmonic properties to amplify the Raman signal. In SERS, the chemical and electromagnetic interactions, occurring between an analyte and AgNPs surface, drive the Raman signal enhancement. However, AgNPs show poor absorption capability and tend to be easily oxidized, due to the local heating produced during the SERS effect, resulting in a poor stability of the Raman enhancement after a few days from the synthesis. Therefore, GO was employed due to it offers several adsorption sites for probe molecules, especially aromatics, through  $\pi$ - $\pi$  and electrostatic interactions. This adsorption sites are at the basis of the chemical enhancement mechanism and are capable of quenching the eventual fluorescence coming from the molecule. The system showed an excellent enhancement of the Raman scattering at a 785 nm laser and 1 mW power with a 7.8-fold increase in comparison to bare AgNPs when tested with rhodamine 6G (R6G). The signal intensity exists a good correlation with the concentration of Rh6G from  $10^{-3}$  to  $10^{-9}$  M ( $r^2 = 0.991$ ) and the detection limit is lower than  $10^{-9}$  M. The enhancement factor (EF) value for a GO-AgNPs substrate for R6G resulted to be  $4.9 \times 10^6$ . The reproducibility of the SERS effect was also evaluated by calculating the standard deviation (RSD) of the average Raman intensity of R6G and the RSD value is smaller than 8%. After being stored in a closed vessel for 180 days, the Raman intensity of R6G measured using Ag NPs as SERS-active substrate drops to 5.2% of the initial value while in the GO-AgNPs system keeps 89% efficiency as can be seen in Figure 2.41. The results confirm that GO with an optimized loading of AgNPs is very effective in reducing the oxidation of silver, providing a better long-term stability to the GO-AgNPs samples.

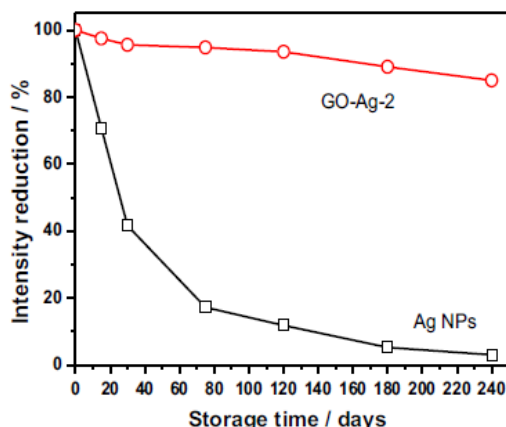


**Figure 2.41** Reduction (%) of Raman intensity of R6G at  $1525\text{ cm}^{-1}$  detected on AgNPs (black square) and GO-AgNPs (red circle) substrates as a function of the storage time [138]

Sun and et al. [139] fabricated AgNPs-coated titanium dioxide nanotube arrays (AgNPs-TiO<sub>2</sub> NTs) via anodization of Ti foil and deposition of AgNPs on the anodized TiO<sub>2</sub> NTs by e-beam evaporation. AgNPs were uniformly distributed on the surface of TiO<sub>2</sub> NTs as can be seen in Figure 2.42. The prepared AgNPs-TiO<sub>2</sub> NTs were employed as the SERS substrates to detect 2-mercaptobenzoxazole (MBO), which shows superior detection sensitivity and uniformity. The TiO<sub>2</sub> NTs not only had a synergistic effect to improve the SERS performance, but also used as a photocatalyst. When the probing molecules are degraded via ultra-violet (UV) irradiation, the AgNPs-TiO<sub>2</sub> NTs substrates can be recyclable. The SERS signals of MBO in different concentrations were obtained from  $10^{-5}\text{ M}$  to  $10^{-9}\text{ M}$ . The Raman signal can be clearly observed even the concentration of MBO was down to  $10^{-9}\text{ M}$ , which means the prepared Ag-coated TiO<sub>2</sub> NTs have an extremely low detection limit. Moreover, the enhancement factor (EF) was calculated to be  $2.26 \times 10^8$ , which indicates a great SERS performance. The RSD value of the intensities was also calculated to be 12.0%. The low RSD values further confirm that the Ag-TiO<sub>2</sub> NTs substrate was well uniformly prepared and it is suitable for highly reproducibility active SERS substrate.

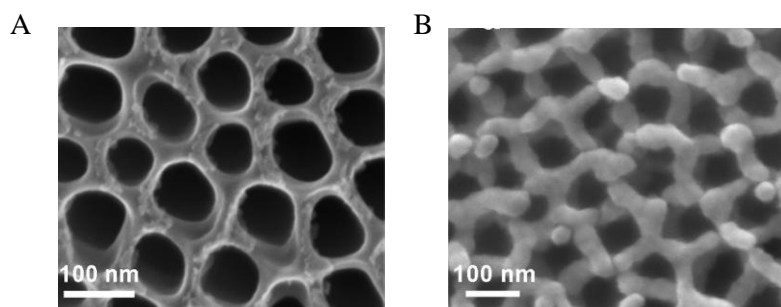


**Figure 2.42 SEM images of (A) TiO<sub>2</sub> NTs and (B) Ag-coated TiO<sub>2</sub> NTs [139]**

Fang and et al. [140] prepared AgNPs decorated TiO<sub>2</sub> nanorod arrays (TiO<sub>2</sub> NRs) by two simple processes. TiO<sub>2</sub> NRs were first fabricated by the hydrothermal route and then AgNPs were decorated on the nanorods by the chemical reduction impregnation method. The formed 3D AgNPs-TiO<sub>2</sub> NRs were used as an active substrate for SERS measurement. The results show that the detection limit for R6G was as low as  $10^{-7}$  M and the enhancement factor (EF) was as large as  $10^5$ , which is sufficient for the ultrasensitive detection. The prepared 3D arrays can be used to detect R6G in the range from  $10^{-3}$  to  $10^{-7}$  M. To investigate whether the substrate could give reproducible SERS signals, the uniformity of the Raman enhancement of the substrate was demonstrated by point-to-point Raman mapping over a large area. The Raman mapping were recorded on a randomly selected  $10\ \mu\text{m} \times 10\ \mu\text{m} = 100\ \mu\text{m}^2$  area with a step size of  $1\ \mu\text{m}$  on the AgNPs-TiO<sub>2</sub> NRs surface. In this case, the RSD values of the Raman signal intensities of major SERS peaks for R6G are below 22%. Figure 2.43 shows the FE-SEM image of AgNPs-TiO<sub>2</sub> NRs.

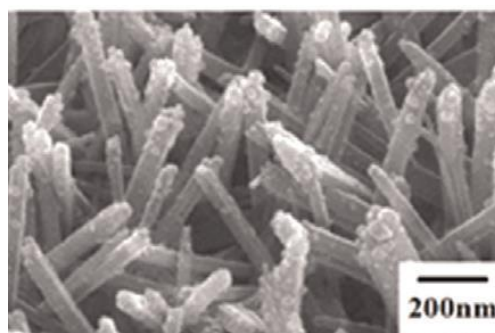


**Figure 2.43 FE-SEM micrographs of AgNPs-TiO<sub>2</sub> NRs [140]**

Yang and et al. [141] synthesizes a single-crystalline TiO<sub>2</sub> nanosheet (TiO<sub>2</sub> NSs) arrays with decorated with AgNPs by a simple hydrothermal method and a magnetron sputtering method. The TiO<sub>2</sub> NSs grow on the substrate exhibit the regular tetragonal sheet-structured as shown in Figure 2.44. The sensitivity and uniformly of the SERS substrates were examined by using R6G as the probe molecules. It is noted that the TiO<sub>2</sub> NSs with 10 second Ag-sputtering achieved the highest Raman signals due to a close-packed AgNPs generate a high density of hotspots, and the intensity of the SERS spectra on AgNPs-TiO<sub>2</sub> NSs has a significant enhancement compared with Ag film. This could be attributed to semiconductor/metal composites have stronger Raman enhancement which associated with localized surface plasmon resonance (LSPR) of metallic nanostructures, induced by a charge-transfer mechanism at the semiconductor-metal interface. The typical SERS spectra of R6G can be detected in the range from 10<sup>-5</sup> M to 10<sup>-9</sup> M. The characteristic Raman peaks of R6G remained clearly observable even with a solution of 10<sup>-9</sup> M. This indicates that AgNPs-TiO<sub>2</sub> NSs as SERS substrates have high sensitivity. In addition, the enhancement factor (EF) estimated to be about 3.0×10<sup>5</sup>. To evaluate the uniformity of the AgNPs-TiO<sub>2</sub> NSs, SERS spectra of R6G by point mapping mode on a 20 × 20 μm area was collected and the RSD of twenty different locations was about 13.4%. The above results clearly demonstrated the excellent uniformity and reproducibility of the AgNPs-TiO<sub>2</sub> NSs SERS substrates.

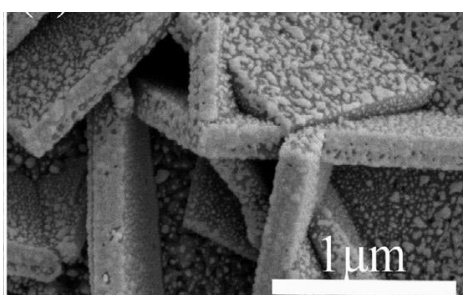


**Figure 2.44 SEM images of TiO<sub>2</sub> NSs after Ag-sputtering for 10 second [141]**

In this research, titanium dioxide nanotube arrays (TiO<sub>2</sub> NTs) decorated AgNPs and covered with reduced graphene oxide (rGO) have been prepared and used as a SERS substrate. According to the above reviews, nanotubular TiO<sub>2</sub> possess excellent SERS performance in a term of reproducibility than the others due to a well-

ordered array of the nanotubes. Therefore,  $\text{TiO}_2$  NTs is selected as a SERS substrate and they were decorated with AgNPs in order to enhance SERS sensitivity. In order to improve stability of the substrate, rGO was introduced onto the surface of  $\text{TiO}_2$  NTs/AgNPs hybrids. Moreover, the rGO could enhance electromagnetic mechanism because of the coupling between AgNPs and rGO, and it could also facilitate charge transfer between adsorbate and rGO materials, leading to chemical mechanism enhancement. Therefore, the  $\text{TiO}_2$  NTs/AgNPs-rGO is employed as a sensor for detection of glyphosate herbicide in order to obtain high-performance SERS activity. For comparison, many kinds of nanomaterials with different size and shape have been proposed as a substrate platform for SERS application and their characteristics are summarized in Table 2.7.

**Table 2.7 Various kinds of nanomaterials used as a SERS substrate**

SERS substrate	Probe molecule	EF	LOD	Precision	References
rGO/AgNPs	Methylene blue	$4.6 \times 10^5$	$10^{-7}$ M	-	[142]
rGO/AgNPs	Rhodamine 6G	-	$10^{-7}$ M	-	[143]
rGO/AgNPs	Rhodamine-6G 4-MBA	$1.29 \times 10^5$ $1.18 \times 10^5$	-	-	[144]
rGO/AgNPs	Rhodamine-6G	$8.9 \times 10^8$	-	5.1%	[145]
rGO/AgNPs/Cu <sub>2</sub> O	4-MBA	$8.2 \times 10^4$	-	-	[146]
Sulfonated-rGO/AgNPs	Malachite green and rhodamine 6G	$1 \times 10^9$	$10^{-6}$ M	7.9%	[147]
Dendron-exfoliated- rGO/AgNPs	Malachite green	$8.8 \times 10^6$	-	-	[148]
GN/AgNPs	Rhodamine-6G	$3.38 \times 10^7$	$10^{-13}$ M	<0.3%	[149]
GN/Ag nanocubes	2-naphthalenethiol	$3.9 \times 10^8$	-	12%	[150]
3D wrinkled-GN/AgNPs	Rhodamine-6G	$1.6 \times 10^5$	$10^{-9}$ M	-	[151]
TiO <sub>2</sub> NPs/rGO	4-MBA	$5.5 \times 10^6$	$10^{-7}$ M	3.3%	[152]
TiO <sub>2</sub> NTs/AgNPs	Rhodamine-6G	-	$10^{-8}$ M	-	[153]
TiO <sub>2</sub> NWs/AgNPs	Rhodamine-6G	-	$10^{-6}$ M	-	[154]
TiO <sub>2</sub> NFs/AgNPs	Methylene blue	$4.4 \times 10^5$	$10^{-8}$ M	-	[155]
TiO <sub>2</sub> nanotree/AgNPs	Rhodamine-6G	$5.3 \times 10^5$	$10^{-12}$ M	1.2%	[156]
TiO <sub>2</sub> /rGO-AgNCs	Rhodamine-6G	$1.3 \times 10^5$	-	-	[157]
TiO <sub>2</sub> NRs/GO-AgNPs	Rhodamine-6G	$5.9 \times 10^5$	$10^{-12}$ M	8.7%	[158]

AgNPs: silver nanoparticles, AgNCs: silver nanocrystals, rGO: reduced graphene oxide, GN: graphene, TiO<sub>2</sub> NPs: titanium dioxide nanoparticles, TiO<sub>2</sub> NFs: titanium dioxide nanofiber, 4-MBA: 4-mer-captobenzoic acid, EF: enhancement factor, LOD: limit of detection

Moreover, the determination of glyphosate and other pesticides based on nanomaterials-based SERS substrate are also presented below.

Sharma and et al. [159] reported the fabrication of SERS substrate by coating a Cu-grid with carbon layers before loading of colloidal silver nanoparticles based on galvanic displacement reactions. SERS measurements were carried out within 2-3 h of preparing the substrate with a 785 nm He-Ne laser excitation at 10 mW and 10% laser power with laser spot size of 100  $\mu\text{m}$ . A 3  $\mu\text{L}$  droplet of 0.5 mM R6G was spotted onto the substrate and air-dried. A Whatman filter paper and a commercial product Klarite substrate loaded with 3  $\mu\text{L}$  of 20 mM R6G were used as reference substrates to compare the performance of the nanostructured Ag-Cu-grid substrate. The substrate demonstrated excellent SERS reproducibility with a significant SERS enhancement factor of  $6.1 \times 10^5$  in comparison to Klarite substrate (Figure 2.45(A)). The SERS substrate was further applied for the detection of trace residue of glyphosate. The changes in the peak height at  $1440\text{ cm}^{-1}$  from the recorded Raman spectra for glyphosate concentrations ranged from 0.845-169 ppm, as showed in Figure 2.45(B), were calculated and the detection limit of glyphosate on Ag-Cu-grid was 0.845 ppm (5  $\mu\text{M}$ ). This detection limit is well below the currently accepted level of 20 mg/L for glyphosate in genetically modified soya.

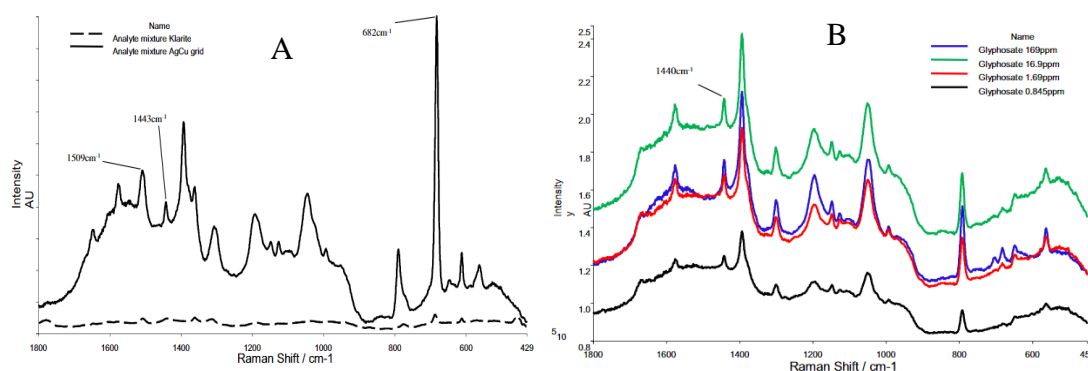


**Figure 2.45 (A) Raman spectra of Klarite and Ag-Cu-grid substrate for R6G detection and (B) An overlay of Raman spectra of the four test concentrations of glyphosate using the Ag-Cu-grid substrate [159]**

Xu and et al. [160] proposed a simple and sensitive method for the determination of glyphosate by combining ninhydrin reaction and SERS. The N atom from glyphosate combines with ninhydrin, forming a new C=N bond and linking glyphosate with ninhydrin. The product (ninhydrin-linked glyphosate) of the ninhydrin reaction is found to SERS-active, and directly correlates with the glyphosate concentration. Representative concentration-dependent SERS spectra of the products are shown in Figure 2.46. The SERS intensity at  $658\text{ cm}^{-1}$  shows a good linear relation with the concentrations of product in the range of  $1.0\times 10^{-7}$  to  $1.0\times 10^{-4}\text{ M}$  with  $r^2 = 0.9523$ . The limit of detection is calculated to be  $1.43\times 10^{-8}\text{ M}$ . The proposed method exhibited a good selectivity for the detection of the product derived from glyphosate.

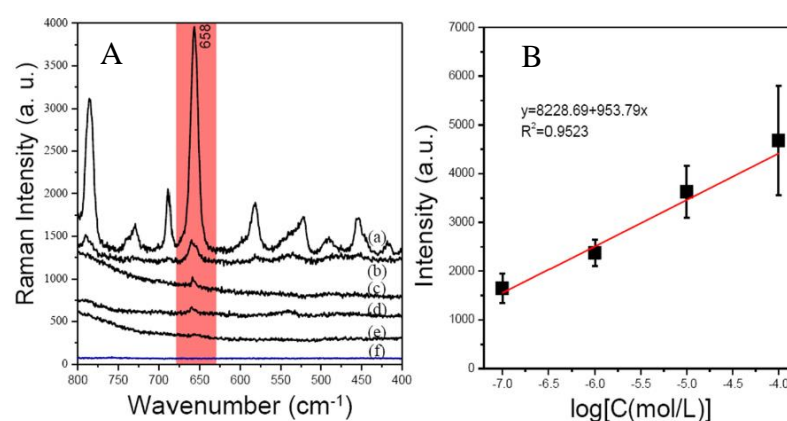


**Figure 2.46** (A) Representative concentration-depend SERS spectra of (a)  $10^{-3}$  (b)  $10^{-4}$  (c)  $10^{-5}$  (d)  $10^{-6}$  (e)  $10^{-7}\text{ M}$  ninhydrin-linked glyphosate and its corresponding standard curve [160]

Jiao and et al. [161] presented worm-like AuAg nanochains with highly interconnected ultrafine ( $\sim 6.2\text{ nm}$ ) bimetallic particles as an excellent SERS sensor via laser-assisted strategy. The enhanced SERS performances of the AuAg nanochains were illustrated by using crystal violet (CV) as the probe molecules. For comparison, mono-dispersed Au nanotwins were selected as a reference SERS substrate. The obvious comparative result confirms that the bimetallic AuAg nanochains have a strong advantage in the SERS applications. The SERS tests of CV molecules with different concentrations of  $10^{-5}$  to  $10^{-9}\text{ M}$  were obtained with the ultrasensitive detection limit in



the nM range. The AuAg nanochains-based SERS analyses were carried out to identify thiram pesticides on apple surfaces. As shown in Figure 2.47(A), it should be noted that the dominating characteristic bands of thiram molecules are clearly distinguishable even the concentration decreased to  $10^{-7}$  M (0.03 ppm), which is about 200 times lower than the maximal residue limit (MRL) of 7 ppm in fruit prescribed by the U.S. Environmental Protection Agency (EPA). The variations of SERS intensities at 560, 1145, 1442, 1386 and  $1518\text{ cm}^{-1}$  were plotted as a function of thiram concentration from  $10^{-3}$  to  $10^{-7}$  M and the five well-defined linear relationships were obtained, as showed in Figure 2.47(B).

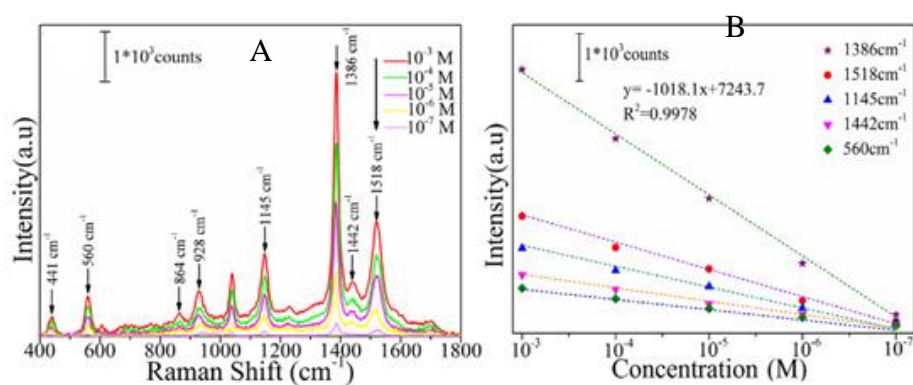


**Figure 2.47 (A) The SERS spectra of different concentration of thiram on AuAg nanochains and (B) its corresponding standard curve [161]**

Wang and et al. [162] constructed a SERS substrate based on Ag-nanoplates decorated graphene-sheets (Ag-NP@GN) for ultra-sensitive SERS detection of organic pesticides, including thiram and methyl parathion (MP). The Ag-nanoplates are held by the graphene and stay closely to each other, creating hot-spots for SERS signal amplification. On the other hand, the graphene sheets can serve as pesticides molecules assembler because of its strong absorption ability and  $\pi$ - $\pi$  interaction with pesticides molecules. The SERS enhancement factor of the Ag-NP@GN substrate was calculated using R6G as a probe molecule and the EF found to be  $4.7 \times 10^8$ . The Ag-NP@GN substrate shows good SERS-signal reproducibility with a relative signal deviation down to 5.6%. A very good linear response for thiram was found at the concentration ranging from  $10^6$  nM to 10 nM with the  $r^2$  of 0.995 and limit of detection

of 40 nM. In addition, a good linear relationship of the concentration ranging from  $5 \times 10^5$  nM to  $1 \times 10^3$  nM with a correlation coefficient of 0.993 and limit of detection of 5  $\mu$ M were obtained for MP detection. The prepared Ag-NP@GN substrate was also applied to detect the mixture of thiram and MP. Figure 2.48 shows the SERS spectra of the mixture of 100 nM thiram and  $5 \times 10^3$  nM MP in water. The characteristic peaks of each pesticides could be clearly identified, indicating the successful detection of multiplex pesticides using the Ag-NP@GN substrate.

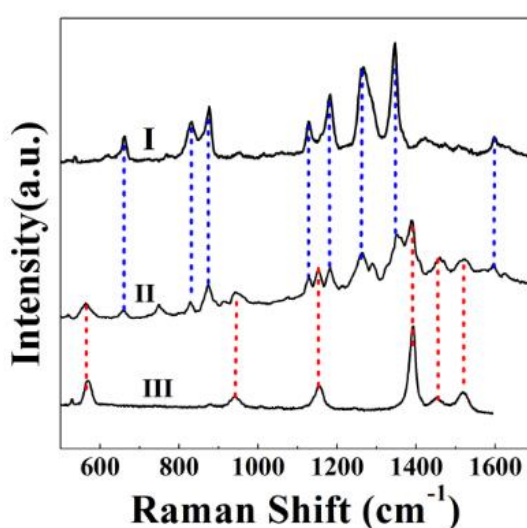


**Figure 2.48** SERS spectrum of  $1 \times 10^2$  nM thiram (Curve I), the mixture of  $1 \times 10^2$  nM thiram and  $5 \times 10^3$  nM MP (Curve II), and  $5 \times 10^3$  nM MP (Curve III) on the Ag-NP@GN substrate [162]



## **CHAPTER 3**

### **EXPERIMENTAL**

This chapter describes the instruments, equipment, chemicals and reagents used in this thesis. Each part, chemical preparations, sensor and biosensor fabrications, and the measurement procedures are clearly explained step by step. In addition, real sample preparations for determination with the designed sensors and biosensors compared to standard methods are also described.

#### **3.1 Instruments and equipment**

All instruments and equipment are presented in Table 3.1 and Table 3.2, respectively.

**Table 3.1 Instruments**

<b>Instrument</b>	<b>Model</b>	<b>Company</b>
Direct current power supply	N5751A	KEYSIGHT
Direct current magnetron sputtering	EMACE600	Leica
Energy dispersive X-ray spectrometer (EDS)	OCTANEPLUS	AMETEK materials analysis division
Fourier transform infrared spectrometer (FTIR)	Nicolet 6700	Thermo Scientific
High performance liquid chromatography (HPLC)	Ultimate 3000	Thermo Dionex
Potentiostat/galvanostat	PGSTAT12	Metrohm
Raman spectrophotometer	1024x256-OE	Horiba Instrument
Scanning electron microscope (SEM)	JSM-6010-LV	JEOL
Solar simulator	SS150&4200SCS	SCIENCETECH Inc.
Ultra-high performance liquid chromatography (UHPLC)	1290 Infinity II	Agilent

**Table 3.1 Instruments (continued)**

<b>Instrument</b>	<b>Model</b>	<b>Company</b>
UV-vis spectrophotometer	Cary 5000 UV-vis NIR	Agilent Technologies
X-ray diffraction spectrometer (XRD)	X'Pert-MPD	PHILIPS
X-ray photoelectron spectrometer (XPS)	KRATOC analytical	SHIMADZU

**Table 3.2 Equipment**

<b>Equipment</b>	<b>Model</b>	<b>Company</b>
Aluminum stub	12.2 mm diameter x 5 mm dept	JEOL
Autoclave	AL02-10	Advantage-Lab
Auxiliary electrode	Platinum wire (2 mm diameter)	Metrohm
Biosafety cabinet	Jouan MSC 12 Class II A2	Thermo Fisher Scientific
Copper wire	Silicone shielded copper wire	-
C-18 column	1.8 $\mu$ m (2.1 $\times$ 50 mm)	Agilent technologies
Grinder	A11 basic Analytical Mill	Industries Kaiser Argentina
Incubator	IN260plus	Memmert
Microcentrifuge	GL 083 MiniSpin® Plus	Eppendorf
Microcentrifuge tubes	1 mL and 2 mL	Eppendorf
Micropipette	1-10 $\mu$ L, 2-20 $\mu$ L, 20-200 $\mu$ L, 200-1000 $\mu$ L	Eppendorf
Microscope glass slide	Ground edges 1"×3" (1 mm-1.2 mm thick)	Sail Brand
pH meter	pH series 510	Eutech Instruments
Platinum foil	99.9%, 0.025 mm thickness	Sigma Aldrich
Reference electrode	Ag/AgCl (3 M KCl)	Metrohm

**Table 3.2 Equipment (continued)**

<b>Equipment</b>	<b>Model</b>	<b>Company</b>
Rotary evaporator	Hei-VAP Precision	Heidolph Instruments
Sieving	ASTM E11 (300 Mic)	Endecotts Ltd
Silver target	99.99%, 54×0.3 mm	Ted Pella, InC.
Teflon holder electrode	PTFE Teflon rod	-
Teflon sheet	PTFE Teflon sheet	-
Titanium foil	0.125 mm thick, purity > 99.6%	Goodfellow
Ultrasonicator	CP1100T	CREST ultrasonics
Vortex mixer	G560E	Scientific Industries

### 3.2 Chemicals and reagents

Chemicals are purchased from various companies as shown in Table 3.3.

**Table 3.3 List of chemicals and reagents**

<b>Chemicals</b>	<b>Formula</b>	<b>Detail</b>	<b>Company</b>
Acetic acid	C <sub>2</sub> H <sub>4</sub> O <sub>2</sub>	≥ 99.7%, glacial, ACS reagent	Sigma-Aldrich
Acetonitrile	C <sub>2</sub> H <sub>3</sub> N	99.8% (anhydrous)	Sigma-Aldrich
Acid phosphatase (ACP)	-	Type I from wheat germ, 0.5 units/mg	Sigma-Aldrich
Ammonium fluoride	NH <sub>4</sub> F	≥ 98.0%, ACS reagent	Sigma-Aldrich
Barium hydroxide	Ba(OH) <sub>2</sub>	≥ 98.0%, ACS reagent	Sigma-Aldrich
Bisphenol A (BPA)	C <sub>15</sub> H <sub>16</sub> O <sub>2</sub>	≥ 99%	Sigma-Aldrich
Bovine serum albumin (BSA)	-	≥ 98%, lyophilized powder, essentially fatty acid free	Sigma-Aldrich

**Table 3.3 List of chemicals and reagents (continued)**

<b>Chemicals</b>	<b>Formula</b>	<b>Detail</b>	<b>Company</b>
1-butyl-2,3-dimethyl imidazolium tetrafluoroborate (Ionic liquid, IL)	$\text{C}_9\text{H}_{17}\text{BF}_4\text{N}_2$	$\geq 97\%$	Sigma-Aldrich
Carbon ink	C	Carbon paste, C2030519P4	SunChemical
Carcinoembryonic antigen (CEA)	-	$\geq 95\%$ (SDS- PAGE), buffered aqueous solution	Sigma-Aldrich
4-chloro-3 5- dinitrobenzotrifluoride	$\text{ClC}_6\text{H}_2(\text{NO}_2)_2$ $\text{CF}_3$	98%	Sigma-Aldrich
Dichloromethane	$\text{CH}_2\text{Cl}_2$	$\geq 99.9\%$ , HPLC Plus for HPLC, GC, and residue analysis	Sigma-Aldrich
Dimethylformamide (DMF)	$\text{C}_3\text{H}_7\text{NO}$	99.8% (anhydrous)	Sigma-Aldrich
Disodium hydrogen phosphate heptahydrate	$\text{Na}_2\text{HPO}_4 \cdot$ $7\text{H}_2\text{O}$	98.0-102.0%, ACS reagent	Sigma-Aldrich
Disodium phenyl phosphate dibasic dihydrate	$\text{C}_6\text{H}_5\text{Na}_2\text{O}_4\text{P} \cdot$ $2\text{H}_2\text{O}$	$\geq 95\%$	Sigma-Aldrich
Ethanol	$\text{CH}_3\text{CH}_2\text{OH}$	Absolute ethanol, ACS reagent (anhydrous)	Sigma-Aldrich
Ethylene glycol	$\text{C}_2\text{H}_6\text{O}_2$	RPE for analysis	Carlo Erba
Formic acid	$\text{CH}_2\text{O}_2$	$\geq 95.0\%$ , reagent grade	Sigma-Aldrich

**Table 3.3 List of chemicals and reagents (continued)**

<b>Chemicals</b>	<b>Formula</b>	<b>Detail</b>	<b>Company</b>
Glassy carbon powder	C	99.95% trace metals basis, spherical powder, 2-12 $\mu\text{m}$	Sigma-Aldrich
Glutaraldehyde	$\text{C}_5\text{H}_8\text{O}_2$	Grade II, 25% in $\text{H}_2\text{O}$	Sigma-Aldrich
Glyphosate	$\text{C}_3\text{H}_8\text{NO}_5\text{P}$	PESTANAL®, analytical standard	Sigma-Aldrich
Gold (III) chloride trihydrate	$\text{HAuCl}_4 \cdot 3\text{H}_2\text{O}$	$\geq 99.9\%$ , trace metals basis	Sigma-Aldrich
Graphene nanoplatelet	C	15 $\mu\text{m}$ particle size, surface area 120-150 $\text{m}^2/\text{g}$	Sigma-Aldrich
Graphene oxide	C	15-20 sheets, 4-10% edge-oxidized	Sigma-Aldrich
Hexane	$\text{C}_6\text{H}_{14}$	95% (anhydrous)	Sigma-Aldrich
Human serum	-	Serum from human male AB plasma	Sigma-Aldrich
Hydrochloric acid	HCl	37%, ACS reagent	Fluka
Iron (II, III) oxide	$\text{Fe}_3\text{O}_4$	Nanopowder, < 50 nm particle size	Sigma-Aldrich
Manganese (II) sulfate tetrahydrate	$\text{MnSO}_4 \cdot 4\text{H}_2\text{O}$	For analysis EMSURE®	Sigma-Aldrich
Methylene blue	$\text{C}_{16}\text{H}_{18}\text{ClN}_3\text{S}$	Solid powder	Sigma-Aldrich
Mineral oil	-	Light	Sigma-Aldrich
Monoclonal anti-carcinoembryonic antigen antibody (anti-CEA)	-	Monoclonal antibody produced in mouse	Sigma-Aldrich



**Table 3.3 List of chemicals and reagents (continued)**

<b>Chemicals</b>	<b>Formula</b>	<b>Detail</b>	<b>Company</b>
Phenol	C <sub>6</sub> H <sub>6</sub> O	≥99.0%, ACS reagent	Sigma-Aldrich
Potassium bromide	KBr	≥ 99% trace metals basis, FT-IR grade	Sigma-Aldrich
Potassium chloride	KCl	≥ 99.0%, BioXtra	Sigma-Aldrich
Potassium hexacyanoferrate (II)	K <sub>4</sub> [Fe(CN) <sub>6</sub> ]	≥ 99.95% trace metals basis	Sigma-Aldrich
Potassium hexacyanoferrate (III)	K <sub>3</sub> [Fe(CN) <sub>6</sub> ]	99.98% trace metals basis	Sigma-Aldrich
Potassium permanganate	KMnO <sub>4</sub>	≥ 99.0%, ACS reagent	Sigma-Aldrich
Silver ink	AgCl	Ag/AgCl paste 60:40, C2130809D5	SunChemical
Silver nitrate	AgNO <sub>3</sub>	≥ 99.0%, ACS reagent	Sigma-Aldrich
Sodium acetate	CH <sub>3</sub> COONa	≥ 99.0%, ACS reagent	Sigma-Aldrich
Sodium borohydride	NaBH <sub>4</sub>	≥ 98.0%, powder	Sigma-Aldrich
Sodium dihydrogen phosphate monohydrate	NaH <sub>2</sub> PO <sub>4</sub> ·H <sub>2</sub> O	≥ 99.0%, BioXtra	Sigma-Aldrich
Sodium hydroxide	NaOH	≥ 98%, reagent grade (anhydrous)	Sigma-Aldrich
Sodium sulfate	Na <sub>2</sub> SO <sub>4</sub>	≥ 99%, ACS reagent (anhydrous)	Sigma-Aldrich

### 3.3 Carbon composite nanomaterials-based sensor: electrochemical sensor for bisphenol A detection

The electrochemical sensor is fabricated based on glassy carbon paste electrode (GCPE) modified with a composite of graphene nanoplatelet (GNP) and 1-butyl-2, 3-dimethylimidazolium tetrafluoroborate (Ionic liquid, IL) for detection of bisphenol A (BPA) using differential pulse voltammetry (DPV). This sensor is applied for food applications, drinking waters and plastic drinking water bottles. The preparation of all chemicals and real samples, the process of sensor construction, characterization of the sensor, and the measurement procedures are subsequently explained.

#### 3.3.1 Chemical and real sample preparations

##### 3.3.1.1 Phosphate buffer solution (0.1 M)

13.4xxx g of disodium hydrogen phosphate ( $\text{Na}_2\text{HPO}_4 \cdot 7\text{H}_2\text{O}$ ) and 6.9xxx g of monosodium dihydrogen phosphate ( $\text{NaH}_2\text{PO}_4 \cdot \text{H}_2\text{O}$ ) were dissolved separately into 500 mL volumetric flask with DI water. After that, phosphate buffer solution is prepared by mixing of  $\text{Na}_2\text{HPO}_4$  and  $\text{NaH}_2\text{PO}_4$  and then adjusted the pH to the desired pH value by 1 M NaOH or 1 M HCl as required.

##### 3.3.1.2 Potassium hexacyanoferrate (5 mM $\text{Fe}(\text{CN})_6^{3-/4-}$ )

0.74xx g of potassium chloride (KCl) was dissolved with DI water into 100 mL volumetric flask to get 0.1 M KCl. Then, 5 mM of  $\text{Fe}(\text{CN})_6^{3-/4-}$  was prepared by dissolution of 0.16xx g  $\text{K}_3[\text{Fe}(\text{CN})_6]$  and 0.15xx g  $\text{K}_4[\text{Fe}(\text{CN})_6]$  in 100 mL of 0.1 M KCl solution.

##### 3.3.1.3 Bisphenol A stock solution (1 mM BPA)

Stock solution of BPA was prepared by dissolution of 0.002x g BPA powder into 10 mL volumetric flask with anhydrous ethanol. After that, working solutions of BPA were prepared by dilution of 1 mM BPA with anhydrous ethanol.

##### 3.3.1.4 Plastic bottles for water containing preparation

Plastic bottles were purchased from a local supermarket in Ubon Ratchathani. The extraction of BPA from plastic bottles were conducted by cutting of the samples into small pieces and cleaned thoroughly with highly pure water. The cleaned samples were then powdered using a grinder and the large powder particles (> 300 micron) are discarded by sieving. After that, about 1.00 g of small plastic powder were added to 20 mL of acetonitrile and extracted by ultrasonication for 2 h. After

filtration, the liquid phase was concentrated by a rotary evaporator at the temperature of 50 °C and then the final volume was adjusted to 2 mL with acetonitrile.

#### 3.3.1.5 Drinking water preparation

100 mL drinking water from the above three plastic bottles were placed into a 250 mL separatory funnel. The extractions were performed with 45 mL of dichloromethane for three times and then washed with anhydrous sodium sulfate. After that, solvent was removed by a rotary evaporator at the temperature of 50 °C till dryness. The sample residues were re-dissolved with 40 mL hexane and 30 mL acetonitrile, and the extractions were performed again. The acetonitrile phase was collected and concentrated by a rotary evaporator at the temperature of 50 °C. Finally, final volume of the extracted samples was adjusted to 2 mL with acetonitrile.

### 3.3.2 Electrochemical sensor preparation

#### 3.3.2.1 Glassy carbon paste electrode (GCPE)

The GCPE is prepared by mixing manually glassy carbon powder with mineral oil (70:30 m:m) in a mortar and grinding homogeneously. Then, glassy carbon paste was filled in the drilling hole of an electrode holder with a diameter of 1 cm and a depth of 0.5 cm. Contact to the paste was made with a copper wire through the electrode holder. Finally, the surface of the paste was smoothed with a Teflon sheet to a smooth and shiny appearance. The composition of GCPE and the electrode surface are shown in Figure A.1 (Appendix A.1).

#### 3.3.2.2 Graphene nanoplatelet-ionic liquid composite (GNP-IL)

The GNP-IL composites were prepared by dispersion of the graphene nanoplatelet (GNP) in dimethylformamide (DMF) using an ultrasonicator for about 2 h to get a homogeneous suspension at the concentration of 1.0 mg/mL. Next, 20  $\mu$ L of 1-butyl-2,3-dimethylimidazolium tetrafluoroborate (Ionic liquid, IL) were added to the well-dispersed GNP suspension and sonicated for further 30 min. Finally, the resulting mixture was centrifuged at 10,000 rpm for 10 min. The supernatant was discarded and the solid residues were re-dispersed in 500  $\mu$ L DMF.

#### 3.3.2.3 GCPE modified with GNP-IL composites (GCPE/GNP-IL)

7  $\mu$ L of the GNP-IL mixtures were directly dropped onto surface of the GCPE (0.8 cm of diameter) and allowed to dry completely at room temperature to

get the sensor (GCPE/GNP-IL). The procedure for the preparation of the modified electrode is illustrated in Figure 3.1.

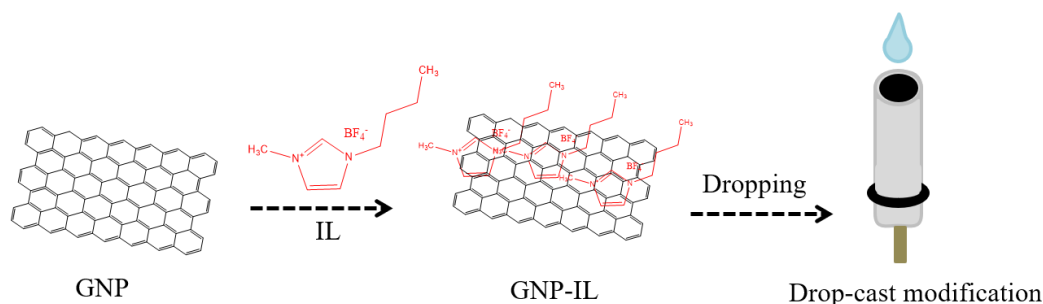


**Figure 3.1 Schematic diagram of the electrochemical sensor preparation**

### 3.3.3 Characterizations of the GCPE/GNP-IL

#### 3.3.3.1 Characterization of the GCPE/GNP-IL by SEM

The morphology of GCPE and GCPE/GNP-IL were studied by scanning electron microscopy (SEM). These electrodes were attached on aluminum stubs and then sputter coated with platinum. The accelerating voltage and the magnification for all images was 20 kV and 3000x, respectively. The results are displayed in section 4.1.1.1.

#### 3.3.3.2 Characterization of GNP-IL composites by FTIR

The GNP, IL and GNP-IL nanomaterials were characterized by Fourier transforms infrared spectroscopy (FTIR) and the spectra are recorded in the transmission mode using the KBr pellet technique by mixing of 1 mg nanomaterials with 0.1 g KBr. The results are presented in section 4.1.1.2.

### 3.3.4 Electrochemical characterizations of the GCPE/GNP-IL

Electrochemical characterizations of the GCPE/GNP-IL were performed using a computer-controlled electrochemical workstation and evaluated with the corresponding NOVA software. A three-electrode systems were carried out with a modified GCPE as the working electrode, an Ag/AgCl (3 M KCl) as the reference electrode, and a platinum wire as the counter electrode. The apparatus scheme of the electrochemical measurement system and three-electrode arrangements are displayed in Figure A.2 (Appendix A.1).

### 3.3.4.1 CV and EIS measurements of the GCPE/GNP-IL

The performance of various electrodes, including unmodified GCPE, GCPE modified with IL (GCPE/IL), GNP (GCPE/GNP), and GNP-IL composites (GCPE/GNP-IL), were investigated in a 10 mL electrochemical cell containing 5 mM  $\text{Fe}(\text{CN})_6^{3-/4-}$ . Cyclic voltammetry (CV) was carried out by sweeping the potential from -0.5 to +1.0 V at a scan rate of 0.1 V/s. Electrochemical impedance spectroscopy (EIS) was performed within a frequency range of 10,000-0.1 Hz and an amplitude of 0.01 V. The results are presented in section 4.1.2.1.

### 3.3.4.2 DPV measurements of the GCPE/GNP-IL

The performance of the GCPE/GNP-IL for detection of BPA was evaluated by differential pulse voltammetry (DPV), in comparison to unmodified GCPE, GCPE/IL, and GCPE/GNP. The measurements were recorded in 0.1 M phosphate buffer solution (pH 8.0) containing 2  $\mu\text{M}$  BPA in the potential range from +0.3 to +1.0 V with a pulse amplitude of 50 mV, a step potential of 50 mV and a scan rate of 50 mV/s. The results are shown in section 4.1.2.2.

### 3.3.4.3 CV measurements at different scan rate of the GCPE/GNP-IL

The mechanism of electron transfer at surface of the GCPE/GNP-IL were investigated by CV in both redox probe solution and BPA solution. CV measurements were performed by sweeping the potential from -0.5 to +1.0 V at different scan rates between 0.02 and 0.2 V/s in 5 mM  $\text{Fe}(\text{CN})_6^{3-/4-}$  solution and scanning the potential from +0.2 to +1.0 V at different scan rates between 0.01 and 0.15 V/s in 0.1 M phosphate buffer solution containing 1  $\mu\text{M}$  BPA. The results are showed in section 4.1.2.3.

## 3.3.5 Optimization study of the GCPE/GNP-IL

Parameters affecting electrochemical performance for BPA detection based on the GCPE/GNP-IL were evaluated by DPV. The measurements were carried out by scanning the potential from +0.3 to +1.0 V in 0.1 M phosphate buffer solution containing 1  $\mu\text{M}$  BPA and the electrochemical system was conducted as described in section 3.3.4.

### 3.3.5.1 Study effect of amount of IL and GNP-IL composite

Firstly, the influences of IL amount for functionalization on the GNP were investigated by mixing of 0, 5, 10, 15, 20, and 25  $\mu\text{L}$  of IL with GNP suspension, which were calculated as 0.0, 0.1, 0.2, 0.3, 0.4, and 0.5  $\text{mg}\cdot\text{cm}^{-2}$  of IL on the GCPE

surface (Appendix C.1 and C.2). Next, the effects of GNP-IL composite loading were demonstrated by dropping of the composites at 2, 4, 5, 6, 7, 8, and 10  $\mu\text{L}$  on the GCPE, which were calculated as 8, 16, 20, 24, 28, 32 and 40  $\mu\text{g}\cdot\text{cm}^{-2}$  of GNP on the GCPE surface (Appendix C.3). The results are showed in section 4.1.3.1.

#### 3.3.5.2 Study effect of pH solution on the detection of BPA

0.1 M phosphate buffer solution with various pH value of 5, 6, 7, 8, and 9 were prepared and investigated. The results are presented in section 4.1.3.2.

#### 3.3.5.3 Study effect of pulse potential, step potential, and scan rate

The parameters for DPV measurements, including pulse potential (25, 50, 75, 100, 125, 150, 175, and 200 mV), step potential (10, 20, 30, 40, 50, and 60 mV), and scan rate (10, 25, 50, 75, 100, and 125 mV/s) were optimized. The results are presented in section 4.1.3.3.

### 3.3.6 Analytical performance investigation of the GCPE/GNP-IL

Analytical performances of the GCPE/GNP-IL for BPA detection were investigated under optimum conditions by DPV. The measurements were carried out by scanning the potential from +0.3 to +1.0 V in 0.1 M phosphate buffer solution (pH 8) containing 1  $\mu\text{M}$  BPA with a pulse amplitude, step potential and scan rate of 150 mV, 30 mV, and 50 mV/s, respectively. The electrochemical system was conducted as described in section 3.3.4.

#### 3.3.6.1 Investigation of linear range, LOD and LOQ

Firstly, linearity of the GCPE/GNP-IL for BPA detection was studied compared to the bare GCPE, GCPE/GNP, and GCPE/IL. Various concentrations of BPA were tested at 0.02, 0.10, 0.20, 0.40, 0.80, 1.2, 1.6, 2.0, 2.5, 3.0, 3.5, 4.0, 4.5, and 5.0  $\mu\text{M}$ . Next, limit of detection (LOD) and limit of quantification (LOQ) are determined by successive detection of 0.02  $\mu\text{M}$  BPA, the lowest concentration of calibration curve, for ten times ( $n=10$ ). Then, the LOD and LOQ were calculated on a basis of  $3\text{SD}/\text{slope}$  and  $10\text{SD}/\text{slope}$ , respectively, where SD is standard deviation of BPA signal at a concentration of 0.02  $\mu\text{M}$  and slope was obtained from the calibration curve. The results are presented in section 4.1.4.1.

#### 3.3.6.2 Study reproducibility and repeatability of the GCPE/GNP-IL

Reproducibility of the sensor was evaluated by using five different freshly-prepared electrodes ( $n = 5$ ) and repeatability was investigated by measuring the

current response of 1  $\mu\text{M}$  BPA with five successive measurements ( $n = 5$ ). Then, relative standard deviation (%RSD) was calculated. The results are showed in section 4.1.4.2.

#### 3.3.6.3 Study stability of the GCPE/GNP-IL

Stability of the GCPE/GNP-IL was investigated by detection of 1  $\mu\text{M}$  BPA every day in triplicate for 2 weeks. The results are showed in section 4.1.4.3.

#### 3.3.6.4 Study selectivity of the GCPE/GNP-IL

Selectivity of BPA detection using the GCPE/GNP-IL was estimated by study interferent effects of common interferences in the detection of BPA, including phenol (1  $\mu\text{M}$ ), 1-napthol (1  $\mu\text{M}$ ), and 4-nitrophenol (10  $\mu\text{M}$ ), some possible interfering substances in natural water samples, such as organic compounds like glucose (100  $\mu\text{M}$ ) and sucrose (100  $\mu\text{M}$ ), and some inorganic ions at a concentration of 100  $\mu\text{M}$ , such as  $\text{Na}^+$ ,  $\text{Ca}^{2+}$ ,  $\text{Mg}^{2+}$ ,  $\text{Al}^{3+}$ ,  $\text{Zn}^{2+}$ ,  $\text{Cu}^{2+}$ ,  $\text{Fe}^{2+}$ ,  $\text{Pb}^{2+}$ , and  $\text{Cd}^{2+}$ . These interferences were mixed with BPA solution (1  $\mu\text{M}$ ) and their current signal were recorded, in comparison to the signal of pure BPA solution (1  $\mu\text{M}$ ). The results are displayed in section 4.1.4.4.

### 3.3.7 Determination of BPA in real samples

Three plastic drinking bottles and drinking water samples were extracted as described in experiment 3.3.1.4 and 3.3.1.5, respectively. In order to check recovery of the extraction procedures, standard BPA solution (1 mg/L) was spiked into the samples and the amount of BPA in samples and spiked samples were checked by the electrochemical sensor and high-performance liquid chromatography as a standard method.

#### 3.3.7.1 Determination of BPA by the GCPE/GNP-IL sensor

0.5 mL of the samples and spiked samples solution were injected into a 5 mL electrochemical cell containing 0.1 M phosphate buffer solution (pH 8.0). The signals were detected by the GCPE/GNP-IL sensor with DPV under optimum conditions. Each sample solution underwent three parallel determinations by the standard addition method. The standard addition curve was plotted between current signal and concentration of BPA (0.0, 0.2, 0.4, and 0.6 mg/L). The amount of BPA in real samples and recovery percentage were then calculated. The results are showed in section 4.1.5.1.

### 3.3.7.2 Determination of BPA by HPLC

High performance liquid chromatography (HPLC) was performed with external calibration method. The experiments were performed under a flow rate of 1.0 mL/min, a detection wavelength at 228 nm using a diode array detector (Ultimate 3000, DIONEX, Germany), an autosampler injector with a 100  $\mu$ L sample loop, C18 column (4.6 $\times$ 250 mm, Acclaim<sup>TM</sup>120), and isocratic elution of a mixture of acetonitrile and water (60:40, v/v) as mobile phase. All the standard and sample solutions were filtered with a 0.45  $\mu$ m nylon syringe filter before analysis and the mobile phase was degassed before use. First of all, calibration curve was conducted in which the peak area was plotted against BPA concentration from 0.05-200 mg/L. Then, amount of BPA in real samples and spiked samples were detected in triplicate. Finally, recovery percentage were calculated and a paired t-test analysis at a confidence interval of 95% probability was used to compare the results from two methods. The results are showed in section 4.1.5.2.

## 3.4 Carbon composite nanomaterials-based biosensor: electrochemical biosensor for detection of CEA biomarker

The electrochemical biosensor for analysis of carcinoembryonic antigen (CEA) was constructed based on immobilization of antibody conjugated core shell Fe<sub>3</sub>O<sub>4</sub>@Au nanoparticles on the surface on screen-printed carbon electrode (SPCE) modified with manganese dioxide (MnO<sub>2</sub>) deposited graphene nanoplatelet (GNP). The biosensor was applied for determination of CEA in human serum sample using linear sweep voltammetry (LSV) and electrochemical impedance spectroscopy (EIS). The preparation of chemicals and serum samples, the procedure of biosensor construction, characterization of the biosensor and the measurement strategy were respectively explained.

### 3.4.1 Chemical and human serum sample preparations

#### 3.4.1.1 Antibody solution (200 $\mu$ g/mL anti-CEA)

Antibody solution at a concentration of 200  $\mu$ g/mL was prepared by pipette 29  $\mu$ L CEA antibody stock solution (6,800  $\mu$ g/mL) into a 1-mL microcentrifuge tube and adjust a volume with phosphate buffer solution pH 7.4 (experimental 3.3.1.1).



#### 3.4.1.2 Antigen solution (CEA solution)

Stock solution of CEA antigen (50  $\mu\text{g/mL}$ ) was prepared by dissolution of 25  $\mu\text{g}$  CEA pellets with 0.5 mL phosphate buffer solution pH 7.4. After that, working solution of CEA at different concentrations were prepared by dilution of the stock solution with phosphate buffer solution.

#### 3.4.1.3 Bovine serum albumin solution (1 %w/v BSA)

BSA at the concentration of 1 %w/v was prepared by dissolution of 0.01xx g of BSA pellets with 1 mL phosphate buffer solution pH 7.4.

#### 3.4.1.4 Human serum sample

Human serum samples from human male AB plasma was diluted with 0.1 M phosphate buffer solution (pH 7.4) for 10-fold and 100-fold times.

#### 3.4.1.5 Potassium permanganate solution (10 mM $\text{KMnO}_4$ )

$\text{KMnO}_4$  solution at a concentration of 10 mM was prepared by dissolution of 0.08xx g  $\text{KMnO}_4$  powder in a 50 mL-volumetric flask with DI-water.

#### 3.4.1.6 $\text{Fe}_3\text{O}_4$ suspension (0.25 mM $\text{Fe}_3\text{O}_4$ )

$\text{Fe}_3\text{O}_4$  suspension with a concentration of 0.25 mM was prepared by dispersion of 0.001x g of  $\text{Fe}_3\text{O}_4$  powder with 25 mL DI-water in a volumetric flask.

#### 3.4.1.7 Gold solution (0.25 mM $\text{HAuCl}_4$ )

0.002x g of  $\text{HAuCl}_4 \cdot 3\text{H}_2\text{O}$  pellets were dissolved with a cooled DI-water in a volumetric flask (25 mL) in order to obtain 0.25 mM  $\text{HAuCl}_4$  solution.

#### 3.4.1.8 Sodium borohydride solution (0.1 M $\text{NaBH}_4$ )

0.018x g of  $\text{NaBH}_4$  powder were dissolved with 5 mL cooled DI-water in a volumetric flask in order to obtain 0.1 M  $\text{NaBH}_4$ . Then, the solution was protected from light by covering with aluminum foil.

### 3.4.2 Electrochemical biosensor preparation and detection

#### 3.4.2.1 Screen printed carbon electrode (SPCE) and electrode holder

The SPCEs were prepared by manually printing carbon ink and silver ink onto a transparent projector film (PVC) through the block screen fabricated by Silkcut LP. Professional graphic and screen services (Bangkok, Thailand). The SPCEs were consisted of three electrodes on the same substrate, including working electrode (WE), reference electrode (RE) and counter electrode (CE), as shown in Figure A.3 (Appendix A.4.2). The WE, CE, and RE were made from carbon, carbon,

and silver, respectively. The SPCE was fixed in a home-made electrochemical cell, which was made from Acrylic sheet with a size of  $6 \times 7.3 \times 1.4$  cm. A neodymium external magnet with a cylindrically shape was assembled on the base at the middle, while the lid was drilled to make a sample injection hole (diameter of 1 cm) located at the center, as can be seen in Figure A.4 (Appendix A.4.2).

#### 3.4.2.2 Manganese oxide-graphene nanoplatelets composite (GNP-MnO<sub>2</sub>)

The GNP-MnO<sub>2</sub> composite was synthesized by dispersion of 5 mg GNP and 2 mg of manganese (II) sulfate tetrahydrate (MnSO<sub>4</sub>·4H<sub>2</sub>O) in 50 mL DI-water. The mixed solution was sonicated for 2 h to obtain a homogeneous suspension. Then, 50 mL of 10 mM KMnO<sub>4</sub> (experiment 3.4.1.5) was slowly dropwise into the mixture under vigorously stirring at room temperature. After 6 h, a dark brown precipitate is formed. The obtained products were washed several times with DI-water and ethanol, respectively. Next, the clean products were centrifuged three times at 5000 rpm and dried at 60°C for 12 h. Finally, 0.2 mg of the solid residues were re-dispersed in 1 mL DI-water.

#### 3.4.2.3 Core shell Fe<sub>3</sub>O<sub>4</sub>@Au nanoparticles

Core shell Fe<sub>3</sub>O<sub>4</sub>@Au nanoparticles with a ratio of Fe<sub>3</sub>O<sub>4</sub>:Au as 1:0.8 is synthesized by mixing of 10 mL Fe<sub>3</sub>O<sub>4</sub> suspension (experimental 3.4.1.6) with 8 mL HAuCl<sub>4</sub> solution (experimental 3.4.1.7) and 22 mL cooled DI-water under ultrasonication for 15 min. Subsequently, a freshly prepared NaBH<sub>4</sub> solution (experimental 3.4.1.8) was added rapidly to the mixed cooled suspension and then sonicated for 10 min. Finally, the core shell Fe<sub>3</sub>O<sub>4</sub>@Au suspension was covered with aluminum foil to protect light.

#### 3.4.2.4 Core shell Fe<sub>3</sub>O<sub>4</sub>@Au conjugated antibody (Fe<sub>3</sub>O<sub>4</sub>@Au/anti-CEA)

Antibody conjugated core shell Fe<sub>3</sub>O<sub>4</sub>@Au (Fe<sub>3</sub>O<sub>4</sub>@Au/anti-CEA) was prepared by mixing 1.5 mL of the synthesized Fe<sub>3</sub>O<sub>4</sub>@Au (experiment 3.4.2.3) with 0.5 mL of 200 µg/mL CEA-antibody solution (experiment 3.4.1.1). Then, the mixed solution was incubated at 4°C in a refrigerator overnight. Resultant Fe<sub>3</sub>O<sub>4</sub>@Au/anti-CEA was collected via an external magnet. After being rinsed with 0.1 M phosphate buffer solution at pH 7.4 (experiment 3.3.1.1), the products are dispersed in 1% BSA solution (experiment 3.4.1.3) and kept at 4°C in a refrigerator for 2 h to block possible

nonspecific binding sites. Finally, the resulting products were collected using a magnet and re-dispersed in 0.5 mL phosphate buffer solution (pH 7.4).

#### 3.4.2.5 SPCE modified with GNP-MnO<sub>2</sub> and Fe<sub>3</sub>O<sub>4</sub>@Au/anti-CEA (SPCE/ GNP-MnO<sub>2</sub>/Fe<sub>3</sub>O<sub>4</sub>@Au/anti-CEA)

The process for the preparation of biosensor is illustrated in Figure 3.2. Firstly, 10  $\mu$ L GNP-MnO<sub>2</sub> nanocomposites (experiment 3.4.2.2) was directly dropped onto active area of the SPCE and allowed to dry under ambient atmosphere. Next, 5  $\mu$ L of Fe<sub>3</sub>O<sub>4</sub>@Au/anti-CEA conjugation (experiment 3.4.2.4) was dropped on the modified SPCE and then incubated for 2 h at 37  $^{\circ}$ C in an incubator. The conjugated antibodies were attached on the electrode surface by an external magnet embedded in the electrode holder, while the unbound conjugated antibodies were removed from the surface of electrode by thoroughly washing with phosphate buffer solution. After washing and drying, the biosensor was ready for electrochemical measurements.

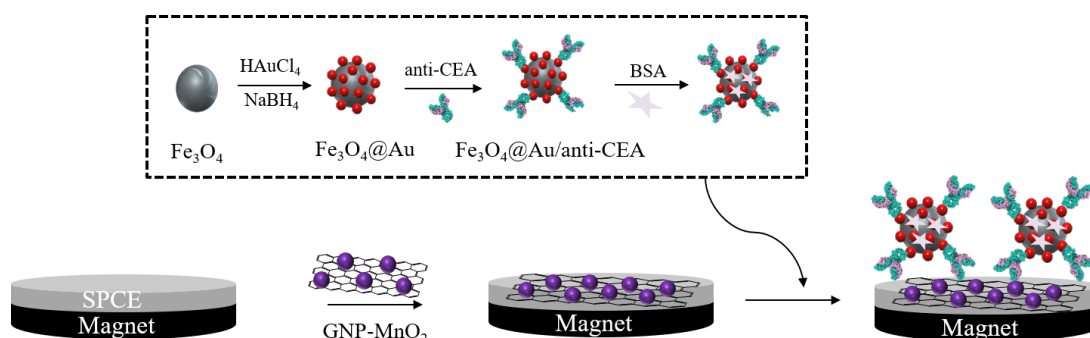


**Figure 3.2 Schematic diagram of the electrochemical biosensor preparation**

#### 3.4.2.6 CEA detection by the electrochemical biosensor

After producing the biosensor (experiment 3.4.2.5), 100  $\mu$ L of 0.1 M phosphate buffer solution (pH 7.4) containing 5 mM Fe(CN)<sub>6</sub><sup>3-/4-</sup> (experiment 3.3.1.2) was injected through a sample injection hole and then electrochemical measurements were performed by using linear sweep voltammetry (LSV) and electrochemical impedance spectroscopy (EIS). The LSV and EIS signals were recorded, which referred as the response before immunoreaction. After drying with N<sub>2</sub> flow, 5  $\mu$ L of CEA solution (experiment 3.4.1.2) was dropped onto the biosensor surface and then incubated for further 2 h at 37  $^{\circ}$ C. Next, the LSV and EIS signals were recorded again, which

considered as the immunosensor response. A change in signal before and after presenting CEA was corresponding directly to the CEA concentration. Figure 3.3 represents the label-free detection of CEA based on SPCE/GNP-MnO<sub>2</sub>/Fe<sub>3</sub>O<sub>4</sub>@Au/anti-CEA biosensor.

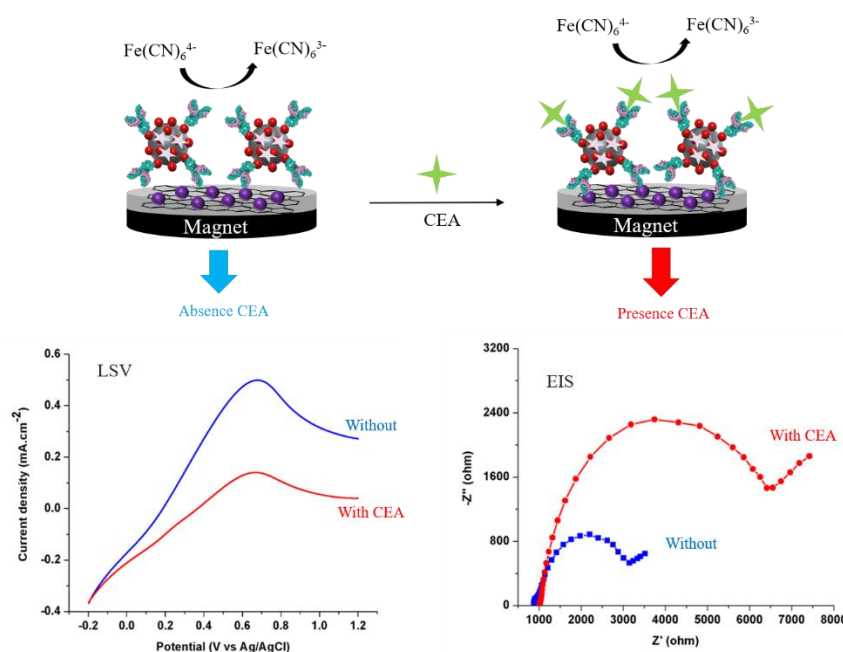


**Figure 3.3 Schematic demonstration of the electrochemical biosensor for label-free detection of CEA**

### 3.4.3 Characterization of the SPCE/GNP-MnO<sub>2</sub>/Fe<sub>3</sub>O<sub>4</sub>@Au/anti-CEA

#### 3.4.3.1 Characterization of the nanocomposites by XRD

The GNP, MnO<sub>2</sub>, GNP-MnO<sub>2</sub>, AuNPs, Fe<sub>3</sub>O<sub>4</sub> and Fe<sub>3</sub>O<sub>4</sub>@Au were characterized by X-ray diffraction spectroscopy (XRD) using a Cu target in a range of diffraction angle  $2\theta = 10^\circ$ - $80^\circ$ . The XRD patterns were compared with the XRD database (The international center of diffraction data, ICDD) and displayed in section 4.2.1.1.

#### 3.4.3.2 Characterization of the nanocomposites by FTIR

The GNP, MnO<sub>2</sub>, GNP-MnO<sub>2</sub> composite, Fe<sub>3</sub>O<sub>4</sub>, Fe<sub>3</sub>O<sub>4</sub>@Au, and Fe<sub>3</sub>O<sub>4</sub>@Au/anti-CEA were characterized by Fourier transforms infrared spectroscopy

(FTIR). The FTIR spectra were recorded in the transmission mode using the KBr pellet technique by mixing of 1 mg samples with 0.1 g KBr. The results are showed in 4.2.1.2.

#### 3.4.3.3 Characterization of the biosensor by SEM

The morphology of the unmodified SPCE and SPCE modified with GNP,  $\text{MnO}_2$ , GNP- $\text{MnO}_2$ ,  $\text{Fe}_3\text{O}_4@\text{Au}$ , and  $\text{Fe}_3\text{O}_4@\text{Au}/\text{anti-CEA}$  were measured by scanning electron microscopy (SEM). The samples were attached on aluminum stubs and then sputter coated with platinum. The accelerating voltage for all the images was 15 kV and the magnification was 50,000x. The SEM micrograph are showed in section 4.2.1.3.

### 3.4.4 Electrochemical characterization of the biosensor

The electrochemical measurements are performed using a computer-controlled electrochemical workstation and evaluated with the corresponding NOVA software. The SPCE consisted of three electrodes was hold in a home-made electrochemical cell assembled with a neodymium external magnet. 100  $\mu\text{L}$  of 0.1 M phosphate buffer solution (pH 7.4) containing 5 mM  $\text{Fe}(\text{CN})_6^{3-/4-}$  was injected through a sample injection hole before the measurement.

#### 3.4.4.1 CV and EIS measurements of the SPCE/GNP- $\text{MnO}_2/\text{Fe}_3\text{O}_4@\text{Au}$

The electrochemical performance of SPCE/GNP- $\text{MnO}_2/\text{Fe}_3\text{O}_4@\text{Au}$  was investigated by CV and EIS compared to SPCE modified with GNP,  $\text{MnO}_2$ , GNP- $\text{MnO}_2$ , and  $\text{Fe}_3\text{O}_4@\text{Au}$ . CV measurement was carried out by scanning the potential from -0.5 to +1.0 V at a scan rate of 0.1 V/s. EIS signal was recorded within a frequency range of 10,000-0.1 Hz and an amplitude of 0.01 V. The results are presented in section 4.2.2.1.

#### 3.4.4.2 CV of the SPCE/GNP- $\text{MnO}_2/\text{Fe}_3\text{O}_4@\text{Au}$ at different scan rate

The electron transfer process of the SPCE/GNP- $\text{MnO}_2/\text{Fe}_3\text{O}_4@\text{Au}$  was investigated by CV in the potential range from -0.5 to +1.0 V at different scan rates between 0.01 and 0.09 V/s. The result is showed in section 4.2.2.2.

#### 3.4.4.3 Characterization of the SPCE/GNP- $\text{MnO}_2/\text{Fe}_3\text{O}_4@\text{Au}/\text{anti-CEA}$

The electrochemical performance of the SPCE/GNP- $\text{MnO}_2/\text{Fe}_3\text{O}_4@\text{Au}$  for detection of 10 ng/mL CEA was investigated by EIS, in comparison to unmodified SPCE and SPCE modified with GNP- $\text{MnO}_2$  and  $\text{Fe}_3\text{O}_4@\text{Au}$ . The biosensor fabrication (experiment 3.4.2.5) and the electrochemical measurements

(experiment 3.4.2.6) were performed as already described. EIS signals were recorded within a frequency range of 10,000-0.1 Hz and an amplitude of 0.01 V. The results displayed in section 4.2.2.3.

#### 3.4.4.4 Investigation of the process for biosensor fabrication

Process for the SPCE/GNP-MnO<sub>2</sub>/Fe<sub>3</sub>O<sub>4</sub>@Au/anti-CEA biosensor fabrication was investigated by LSV and EIS. The biosensor fabrication (experiment 3.4.2.5) and the electrochemical measurements (experiment 3.4.2.6) were performed as already described. LSV signals were recorded in the potential ranged from -0.2 to 1.2 V at a scan rate of 50 mV/s and EIS signals were recorded within a frequency range of 10,000-0.1 Hz at an amplitude of 0.01 V. The results are displayed in section 4.2.2.4.

### 3.4.5 Optimization study of the SPCE/GNP-MnO<sub>2</sub>/Fe<sub>3</sub>O<sub>4</sub>@Au/anti-CEA

Parameters affecting the electrochemical performance for CEA analysis (10 ng/mL) based on the SPCE/GNP-MnO<sub>2</sub>/Fe<sub>3</sub>O<sub>4</sub>@Au/anti-CEA were evaluated by LSV and EIS with 0.1 M phosphate buffer solution containing 5 mM Fe(CN)<sub>6</sub><sup>3-/4-</sup> redox probe. The biosensor fabrication and the electrochemical measurements were conducted as described in section 3.4.2.5 and 3.4.2.6, respectively. LSV measurements were carried out by scanning the potential ranged from -0.2 to 1.2 V at a scan rate of 50 mV/s, while EIS experiments were performed within a frequency range of 10,000-0.1 Hz at an amplitude of 0.01 V.

#### 3.4.5.1 Study effect of amount of GNP and MnO<sub>2</sub>

Firstly, amount of GNP on the electrode surface were investigated by dispersing 0.10, 0.15, 0.20, 0.25, 0.30, 0.40, and 0.50 mg of the synthesized GNP-MnO<sub>2</sub> in 1 mL DI-water and then drop-casting onto the electrode surface, which were calculated as 2.50, 3.75, 5.00, 6.25, 7.50, 10.00, and 12.50 µg.cm<sup>-2</sup> of GNP on SPCE surface (Appendix C.4 and C.5). Next, the amount of MnO<sub>2</sub> decorated on the GNP sheet was optimized by mixing of 5 mg GNP with 0, 1, 2, 3, 4, 8, and 22 mg of MnSO<sub>4</sub>.4H<sub>2</sub>O, which were calculated as a weight ratio of GNP:Mn at 1:0.0, 1:0.05, 1:0.1, 1:0.15, 1:0.2, 1:0.4, and 1:1.1, respectively (Appendix C.6). The results are displayed in section 4.2.3.1.

#### 3.4.5.2 Study concentration of CEA antibody

The concentration of CEA antibody was evaluated at 50, 100, 150, 200, 250, and 300 µg/mL. The results were presented in section 4.2.3.2.

### 3.4.5.3 Study effect of pH solution and incubation temperature

Firstly, the effect of pH value on the performance of the biosensor for CEA detection was investigated at 5.0, 6.0, 6.5, 7.0, 7.4, 8.0, 8.5, and 9.0 using 0.1 M phosphate buffer solution. Next, temperature for the incubation of the CEA antigen and antibody on the SPCE surface was evaluated at 25.0, 30.0, 35.0, 37.0, 40.0, 45.0, and 50.0°C. The results are presented in section 4.2.3.3.

### 3.4.5.4 Study incubation time and reaction time on the detection of CEA

The incubation time of the anti-CEA on the electrode surface was studied at 30, 60, 80, 100, 120, 140, 160, 180, and 200 minutes. Then, the reaction time for formation of the antigen-antibody complex at the electrode interface was investigated every 15 minutes from 30-150 minutes. The results are showed in section 4.2.3.4.

## 3.4.6 Analytical performance of the SPCE/GNP-MnO<sub>2</sub>/Fe<sub>3</sub>O<sub>4</sub>@Au

Analytical performances of the SPCE/GNP-MnO<sub>2</sub>/Fe<sub>3</sub>O<sub>4</sub>@Au/anti-CEA for CEA analysis were evaluated under optimum conditions by LSV and EIS. LSV measurements were carried out by scanning the potential ranged from -0.2 to 1.2 V at a scan rate of 50 mV/s, while EIS experiments were performed within a frequency range of 10,000-0.1 Hz at an amplitude of 0.01 V. The experiments were performed in 0.1 M phosphate buffer solution (pH 7.4) containing 5 mM Fe(CN)<sub>6</sub><sup>3-/4-</sup>. The biosensor fabrication and the electrochemical measurements were conducted as described in section 3.4.2.5 and 3.4.2.6, respectively.

### 3.4.6.1 Investigation of linear range and LOD for CEA detection

Linearity of the SPCE/GNP-MnO<sub>2</sub>/Fe<sub>3</sub>O<sub>4</sub>@Au/anti-CEA for analysis of CEA with different concentrations at 0.001, 0.01, 0.1, 1.0, 10, and 100 ng/mL were studied. The obtained signals from LSV and EIS are plotted against log concentration of CEA. Next, the limit of detection (LOD) was determined based on the definition of the detection limit prescribed by the international union of pure and applied chemistry (IUPAC). The signals of blank, using phosphate buffer solution instead of CEA, are detected for 10 repetitions (n=10) by using LSV and EIS. After that, a mean and standard deviation (SD) were calculated. The results are presented in section 4.2.4.1.

### 3.4.6.2 Investigation of reproducibility and repeatability of the biosensor

Reproducibility of the biosensor was evaluated by using five different freshly-prepared electrodes ( $n=5$ ). Repeatability of the biosensor was investigated by measuring the LSV and EIS signal of 1 ng/mL CEA with five successive measurements ( $n=5$ ). The results are showed in section 4.2.4.2.

### 3.4.6.3 Study stability of the SPCE/GNP-MnO<sub>2</sub>/Fe<sub>3</sub>O<sub>4</sub>@Au/anti-CEA

Stability of the biosensor for storage in 1 week was investigated. The biosensors were kept at 4 °C in a refrigerator when not in use. Analysis was performed every day in triplicate using 1 ng/mL CEA. The results are showed in section 4.2.4.3.

### 3.4.6.4 Study selectivity of the SPCE/GNP-MnO<sub>2</sub>/Fe<sub>3</sub>O<sub>4</sub>@Au/anti-CEA

The possible interfering substances on the CEA detection were examined, including prostate-specific antigen (PSA), human immunoglobulin (IgG), human serum albumin (HSA), bovine serum albumin (BSA), cholesterol, glucose, sucrose, cysteine, ascorbic acid, and uric acid. 500 ng/mL of theses inferences were prepared and mixed with standard CEA solution (1 ng/mL). Then, LSV and EIS signals were recorded and the results are showed in section 4.2.4.4.

## 3.4.7 Determination of CEA in human serum samples

The content of CEA in human serum samples was checked by the proposed electrochemical biosensor using external calibration method. The purchased human serum samples were diluted for 10-fold and 100-fold times with 0.1 M phosphate buffer solution (experiment 3.4.1.4). In order to check accuracy of the methods, different amounts of CEA (0, 1, 10, and 50 ng/mL) were subsequently fortified into each sample dilution. Before the measurement, the diluted human serums and spiked samples were incubated at 37°C for 2 h in order to activate the biomarker. The LSV and EIS were detected in phosphate buffer solution (pH 7.4) containing 5 mM Fe(CN)<sub>6</sub><sup>3-/4-</sup> under optimum conditions. Concentration of CEA in the samples were calculated by substituting the signal values into the calibration curve obtained in the section 4.2.4.1. Moreover, amount of CEA in the samples were also determined by an electrochemiluminescence (ECL) immunoassay as a comparative method. The ECL results were obtained from the National Cancer Institute (Thailand). Finally, recovery percentage and relative error were calculated. The results from two methods are compared as presented in section 4.2.5.



### **3.5 Carbon composite nanomaterials-based biosensor: electrochemical enzymatic biosensor for glyphosate detection**

The electrochemical enzymatic biosensor for detection of glyphosate herbicide was fabricated based on immobilization of acid phosphatase enzyme (ACP) on a screen-printed carbon electrode (SPCE) modified with reduced graphene oxide (rGO) and silver nanoparticles (AgNPs). The enzymatic biosensor was applied for determination of glyphosate herbicide in environmental waters and soils using chronoamperometry based on enzyme inhibition method. The preparation of chemicals and samples, the procedure of biosensor construction, characterization of the biosensor and the measurement strategy were explained, respectively.

#### **3.5.1 Chemical and environmental sample preparations**

##### **3.5.1.1 Acetate buffer solution (0.1 M)**

4.1xxx g of sodium acetate was dissolved into 500 mL volumetric flask with DI water. Meanwhile, 2.9 mL of glacial acetic acid (99.7%) was added into the volumetric flask and adjust the volume to 500 mL with DI water. After that, acetate buffer solution was prepared by mixing of the above-prepared sodium acetate and acetic acid solution and then adjusted the pH to the desired pH value by 1 M NaOH or 1 M HCl.

##### **3.5.1.2 Acid phosphatase (25 mg/mL ACP)**

0.025x g of ACP enzyme was dissolved with 1 mL acetate buffer solution (pH 7.0) and then the solution was mixed using vortex mixer in order to obtain 25 mg/mL ACP solution. The enzyme solution was kept at 4 °C in refrigerator when not in use.

##### **3.5.1.3 Glutaraldehyde (5% GA)**

5% GA were prepared by pipette 0.2 mL of stock GA solution (25%) into a microcentrifuge tube and then adjust the volume to 1 mL with DI water.

##### **3.5.1.4 Disodium phenyl phosphate (20 g/L)**

Disodium phenyl phosphate at a concentration of 20 g/L was prepared by dissolution of 0.02xx g with 1 mL acetate buffer solution (pH 7.0).

##### **3.5.1.5 Glyphosate solution (1,000 mg/L)**

Stock solution of glyphosate was prepared by dissolution of 0.005x g glyphosate powder into 5 mL volumetric flask with DI water. After that, working

solutions of glyphosate were prepared by dilution of the glyphosate stock solution with acetate buffer solution (pH 7.0).

#### 3.5.1.6 Phenol solution (5 mg/L phenol)

Stock phenol solution (2,000 mg/L) was prepared by dissolution of 0.01xx g phenol pellets with DI water in a 5 mL volumetric flask. After that phenol solution at a concentration of 5 mg/L was prepared by pipette 25  $\mu$ L of stock phenol solution into a volumetric flask and adjust the volume with DI water to 10 mL.

#### 3.5.1.7 Potassium chloride solution (0.1 M KCl)

0.74xx g of KCl was dissolved with DI water into 100 mL volumetric flask to get 0.1 M KCl.

#### 3.5.1.8 Graphene oxide suspension (0.2 mg/mL GO)

Firstly, stock suspension of GO was prepared by dissolution of 0.001x g commercial GO powder with 1 mL DI water by ultrasonication for 2 h to form a brown GO colloidal dispersion with a concentration of 1 mg/mL. Then, a suspension of 0.2 mg/mL GO was prepared by pipette 0.2 mL of the 1 mg/mL rGO suspension into microcentrifuge tube and adjust the volume to 1 mL with DI water.

#### 3.5.1.9 Silver nitrate solution (4 mM AgNO<sub>3</sub>)

0.1 M of KNO<sub>3</sub> solution was firstly prepared by dissolution of 1.011x g of KNO<sub>3</sub> powder with DI water into 100 mL volumetric flask. Then, 0.033x g sodium acetate and 0.068x g AgNO<sub>3</sub> are dissolved with 0.1 M KNO<sub>3</sub> solution in 100 mL volumetric flask in order to get 4 mM AgNO<sub>3</sub> solution containing 4 mM sodium acetate as a stabilizer.

#### 3.5.1.10 Environmental waters preparation

50 mL of water samples collected from Khon Kaen province are sonicated for 15 min. The samples were filtered with 0.45  $\mu$ m nylon membrane filter. Then, 1.0 mM Ba(OH)<sub>2</sub> was added into the collected solutions. After that, the sample solutions are sonicated and centrifuged at 10,000 rpm for 10 min to eliminate sulfate radical and most metal ions. The pH of the collected supernatants was then adjusted to pH 7.0 by 1 M HCl and the neutral solutions were centrifuged at 10,000 rpm for another 10 min. Finally, 10 mL of the extracted samples were freeze-dried and kept at -20°C for further use. Before analysis, 1 mL DI-water was injected into the dried samples in order to pre-concentration for 10-times.

### 3.5.1.11 Soil samples preparation

60 mL of 1 M NaOH as the extracting solution was added to 25 g of the soil samples collected from Khon Kaen province. The sample suspensions were stirred for 30 min under magnetic stirring and then the mixtures were centrifuged for 10 min at 5000 rpm. The supernatants were separated and then filtered with 0.45  $\mu$ m nylon membrane filter. The pH of the collected solutions was then adjusted to pH 7.0 by 1 M HCl and the neutral solutions were centrifuged at 5,000 rpm for another 10 min. The resultants were diluted to 100 mL using DI-water. Finally, 10 mL of the extracted samples were freeze-dried and kept at -20°C for further use. Before analysis, 1 mL DI-water was injected into the dried samples in order to pre-concentration for 10-times.

### 3.5.1.12 Derivatization procedure for UHPLC analysis

Firstly,  $\text{H}_3\text{BO}_3$ - $\text{Na}_2\text{B}_4\text{O}_7$  buffer solution was prepared by mixing 0.2 M  $\text{H}_3\text{BO}_3$  solution with 0.05 M  $\text{Na}_2\text{B}_4\text{O}_7$  solution and then the pH value was adjusted to pH 9.5 by 1 M NaOH. The stock glyphosate standard solution was prepared in  $\text{H}_3\text{BO}_3$ - $\text{Na}_2\text{B}_4\text{O}_7$  buffer and working standards are prepared by diluting the stock solutions with DI-water. Then, 300  $\mu$ L of  $\text{H}_3\text{BO}_3$ - $\text{Na}_2\text{B}_4\text{O}_7$  buffer, working standards solution of glyphosate, 100  $\mu$ L of 2.5 mM 4-chloro-3,5-dinitrobenzotrifluoride (CNBF) prepared in methanol solution, and 100  $\mu$ L of water solutions or soil samples are added into 1 mL HPLC vial. After that, the whole solution was adjusted to 1.0 mL with DI-water and then incubated at 60 °C in a water bath. After 30 min, 10  $\mu$ L of 2 M HCl were added to quench the reaction. Finally, the resulting solutions were filtered through 0.45  $\mu$ m nylon filters.

## 3.5.2 Electrochemical enzymatic biosensor preparation and detection

### 3.5.2.1 Enzymatic biosensor preparation (SPCE/rGO-AgNPs/ACP)

Firstly, the SPCE consisting of three electrodes on the same substrate, including working electrode (WE), reference electrode (RE) and counter electrode (CE), and its holder cell were prepared following the description in 3.4.2.1. Then, 10  $\mu$ L of 0.2 mg/mL GO dispersion was uniformly spread onto the SPCE. After 30 minutes of drying, GO film was electrochemically reduced to form rGO film on the SPCE by scanning the potential from 0.0 to -1.2 V with cyclic voltammetry (CV) at a scan rate of 50 mV/s for 10 cycles in 100  $\mu$ L of 0.1 M KCl solution. After that, AgNPs were deposited onto the surface of SPCE/rGO by scanning the potential from 0.0 to -

0.5 V at scan rate of 50 mV/s for 10 cycles in 0.1 M  $\text{KNO}_3$  solution containing 4 mM  $\text{AgNO}_3$ . After deposition, the SPCE/rGO-AgNPs were washed with DI water and dried by a  $\text{N}_2$  flow at room temperature. Then, 5  $\mu\text{L}$  of 25 mg/mL ACP was casted onto the modified electrode by cross-linking with 5% glutaraldehyde (5  $\mu\text{L}$ ) in order to obtain the enzymatic biosensor. After drying, the enzymatic biosensor was ready for electrochemical measurements. The process for the preparation of enzymatic biosensor is illustrated in Figure 3.4.

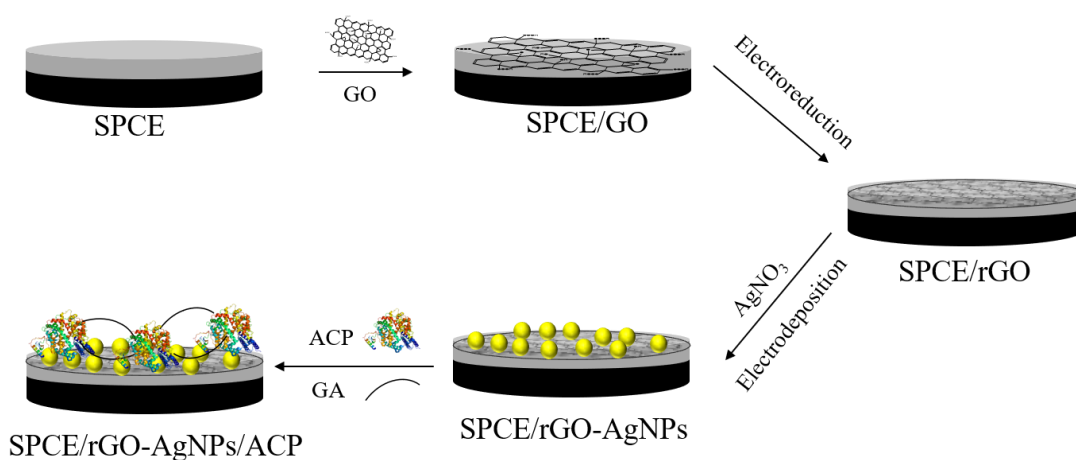


**Figure 3.4 Schematic of the electrochemical enzymatic biosensor preparation**

### 3.5.2.2 Glyphosate detection by the enzymatic biosensor

Indirect detection of glyphosate herbicide was conducted based on inhibition of ACP activity using the SPCE/rGO-AgNPs/ACP. The measurements were performed by injection of 100  $\mu\text{L}$  of a fixed saturated amount of disodium phenyl phosphate (20 g/L) prepared in acetate buffer solution (0.1 M, pH 7.0) on the biosensor surface. Chronomperometry was started by apply the potential of +0.4V and a steady-state current was recorded as  $I_0$ . After the signal had reached the constant current value, standard glyphosate solution (2  $\mu\text{L}$ ) was added to three times per each solution and the currents were then recorded as  $I_1$ . In the absence of glyphosate, ACP enzyme converts the substrate disodium phenyl phosphate into phosphoric acid and phenol products. Then, the obtained phenol compounds subsequently oxidize to benzoquinones, resulting in amperometric signal could be measured. Meanwhile, in the presence of glyphosate inhibitor, the ACP acitivities were inhibited, leading to less product formation and

decrease in the detected signal. Thus, the inhibited response was determined using the peak heights before and after introduction of glyphosate ( $\Delta I = I_0 - I_1$ ), that was proportional to glyphosate concentration. Figure 3.5 represents the process for indirect detection of glyphosate based on enzyme inhibition by the enzymatic biosensor.

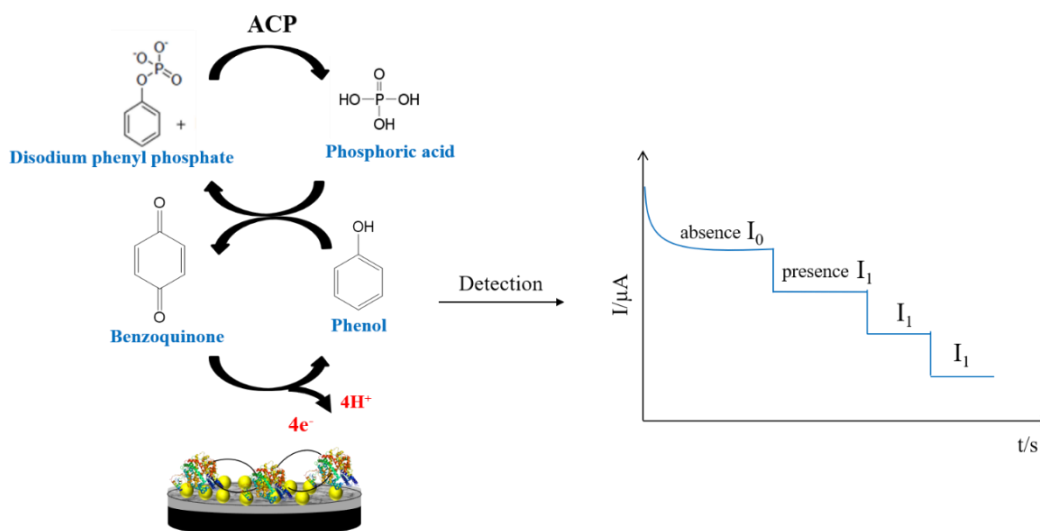


**Figure 3.5 Schematic demonstration of the electrochemical biosensor for indirect detection of glyphosate based on enzyme inhibition**

### 3.5.3 Characterization of the SPCE/rGO-AgNPs/ACP

#### 3.5.3.1 Characterization of the modified electrodes by XRD

The bare SPCE and SPCE modified with rGO, AgNPs, and rGO-AgNPs are characterized by X-ray diffraction spectroscopy (XRD) using a Cu target in a range of diffraction angle  $2\theta = 10^\circ$ - $80^\circ$ . The XRD patterns were compared with the XRD database (The international center of diffraction data, ICDD) and displayed in section 4.3.1.1.

#### 3.5.3.2 Characterization of the modified electrodes by Raman

The unmodified SPCE and SPCE modified with GO, rGO, and rGO-AgNPs were characterized by Raman spectroscopy. The Raman spectra were recorded in the range from  $200$ - $2000\text{ cm}^{-1}$  on the Raman spectrophotometer equipped with a microscope ( $100\times$  objective lens) and laser source at  $532\text{ nm}$ . The laser power at  $50\text{ mW}$  with a laser spot size of  $0.9\text{ }\mu\text{m}$  was focused on the substrate through a  $600\text{ g/mm}$

grating. The exposure time and accumulation number used for each spectrum were 5 seconds and 3 cycles, respectively. The results are showed in 4.3.1.2.

### 3.5.3.3 Characterization of the SPCE/rGO-AgNPs by EDS

The elemental distribution of the SPCE/rGO-AgNPs was characterized by an energy dispersive X-ray spectrometer (EDS) in a mode of spectrum and mapping analysis. The accelerating voltage and current were 15 kV and 10  $\mu$ A, respectively. The EDS spectrum and maps are showed in section 4.3.1.3.

### 3.5.3.4 Characterization of the SPCE/rGO-AgNPs/ACP by SEM

The morphologies of the SPCE, SPCE/rGO, SPCE/rGO-AgNPs, and SPCE/rGO-AgNPs/ACP were measured by scanning electron microscopy (SEM). The samples were attached on aluminum stubs and then sputter coated with platinum. The accelerating voltage for all the images was 5 kV and the magnification was 100,000x. The SEM micrograph are showed in section 4.3.1.4.

## 3.5.4 Electrochemical characterization of the enzymatic biosensor

The electrochemical measurements were performed using a computer-controlled electrochemical workstation and evaluated with the corresponding NOVA software. The SPCE consisted of three electrodes was hold in a home-made electrochemical cell as described in section 3.4.2.1. The analyte solution (100  $\mu$ L) was injected through a sample injection hole before the measurement.

### 3.5.4.1 CV and EIS measurements of the SPCE/rGO-AgNPs

The electrochemical performance of the SPCE/rGO-AgNPs was investigated by CV and EIS in 1 mM  $\text{Fe}(\text{CN})_6^{3-/4-}$  compared to SPCE, SPCE/AgNPs, and SPCE/rGO. CV measurement was carried out by scanning the potential from -0.5 to +1.0 V at a scan rate of 0.1 V/s. EIS signal was recorded within a frequency range of 10,000-0.1 Hz and an amplitude of 0.01 V. The results are presented in section 4.3.2.1.

### 3.5.4.2 CV measurements of the SPCE/rGO-AgNPs in phenol solution

The electrochemical performance of the SPCE/rGO-AgNPs for detection of phenol, which was the product from enzymatic reaction, was investigated by using CV method, in comparison to the bare SPCE, SPCE/rGO, and SPCE/AgNPs. The CV experiments were performed by scanning the potential from 0.0 to +0.9 V at a scan rate of 0.1 V/s in 5 mg/L phenol solution. The results are displayed in section 4.3.2.2.

#### 3.5.4.3 CV of the SPCE/rGO-AgNPs measure at different scan rate

The electron transfer process of the SPCE/rGO-AgNPs was investigated by CV in 1 mM  $\text{Fe}(\text{CN})_6^{3-/4-}$  solution scanning in the potential range from -0.2 to +0.7 V at different scan rates between 0.01 and 0.10 V/s. Moreover, the CV measurement was also performed in buffer solution containing 5 mg/L phenol solution in the range from 0.3 to 0.9 V at different scan rates between 0.002 to 0.020 V/s. The result is showed in section 4.3.2.3.

#### 3.5.4.4 CV measurements of the SPCE/rGO-AgNPs/ACP biosensor

The SPCE/rGO-AgNPs/ACP is evaluated in 50 mg/L phenol solution, 10 g/L disodium phenyl phosphate, and 10 g/L disodium phenyl phosphate containing 50 mg/L glyphosate by CV. The CV measurements are performed by scanning the potential from 0.0 to +1.0 V at a scan rate of 0.1 V/s. The results are illustrated in section 4.3.2.4.

### 3.5.5 Optimization study of the SPCE/rGO-AgNPs/ACP biosensor

Parameters affecting the electrochemical performance for indirect detection of glyphosate using the SPCE/rGO-AgNPs/ACP are evaluated by chronoamperometry. The detection was based on ACP enzyme inhibition assay using disodium phenyl phosphate as an enzyme substrate and glyphosate (0.2 mg/L) as an inhibitor. The biosensor was constructed and the electrochemical experiment was performed as described in section 3.5.2.1 and 3.5.2.2, respectively.

#### 3.5.5.1 Study effect of potential apply

The operating potentials were studied in the range of 0.0 to 0.7 V. Disodium phenyl phosphate (10 g/L) was injected on the biosensor surface. Then, a constant potential was applied by chronoamperometry and the inhibited signals owing to 0.2 mg/L glyphosate were detected. The results are presented in section 4.3.3.1.

#### 3.5.5.2 Study effect of amount of rGO and AgNPs

Firstly, amount of rGO on the electrode surface were investigated by dispersing 0.00, 0.10, 0.15, 0.20, 0.25, 0.30, 0.40, and 0.50 mg of the commercial GO powder in 1 mL DI-water and then drop-casting onto the electrode surface. After that, GO was electrochemically reduced to form rGO film on the SPCE, which were calculated as 0.00, 2.50, 3.75, 5.00, 6.25, 7.50, 10.00, and 12.50  $\mu\text{g}\cdot\text{cm}^{-2}$  (Appendix C.7). Next, the amount of AgNPs decorated on the rGO film was optimized by

electrochemically reduction of 0, 1, 2, 3, 4, and 5 mM AgNO<sub>3</sub> solution, which were calculated as 0.0, 0.2, 0.5, 0.8, 1.1, and 1.4 mg.cm<sup>-2</sup>, respectively (Appendix C.8). The results are discussed in section 4.3.3.2.

#### 3.5.5.3 Study concentration of ACP enzyme and its substrate

The concentration of ACP enzyme was studied at 0, 5, 10, 15, 20, 25, and 30 mg/mL, which were calculated as 0.00, 0.03, 0.06, 0.09, 0.12, 0.15, and 0.18 unit.cm<sup>-2</sup>, respectively (Appendix C.9). Then, the concentration of enzyme substrate, which is disodium phenyl phosphate, was evaluated at 0.5, 1, 5, 10, 20, 30, 40, and 50 g/L. The results are presented in section 4.3.3.3.

#### 3.5.5.4 Study effect of pH solution on the detection of glyphosate

The effect of pH value on the performance of the biosensor for indirect detection of glyphosate (0.2 mg/L) was investigated at 3.0, 4.0, 5.0, 6.0, 7.0, 7.5, and 8.0 using 0.1 M acetate buffer solution. The results are presented in section 4.3.3.4.

### 3.5.6 Investigation of enzyme kinetics

Firstly, enzyme-substrate kinetic of the SPCE/rGO-AgNPs/ACP biosensor was evaluated by study the catalytic reaction of ACP to disodium phenyl phosphate substrate under the optimal conditions. The biosensor was fabricated as described in section 3.5.2.1. Then, 100 µL of acetate buffer solution (pH 7.0) was injected on the biosensor surface through the sample injection hole. The constant potential at 0.4 V was applied by chronoamperometry. After the background current reached stable, disodium phenyl phosphate solutions with various concentrations at 50, 100, 150, 200, 250, 300, 350, 400, 450, and 500 mg/L were injected on the biosensor surface and the oxidation current responses are recorded continuously. Next, the inhibitory effect of glyphosate on the ACP activity was determined by dropping of 1 mg/L glyphosate solution on the SPCE/rGO-AgNPs/ACP. Then, the measurements were performed as the same conditions with enzyme-substrate kinetic study. Finally, the responses obtained from the study of enzyme-substrate kinetic and inhibition kinetic are plotted against the concentrations of disodium phenyl phosphate in a range from 50 to 500 mg/L by using Lineweaver-Burk plot. The results are presented in section 4.3.4.



### 3.5.7 Study interaction of enzyme-substrate and enzyme-glyphosate complexes

The interactions of disodium phenyl phosphate substrate and glyphosate on ACP enzyme were studied by molecular docking. The two compounds were docked into the active site of the ACP enzyme from red kidney bean (PDB code 4KBP) by *AutoDock Vina*. The X-ray structure data files of the ACP docked ligands were downloaded from PubChem (<https://pubchem.ncbi.nlm.nih.gov>) and further formatted in structural coordinates by eLBOW. The results are presented in section 4.3.5.

### 3.5.8 Analytical performance investigation of the SPCE/rGO-AgNPs/ACP

Analytical performances of the SPCE/rGO-AgNPs/ACP for indirect detection of glyphosate were evaluated under optimum conditions by chronoamperometry at a potential of 0.4 V. The measurements were carried out based on inhibition assay of ACP enzyme using 20 g/L disodium phenyl phosphate prepared in 0.1 M acetate buffer solution (pH 7.0) as the enzyme substrate. The biosensor was constructed and the electrochemical experiment was performed as described in section 3.5.2.1 and 3.5.2.2, respectively.

#### 3.5.8.1 Evaluation of linear range, LOD and LOQ for glyphosate detection

Linearity of the biosensor for determination of glyphosate herbicide was investigated in a range from 0.05 to 22.0 mg/L. Next, limit of detection (LOD) and limit of quantification (LOQ) were determined by successive detection of 0.05 mg/L glyphosate, the lowest concentration of calibration curve, for ten times ( $n=10$ ). Then, the LOD and LOQ were calculated on a basis of  $3SD/\text{slope}$  and  $10SD/\text{slope}$ , respectively, where SD was standard deviation of glyphosate signal at 0.05 mg/L and slope was obtained from the calibration curve. The results are presented in section 4.3.6.1.

#### 3.5.8.2 Investigation of reproducibility of the SPCE/rGO-AgNPs/ACP

Reproducibility of the biosensor was evaluated by using five different freshly-prepared electrodes ( $n=5$ ). The intra-day reproducibility was investigated by measuring the signals of 0.2 mg/L glyphosate in a single day. Meanwhile, the inter-day reproducibility of 0.2 mg/mL glyphosate was evaluated in the different days. The results are showed in section 4.3.6.2.

### 3.5.8.3 Study stability of the SPCE/rGO-AgNPs/ACP

Stability of the biosensor for storage in 1 week was investigated. The biosensors were kept at 4 °C in a refrigerator when not in use. Analysis was performed every day in triplicate using 0.2 mg/L glyphosate. The results are showed in section 4.3.6.3.

### 3.5.8.4 Study selectivity of the SPCE/rGO-AgNPs/ACP

Selectivity of glyphosate detection using the SPCE/rGO-AgNPs/ACP was estimated by study interferent effects of common pesticides used in agricultural activity, including polyethoxylated tallow amine (POEA), glycine, chlorpyrifos, paraquat, carbaryl, and carbendazim at a concentration of 0.2 mg/L. In addition, some possible ions in environmental samples, such as  $\text{Mg}^{2+}$  (0.2 mg/L),  $\text{Zn}^{2+}$  (0.2 mg/L),  $\text{PO}_4^{2-}$  (2 mg/L),  $\text{SO}_4^{2-}$  (2 mg/L),  $\text{CO}_3^{2-}$  (20 mg/L),  $\text{NO}_3^-$  (20 mg/L),  $\text{Cl}^-$  (20 mg/L),  $\text{K}^+$  (20 mg/L),  $\text{Na}^+$  (20 mg/L),  $\text{Ca}^{2+}$  (20 mg/L),  $\text{Cu}^{2+}$  (20 mg/L), and  $\text{Cd}^{2+}$  (20 mg/L) are also evaluated. These interferences were mixed with glyphosate solution (0.2 mg/L) and their current signal are recorded, in comparison to the signal of pure glyphosate solution (0.2 mg/L). The results are displayed in section 4.3.6.4.

## 3.5.9 Determination of glyphosate in real samples

Three water samples and three soil samples collected from Khon Kaen province were extracted as described in experiment 3.5.1.10 and 3.5.1.11, respectively. In order to check accuracy of the developed methods, standard glyphosate solutions (0.5 and 1.0 mg/L for water, 2 and 4 mg/kg for soil) were spiked into the samples. The concentration of glyphosate in samples and spiked samples were determined by the electrochemical biosensor and ultra-high performance liquid chromatography (UHPLC) as a standard method.

### 3.5.9.1 Determination of glyphosate by the enzymatic biosensor

100  $\mu\text{L}$  of 20 g/L disodium phenyl phosphate prepared in acetate buffer solution (0.1 M, pH 7.0) was injected on the biosensor surface. Chronomperometry was started by apply the potential of +0.4V and a steady-state current was recorded as  $I_0$ . After the signal had reached the constant value, 2  $\mu\text{L}$  of the samples or spiked samples solution was added and the current signals were then recorded as  $I_1$ . Subsequently, 0.1 mg/L standard glyphosate solution was injected to three times per measurement in order to perform standard addition analysis. The

standard addition curve was plotted between the inhibited signals ( $\Delta I = I_0 - I_1$ ) and concentration of glyphosate (0.0, 0.1, 0.2, and 0.3 mg/L). The concentration of glyphosate in real samples and recovery percentage were then calculated. The results are showed in section 4.3.7.1.

#### 3.5.9.2 Determination of glyphosate by UHPLC

Ultra-high performance liquid chromatography (UHPLC) was performed with external calibration method. The HPLC separation of derivative glyphosate (experiment 3.5.1.12) was performed on C18 column (2.1×50 mm, 1.8  $\mu$ m) under a flow rate of 0.2 mL/min, a detection wavelength at 360 nm, an injection volume of 15  $\mu$ L, and column temperature of 40°C. The mixture of acetonitrile and 0.2% formic acid prepared in DI-water was used as mobile phase. The elution programs were set for a linear gradient starting from 5% of acetonitrile to reach 100% of the solvent at 10 min. Calibration curve was conducted in which the peak area was plotted against glyphosate concentration from 0.1-10 mg/L. Then, amount of glyphosate in real samples and spiked samples were detected in triplicate. Finally, concentration of glyphosate in the samples and recovery percentage were calculated and a paired t-test analysis at a confidence interval of 95% probability was used to compare the results from two methods. The results are showed in section 4.3.7.2.

### 3.6 Carbon composite nanomaterials-based sensor: SERS for glyphosate detection

The substrate for surface enhanced Raman spectroscopy (SERS substrate) was designed based on titanium dioxide nanotube arrays (TiO<sub>2</sub> NTs) modified with silver nanoparticles (AgNPs) and reduced graphene oxide (rGO). The SERS substrate was applied for detection of glyphosate herbicide contaminated in environmental waters and soils compared to high performance liquid chromatography (HPLC) as a standard method. The preparation of all chemicals and real samples, the process for construction of the substrate, method for characterization, and the measurement procedures are subsequently explained.

### 3.6.1 Preparation of chemical reagents

3.6.1.1 Electrolyte for anodization (0.5 wt%  $\text{NH}_4\text{F}$  and 3 vol% water in ethylene glycol)

0.5xxx g of ammonium fluoride ( $\text{NH}_4\text{F}$ ) was dissolved with 3 mL DI-water. Then, the final volume was adjusted with ethylene glycol (EG) solution in a 100 mL-volumetric flask.

3.6.1.2 Graphene oxide suspension (0.1 mg/mL GO suspension)

Firstly, 0.1 M phosphate buffer solution (pH 9.32) was prepared by dissolution of 13.4xxx g of disodium hydrogen phosphate ( $\text{Na}_2\text{HPO}_4$ ) and 6.9xxx g of monosodium dihydrogen phosphate ( $\text{NaH}_2\text{PO}_4$ ) into a 500 mL-volumetric flask with DI water. Then, pH value was adjusted to 9.32 by addition of a small amount of 1 M NaOH. Secondly, 5 mg of the commercial GO was exfoliated in 5 mL phosphate buffer solution by an ultrasonicator for about 2 h to form a brown GO colloidal dispersion with a concentration of 1.0 mg/mL. Finally, 0.5 mL of the stock GO suspension was transferred to a 5-mL volumetric flask and the final volume was adjusted by phosphate buffer solution.

3.6.1.3 Methylene blue solution (1 mM and 1 nM MB solution)

First of all, 1 mM MB was prepared by dissolution of 1.6 mg MB in a 5 mL-volumetric flask with DI-water. Then, MB at the concentration of 1 nM was prepared by dilution of 1 mM MB with DI-water.

### 3.6.2 $\text{TiO}_2$ NTs/AgNPs-rGO fabrication

3.6.2.1 Anodization of  $\text{TiO}_2$  NTs

Ti foils were cut in coupons ( $0.5 \times 1.0$  cm) and initially cleaned in acetone and DI-water for 15 min through ultrasonication, respectively. The anodization was carried out using a conventional two-electrode configuration where a treated Ti foil and platinum foil were used as the anode and cathode, respectively. The experiment was performed in ethylene glycol solution with 0.5 wt%  $\text{NH}_4\text{F}$  and 3 vol% DI-water (experiment 3.6.1.1) at room temperature for 30 min with a voltage of 30 V using a DC power supply. Then, the array of  $\text{TiO}_2$  NTs was conducted at  $450^\circ\text{C}$  for 2 h to convert the amorphous oxide into the anatase phase and to improve its mechanical stability.

### 3.6.2.2 Preparation of TiO<sub>2</sub> NTs/AgNPs

The fabrication of TiO<sub>2</sub> NTs decorated with AgNPs was conducted through a direct current sputtering technique at a magnetron current of 35 mA and base pressure of  $4 \times 10^{-2}$  mbar by controlling of the AgNPs thickness as 11 nm.

### 3.6.2.3 Preparation of TiO<sub>2</sub> NTs/AgNPs-rGO

The TiO<sub>2</sub> NTs/AgNPs was covered with rGO by using electrochemical method, which was prepared through a three-electrode system on electrochemical workstation where the TiO<sub>2</sub> NTs/AgNPs (experimental 3.6.2.2) as the working electrode, a Pt foil as the counter electrode and an Ag/AgCl electrode as the reference electrode, respectively. The electrodeposition of rGO was conducted by cyclic voltammetry with the potential scan from -1.5 to 1.0 V at scan rate of 50 mV/s for 40 cycles under magnetic stirring in 0.1 M phosphate buffer solution (pH 9.32) containing 0.1 mg/mL GO suspension (experimental 3.6.1.2). Finally, the TiO<sub>2</sub> NTs/AgNPs-rGO substrate was rinsed thoroughly with ethylene glycol and deionized water several times to remove remaining non-reduced graphene oxide and residual ions, and then dried at room temperature. The processes for fabrication of the TiO<sub>2</sub> NTs/AgNPs-rGO substrate is showed in Figure 3.6.

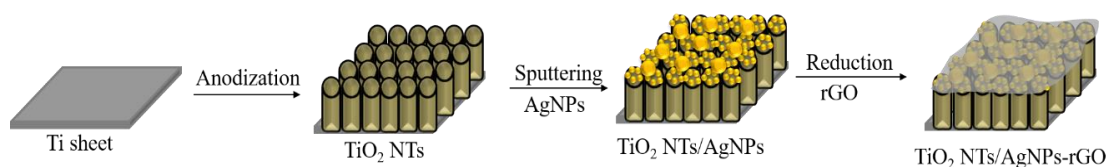


**Figure 3.6 Schematic process for fabrication of TiO<sub>2</sub> NTs/AgNPs-rGO substrate**

## 3.6.3 Characterization of the TiO<sub>2</sub> NTs/AgNPs-rGO substrate

### 3.6.3.1 Characterization by UV-visible spectrophotometry

The Ti sheet, TiO<sub>2</sub> NTs, TiO<sub>2</sub> NTs/AgNPs, and TiO<sub>2</sub> NTs/AgNPs-rGO were characterized by UV-visible spectrophotometry recorded in the wavelength range from 200-800 nm using reflectance detected mode (%R). The air and lab-sphere certified reflectance standard were measured and calibrated as blank. Finally, the %R was converted to absorbance value (A). The UV-vis spectra are showed in section 4.4.1.1.

### 3.6.3.2 Characterization of the substrate by EIS

The mechanism of charge transfer resistance of the various substrates, including Ti, TiO<sub>2</sub> NTs, TiO<sub>2</sub> NTs/AgNPs, TiO<sub>2</sub> NTs/rGO, and TiO<sub>2</sub> NTs/AgNPs-rGO were checked by electrochemical impedance spectroscopy (EIS) which were recorded in 0.1 M KCl containing the mixed solution of 5 mM K<sub>3</sub>[Fe(CN)<sub>6</sub>] and 5 mM K<sub>4</sub>[Fe(CN)<sub>6</sub>] within a frequency range of 10,000-0.1 Hz and an amplitude of 0.01 V. The results are presented in section 4.4.1.2.

### 3.6.3.3 Characterization of the substrate by XRD

The Ti, TiO<sub>2</sub> NTs, TiO<sub>2</sub> NTs/AgNPs, TiO<sub>2</sub> NTs/rGO, and TiO<sub>2</sub> NTs/AgNPs-rGO were characterized by X-ray diffraction spectroscopy (XRD) equipped with Cu K $\alpha$  radiation in a range of diffraction angle  $2\theta = 10^\circ$ - $80^\circ$ . The XRD patterns were compared with the XRD database (The International Centre of Diffraction Data, ICDD). The results are displayed in section 4.4.1.3.

### 3.6.3.4 Characterization of the substrate by Raman spectroscopy

Raman spectra of the different substrates, including Ti, TiO<sub>2</sub> NTs, TiO<sub>2</sub> NTs/GO, TiO<sub>2</sub> NTs/rGO, and TiO<sub>2</sub> NTs/AgNPs-rGO, were recorded in the range from 200 to 3600 cm<sup>-1</sup> by a Raman spectrophotometer at an excitation wavelength of 532 nm. The results are illustrated in section 4.4.1.4.

### 3.6.3.5 Characterization of the TiO<sub>2</sub> NTs/AgNPs-rGO by XPS

The chemical states information of titanium, oxygen, silver, and carbon in the TiO<sub>2</sub> NTs/AgNPs-rGO were analyzed by X-ray photoelectron spectroscopy (XPS) with monochromatic Al-K $\alpha$  X-ray source. The collected spectral data were calibrated by the C 1s peak at binding energy of 285.0 eV. The results are showed in section 4.4.1.5.

### 3.6.3.6 Characterization of the TiO<sub>2</sub> NTs/AgNPs-rGO by EDS

The elemental composition of the TiO<sub>2</sub> NTs/AgNPs-rGO was detected by an energy dispersive x-ray spectrometer (EDS) equipped in SEM instrument. The accelerating voltage and current are 15 kV and 10  $\mu$ A, respectively. The EDS spectrum is showed in section 4.4.1.6.

## 3.6.4 Optimization study of Raman parameters

The conditions influence on the SERS measurements such as laser excitation wavelengths, objective lens, acquisition times and number of accumulations were

investigated. 5  $\mu\text{L}$  of 1 nM MB solution (experiment 3.6.1.3) was dropped directly on the prepared  $\text{TiO}_2$  NTs/AgNPs-rGO (experiment 3.6.2.3) and then the substrate was dried for 15 minutes at room temperature. Raman measurements were performed on Raman spectrophotometer equipped with a microscope. The laser source at different wavelengths were focused on the substrate through a 600 g/mm grating. For each sample, twenty Raman spectra recorded in the range from 200-2000  $\text{cm}^{-1}$  were collected from the different spots of the substrate. The  $\text{TiO}_2$  NTs/AgNPs-rGO substrate, Raman analysis system and Raman instrumentation are displayed in Figure A.5 (Appendix A.3).

#### 3.6.4.1 Study effect of laser excitation wavelength and objective lens

Raman intensity of the  $\text{TiO}_2$  NTs/AgNPs-rGO are recorded on Raman spectrophotometer equipped with a microscope (10 $\times$ , 50 $\times$ , and 100 $\times$  objective lens). The laser source at 325 nm, 532 nm, 633 nm, and 785 nm are focused on the substrate. The exposure time and accumulation number used for each spectrum is 5 second and 3 cycles, respectively. The results are showed in section 4.4.2.1.

#### 3.6.4.2 Study effect of acquisition times and number of accumulations

Raman spectra of the  $\text{TiO}_2$  NTs/AgNPs-rGO for detection of 1 nM MB was recorded by Raman spectrophotometer equipped with a 50 $\times$  microscope objective lens. The laser source at 532 nm with a laser power of 50 mW and a laser spot size of 0.9  $\mu\text{m}$  was focused on the substrate. The exposure time of 1, 3, 5, 7, 10, and 15 second was investigated and the accumulation number used for each spectrum were also evaluated at 1, 3, 5, 7, and 10. The results are presented in section 4.4.2.2

### 3.6.5 Optimization study of SERS structure

5  $\mu\text{L}$  of 1 nM MB solution was casted on the surface of  $\text{TiO}_2$  NTs/AgNPs-rGO (experiment 3.6.2.3). After 15 minutes of drying, Raman intensities were detected on Raman spectrophotometer equipped with a 50 $\times$  objective lens at 532 nm laser excitation with a laser power of 50 mW and a laser spot size of 0.9  $\mu\text{m}$ . Raman spectrum was recorded in the range from 200-2000  $\text{cm}^{-1}$  through a 600 g/mm grating for 10 second and 5 accumulation. Twenty Raman spectra were collected and analyzed for each condition.

#### 3.6.5.1 Study effect of anodization potential for $\text{TiO}_2$ NTs construction

The  $\text{TiO}_2$  NTs were prepared by electrochemical anodization at a voltage of 0V, 10V, 20V, 30V, 40V and 50V. After that, AgNPs with the thickness of

5 nm were deposited on the surface of TiO<sub>2</sub> NTs using a magnetron sputtering. Raman spectra of 1 nM MB on the TiO<sub>2</sub> NTs/AgNPs were detected as shown in section 4.4.3.1. Furthermore, the top surface and cross-sectional microstructure of the TiO<sub>2</sub> NTs prepared with different anodic potential were also investigated by SEM.

#### 3.6.5.2 Study effect of anodization time for TiO<sub>2</sub> NTs fabrication

The TiO<sub>2</sub> NTs were fabricated by electrochemical anodization with a voltage of 30V for 10, 20, 30, 60, 90, 120, 150, and 180 minutes. Then, 5 nm thickness of AgNPs were deposited on the surface of TiO<sub>2</sub> NTs using a magnetron sputtering. Raman measurements were carried out by detection of 1 nM MB on the TiO<sub>2</sub> NTs/AgNPs. The top-surface and cross-sectional microstructure of the TiO<sub>2</sub> NTs prepared with different anodic time were also evaluated by SEM. The results are displayed in section 4.4.3.2.

#### 3.6.5.3 Study effect of AgNPs thickness loaded on the TiO<sub>2</sub> NTs

Firstly, the TiO<sub>2</sub> NTs were prepared by anodization at a voltage of 30V for 30 min. After that, AgNPs with different thickness of 3, 5, 7, 9, 11, 13, 15, and 17 nm were deposited on the surface of TiO<sub>2</sub> NTs using a magnetron sputtering. Then, Raman spectra of 1 nM MB on the TiO<sub>2</sub> NTs/AgNPs were recorded. The top view morphology of the TiO<sub>2</sub> NTs/AgNPs were measured by SEM. Moreover, the real thickness of AgNP was investigated by atomic force microscopy (AFM). The sample was prepared by attaching a tape on the portion of a cleaned Si wafer and then removed it after Ag deposition. Next, the thickness was determined by measuring the height of the step that is created by the tape. The results are displayed in section 4.4.3.3.

#### 3.6.5.4 Study effect of rGO amount on the TiO<sub>2</sub> NTs/AgNPs

First of all, the TiO<sub>2</sub> NTs/AgNPs was prepared under optimized conditions. Then, rGO was introduced onto TiO<sub>2</sub> NTs/AgNPs surface using electrochemical deposition. The electrodeposition of rGO was conducted in 0.1 M phosphate buffer solution pH 9.32 containing GO suspension at the concentration of 0, 0.010, 0.050, 0.075, 0.100, 0.125, 0.150, 0.200, and 0.300 mg/mL. Cyclic voltammetry was employed with the potential scan in the range from -1.5 to 1.0 V at a scan rate of 50 mV/s for 10, 20, 30, 35, 40, 45, and 50 cycles under magnetic stirring. Finally, Raman spectra and SEM images of the TiO<sub>2</sub> NTs/AgNPs-rGO was recorded as displayed in section 4.4.3.4.



### 3.6.6 Investigation of analytical performance of the TiO<sub>2</sub> NTs/AgNPs-rGO

The TiO<sub>2</sub> NTs/AgNPs-rGO substrate was fabricated under optimum conditions as described in section 3.6.2.3. Then, 5  $\mu$ L of MB solution was dropped on the TiO<sub>2</sub> NTs/AgNPs-rGO and the analytical performances of the SERS substrate were evaluated at laser excitation of 532 nm with a laser power of 50 mW and a laser spot size of 0.9  $\mu$ m. The SERS intensities were detected on Raman spectrophotometer equipped with a 50 $\times$  microscope objective lens in the range from 200-2000 cm<sup>-1</sup> through a 600 g/mm grating. For each sample, twenty Raman spectra were recorded by using acquisition time of 10 second and co-addition of 5.

#### 3.6.6.1 SERS performance of the TiO<sub>2</sub> NTs/AgNPs-rGO

The performance of the TiO<sub>2</sub> NTs/AgNPs-rGO was studied compared to the Ti, TiO<sub>2</sub> NTs, Ti/rGO, TiO<sub>2</sub> NTs/rGO, Ti/AgNPs, TiO<sub>2</sub> NTs/AgNPs, and Ti/AgNPs-rGO substrates. The Raman intensity of 1 mM MB on the different substrates were detected as shown in section 4.4.4.1.

#### 3.6.6.2 Investigation of linear range and LOD of the TiO<sub>2</sub> NTs/AgNPs-rGO

Linearity of the TiO<sub>2</sub> NTs/AgNPs-rGO for detection of MB at various concentrations from 10<sup>-1</sup> to 10<sup>-13</sup> M was studied. Besides, detection limit (LOD) was calculated based on the definition of the LOD prescribed by the international union of pure and applied chemistry (IUPAC). The signals of substrate background were detected for 20 repetitions (n=20). Then, a mean and standard deviation (SD) were calculated. The results are demonstrated in section 4.4.4.2.

#### 3.6.6.3 Study enhancement factor of the TiO<sub>2</sub> NTs/AgNPs-rGO

The enhancement ability of the TiO<sub>2</sub> NTs/AgNPs-rGO for MB detection was quantified by calculating the analytical enhancement factor (AEF). To receive normal Raman intensity, 5  $\mu$ L of 0.1 M MB solution was dropped on the bare Ti sheet. Meanwhile, 5  $\mu$ L of 1 nM MB solution was dropped on the surface of the TiO<sub>2</sub> NTs/AgNPs-rGO in order to obtain SERS intensity. Raman spectra of MB on the normal substrate and SERS substrate were then recorded. The results are displayed in section 4.4.4.3.

#### 3.6.6.4 Investigation of repeatability and reproducibility of the substrate

The repeatability was evaluated by measuring the Raman signal to 1 mM MB with twenty different spots (n = 20) within an area of 30 $\times$ 30  $\mu$ m. The

reproducibility of the SERS substrate was also evaluated by measuring the Raman intensity of 1 mM MB with ten different prepared TiO<sub>2</sub> NTs/AgNPs-rGO substrates ( $n = 10$ ). Then, a relative standard deviation (%RSD) was determined. The results are showed in section 4.4.4.4.

#### 3.6.6.5 Investigation of stability of the TiO<sub>2</sub> NTs/AgNPs-rGO

Stability of the TiO<sub>2</sub> NTs/AgNPs-rGO for storage within 30 days period was investigated on the detection of 1 mM MB compared with the TiO<sub>2</sub> NTs/AgNPs. The substrates were kept under air ambient condition when not in use. Analysis was performed every two days and the Raman signals were recorded under optimal conditions. The results are showed in section 4.4.4.5.

#### 3.6.6.6 Investigation of reusability of the TiO<sub>2</sub> NTs/AgNPs-rGO

The reusability of the TiO<sub>2</sub> NTs/AgNPs-rGO was tested by detecting 1 mM MB on a freshly prepared TiO<sub>2</sub> NTs/AgNPs-rGO under optimum conditions. Then, the tested substrate was placed in a quartz cell containing DI-water and irradiated under Xenon arc lamp equipped with a solar simulator at a power of 150 mW/cm<sup>2</sup> for 2 h, as shown in Figure A.6 (Appendix A.4). After that, the cleaned substrate was tested again under the same process for three cycles. The results are showed in section 4.4.4.6.

#### 3.6.6.7 Performance comparison with commercial SERS substrates

Three commercial SERS substrates were purchased from ATOID<sup>TM</sup>, Ocean optics, and Hamamatsu company in order to compare the performances with the TiO<sub>2</sub> NTs/AgNPs-rGO substrate. 5  $\mu$ L of 1 mM MB was employed to investigate enhancement factor (EF), repeatability, reproducibility, and stability. The measurements were performed under laser excitation of 532 nm with a laser power of 50 mW and a laser spot size of 0.9  $\mu$ m<sup>2</sup>. The SERS intensities were detected on Raman spectrophotometer equipped with a 100 $\times$  microscope objective lens in the range from 200-2000 cm<sup>-1</sup> through a 600 g/mm grating. For each sample, twenty Raman spectra were recorded by using acquisition time of 5 second and co-addition of 3. The results are displayed in section 4.4.4.7.

### 3.6.7 Evaluation of SERS substrate performance for glyphosate detection

The TiO<sub>2</sub> NTs/AgNPs-rGO substrate was fabricated under optimum conditions (experiment 3.6.2.3) and then applied for detection of glyphosate herbicide by Raman spectrophotometer equipped with a 100 $\times$  microscope objective lens at laser

excitation of 785 nm with a laser power of 100 mW and a laser spot size of 1.1  $\mu\text{m}$ . The SERS intensities were detected in the range from 200-2000  $\text{cm}^{-1}$  through a 600 g/mm grating by using acquisition time of 10 second and co-addition of 5.

#### 3.6.7.1 Investigation of linear range and LOD for glyphosate detection

Linear range of the  $\text{TiO}_2$  NTs/AgNPs-rGO for glyphosate determination was investigated in a range from 0.1 to 100 mg/L. Moreover, limit of detection (LOD) was determined based on signal-to-noise (3S/N) by detection of background signals of the substrate for 10 repetition ( $n=10$ ). The results are presented in section 4.4.5.1.

#### 3.6.7.2 Investigation of selectivity of the $\text{TiO}_2$ NTs/AgNPs-rGO

Interferent effect on glyphosate detection using the  $\text{TiO}_2$  NTs/AgNPs-rGO substrate was investigated by testing common pesticides used in agricultural activity, including polyethoxylated tallow amine (POEA), glycine, chlorpyrifos, paraquat, carbaryl, and carbendazim at a concentration of 10 mg/L. In addition, some possible inorganic compounds usually found in environmental samples, such as  $\text{KPO}_4$  (50 mg/L),  $\text{NaSO}_4$  (100 mg/L),  $\text{MgSO}_4$  (100 mg/L),  $\text{CuSO}_4$  (100 mg/L),  $\text{KNO}_3$  (100 mg/L),  $\text{NaNO}_3$  (100 mg/L),  $\text{ZnNO}_3$  (100 mg/L),  $\text{CaCO}_3$  (100 mg/L),  $\text{KCl}$  (100 mg/L),  $\text{NaCl}$  (100 mg/L), and  $\text{CaCl}_2$  (100 mg/L) were also evaluated. These interferences were mixed with standard glyphosate solution (10 mg/L) and then SERS intensities were recorded compared to the signal of pure glyphosate solution (10 mg/L). The results are displayed in section 4.4.5.2.

### 3.6.8 Determination of glyphosate in real samples by the $\text{TiO}_2$ NTs/AgNPs-rGO

Three water samples and three soil samples collected from Khon Kaen province were extracted as described in experiment 3.5.1.10 and 3.5.1.11, respectively. In order to check accuracy of the SERS-based sensor, standard glyphosate solutions (0.5 and 1.0 mg/L for water, 2 and 4 mg/kg for soil) were spiked into the samples. The concentration of glyphosate in samples and spiked samples were determined by the sensor fabricated under optimum conditions (experiment 3.6.2.3). Firstly, 5  $\mu\text{L}$  of sample solution was dropped on the  $\text{TiO}_2$  NTs/AgNPs-rGO and then evaluated by Raman spectrophotometer equipped with a 100 $\times$  microscope objective lens at laser excitation of 785 nm with a laser power of 100 mW and a laser spot size of 1.1  $\mu\text{m}$ . The

SERS intensities were detected in the range from 200-2000  $\text{cm}^{-1}$  through a 600 g/mm grating by using acquisition time of 10 second and co-addition of 5. Each sample solution underwent three parallel determinations by external calibration method. Concentration of glyphosate in real samples were calculated by substituting the SERS intensity values into the calibration curve obtained in the section 3.6.7.1. Finally, recovery percentages were calculated and the detected glyphosate concentrations are compared to the standard values obtained from UHPLC method (experiment 3.5.8.2). The results are showed in section 4.4.6.



## CHAPTER 4

### RESULTS AND DISCUSSION

The aims of this thesis are the development of carbon composite nanomaterials-based sensors and biosensors using electrochemical method and surface enhanced Raman spectroscopy (SERS) as detection methods for determination of toxic substances in food and environment, and cancer biomarker for clinical applications. Two sensors and two biosensors were designed, as a consequence, there are 4-sub objectives in this thesis. In this chapter, a fully explanation of all results, including physical and electrochemical characterization, optimizations, analytical performances, and applicability of the sensors and biosensors are discussed.

#### **4.1 Carbon composite Nanomaterials-based sensor: electrochemical sensor for bisphenol A detection**

Bisphenol A (BPA) is a major monomer in the industrial production of food and water containers as well as surface coating of cans. It can easily migrate into food and drinking water contained in the packaging products leading to negative health effects in humans. Therefore, an electrochemical sensor was developed for BPA determination in food applications. The sensor was fabricated based on glassy carbon paste electrode (GCPE) modified with graphene nanoplatelets (GNP) functionalized with ionic liquid (IL). GNP is applied to improve sensitivity and electron transfer ability of the electrode due to a poor response of BPA at traditional electrochemical sensor. However, graphene tends to form irreversible agglomerates through strong  $\pi$ - $\pi$  restacking and *Van der waals* interactions. Thus, IL is functionalized on the GNP surface to prevent the aggregation and increase dispersibility of GNP. The sensor (GCPE/GNP-IL) was performed by differential pulse voltammetry (DPV) for determination of BPA in drinking water and plastic drinking water bottles. The physical characterization and electrochemical characterization of the sensor were firstly investigated. Continuously, conditions for electrode preparation and parameters affecting the measurement are evaluated. Next, analytical performances and applications of the GCPE/GNP-IL for

BPA determination in real samples were tested, in comparison to high performance liquid chromatography (HPLC) as a reference method.

#### 4.1.1 Characterization results of the GCPE/GNP-IL

##### 4.1.1.1 SEM of the GCPE/GNP-IL

The morphology of the unmodified GCPE and GCPE/GNP-IL was characterized by scanning electron microscope (SEM) (experiment 3.3.3.1). The GCPE exhibited well spherical structures with an average diameter of about 4-10  $\mu\text{m}$  (Figure 4.1(A)), which is consistent with the size provided by the supplier (Particles size < 20  $\mu\text{m}$ ). After introduction of GNP-IL composite, a thin wrinkling sheet-like stacked layers was observed (Figure 4.1(B)), which indicated the addition of GNP-IL on the electrode surface. A similar observation has been reported. For instance, a curling layer of graphene-IL film was observed after electrode modification. [163] Gong and et al. [164] revealed that a layered structure and a curly morphology consisting of a thin wrinkling paper-like structure were observed on glassy carbon electrode modified with graphene-nafion composite.

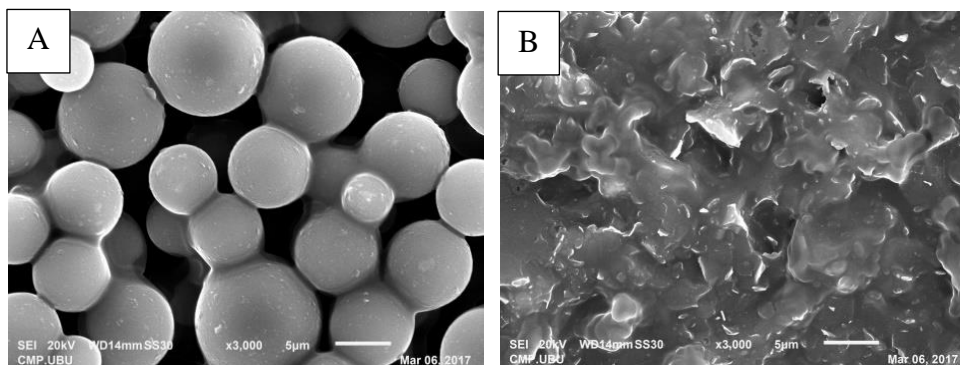


**Figure 4.1 SEM of (A) GCPE and (B) GCPE/GNP-IL**

##### 4.1.1.2 FTIR of the GNP-IL composite

Fourier transform infrared spectroscopy (FTIR) was employed to confirm that IL is successfully linked onto the GNP surface. The FTIR pattern of GNP, IL and GNP-IL were measured (experiment 3.3.3.2) and the results are displayed in Figure 4.2(A), the characteristic absorption peaks of GNP located at 1083  $\text{cm}^{-1}$ , 1635  $\text{cm}^{-1}$  and 3440  $\text{cm}^{-1}$  is attributed to the vibration modes of C-O-C, C=C and O-H bonds, respectively. These characteristic peaks correspond to the  $\text{sp}^2$  carbon skeletal network

and oxygen-containing functional groups on the basal plan of carbon. In case of IL, 1-butyl-2,3-dimethylimidazolium tetrafluoroborate was selected and its structure is presented in Figure 4.2(B). The peaks at  $658\text{ cm}^{-1}$ ,  $756\text{ cm}^{-1}$ ,  $1036\text{ cm}^{-1}$ ,  $1450\text{ cm}^{-1}$ ,  $1580\text{--}1650\text{ cm}^{-1}$ ,  $1635\text{ cm}^{-1}$  are related to the C=C bending, C-H bending, C-N stretching, C-H bending of methyl group, N-H bending of amine group, C=C stretching, respectively. The major peaks of each materials are obviously seen in GNP-IL composites, indicating successful synthesis of the nanocomposites. This results are consistent with research from Sun and et al. [165] who found that the characteristic absorption mode of the  $\text{sp}^2$  carbon (C-C stretching), oxygen functional groups (C-O-C stretching, C-OH stretching, C-O stretching), N-H vibration and C-N bending were observed on IL functionalized graphene oxide.

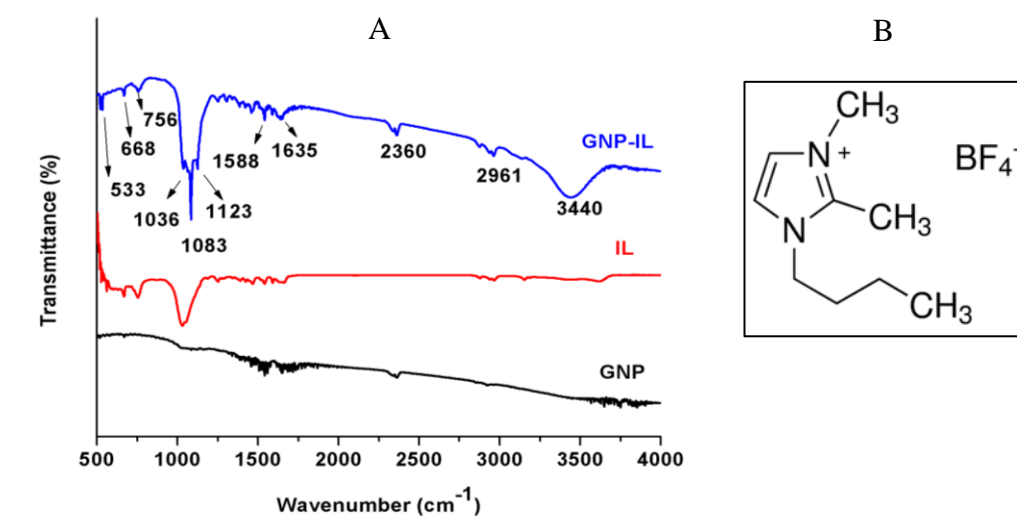


**Figure 4.2 (A) FTIR spectra of GNP, IL and GNP-IL (B) Chemical structure of 1-butyl-2,3-dimethylimidazolium tetrafluoroborate (IL)**

#### 4.1.2 Results of electrochemical characterization of the GCPE/GNP-IL

##### 4.1.2.1 CV and EIS of the GCPE/GNP-IL

The electrochemical behavior of the GCPE/GNP-IL was investigated compared to an unmodified GCPE, GCPE/IL, and GCPE/GNP by cyclic voltammetry (CV) in  $5\text{ mM Fe(CN)}_6^{3-/4-}$  redox solution (experiment 3.3.4.1). As shown in Figure 4.3(A), a pair of well defined quasi-reversible one-electron redox peaks was



observed on the bare GCPE, with a peak-to-peak separation ( $\Delta E_p$ ) of 0.49 V and a peak current density ( $J_p$ ) of  $55.1 \mu\text{A}\cdot\text{cm}^{-2}$ . After modification with IL,  $J_p$  increased to  $67.4 \mu\text{A}\cdot\text{cm}^{-2}$  and  $\Delta E_p$  decreased to 0.20 V. This enhancement is attributed to ion-exchange capability and high ionic conductivity of IL. With GNP as modifier,  $\Delta E_p$  of 0.20 V was obtained and  $J_p$  is slightly higher than the GCPE/IL. This is due to high conductivity and fast electron transfer ability of GNP. In the presence of both nanomaterials, well-defined and enhanced redox peaks of  $123.1 \mu\text{A}\cdot\text{cm}^{-2}$  with a small  $\Delta E_p$  value of 0.12 V were observed. Therefore, it could be concluded that a synergistic between GNP and IL nanomaterials can improve conductivity and promote electron transfer process of the electrode. Moreover, Chaiyo and et al. [166] revealed that the highest signal response was obtained with screen-printed carbon electrode (SPCE) modified with graphene-IL composite, in comparison to a bare SPCE and SPCE/graphene.

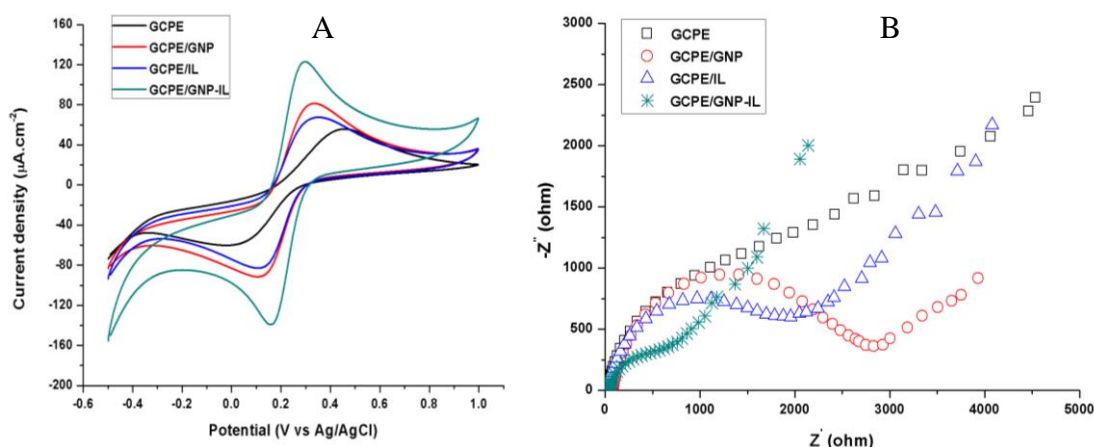


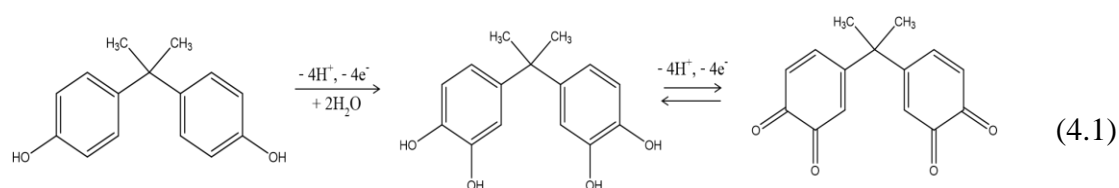
**Figure 4.3 (A) CV and (B) EIS of different electrodes in 5 mM  $\text{Fe}(\text{CN})_6^{3-/4-}$  solution**

Further characterization was performed with electrochemical impedance spectroscopy (EIS) to study the electron transfer ability of the GCPE/GNP-IL, in comparison to GCPE, GCPE/IL, and GCPE/GNP. The experiment was performed in 5 mM  $\text{Fe}(\text{CN})_6^{3-/4-}$  solution (experiment 3.3.4.1). As displayed in Figure 4.3(B), the Nyquist plot of GCPE showed a semicircle with a charge transfer resistance ( $R_{ct}$ ) of 3.14 k $\Omega$ . After modification with IL and GNP, the  $R_{ct}$  decreased to 1.75 and 2.51 k $\Omega$ , respectively. In the presence of both nanomaterials, the  $R_{ct}$  value decreased dramatically to 0.53 k $\Omega$ . The results underline that the GNP-IL composite greatly improves the

conductivity and charge transfer ability of the electrode. This result is corresponded to Santos and co-worker [167] who revealed that  $R_{ct}$  of glassy carbon electrode (1.05 k $\Omega$ ) decreased to 0.67 k $\Omega$  and 0.24 k $\Omega$  after modification with graphene and graphene-IL composite, respectively.

#### 4.1.2.2 DPV of the GCPE/GNP-IL

To evaluate the electrochemical response of the GCPE/GNP-IL to BPA, differential pulse voltammetry (DPV) was performed in 0.1 M phosphate buffer solution (pH 8.0) containing 2  $\mu$ M BPA (experiment 3.3.4.2). Figure 4.4(A) shows a typical DPV voltammograms of the GCPE/GNP-IL compared to GCPE, GCPE/IL, and GCPE/GNP, and Figure 4.4(B) displays the corresponding results. The highest signal of 4.3  $\mu$ A.cm<sup>-2</sup> with a peak potential at +0.55 V was obtained on the GCPE/GNP-IL. This result proved that GNP-IL composites served as a suitable nanomaterial for sensor fabrication for BPA detection. The proposed mechanism of BPA oxidation reaction is given in Equation 4.1, suggesting that the same number of protons and electrons are involved in the oxidation process of BPA. Previous researches, Hou and et al. [168] presented that a very weak response of BPA was observed at unmodified electrode and the significant improvement was obtained after introduction of graphene. Also, Canevari and et al. [109] informed that electrode modified with reduced graphene oxide showed a better electrocatalytic response to BPA than the bare electrode.



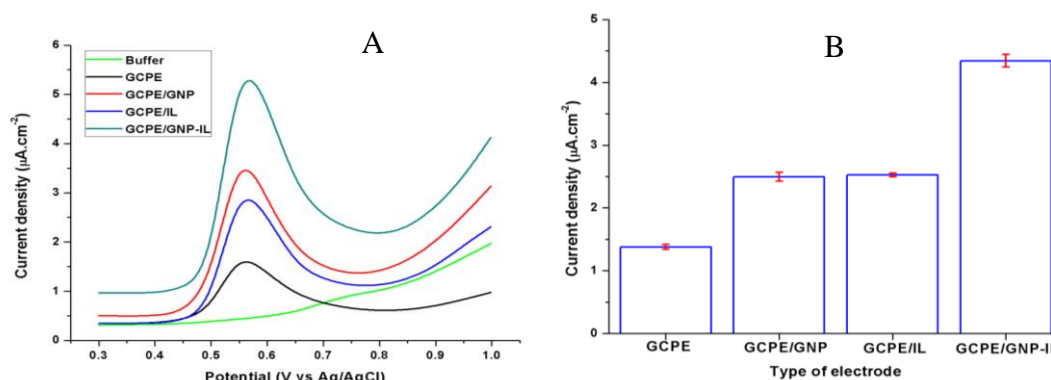


**Figure 4.4 (A) DPV of the different modified electrodes in 2 μM BPA solution and (B) its corresponding results**

#### 4.1.2.3 CV at different scan rate of the GCPE/GNP-IL

The possible kinetic process on the surface of the GCPE/GNP-IL was investigated by CV at different scan rate from 0.02 to 0.20 V/s in 5 mM  $\text{Fe}(\text{CN})_6^{3-/4-}$  solution (experiment 3.3.4.3). The oxidation and reduction peak current increased with the increasing scan rates (Figure 4.5(A)) and exhibited a linear dependence on the square root of the scan rate (Figure 4.5(B)). This behavior can be explained by Randles-Sevcik equation (Equation 4.2). Where,  $I_p$  is the peak current,  $D_0$  is the diffusion coefficient of  $\text{Fe}(\text{CN})_6^{3-/4-}$  ( $\text{cm}^2 \cdot \text{s}^{-1}$ ),  $A$  is the apparent electrode area ( $\text{cm}^2$ ),  $v$  is the scan rate ( $\text{V} \cdot \text{s}^{-1}$ ),  $n$  is the electron transfer number and  $C_0$  is the concentration of  $\text{Fe}(\text{CN})_6^{3-/4-}$  ( $\text{mol} \cdot \text{cm}^{-3}$ ).

$$I_p = 2.69 \times 10^5 \times (D_0) \times A \times v^{1/2} \times n^{3/2} \times C_0 \quad (4.2)$$

The result suggested that kinetics of overall process on the GCPE/GNP-IL surface is mainly controlled by diffusion. As a result, the detected current signal is directly proportional to concentration of analyte. Moreover, the effect of scan rate on the electrooxidation of BPA is also investigated in a range of 0.01-0.15 V/s (experiment 3.3.4.3). The anodic current density increased linearly with the square root of scan rate, as can be seen in Figure 4.5(C) and (D). The GCPE/GNP-IL provided the same behavior in case of study in  $\text{Fe}(\text{CN})_6^{3-/4-}$  redox solution and BPA solution. Therefore, it could be concluded that kinetic process on the surface of GCPE/GNP-IL is a typical diffusion-controlled process. Moreover, Chaiyo and co-worker [166] also

found that the kinetics of screen-printed carbon electrode modified with a composite of nafion, ionic liquid, and graphene is diffusion-controlled process.

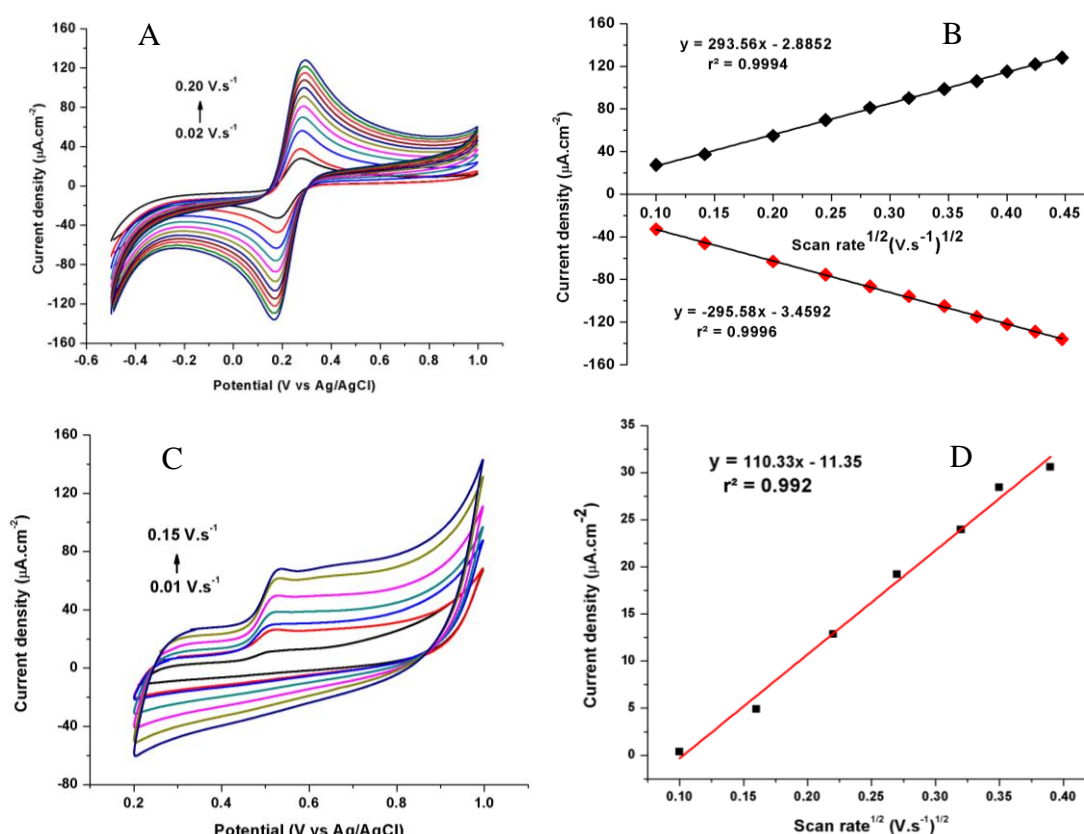


**Figure 4.5** (A) CV of the GCPE/GNP-IL in 5 mM  $\text{Fe}(\text{CN})_6^{3-/4-}$  at different scan rates and (B) its corresponding result (C) CV at different scan rates in 1  $\mu\text{M}$  BPA and (D) its corresponding data

### 4.1.3 Optimum conditions of the GCPE/GNP-IL

#### 4.1.3.1 Amount of IL and GNP-IL composites

The influence of IL functionalized on the GNP was investigated varying its surface concentration from 0.0 to 0.5  $\text{mg}\cdot\text{cm}^{-2}$  (experiment 3.3.5.1). The current signals obtained by DPV measurements in 0.1 M phosphate buffer solution containing 1  $\mu\text{M}$  BPA were analyzed by NOVA program version 1.11, as can be seen in Figure B.1 (Appendix B.1). The graph relationship between current density and amount of IL is illustrated in Figure 4.6(A) and the data is showed in Table B.1 (Appendix B.1). The current signal of the GCPE/GNP-IL is significantly higher than

GCPE/GNP (0.0 mg.cm<sup>-2</sup> IL) due to an excellent electrical conductivity and accelerate electron transfer ability of IL. The anodic peak current increased gradually from 0.1 to 0.4 mg.cm<sup>-2</sup>, whereas it decreased slightly beyond. The reason is possibly due to the ionic charge of IL blocks the delivery of electrons from solution to the electrode surface. The similar trend was also observed with the electrochemical sensor fabricated by Wong et al. [169] and Zhang et al. [170]. Therefore, 0.4 mg.cm<sup>-2</sup> of IL is used for the functionalization on the GNP.

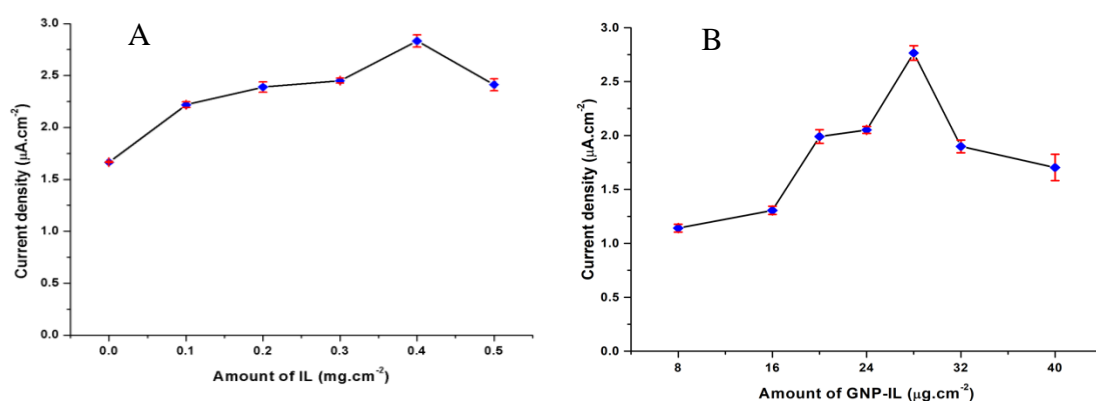


**Figure 4.6 Effect of amount of (A) IL and (B) GNP-IL on 1 μM BPA detection**

The amount of the GNP-IL composite at the electrode surface plays a crucial role in the electrocatalytic behavior of the sensor. Therefore, the effect of GNP-IL loaded on the GCPE surface from 8 to 40 μg.cm<sup>-2</sup> are evaluated (experiment 3.3.5.1). The graph relationship between current density and amount of GNP-IL composite is illustrated in Figure 4.6(B) and that data is showed in Table B.2 (Appendix B.1). The maximum oxidation current of BPA was obtained with the GCPE modified with 28 μg.cm<sup>-2</sup> GNP-IL composite. Too small amount of the composite can ineffectively improve the sensor performance, whilst too much amount of the composite lead to thick layer of the GNP-IL covered on the electrode surface. As a result, the diffusion of BPA to the sensing surface is hindered. Jing and co-worker [163] also reported that a decline of the peak current was observed due to the limited mass transport of BPA inside a thick film when using too much amount of graphene-IL composite. Thus, 28 μg.cm<sup>-2</sup> of GNP-IL composite was used for modification of the GCPE.

#### 4.1.3.2 Effect of pH solution on the BPA detection

The effect of the pH value was investigated over the range from 5.0 to 9.0 using phosphate buffer solution (experiment in section 3.3.5.2). The graph relationship between current density and pH value is illustrated in Figure 4.7 and the data is showed in Table B.3 (Appendix B.1). The oxidation peak current gradually increased when increasing the pH value from 5.0 to 8.0 whereas it decreased in more alkaline solutions. The highest current response to pH is below the  $pK_a$  of BPA ( $pK_a = 9.73$ ), suggesting that non-dissociated form of BPA could be better adsorbed on the surface of GCPE/GNP-IL [97]. The result is well consistent with the literature reviews. Li and et al. [97] revealed that non-dissociated BPA was easily adsorbed to the electrode surface than the dissociated BPA, so the maximum current response correspond to the pH value was lower than the  $pK_a$  of BPA. Jemmeli and co-worker [171] presented that a high sensitivity for BPA detection based on electrochemical sensor can be achieved by using buffer solution pH 8. Therefore, phosphate buffer solution with a pH value of 8.0 was chosen as the supporting electrolyte for the detection of BPA.

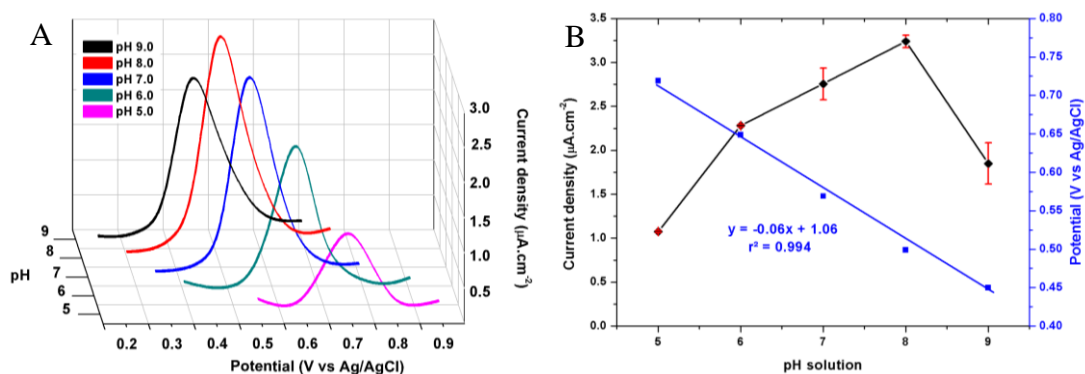


**Figure 4.7 (A) DPV of 1 μM BPA in phosphate buffer solution with different pH values and (B) dependence of the peak potential and current on pH**

The influence of pH value is not only effect on peak current but also affect on peak potential. As can be seen in Figure 4.7(B), the peak potential shifts negatively along with the increase of pH value. The relationship between the oxidation peak potential ( $E_{pa}$ ) and pH provided a linearity with the following equation,  $E_{pa}$  (V) =  $-0.06 \text{ pH} + 1.06$  ( $R = 0.994$ ). A slope of about  $-60 \text{ mV.pH}^{-1}$  is close to the theoretical

value of  $57.6 \text{ mV.pH}^{-1}$ . It indicates that the electron transfer from oxidation reaction of BPA is accompanied by an equal number of electrons and protons. [171, 172] Based on this result, the electron transfer number ( $n$ ) for oxidation of BPA is around 4, meaning that the electrooxidation of BPA at the SPCE/GNP-IL is a four-electron and four-proton process and a probable mechanism is showed in Equation 4.1.

#### 4.1.3.3 Effect of DPV parameter on the BPA detection

Sensitivity and well-shaped peak morphology of BPA analysis can be improved by adjusting DPV parameters such as pulse potential, step potential, and scan rate. Therefore, the effect of these important parameters was optimized (experiment 3.3.5.3). The pulse potential ( $E_{\text{pulse}}$ ) represents the height of the pulse amplitude and it may not be constant depending upon the technique. Figure 4.8(A) and Table B.4 (Appendix B.1) shows the relationship of  $E_{\text{pulse}}$  between 25 mV and 200 mV on the current response of  $1 \mu\text{M}$  BPA. The increasing  $E_{\text{pulse}}$  lead to enhancement of the mass transport of analyte to the electrode surface due to pumping effect. As a consequence, the current signal increased gradually with increasing  $E_{\text{pulse}}$ . However, a losses of mass transfer could be occurred when the  $E_{\text{pulse}}$  is higher than 150 mV. So, 150 mV pulse amplitude was applied in the experiments. Next, step potential ( $E_{\text{step}}$ ) was investigated in the range from 10 to 60 mV and the relationship of  $E_{\text{step}}$  on the current response of BPA is illustrated in Table B.5 (Appendix B.1).  $E_{\text{step}}$  is equal to the difference in voltage between each pulse. The peak current increased with the growth of the  $E_{\text{step}}$ , which is attributed to a faster change of potential (Figure 4.8(B)). However, the sensor response decreased after apply of 30 mV. Thus, 30 mV step potential was chosen for further study.

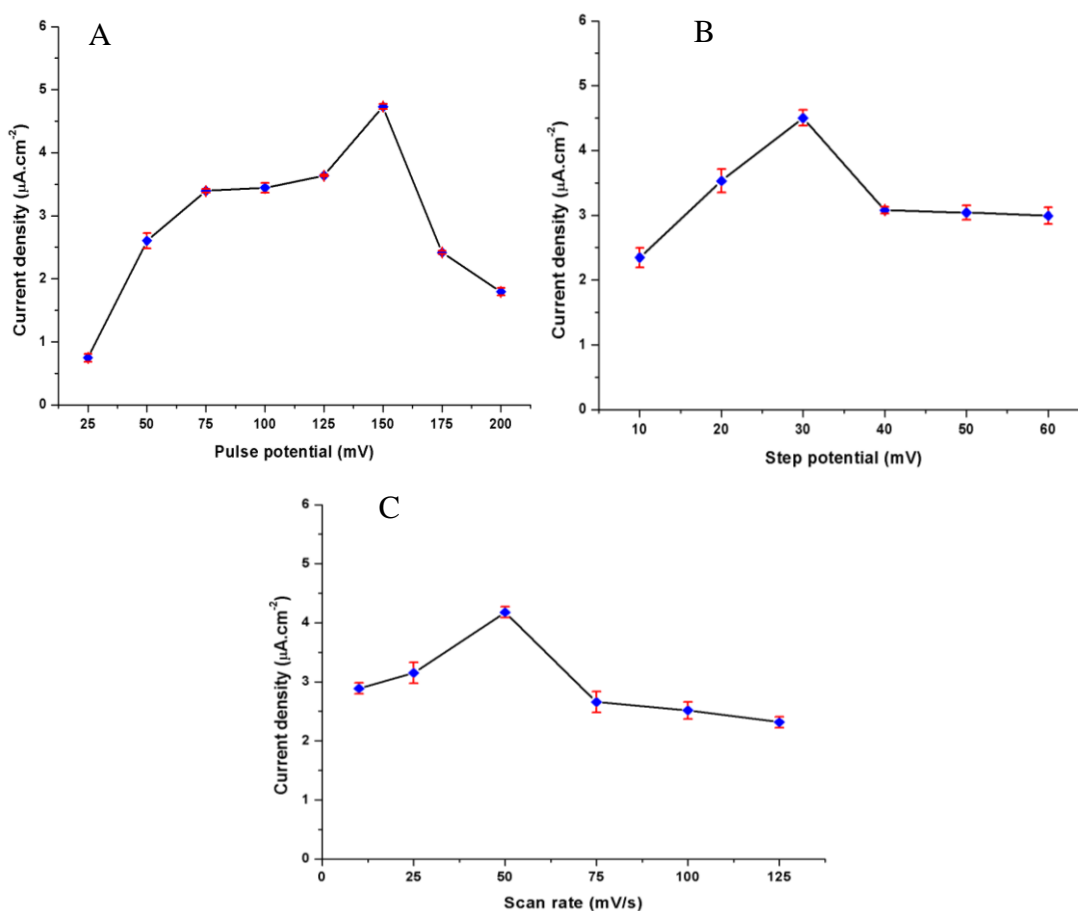


**Figure 4.8 Effect (A) pulse potential, (B) step potential, and (C) scan rate on the sensor response to 1  $\mu\text{M}$  BPA**

Scan rate basically indicates the speed in which pulse can be applied in the electrochemical system. Thus, the verification of scan rate impact on the recorded signal of BPA is also important. The effect of scan rate on the oxidation of BPA was investigated from 10 to 125 mV/s, as depicted in Table B.6 (Appendix B.1). The highest oxidation peak current was achieved at 50 mV/s (Figure 4.8(C)). Thus, the scan rate at 50 mV/s was applied in DPV experiments.

In summary, the optimum conditions for construction of the GCPE/GNP-IL was functionalization of  $0.4\text{ mg}\cdot\text{cm}^{-2}$  IL onto GNP sheet and loading of  $28\text{ }\mu\text{g}\cdot\text{cm}^{-2}$  GNP-IL composite on the electrode surface. The optimum conditions for BPA detection by the GCPE/GNP-IL is as follow: pH solution of 8.0, pulse potential of 150 mV, step potential of 30 mV, and scan rate of 50 mV/s. Under optimum conditions,



analytical performances of the prepared sensor were evaluated and the results are showed in the next part.

#### 4.1.4 Analytical performance of the GCPE/GNP-IL

##### 4.1.4.1 Linear range, LOD and LOQ of the GCPE/GNP-IL

Linearity of the GCPE/GNP-IL for the determination of BPA was evaluated with DPV under optimized experimental conditions (experiment 3.3.6.1). The oxidation peak current increased linearly with the increasing of BPA concentration in the range from 0.02  $\mu\text{M}$  to 5.0  $\mu\text{M}$ , with a linear regression of  $I [\mu\text{A} \cdot \text{cm}^{-2}] = 6.42C [\mu\text{M}] + 0.446$  ( $r^2 = 0.995$ ), as can be seen in Figure 4.9. With BPA concentrations higher than 5.0  $\mu\text{M}$ , the peak current leveled off. This may be due to the nearly saturated adsorption of BPA in the GNP-IL film. In addition, the DPV behaviors of unmodified GCPE, GCPE/IL, GCPE/GNP for BPA determination were also investigated and compared, as showed in Table B.7 (Appendix B.1). The highest sensitivity and the widest linear range for BPA detection was achieved at the GCPE modified with GNP-IL composite. The sensitivity of the GCPE/GNP-IL is about 2 times that of a bare GCPE and 1.5 times that of a GCPE/IL and GCPE/GNP. As a result, this can be suggested that GNP-IL nanocomposite is an excellent candidate for construction of the electrochemical sensor for ultrasensitive detection of BPA.

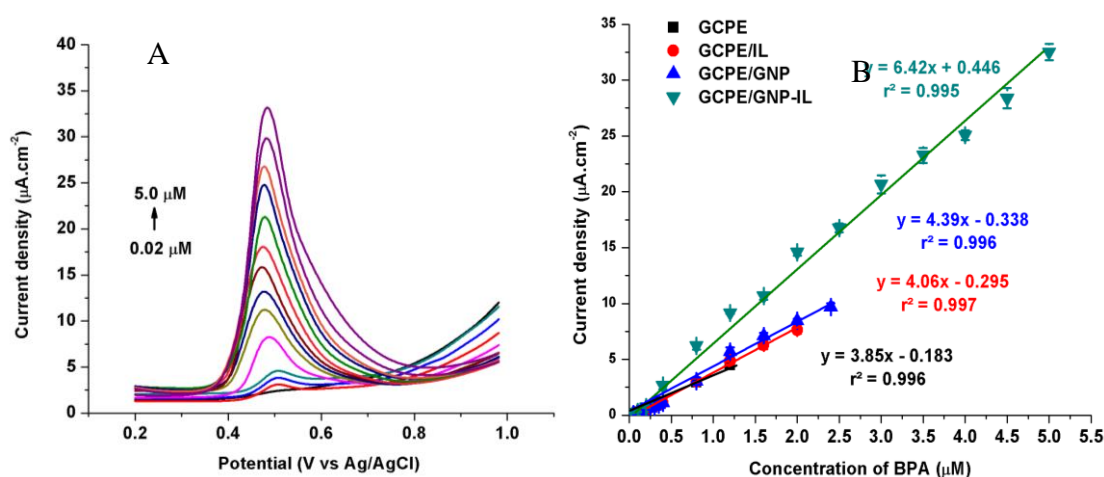


**Figure 4.9 (A) DPV of the GCPE/GNP-IL for detection of BPA and (B) calibration plots obtained with different modified electrodes**

Furthermore, limit of detection limit ( LOD) and limit of quantification (LOQ) of the sensor were calculated, according to Equation 4.3 and 4.4, respectively. Where SD is standard deviation of BPA signal at a concentration of 0.02  $\mu\text{M}$ , the lowest concentration of the linear range, and slope was obtained from the calibration curve.

$$\text{LOD} = \frac{3\text{SD}}{\text{slope}} \quad (4.3)$$

$$\text{LOQ} = \frac{10\text{SD}}{\text{slope}} \quad (4.4)$$

Slope of GCPE/GNP-IL for BPA detection is  $6.42 \mu\text{A} \cdot \mu\text{M}^{-1} \cdot \text{cm}^{-2}$  and SD for BPA detection at 0.02  $\mu\text{M}$  is 0.014, as can be seen in Table B.8 (Appendix B.1). Thus, the LOD and LOQ were calculated to be 6.4 nM and 0.02  $\mu\text{M}$ , respectively. In comparison to literature reviews (Table 2.4), the proposed GCPE/GNP-IL sensor provided higher sensitivity than that of MWCNT/PDDA/AuPd [102] MWCNT/PtNPs/GN [103] GN/PME [104] GN/NP-PtFe [106] rGO/PLL/AgNPs [107] SGrNF/AuNPs [110] and porous graphene functionalized black phosphorus. [112]

#### 4.1.4.2 Reproducibility and repeatability of the GCPE/GNP-IL

Reproducibility of the GCPE/GNP-IL was evaluated by using five independent electrodes and repeatability was evaluated by measuring the signal of 1  $\mu\text{M}$  BPA with five replicated measurements (experiment 3.3.6.2). As showed in Table B.9 (Appendix B.1), the SPCE/GNP-IL presented high repeatability and reproducibility with relative standard deviation (RSD) of 3.3% and 3.8%, respectively. This can be concluded that the prepared GCPE/GNP-IL sensor exhibited good repeatability and reproducibility.

#### 4.1.4.3 Stability of the GCPE/GNP-IL

The storage stability of the GCPE/GNP-IL was investigated during 2 weeks by using 1  $\mu\text{M}$  BPA solution (experiment 3.3.6.3). The electrode was stored at 4  $^{\circ}\text{C}$  in a refrigerator when not in use. The result is demonstrated in Figure 4.10 and Table B.10 (Appendix B.1). The designed sensor retained 80.1% of its original response

after storage for 2 weeks, demonstrating long-term stability of the GCPE/GNP-IL sensor.

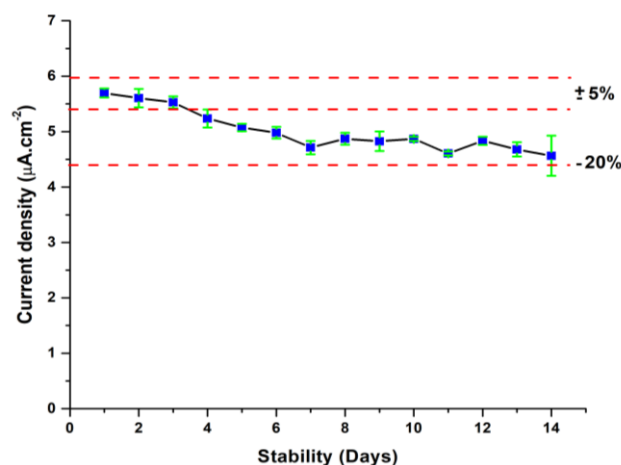


**Figure 4.10** Stability of the GCPE/GNP-IL obtained on 1  $\mu\text{M}$  BPA detection

#### 4.1.4.4 Selectivity of the GCPE/GNP-IL for BPA detection

Selectivity is an important factor for the performance of the electrochemical sensor. Thus, the influence of some potential interferents on the BPA detection were examined under the same experimental conditions to confirm the selectivity of the GNP-IL based-sensor. Phenolic compounds (phenol, 1-naphthol, and 4-nitrophenol), organic compounds (glucose and sucrose), and inorganic ions ( $\text{Na}^+$ ,  $\text{Ca}^{2+}$ ,  $\text{Mg}^{2+}$ ,  $\text{Al}^{3+}$ ,  $\text{Zn}^{2+}$ ,  $\text{Cu}^{2+}$ ,  $\text{Fe}^{2+}$ ,  $\text{Pb}^{2+}$ , and  $\text{Cd}^{2+}$ ) were investigated (experiment 3.3.6.4). The current signal of a pure BPA solution (1  $\mu\text{M}$ ) and a solution of BPA mixed with those interferent substances were measured. The result is showed in Figure 4.11 and the informative data is displayed in Table B.11 (Appendix B. 1). As a result, phenol and 1-naphthol had little influence on the electrochemical response of BPA at the same concentration level but did interfere when being in excess. Meanwhile, 4-nitrophenol interfered the detection of BPA when the concentration is higher than 5-times of BPA. However, this finding does not seem serious in relation to the practical application with plastic food containers because phenolic chemicals, except BPA, are not commonly used in the production of plastics. [ 173] In addition, some possible interfering substances in natural water samples, such as organic compounds like glucose and

sucrose with a concentration 100-fold higher, and some inorganic ions, such as 100-fold concentration of  $\text{Na}^+$ ,  $\text{Ca}^{2+}$ ,  $\text{Mg}^{2+}$ ,  $\text{Al}^{3+}$ ,  $\text{Zn}^{2+}$ ,  $\text{Cu}^{2+}$ ,  $\text{Fe}^{2+}$ ,  $\text{Pb}^{2+}$ , and  $\text{Cd}^{2+}$ , had no obvious influence on BPA determination. Therefore, the specificity toward BPA detection of the proposed sensor is acceptable.

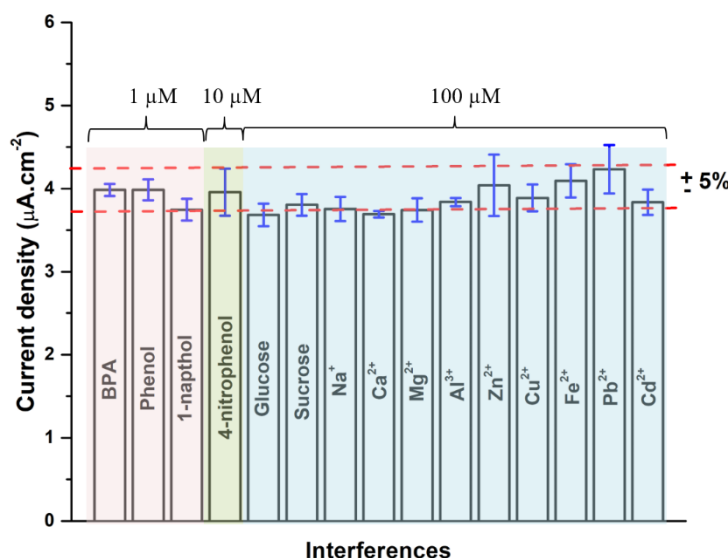


**Figure 4.11** Effect of interferences on the response of the GCPE/GNP-IL sensor

#### 4.1.5 Results of BPA determination in real samples

BPA is a major monomer in the industrial production of polycarbonate polymers and epoxy resins. These have been widely used as containers for feed, water, food, and inner surface coating of cans. However, BPA can easily migrate into food and drinking water from the packaging products leading to negative health effects in humans. Therefore, an amount of BPA in three commercial plastic products for drinking water storage and in water samples in contact with them were determined by the GCPE/GNP-IL and HPLC as a standard method. Moreover, standard BPA solution (1 mg/L) was added into those samples in order to check recovery of the extraction procedures and accuracy of the method.

##### 4.1.5.1 Results of BPA determination by the GCPE/GNP-IL

A certain volume of sample and spiked sample solution was added to a 5 mL electrochemical cell containing phosphate buffer solution (pH 8.0), and then detected by DPV under optimized conditions (experiment 3.3.7.1). The amount of BPA

was determined in triplicate by the standard addition method in the range from 0 to 0.6 mg/L, as showed in Figure 4.12 and Table B.12 (Appendix B.1). As a result, the GCPE/GNP-IL could be applied for determination of BPA contaminated in the three plastic drinking bottles, whilst there was no BPA contaminated in water samples. For recovery testing, standard BPA solution with a concentration of 1 mg/L was spiked into the sample solution and the proposed sensor provided recoveries in the ranged within 95.3-104.5% , indicating that the GCPE/GNP-IL sensor is reliable for practical application.

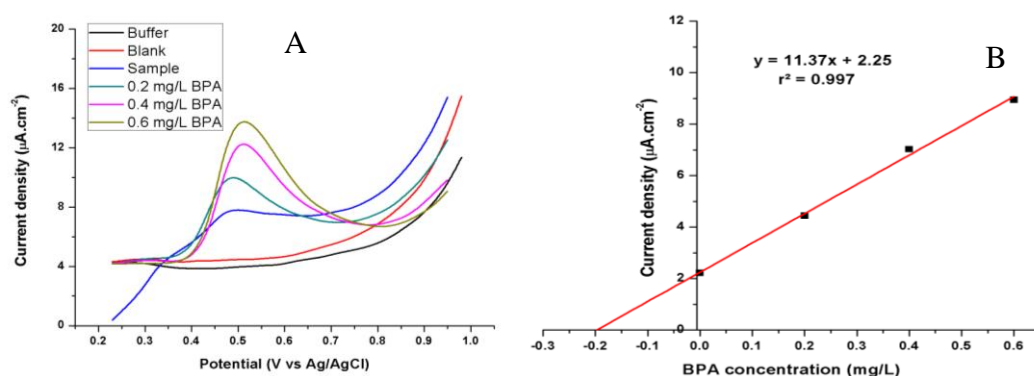


**Figure 4.12 (A) DPV of the GCPE/GNP-IL for BPA determination in real samples by standard addition method and (B) its corresponding curve**

#### 4.1.5.2 Results of BPA determination by HPLC

The amount of BPA contaminated in plastic samples and water samples were also analyzed and compared with a standard method, high performance liquid chromatography (HPLC). HPLC experiments were conducted with external calibration method under a flow rate of 1.0 mL/min, detection wavelength at 228 nm, C18 column (4.6×250 mm) as a stationary phase, and a mixture of acetonitrile and water (60:40, v/v) as a mobile phase (experiment 3.3.7.2). Under these conditions, the peak area increased linearly with the increasing of BPA concentration in the range from 0.05 to 200 mg/L with a linear regression of  $A [\text{mAU}\cdot\text{min}] = 0.598 [\text{mg/L}] + 0.002$  ( $r^2 = 0.999$ ), as can be seen in Figure 4.13. The concentration of BPA in samples and spiked samples were analyzed by HPLC in triplicate using the calibration plot, as shown in Table B.13 (Appendix B.1). The recoveries of 95.0-102.5% upon spiking were received

and the results are in very good agreement with the results obtained by the electrochemical sensor (Table 4.1). Statistical analysis by a paired T-test at a confidence interval of 95% probability was verified to compare the analytical data between HPLC and electrochemical sensor. It is suggested that the two methods provide results which are not statistically significantly different due to the t-value is smaller than the tabulated critical value at a degree of freedom of 2. Therefore, it can be concluded that the BPA concentration as determined from the two methods agrees significantly well with each other.

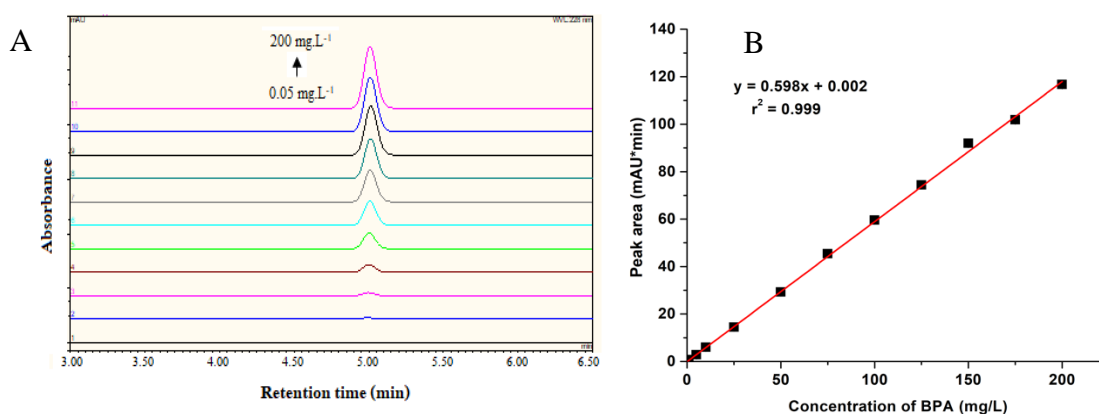


**Figure 4.13 (A) Chromatograms of BPA standard solution in the range from 0.05-200 mg/L and (B) its calibration plots**

**Table 4.1 Determination of BPA in plastic products and in water in contact with them by the sensor and HPLC ( $n=3$ )**

Sample	Added		Determined by sensor			Determined by HPLC			t-test <sup>b</sup>
			Measured		Recovery	Measured		Recovery	
	(mg.Kg <sup>-1</sup> )	(mg.L <sup>-1</sup> )	(mg.Kg <sup>-1</sup> )	(mg.L <sup>-1</sup> )	(%)	(mg.Kg <sup>-1</sup> )	(mg.L <sup>-1</sup> )	(%)	
Plastic A	-		3.48 ± 0.27		-	3.44 ± 0.03		-	0.3
Plastic B	-		2.53 ± 0.01		-	2.59 ± 0.06		-	2.1
Plastic C	-		1.98 ± 0.21		-	1.91 ± 0.02		-	0.6
Spiked plastic A	4.00		7.62 ± 0.20		103.5	7.24 ± 0.42		95.0	1.1
Spiked plastic B	4.00		6.44 ± 0.59		97.8	6.54 ± 0.56		98.8	0.2
Spiked plastic C	4.00		6.16 ± 0.03		104.5	6.01 ± 0.23		102.5	1.0
Water in plastic A		-	n.d. <sup>a</sup>		-	n.d.		-	-
Water in plastic B		-	n.d.		-	n.d.		-	-
Water in plastic C		-	n.d.		-	n.d.		-	-
Spiked water in plastic A		1.00	0.95 ± 0.03		95.3	0.99 ± 0.03		98.7	1.0
Spiked water in plastic B		1.00	0.99 ± 0.02		98.5	1.02 ± 0.01		102.2	2.7
Spiked water in plastic C		1.00	0.97 ± 0.02		97.0	1.01 ± 0.01		101.3	3.6

<sup>a</sup> n.d. means “not detectable”<sup>b</sup> t-test at a confidence level of 95% probability and degree of freedom of 2

## 4.2 Carbon composite nanomaterials-based biosensor: electrochemical biosensor for CEA detection

Carcinoembryonic antigen (CEA) is one of the most important cancer biomarkers used for early diagnosis of cancer and monitoring disease progression in clinical field. Therefore, the electrochemical biosensor for determination of CEA was developed based on a direct binding of CEA to a fixed amount of CEA antibody (anti-CEA) on the biosensing interface of a screen-printed carbon electrode (SPCE). The composite of manganese dioxide decorated on graphene nanoplatelets (GNP-MnO<sub>2</sub>) was employed to improve sensitivity of the biosensor due to high conductivity of GNP and excellent electrocatalytic activity of MnO<sub>2</sub>. Moreover, core shell Fe<sub>3</sub>O<sub>4</sub>@Au nanoparticles was chosen as an immune sensing platform for immobilizing CEA antibody due to magnetic properties of the Fe<sub>3</sub>O<sub>4</sub> core could be handled easily on the biosensing surface by an external magnetic field and good biocompatibility of Au shell could be directly and friendly interacted with antibody. The detection mechanism is based on the measurement of the peak current by linear sweep voltammetry (LSV) and charged transfer resistance by electrochemical impedance spectroscopy (EIS) owing to the redox reaction of hexacyanoferrate [Fe(CN)<sub>6</sub>]<sup>3-/4-</sup> as redox probe. The biosensor was applied for label-free determination of CEA in human serum samples for clinical applications, in comparison to an electrochemiluminescence (ECL) immunoassay as a comparative method. The physical and electrochemical properties of the nanomaterials-based biosensor were firstly characterized. Continuously, conditions for electrode preparation and parameters affecting the measurement are optimized. Next, analytical performances and applications of the SPCE/GNP-MnO<sub>2</sub>/Fe<sub>3</sub>O<sub>4</sub>@Au/anti-CEA for CEA analysis in human serum samples were evaluated.

### 4.2.1 Characterization results of the SPCE/GNP-MnO<sub>2</sub>/Fe<sub>3</sub>O<sub>4</sub>@Au/anti-CEA

#### 4.2.1.1 XRD of GNP-MnO<sub>2</sub> and Fe<sub>3</sub>O<sub>4</sub>@Au nanocomposites

X-ray diffraction (XRD) analysis was carried out to characterize the synthesized nanomaterials (experiment 3.4.3.1). The XRD patterns of the GNP-MnO<sub>2</sub> and core shell Fe<sub>3</sub>O<sub>4</sub>@Au nanocomposites were compared to the single materials such as GNP, MnO<sub>2</sub>, Fe<sub>3</sub>O<sub>4</sub>, and Au. As showed in Figure 4.14(A), GNP shows a strong diffraction peak located at  $2\theta = 26.5^\circ$  corresponding to the (002) diffraction of graphene. The sharp XRD peak indicate that GNP is highly crystalline. The XRD pattern of MnO<sub>2</sub>



has two diffraction peaks at  $2\theta = 35.8^\circ$  (211) and  $63.0^\circ$  (022), which are well matched to the amorphous structural features of  $\text{MnO}_2$  (JCPDS No.44-0141). Moreover, these peaks are broadened, indicating the poor crystallinity of  $\text{MnO}_2$ . The GNP- $\text{MnO}_2$  nanocomposite exhibits diffraction peaks similar to those of  $\text{MnO}_2$  and GNP, proving the successful synthesis of the GNP- $\text{MnO}_2$  nanocomposite. This result was corresponded to the research of Vukojević and et al. [174] who presented that the XRD pattern of  $\text{MnO}_2$ -graphene nanoribbon were observed at  $2\theta = 26.1^\circ$ ,  $36.7^\circ$  and  $66.0^\circ$ , which ascribed to the (002) plane of d-spacing in graphene, and (211) and (002) planes of  $\alpha$ - $\text{MnO}_2$ , respectively.

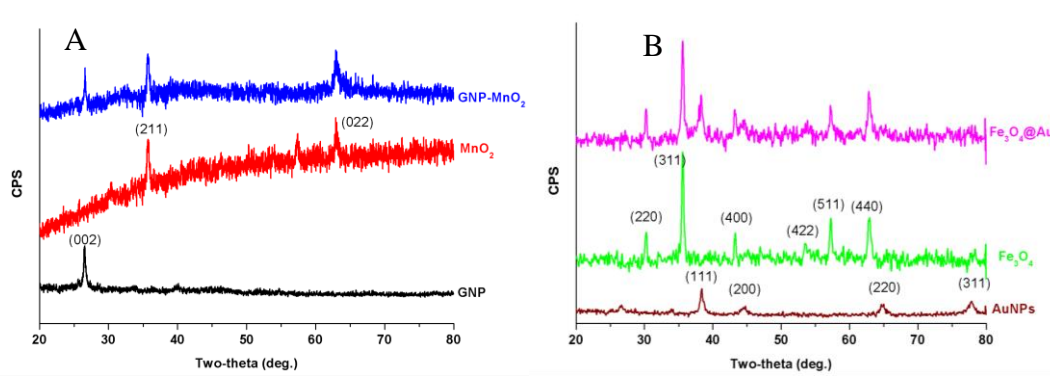


**Figure 4.14 XRD patterns (A) GNP,  $\text{MnO}_2$  and GNP- $\text{MnO}_2$  composite; (B) AuNPs,  $\text{Fe}_3\text{O}_4$  and core shell  $\text{Fe}_3\text{O}_4$ @Au nanoparticles**

As shown in Figure 4.14(B), the diffraction peaks of  $\text{Fe}_3\text{O}_4$  nanoparticles are at  $2\theta$  values =  $30.1^\circ$ ,  $35.4^\circ$ ,  $43.1^\circ$ ,  $53.5^\circ$ ,  $57.0^\circ$ , and  $62.6^\circ$ , assigning to (2 2 0), (3 1 1), (4 0 0), (4 2 2), (5 1 1), and (4 4 0) planes of a cubic spinel structure of  $\text{Fe}_3\text{O}_4$  (JCPDS No.85-1436). Au nanoparticles have four peaks at the positions of  $2\theta = 38.2^\circ$ ,  $44.3^\circ$ ,  $64.5^\circ$ , and  $77.7^\circ$ , which are related to the (1 1 1), (2 0 0), (220), and (311) reflections of Au in face-centered cubic structure. The XRD pattern of core shell  $\text{Fe}_3\text{O}_4$ @Au nanoparticles are corresponded well to the feature of the  $\text{Fe}_3\text{O}_4$  and Au, indicating that Au were decorated on the  $\text{Fe}_3\text{O}_4$  surface. Some previous researches, Izadiyan and et al. [175] reported that core shell  $\text{Fe}_3\text{O}_4$ @Au nanoparticles demonstrated four peaks of (200), (311), (511) and (440) planes of Au and  $\text{Fe}_3\text{O}_4$ .

#### 4.2.1.2 FTIR of GNP-MnO<sub>2</sub> and Fe<sub>3</sub>O<sub>4</sub>@Au nanocomposites

Fourier transform-infrared spectroscopy (FT-IR) was also performed to further characterize the nanomaterials (experiment 3.4.3.2). The IR spectrum of GNP-MnO<sub>2</sub> composite as well as their single material are presented in Figure 4.15(A). As a result, there is no any vibrations clearly observed in GNP while the IR spectrum of the GNP-MnO<sub>2</sub> is totally similar to that of MnO<sub>2</sub> whereas the intensity of vibrations is slightly decreased. The broad band at about 3420 cm<sup>-1</sup> is attributed to the stretching vibration of O-H bonds, while the weak absorption band at 1647 cm<sup>-1</sup> is probably due to the O-H bending vibration of adsorbed water on the surface of Mn atoms. The peak at about 1541 cm<sup>-1</sup> is due to the stretching vibrations of the isolated C=C double bonds while the peak at 1457 cm<sup>-1</sup> is due to the deformation vibration of the hydroxyl groups (M-OH vibration). The peak at 525 cm<sup>-1</sup> is the main characteristic absorption bands of MnO<sub>2</sub> which represents the stretching vibration of Mn-O functional group. Furthermore, El-Deen and et al. [176] found that IR spectrum of carbon nanotubes-MnO<sub>2</sub> composites were observed at around 3400 cm<sup>-1</sup> and 1620 cm<sup>-1</sup>, which corresponded to the O-H stretching and bending vibration, respectively. Meanwhile, the shape peak at 524 cm<sup>-1</sup> was attributed to the Mn-O and Mn-O-Mn vibrations of the MnO<sub>2</sub> in the composite.

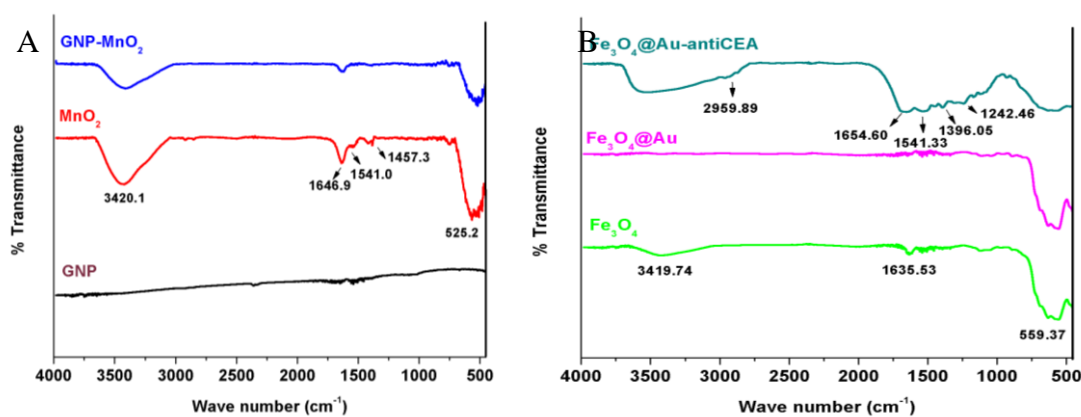


**Figure 4.15** FT-IR spectra of (A) GNP, MnO<sub>2</sub> and GNP-MnO<sub>2</sub> composite; (B) Fe<sub>3</sub>O<sub>4</sub>, core shell Fe<sub>3</sub>O<sub>4</sub>@Au and core shell Fe<sub>3</sub>O<sub>4</sub>@Au-conjugated anti-CEA

Figure 4.15(B) displays the FT-IR spectra of Fe<sub>3</sub>O<sub>4</sub>, core shell Fe<sub>3</sub>O<sub>4</sub>@Au and anti-CEA conjugated with core shell Fe<sub>3</sub>O<sub>4</sub>@Au. The FT-IR spectra of

$\text{Fe}_3\text{O}_4$  displays two absorption bands at  $559\text{ cm}^{-1}$  and  $3419\text{ cm}^{-1}$  that are assigned to the stretching collision of Fe-O and O-H vibration modes, respectively. In case of core shell  $\text{Fe}_3\text{O}_4@\text{Au}$ , the intensity of O-H vibration mode is decreased compared to the uncoated  $\text{Fe}_3\text{O}_4$  because of gold coating instead of adsorbed water. The result is consistent with Ángeles-Pascual and et al. [177] who revealed that core shell  $\text{Fe}_3\text{O}_4@\text{Au}$  nanoparticles showed a peak at  $605\text{ cm}^{-1}$  that was attributed to the vibration of the Fe-O functional group, and the band at  $3360\text{ cm}^{-1}$  was assigned to O-H stretching vibration. In case of anti-CEA conjugated with core shell  $\text{Fe}_3\text{O}_4@\text{Au}$ , the peaks observed in a range of  $2900\text{--}3500\text{ cm}^{-1}$  are assigned to the N-H stretching vibration of nitrogen-containing functional groups of the antibody. The bands at  $1654\text{ cm}^{-1}$ ,  $1541\text{ cm}^{-1}$ ,  $1396\text{ cm}^{-1}$ , and  $1242\text{ cm}^{-1}$  are corresponded to bending vibrations of O-H group, the asymmetry vibration of C=O, the symmetry vibration of C=O, and in plan vibrations of C-N functional group, respectively.

#### 4.2.1.3 SEM of the SPCE/GNP- $\text{MnO}_2$ / $\text{Fe}_3\text{O}_4@\text{Au}$ /anti-CEA

The surface morphologies of the unmodified electrode and electrode modified with nanomaterials, including GNP,  $\text{MnO}_2$ , GNP- $\text{MnO}_2$ ,  $\text{Fe}_3\text{O}_4@\text{Au}$ , and antibody-conjugated  $\text{Fe}_3\text{O}_4@\text{Au}$ , are examined by scanning electron microscope (SEM) (experiment 3.4.3.3). As shown in Figure 4.16(A), the surface of SPCE was composed of flake-like structures and granular carbon particles in size of around 50 nm. Figure 4.16(B) showed a thin wrinkling sheet-like layered structure of GNP on the SPCE.  $\text{MnO}_2$  showed globular morphology with an average diameter of about 200 nm and these near spherical structures were composed of thin flakes-like structures (Figure 4.16(C)). The morphology of GNP- $\text{MnO}_2$  composite indicated that the  $\text{MnO}_2$  are grown successfully on the GNP sheet (Figure 4.16(D)). This result is well-consistent with Rout and et al. [178] who found that as-synthesized  $\text{MnO}_2$  nanostructures showed spherical structures which composed of nanoflakes on the surface with a thickness less than 5 nm. In case of core shell  $\text{Fe}_3\text{O}_4@\text{Au}$  nanoparticles, the morphology looks approximately spherical in shape with an average diameter of around 20-50 nm (Figure 4.16(E)). Moreover, Mahmoudi-Badiki and et al. [179] also found that core shell  $\text{Fe}_3\text{O}_4@\text{Au}$  showed a well homogenized distribution of spherical nanoparticles with average diameters of about  $30 \pm 5\text{ nm}$ . As showed in Figure 4.16(F), a change in morphology of core shell  $\text{Fe}_3\text{O}_4@\text{Au}$  nanoparticles are observed after conjugation with the anti-CEA

due to gold nanoparticles could be a supporting media for immobilization of antibodies. [180]

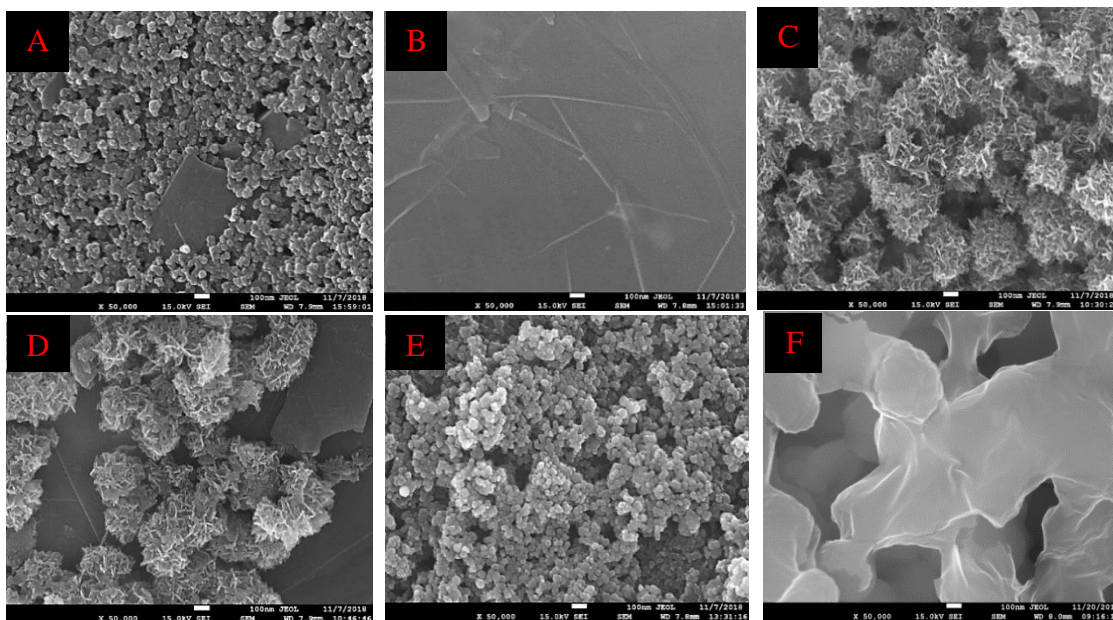


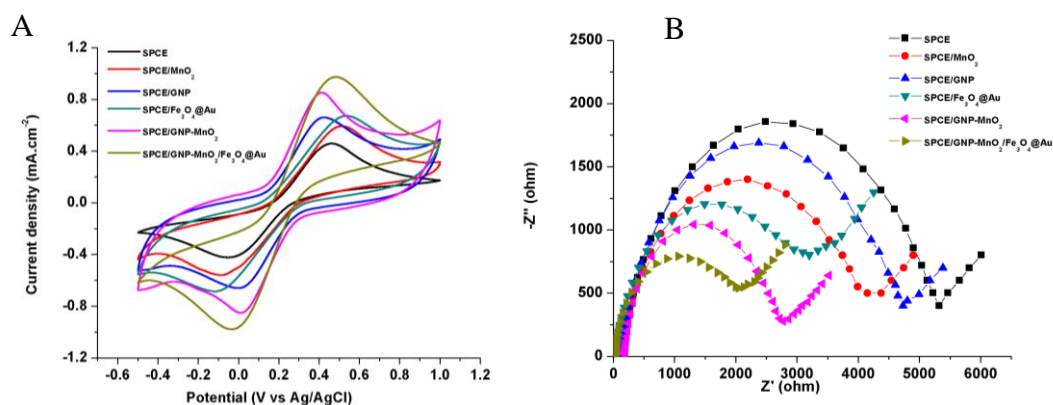
**Figure 4.16** SEM images of (A) SPCE and SPCE modified with (B) GNP, (C)  $\text{MnO}_2$ , (D) GNP- $\text{MnO}_2$ , (E)  $\text{Fe}_3\text{O}_4@Au$ , and (F)  $\text{Fe}_3\text{O}_4@Au/\text{anti-CEA}$

## 4.2.2 Electrochemical characterization results of the biosensor

### 4.2.2.1 CV and EIS of the SPCE/GNP- $\text{MnO}_2/\text{Fe}_3\text{O}_4@Au$

Cyclic voltammetry (CV) and electrochemical impedance spectroscopy (EIS) were performed in a solution of 0.1 M KCl containing 5 mM of  $\text{K}_3[\text{Fe}(\text{CN})_6]$  and 5 mM  $\text{K}_4[\text{Fe}(\text{CN})_6]$  in order to investigate the electrochemical behavior of different modified electrodes (experiment 3.4.4.1). As shown in Figure 4.17(A), a pair of well-defined redox peaks with a peak-to-peak separation ( $\Delta E_p$ ) of 0.48 V and a peak current density ( $J_p$ ) of  $0.51 \text{ mA}\cdot\text{cm}^{-2}$  were obtained at the unmodified SPCE due to  $\text{Fe}(\text{CN})_6^{3-/4-}$  could be easily self-oxidized/reduced by itself. The  $J_p$  had increased after the SPCE is modified with  $\text{MnO}_2$  due to  $\text{Fe}(\text{CN})_6^{3-/4-}$  was able to be catalytically oxidized by manganese species at lower oxidation states ( $\text{Mn}^{\text{II}}$  and  $\text{Mn}^{\text{III}}$ ). In case of GNP modified electrode,  $J_p$  increased and  $\Delta E$  decreased compared to a bare SPCE. This is due to high electrical conductivity and  $\pi$ -conjugated system of GNP can promote the electrical conductivity and facilitate electron transfer ability of the

electrode. The  $J_p$  was further enhanced and the  $\Delta E_p$  was further reduced after modification with GNP-MnO<sub>2</sub> composite, in comparison to SPCE/GNP and SPCE/MnO<sub>2</sub>. This is attributed to the synergistic effect between GNP and MnO<sub>2</sub> that can improve conductivity, facilitate the electron transfer ability and promote electrocatalytic activity of the redox probe on the electrode surface. The highest current density appeared when the GNP-MnO<sub>2</sub> and Fe<sub>3</sub>O<sub>4</sub>@Au were modified on the electrode surface due to excellent conductivity of Au shell and high electrocatalytic activity of Fe<sub>3</sub>O<sub>4</sub> core. This appearance could be ascribed to the fact that the functions of GNP-MnO<sub>2</sub> composite and core shell Fe<sub>3</sub>O<sub>4</sub>@Au together possessed the excellent electrical conductivity and electrocatalytic activity among the other modified electrodes. In comparison to the literature reviews, He and et al. [181] revealed that the redox peak currents are owing to redox reaction of Fe(CN)<sub>6</sub><sup>3-/4-</sup> had raise and the  $\Delta E_p$  had declines after the electrode modified with a composite of reduced graphene oxide (rGO) and MnO<sub>2</sub> because of high electrical conductivity of rGO and excellent electrocatalytic property of MnO<sub>2</sub>. Singhal and et al. [182] suggested that the electrode modified with Fe<sub>3</sub>O<sub>4</sub>@Au had a better electrochemical activity than the bare electrode and electrode modified with single materials.



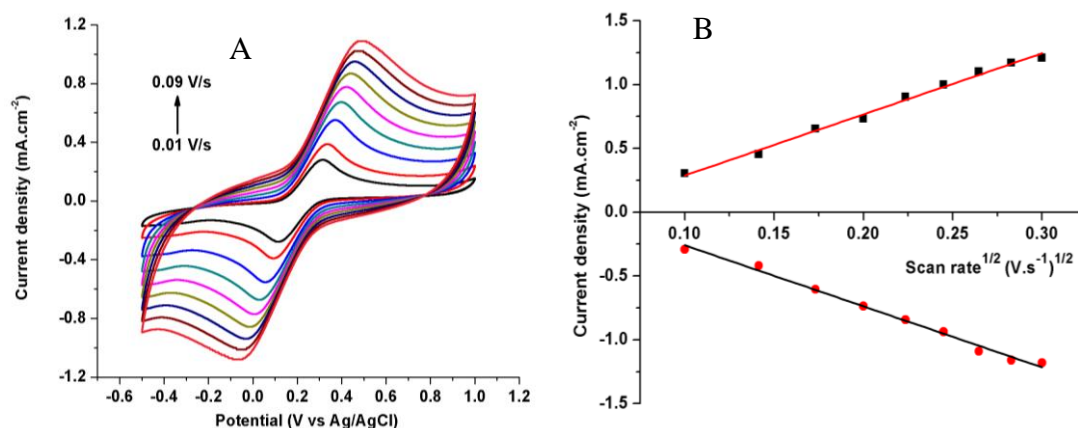
**Figure 4.17 (A) CV and (B) EIS of the different modified electrodes in 5 mM Fe(CN)<sub>6</sub><sup>3-/4-</sup> solution**

Figure 4.17(B) displays the Nyquist plots of different modified SPCE in which the electron transfer resistance ( $R_{ct}$ ) of the electrodes was calculated from the diameter of the semicircle portion. It can be seen that the semicircle diameters

of the SPCE/GNP and SPCE/MnO<sub>2</sub> are shortened compared with the bare SPCE, revealing a lower electron transfer resistance of the electrode after modification with GNP and MnO<sub>2</sub>. The  $R_{ct}$  value is further reduced after the electrode is modified with both GNP and MnO<sub>2</sub>, confirming that the GNP-MnO<sub>2</sub> composite could accelerate the electron transfer process between the electrode surface and the solution. Besides, the shortest width of the semicircle part is obtained at the SPCE/GNP-MnO<sub>2</sub>/Fe<sub>3</sub>O<sub>4</sub>@Au, proving that the GNP-MnO<sub>2</sub> composite and core shell Fe<sub>3</sub>O<sub>4</sub>@Au could be used as a promising material for construction of the electrochemical biosensor. Additionally, Wen and et al. [183] indicated that  $R_{ct}$  value of glassy carbon electrode decreased significantly after modification with rGO-MnO<sub>2</sub> composite and the  $R_{ct}$  was almost a very small semicircle domain and almost a straight line, implying a very low electron transfer resistance.

#### 4.2.2.2 CV at different scan rate of the SPCE/GNP-MnO<sub>2</sub>/Fe<sub>3</sub>O<sub>4</sub>@Au

In order to further investigate the electrochemical characterization of SPCE/GNP-MnO<sub>2</sub>/Fe<sub>3</sub>O<sub>4</sub>@Au, the CV was performed at different rates from 0.01-0.09 V/s in a solution of 0.1 M KCl containing 5 mM of Fe(CN)<sub>6</sub><sup>3-/4-</sup> solution (experiment 3.4.4.2). The redox peak current of the modified electrode had successively risen with the increase of scan rates (Figure 4.18(A)) and the peak current was linearly proportional to the square root of the scan rate, as shown in Figure 4.18(B). According to Randles-Sevcik equation (Equation 4.2), this confirms that the reaction of Fe(CN)<sub>6</sub><sup>3-/4-</sup> probe occurring on the surface of SPCE/GNP-MnO<sub>2</sub>/Fe<sub>3</sub>O<sub>4</sub>@Au is a diffusion-controlled process. This behavior is also in accordance with Wang and co-worker [184] who found that anodic and the cathodic peak currents of the electrode modified with graphene oxide/multiwalled carbon nanotube/ MnO<sub>2</sub>/Au composite increased linearly with the square root of scan rates.



**Figure 4.18 (A) CV and (B) current density dependence on the square root of a scan rate on a SPCE/GNP-MnO<sub>2</sub>/Fe<sub>3</sub>O<sub>4</sub>@Au in 5 mM Fe(CN)<sub>6</sub><sup>3-/4-</sup>**

#### 4.2.2.3 Electrochemical characterization of the biosensor for CEA detection

To evaluate the electrochemical performance of the biosensor for CEA detection, the EIS responses of the SPCE modified with different nanomaterials and CEA antibody before and after detection of CEA in phosphate buffer solution (pH 7.4) containing 5 mM Fe(CN)<sub>6</sub><sup>3-/4-</sup> were recorded (experiment 3.4.4.3). As shown in Figure 4.19, the impedimetric signal is almost unchanged after CEA captured on the bare SPCE and SPCE/GNP-MnO<sub>2</sub>. This implies that carbon materials and GNP-MnO<sub>2</sub> nanocomposite are not suitable to be a supporting media for antibody immobilization. In contrast, the diameter of the EIS response increased remarkably after CEA was immobilized on the surface of SPCE/Fe<sub>3</sub>O<sub>4</sub>@Au due to gold nanoparticles served as an ideal interface for antibody immobilization. The biggest change of semicircle domain of EIS responses was presented on the SPCE/GNP-MnO<sub>2</sub>/Fe<sub>3</sub>O<sub>4</sub>@Au. This result confirmed that GNP-MnO<sub>2</sub> composite could improve sensitivity and electrocatalytic activity of the biosensor, while core shell Fe<sub>3</sub>O<sub>4</sub>@Au nanoparticles could serve as an immune sensing platform for immobilizing antibody.



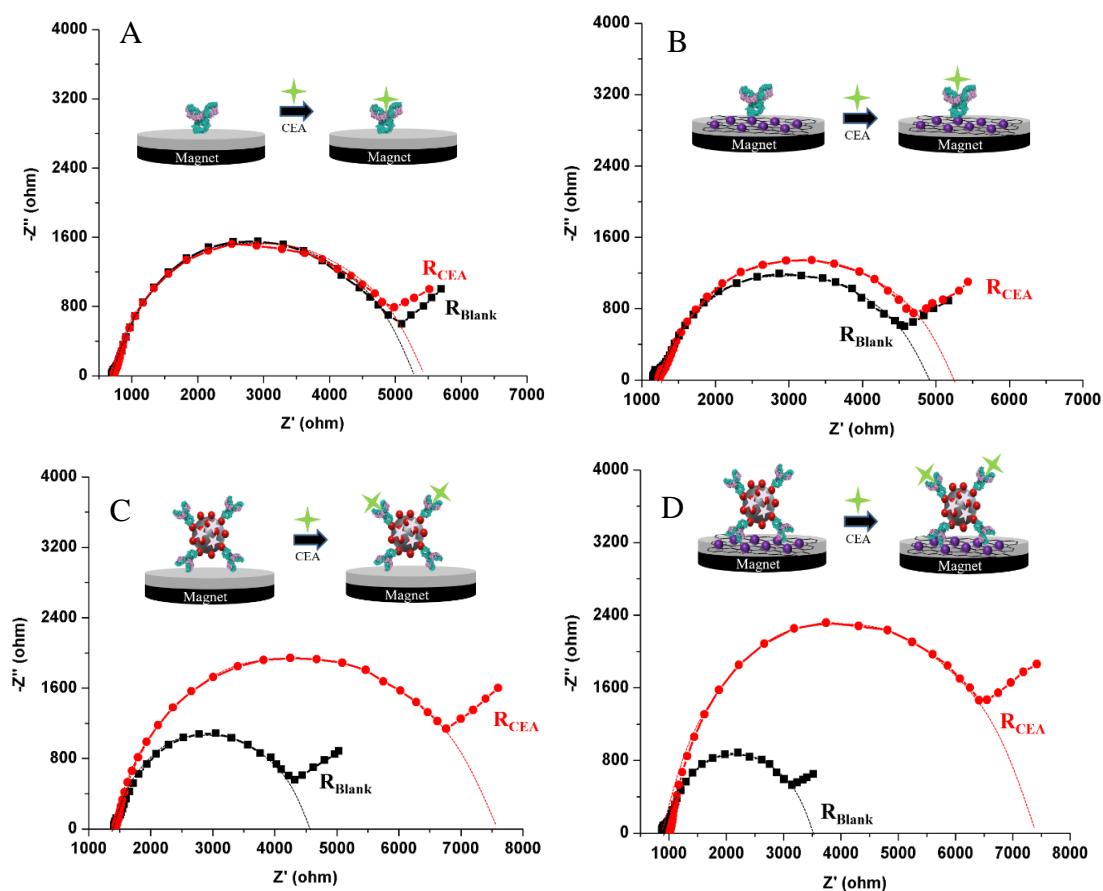


**Figure 4.19** EIS responses on 5 mM  $\text{Fe}(\text{CN})_6^{3-/4-}$  detection of (A) SPCE/anti-CEA, (B) SPCE/GNP-MnO<sub>2</sub>/anti-CEA, (C) SPCE/Fe<sub>3</sub>O<sub>4</sub>@Au/anti-CEA, and (D) SPCE/GNP-MnO<sub>2</sub>/Fe<sub>3</sub>O<sub>4</sub>@Au/anti-CEA in absence (blank line) and presence (red line) of 10 ng/mL CEA

#### 4.2.2.4 The process for biosensor fabrication

The preparation process of each stage during the biosensor fabrication were investigated using both LSV and EIS in phosphate buffer solution (pH 7.4) containing 5 mM  $\text{Fe}(\text{CN})_6^{3-/4-}$  (experiment 3.4.4.4). As can be seen in Figure 4.20, a bare SPCE showed peak current at 0.69 V with the current density of about 0.5 mA.cm<sup>-2</sup> and a  $R_{\text{ct}}$  value of 4.5 kΩ. When the SPCE modified with GNP-MnO<sub>2</sub> nanocomposite, the oxidative peak current is dramatically increased, while the  $R_{\text{ct}}$  value is significantly decreased. This is due to an excellent electrocatalytic activity and a fast electron transfer ability of the nanocomposites. When the modified electrode was immobilized with antibody conjugated Fe<sub>3</sub>O<sub>4</sub>@Au, the peak current decreased slightly



and the  $R_{ct}$  value increased obviously due to a partial insulation of the antibody blocked electron transfer of the redox couple towards the electrode surface. Subsequently, the current signal was reduced and the  $R_{ct}$  value was increased again after the electrode was incubated with CEA. This could be attributed to more insulating effect owing to the immunoreaction between antigen and antibody at the electrode surface. Zhang and et al. [185] presented that the redox peak current increased distinctly after modification with Au nanoparticles compared with bare electrode. But when the antibody, bovine serum albumin, and CEA were coated on the surface of electrode in sequence, the redox peak current decreased orderly because the bioactive substances greatly inhibited the efficiency of electron transfer.

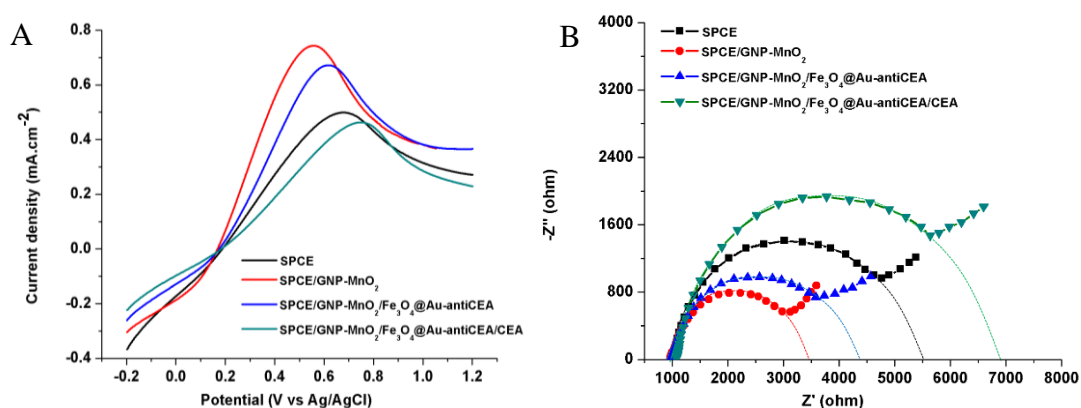


**Figure 4.20 (A) LSV and (B) EIS response of different stages during the biosensor fabrication in 5 mM  $\text{Fe}(\text{CN})_6^{3-/4-}$  and 10 ng/mL CEA**

### 4.2.3 Optimization of the SPCE/GNP-MnO<sub>2</sub>/Fe<sub>3</sub>O<sub>4</sub>@Au/anti-CE

#### 4.2.3.1 Amount of GNP and MnO<sub>2</sub> deposited on GNP

In order to achieve the best optimum conditions for the biosensor fabrication, the amount of GNP on the electrode surface and the amount of MnO<sub>2</sub> deposited on GNP sheet were investigated using LSV and EIS detected in phosphate buffer solution containing 5 mM  $\text{Fe}(\text{CN})_6^{3-/4-}$  (experiment 3.4.5.1). The LSV and EIS signal were analyzed by NOVA program version 1.11, as can be seen in Figure B.2 (Appendix B.2). The relationship between the biosensor response and the GNP loading in a range from 2.5 to 12.5 mg.cm<sup>-2</sup> is displayed in Figure 4.21(A) and Table B.14

(Appendix B.2). An enhancement of the response was observed with increase of the GNP amount from 2.5 to 5.0  $\text{mg}\cdot\text{cm}^{-2}$ , and then the corrected signal was gradually decreased. The reason might be due to the thicker film of the GNP hinder the mass diffusion of redox probe to the electrode surface. Furthermore, Ensafi and co-worker [186] revealed that the peak current was increased with the amount of GNP, but the signal was reduced for a higher concentration of GNP because the GNP film was too thick and the electron transfer between solution and the electrode surface was hindered. Therefore, 5.0  $\text{mg}\cdot\text{cm}^{-2}$  of GNP was chosen as the optimum amount for electrode modification.

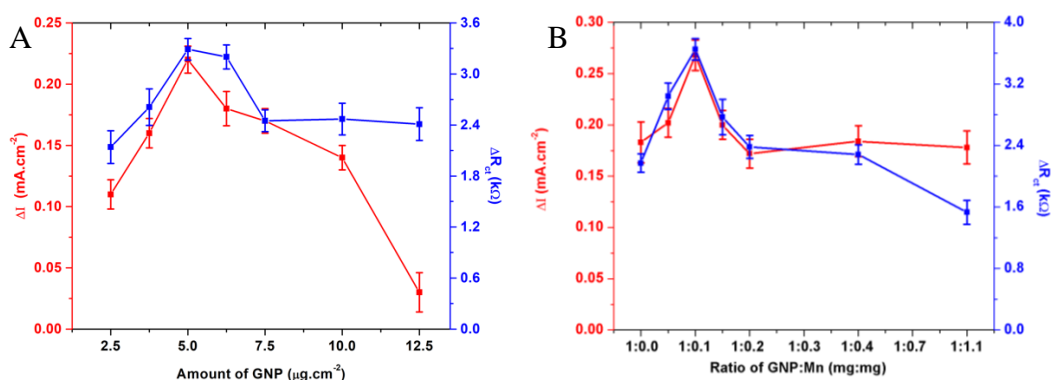


**Figure 4.21** Amount of (A) GNP on the electrode surface and (B) MnO<sub>2</sub> deposited on GNP sheet toward 10 ng/mL CEA detected in 5 mM  $\text{Fe}(\text{CN})_6^{3-/4-}$

The amount MnO<sub>2</sub> decorated on the GNP sheet was further investigated as a form of mass ratios between GNP and Mn atom. As seen in Figure 4.21(B) and Table B.15 (Appendix B.2), the maximum response of the biosensor was achieved with the ratio of GNP:Mn at 1:0.1 (mg:mg), and this ratio was selected for following measurements. The signal increased with the increasing of MnO<sub>2</sub> nanoparticles because a high concentration might be favorable for modification to improve electrocatalytic activity of the biosensor. However, the response of the biosensor started to decrease when the mass ratio was higher than 1:0.1, which may be attributed to non-conductive oxide of MnO<sub>2</sub> partial block the electrical conductivity.

#### 4.2.3.2 Concentration of CEA antibody

Since the antibody concentration is a crucial parameter for the biosensor fabrication, the effect of the antibody loading within the range from 50 to 300  $\mu\text{g/mL}$  on the sensitivity of CEA detection was evaluated by using LSV and EIS in 5 mM  $\text{Fe}(\text{CN})_6^{3-/4-}$  (experiment 3.4.5.2). As showed in Figure 4.22 and Table B.16 (Appendix B.2), the signal response gradually increased with increase of the antibody concentration until reaching 200  $\mu\text{g/mL}$ , and the signal remained almost constant owing to the saturated amount of the antibody on the modified electrode surface. Thus, the CEA antibody of 200  $\mu\text{g/mL}$  was referred as the optimum concentration for the biosensor construction. In addition, Gu and et al. [187] reported that the peak current significantly increased with an increasing antibody concentration until the peak current reached a plateau at 200  $\mu\text{g/mL}$ .

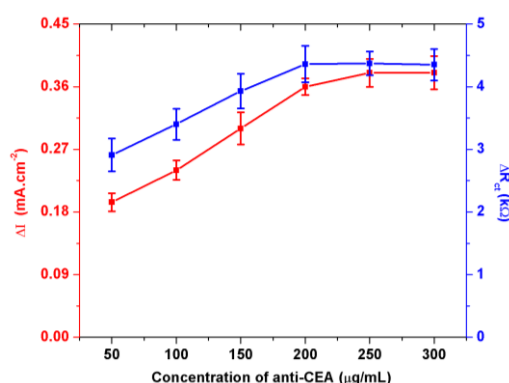


**Figure 4.22 Effect of antibody concentration on the detection of 10 ng/mL CEA**

#### 4.2.3.3 Effect of pH solution and incubation temperature

The pH value plays a crucial role in the performance of the biosensor because highly acidic and alkaline electrolytes could affect the bioactivity of the immobilized antibody and cause the antibody denaturation. Therefore, the effect of pH was optimized using LSV and EIS techniques (experiment 3.4.5.3). Figure 4.23(A) and Table B.17 (Appendix B.2) showed that the highest activity was achieved at pH of 7.4 because it is the normal pH value in human body. Hence, 0.1 M phosphate buffer solution at pH 7.4 was suitable for the CEA measurement. The result is also in great consensus with previously reported electrochemical biosensors. For example, Wang and

et al. [188] revealed that the maximal current response of the electrochemical biosensor developed for detecting CEA based on AgPt nanorings supported on reduced graphene oxide appeared at pH 7.5.

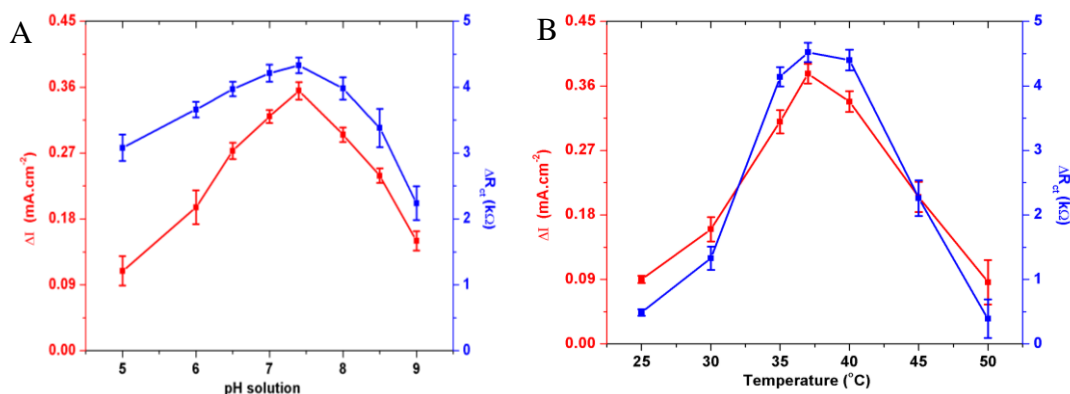


**Figure 4.23** Effect of (A) pH and (B) temperature on detection of 10 ng/mL CEA

The temperature for the incubation is another important factor on the sensitivity of the immunoassay. Thus, the effect of the incubation temperature on the biosensor response was examined from 25°C to 50°C (experiment 3.4.5.3). As observed in Figure 4.23(B) and Table B.18 (Appendix B.2), the biosensor response was rapidly enhanced from 25 to 37°C, and it levelled off after 37°C. This indicates that antigen-antibody complex could be inactivated at lower temperatures and it could be irreversibly denatured at higher temperatures. Moreover, Gao and et al. [125] reported that an optimal temperature of the immunoreaction would be 37°C and higher temperature would be harmful to the biomolecule activity. Thus, the immunoreaction between the CEA antigen and its antibody was controlled at 37°C.

#### 4.2.3.4 Incubation time and reaction time

To enhance the sensitivity of the immunosensor, the incubation time of antibody on the modified electrode surface and the reaction time for formation of the antigen-antibody complex at the electrode interface were further optimized as described in experiment 3.4.5.4. In case of studying incubation time, 5  $\mu$ L of CEA antibody conjugated Fe<sub>3</sub>O<sub>4</sub>@Au was dropped onto the modified electrode surface and then the electrode was incubated in an incubator at 37°C from 30 min to 120 min. The LSV and EIS response of the biosensor increased greatly with increasing of the time and they

were nearly saturated after 120 min, as displayed in Figure 4.24(A) and Table B.19 (Appendix B. 2). The information indicated that CEA antibodies are captured and saturated on the biosensing interface after 120 min. Thus, the optimum incubation time of CEA antibody was 120 min. The similar trend is also observed with various previous reported. For instance, Zhou and et al. [189] presented that biosensor response rapid increased from 60 min to 90 min and reached a plateau when the incubation time was longer than 90 min.

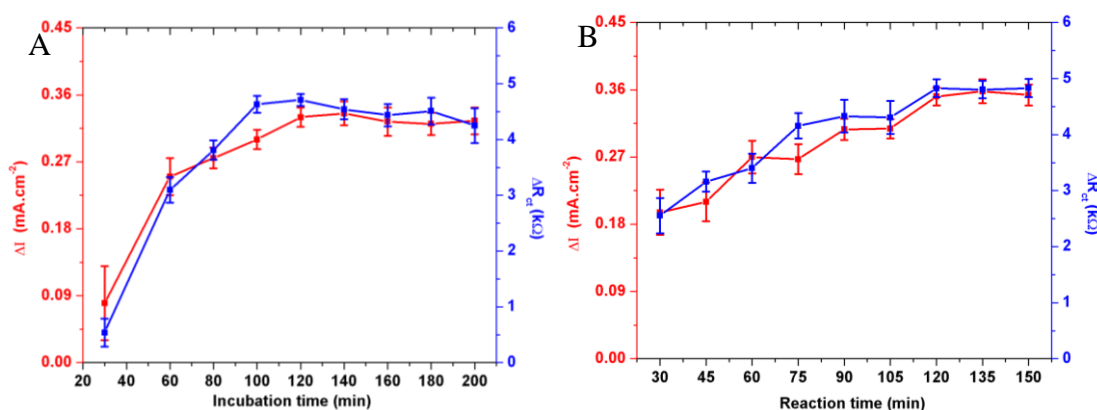


**Figure 4.24 Effect of (A) incubation time and (B) reaction time on the detection of 10 ng/mL CEA**

In case of studying reaction time, 5  $\mu$ L of CEA was incubated on the biosensor surface for different time periods from 30 min to 150 min. As shown in Figure 4.24(B) and Table B.20 (Appendix B. 2), the signal obtained from EIS and LSV techniques increased slowly from 30 min to 120 min and achieved a platform after 120 min. The results indicated that binding of the CEA on the biosensor surface reached to an equilibrium for the immunoreaction between the antigen and its antibody under the reaction time at 120 min. The similar trend was also observed by Yang and et al. [115] who revealed that the inhibition ratio of current response for detecting CEA increased with incubation time and trended to the constant values after 50 min, indicating the saturation capture of CEA on the anti-CEA for the immunoreaction. Therefore, 120 min was referred as the best time for immunoreaction of CEA on the SPCE/GNP-MnO<sub>2</sub>/Fe<sub>3</sub>O<sub>4</sub>@Au/anti-CEA biosensor.

In summary, the optimum conditions for fabrication of the biosensor were as follow:  $5.0 \text{ mg.cm}^{-2}$  of GNP, the amount of  $\text{MnO}_2$  decorated on the GNP sheet calculated as a mass ratio at 1:0.1 (GNP:Mn/mg:mg), and loading of  $200 \text{ }\mu\text{g/mL}$  anti-CEA on the electrode surface. The optimum conditions for CEA detection by the SPCE/GNP- $\text{MnO}_2/\text{Fe}_3\text{O}_4$ @Au/anti-CEA were as follow: pH solution of 7.4, temperature of  $37^\circ\text{C}$ , incubation time for 120 min, and reaction time for 120 min. Under optimum condition, the analytical performances of the biosensor were evaluated and the results are showed in the next part.

#### **4.2.4 Analytical performance of the SPCE/GNP- $\text{MnO}_2/\text{Fe}_3\text{O}_4$ @Au/anti-CEA**

##### **4.2.4.1 Linear range and detection limit on detection of CEA**

The electrochemical biosensor based on SPCE/GNP- $\text{MnO}_2/\text{Fe}_3\text{O}_4$ @Au was applied for determination of CEA at different concentrations under the optimum conditions by using LSV and EIS scanned in  $0.1 \text{ M}$  phosphate buffer solution (pH 7.4) containing  $5 \text{ mM}$  of  $\text{Fe}(\text{CN})_6^{3-/4-}$  (experiment 3.4.6.1). The informative data are showed in Table B.21 (Appendix B. 2). The current signal obtained from LSV measurement decreased linearly with the increase of the CEA concentrations in a range from  $0.001$  to  $100 \text{ ng/mL}$  (Figure 4.25(A)). A linear relationship between the calculated signal and the logarithmic value of the CEA concentration is depicted in Figure 4.25(B). For EIS measurement, the impedimetric signal increased gradually with increase of the CEA concentration (Figure 4.25(C)), which provided a good linear calibration plot for CEA determination in a range from  $0.001$  to  $100 \text{ ng/mL}$ , as presented in Figure 4.25(D). As the CEA concentration increased, a large amount of CEA are specifically captured with the antibodies immobilized on the electrode surface. As a result, the LSV peak current is reduced, while the EIS response is enhanced in proportion to the concentration of CEA.

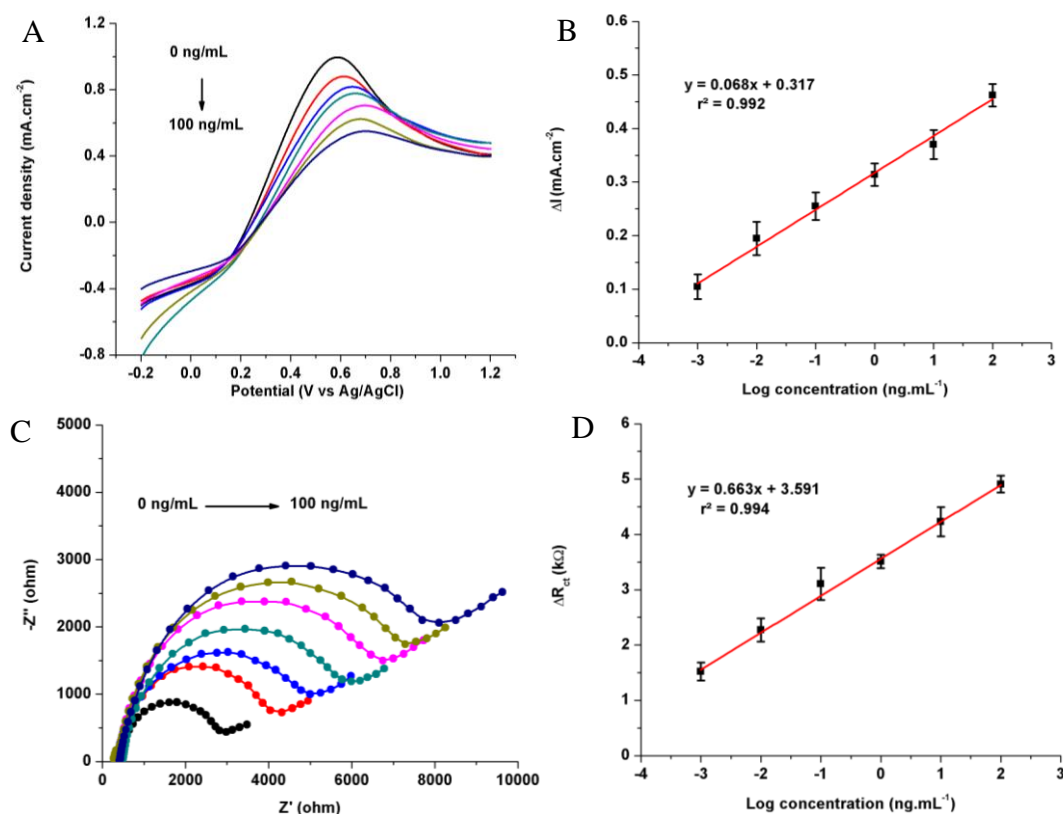


**Figure 4.25** (A) LSV and (B) its calibration plot; (C) EIS response and (D) its calibration plot for CEA detection using 5 mM  $\text{Fe(CN)}_6^{3-/4-}$ .

The limit of detection (LOD), which is the concentration derived from the lowest signal response, was calculated based on the definition revealed by the international union of pure and applied chemistry (IUPAC). [27, 190] The lowest signals were obtained by measuring blank, phosphate buffer solution instead of CEA, for 10 repetitions ( $n=10$ ) using LSV and EIS, as shown in Table B.22 (Appendix B.2). Then, the LOD was calculated and the proposed electrochemical biosensor achieved a LOD of 0.10 pg/mL and that of 0.30 pg/mL for LSV and EIS measurements, respectively. In comparison to other published electrochemical biosensors (Table 2.5), the proposed biosensor based on SPCE/GNP- $\text{MnO}_2/\text{Fe}_3\text{O}_4/\text{Au}$  exhibited a wider linear range and a lower detection limit than that of poly(3,4-ethylenedioxythiophene)/AuNPs [115] chitosan/Pd-Ir [118] AuNPs/thionine/  $\text{MoS}_2$  [121]  $\text{TiO}_2$  microparticles/chitosan/AuNPs [123] rGO/Nile blue/AuNPs [125] sulfonated graphene/thionine/chitosan/nanotubular mesoporous PdCu [126] and amino functional graphene/thionine/AuNPs. [127] In

addition, LOD of the proposed biosensor was also lower than various commercial CEA ELISA kits, such as 0.38 ng/mL for BioVision Inc. (Human, E4740-100); 37.5 pg/mL for BioVision Inc. (Mouse, E4741-100); 0.1 ng/mL for BioVision Inc. (Rat, E4742-100); 0.2 ng/mL for Sigma-Aldrich (RAB0411); 0.2 ng/mL for RayBiotech Inc. (P06731); 1.0 ng/mL for Diagnostic Automation Inc. (5201-16). Therefore, it can be suggested that GNP-MnO<sub>2</sub>/Fe<sub>3</sub>O<sub>4</sub>@Au nanocomposite is an excellent candidate for construction of the electrochemical biosensor for ultrasensitive detection of CEA biomarker.

#### 4.2.4.2 Reproducibility and repeatability of the biosensor

The repeatability of the immunoassays based on SPCE/GNP-MnO<sub>2</sub>/Fe<sub>3</sub>O<sub>4</sub>@Au and the reproducibility of that biosensor were evaluated by LSV and EIS (experiment 3.4.6.2). According to the calculation of the signal toward CEA at 1 ng/mL as depicted in Table B.23 (Appendix B.2), the relative standard deviation (RSD) value of the five repeated immunoassays (n=5) was in a range of 2.3-3.3% and that of the five different biosensors (n=5) was less than 5.0%, indicating that the developed biosensor had great repeatability and reproducibility.

#### 4.2.4.3 Stability of the SPCE/GNP-MnO<sub>2</sub>/Fe<sub>3</sub>O<sub>4</sub>@Au/anti-CEA

Stability of the SPCE/GNP-MnO<sub>2</sub>/Fe<sub>3</sub>O<sub>4</sub>@Au/anti-CEA was tested by LSV and EIS methods and the biosensor was kept in a refrigerator at 4°C when not in use (experiment 3.4.6.3). As displayed in Figure 4.26 and Table B.24 (Appendix B.2), the measured responses are maintained at more than 80% of the original value after storage for a week, indicating that the fabricated biosensor is acceptable for long-term stability even using potable SPCE as a transducer.



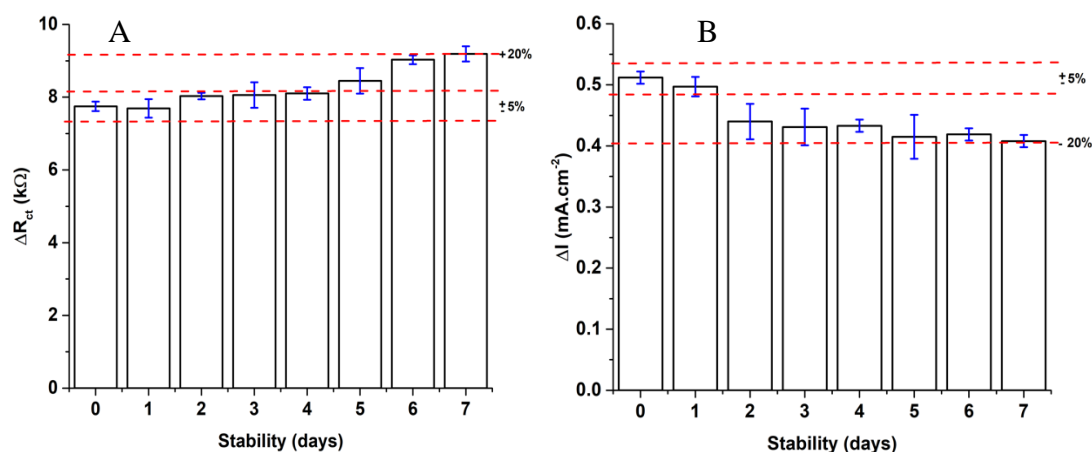


**Figure 4.26** Stability of the SPCE/GNP-MnO<sub>2</sub>/Fe<sub>3</sub>O<sub>4</sub>@Au biosensor obtained on 1 ng/mL CEA detection by (A) LSV and (B) EIS

#### 4.2.4.4 Selectivity of the SPCE/GNP-MnO<sub>2</sub>/Fe<sub>3</sub>O<sub>4</sub>@Au/anti-CEA

Specificity is one of the potential advantages of using biological molecules as a recognition element. The possible interfering substances, including prostate-specific antigen (PSA), human serum albumin (HSA), human immunoglobulin (IgG), bovine serum albumin (BSA), cholesterol, glucose, sucrose, cysteine, ascorbic acid, and uric acid were tested at a 500-fold higher concentration than CEA in order to evaluate selectivity of the biosensor. Moreover, these interferences were also mixed with 1 ng/mL CEA and the selectivity is tested by the LSV and EIS techniques (experiment 3.4.6.4). As shown in Figure 4.27 and Table B.25 (Appendix B.2), the electrochemical signals obtained from individual interfering substances are almost the same with blank signal, and the response observed with the target CEA is evidently higher than that of interferences. Moreover, when CEA coexisted with these interfering agents, no apparent signal change took place in comparison with that of only CEA. Thus, it can be suggested that the established electrochemical biosensor based on SPCE/GNP-MnO<sub>2</sub>/Fe<sub>3</sub>O<sub>4</sub>@Au/anti-CEA possessed high selectivity and it could be applied for practical analysis of CEA in real complex samples.

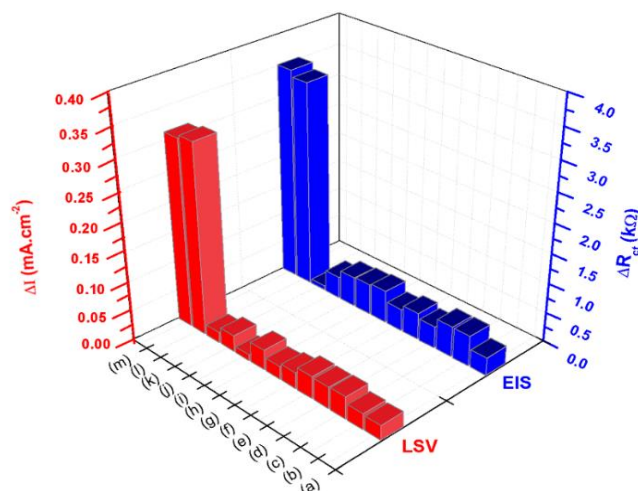


**Figure 4.27** Selectivity of the biosensor for (a) blank, (b) PSA, (c) HSA, (d) IgG, (e) BSA, (f) cholesterol, (g) glucose, (h) sucrose, (i) cysteine, (j) ascorbic acid, (k) uric acid (l) mixed interferences with CEA, and (m) CEA (500 ng/mL interferences and 1 ng/mL CEA)

#### 4.2.5 Results of CEA determination in human serum samples

In order to investigate the applicability of the electrochemical biosensor for CEA detection, a recovery test compared with an available electrochemiluminescence (ECL) immunoassay were conducted. The serum samples were diluted to 10 and 100 times with phosphate buffer solution (pH 7.4) and different amounts of CEA (0, 1, 10, and 50 ng/mL) were subsequently fortified into each sample dilution (experiment 3.4.7). The concentrations of CEA in the prepared samples were analyzed by LSV and EIS methods and continuously calculated by substituting the signal values into the above calibration curve (Figure 4.25). As summarized in Table 4.2, the electrochemical biosensor presented the recovery in a range from 90.4 to 109.8% with the RSD varying in a range of 1.7% to 9.5%. The data is demonstrated in Table B.26 (Appendix B.2). Furthermore, the CEA content in the diluted human serum samples were also tested by the ECL immunoassay in which the results were obtained from the National Cancer Institute, Thailand. The relative error between the two methods were less than 12%, indicating that the designed biosensor is well fitted to the ECL method. Thus, it can be concluded that the SPCE/GNP-MnO<sub>2</sub>/Fe<sub>3</sub>O<sub>4</sub>@Au/anti-CEA has a satisfactory potential for detection of CEA in real serum samples



**Table 4.2 Detection of CEA in diluted human serum samples by the electrochemical biosensor (n = 3) in comparison with that by the ECL immunoassay (n = 3)**

Serum dilutions	Added (ng/mL)	Electrochemical biosensor						ECL immunoassay		
		LSV			EIS			Detected (%)	RSD (%)	Recovery (%)
		Detected (ng/mL)	RSD (%)	Recovery (%)	Detected (ng/mL)	RSD (%)	Recovery (%)			
10×	0	n.d. <sup>a</sup>	-	-	n.d.	-	-	n.d.	-	-
	1	1.03 ± 0.10	9.5	103.0	1.05 ± 0.09	8.6	105.0	0.94 ± 0.03	3.1	94.0
	10	10.42 ± 0.45	4.3	104.2	10.26 ± 0.33	3.2	102.6	9.51 ± 0.04	0.1	95.1
	50	53.70 ± 2.53	4.7	107.4	54.9 ± 1.30	2.3	109.8	51.6 ± 0.20	0.1	103.2
100×	0	n.d.	-	-	n.d.	-	-	n.d.	-	-
	1	0.90 ± 0.08	8.9	90.4	0.91 ± 0.06	6.5	91.4	0.92 ± 0.03	3.2	92.0
	10	10.69 ± 0.31	2.9	106.9	10.47 ± 0.18	1.7	104.7	9.71 ± 0.04	0.1	97.1
	50	46.77 ± 2.23	4.8	93.5	47.86 ± 1.36	2.8	95.7	51.1 ± 0.23	0.1	102.2

<sup>a</sup> n.d. means “not detectable”



### **4.3 Carbon composite nanomaterials-based biosensor: electrochemical biosensor for glyphosate detection**

Glyphosate, a kind of organophosphates herbicide, is one of the extensively used herbicides in agricultural situations worldwide. The contamination of glyphosate in agricultural products and environments could lead to negative indirect health effects due to it is classified as probably carcinogenic to humans. Therefore, electrochemical biosensor was developed for glyphosate determination in environmental applications. The biosensor was fabricated based on screen-printed carbon electrode (SPCE) modified with reduced graphene oxide (rGO) and silver nanoparticles (AgNPs). The rGO and AgNPs are employed to improve sensitivity, electrocatalytic activity and electron transfer ability of the electrode due to glyphosate cannot be detected by a direct electrochemical biosensor. [135] Therefore, an indirect detection of glyphosate based on enzyme inhibition assay was fabricated by using acid phosphatase (ACP) as a receptor due to it selectively catalyze the hydrolysis of phosphate containing molecules. The ACP was chemically immobilized on the surface of SPCE/rGO-AgNPs via glutaraldehyde cross-linking. The current signal owing to the enzymatic reaction of ACP and its substrate, disodium phenyl phosphate, was measured by chronoamperometry. The decrease in signal owing to inhibition of ACP activity in the presence of glyphosate is quantitative proportional to glyphosate concentration. The biosensor was applied for determination of glyphosate in water and soil samples. The physical characterization and electrochemical characterization of the biosensor were firstly investigated. Continuously, conditions for electrode preparation and parameters affecting the measurement were evaluated. Next, enzyme kinetic and inhibition mechanism were also evaluated. Finally, analytical performances and applications of the SPCE/rGO-AgNPs for indirect detection of glyphosate in real samples were tested, in comparison to high performance liquid chromatography (HPLC) as a reference method.

#### **4.3.1 Characterization results of the SPCE/rGO-AgNPs biosensor**

##### **4.3.1.1 XRD of the SPCE/rGO-AgNPs**

The crystalline nature of the SPCE/rGO-ANPs was confirmed by X-ray diffraction (XRD) analysis (experiment 3.5.3.1). The XRD patterns of the bare SPCE and SPCE modified with rGO, AgNPs, and rGO-AgNPs were compared, as

showed in Figure 4.28. The SPCE exhibits a sharp diffraction peak at  $2\theta = 26.5^\circ$ , corresponding to the (002) plane of the typical crystal structure of graphite. [191] There is no significant different in XRD pattern after the SPCE was modified with rGO because the diffraction peak of rGO is also located at  $2\theta = 26.5^\circ$ . The result is in full agreement with the previous works. Oghli and co-worker [192] revealed that the XRD spectrum of GO showed a strong peak at  $2\theta = 11.0^\circ$ , whereas this peak was disappeared and a diffraction peak at  $25.0^\circ$  was instead observed in the XRD spectrum of rGO, which is the characteristic peak of rGO resulting from the reduction of GO. For electrode modified with AgNPs and rGO-AgNPs, the prominent peaks located at  $2\theta$  of  $38.2^\circ$ ,  $44.4^\circ$ ,  $66.6^\circ$ , and  $78.5^\circ$  are related to (111), (200), (220), and (311) planes of face centered cubic (FCC) crystalline silver (JCPDS No. 04-0783). Moreover, Satyanarayana and et al. [193] reported that XRD pattern of AgNPs were observed at  $38.2^\circ$ ,  $44.4^\circ$ ,  $64.6^\circ$ ,  $77.5^\circ$  and  $81.8^\circ$ , representing to the (111), (200), (220), (311) and (222) crystallographic planes of silver, respectively.

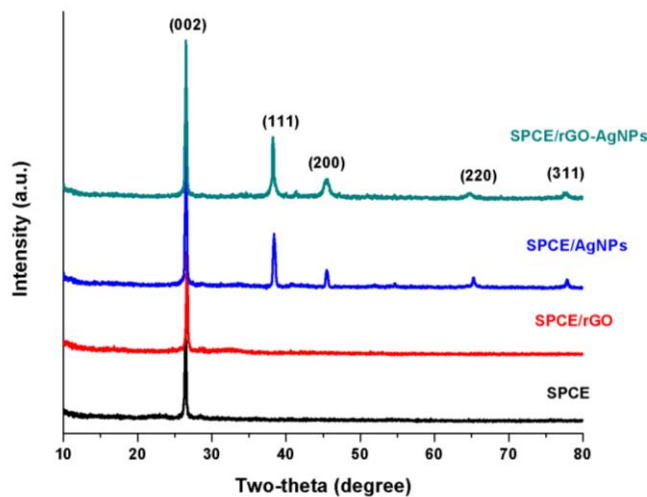


**Figure 4.28 XRD pattern of the different modified electrodes**

#### 4.3.1.2 Raman spectra of the SPCE/rGO-AgNPs

Raman spectroscopy is a well-known and very common technique for the analysis of carbon-based nanomaterials. Therefore, modifications on the SPCE surface with rGO-AgNPs composites was evaluated by Raman compared to a bare SPCE, SPCE/GO, and SPCE/rGO (experiment 3.5.3.2). The observed peaks at 1351

$\text{cm}^{-1}$  and  $1588 \text{ cm}^{-1}$  are known as D and G bands, which are related to  $\text{sp}^3$  and  $\text{sp}^2$  in-plane vibrations of graphene materials. The ratio of the D and G peaks intensities ( $I_D/I_G$ ) are widely used to estimate the degree of defect and graphitization in the bonded carbon structure. [194, 195] As can be seen in Figure 4.29, the modification of the SPCE with GO led to a decrease in the  $I_D/I_G$  ratio from 1.00 to 0.86 due to the GO contributed to increase in the number of  $\text{sp}^2$  bonds. On the other hand, the ratio of  $I_D/I_G$  increased to 1.35 and 1.10 in rGO and rGO-AgNPs, respectively. This indicates that more defects and disorders in the graphitized structures are formed and the  $\text{sp}^2$  bonds are reduced because of the decreasing of C=O bonds during the reduction process of the GO. The results indicated that GO had been successfully deoxygenated and reduced by electrochemical method. Moreover, the  $I_D/I_G$  ratio were found to be smaller for the SPCE/rGO-AgNPs compared to the SPCE/rGO, indicating that the AgNPs covered the rGO films. The results are in good accordance with the results reported by Wan and et al. [196] They found that the intensity ratio of D band to G band is 0.88 in GO, and the intensity ratio is 1 after the electrochemical reduction.

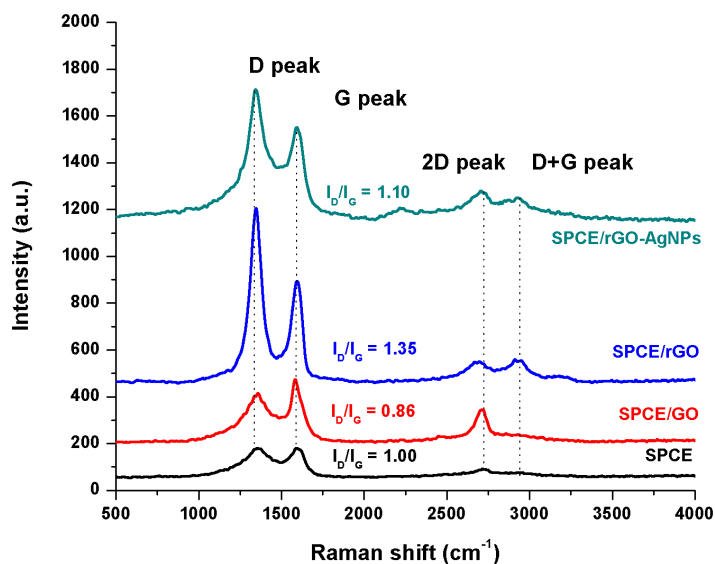


**Figure 4.29** Raman spectra of the different modified electrodes

Furthermore, another Raman feature at around  $2700 \text{ cm}^{-1}$  was observed, which is known as the secondary D peak named 2D band. Depending on its shape, the 2D band was usually used to determine the number of layers of graphene.



[197] The ratio intensities between 2D and G ( $I_{2D}/I_G$ ) of the rGO was less than 0.8, indicating a few layers of rGO covered on the electrode surface due to the  $\pi-\pi$  interaction.

#### 4.3.1.3 EDS analysis of the SPCE/rGO-AgNPs

The elemental compositions of the SPCE/rGO-AgNPs were characterized by energy dispersive spectroscopy (EDS) as described in experimental section 3.5.3.3. Figure 4.30(A) shows the characteristic peaks of C, O, and Ag corresponding to the elements of the nanomaterials and Cl associating to the KCl electrolyte solution used in the electrochemical reduction process. The result confirms the existing of rGO-AgNPs composite on the SPCE surface. Figure 4.30(B) displays the corresponding elemental mapping images for the SPCE/rGO-AgNPs. The blue, green, yellow, and red color images are associated with the Ag, O, Cl, and C elements, respectively. This indicates that the elements are uniformly distributed on the electrode surface in random form.

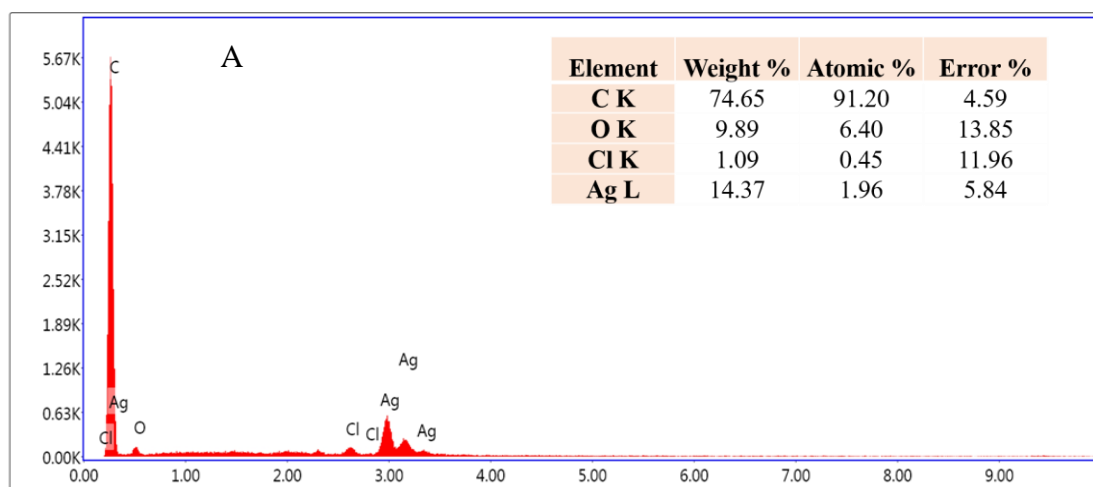


**Figure 4.30** EDS (A) spectrum and (B) mapping of the SPCE/rGO-AgNPs

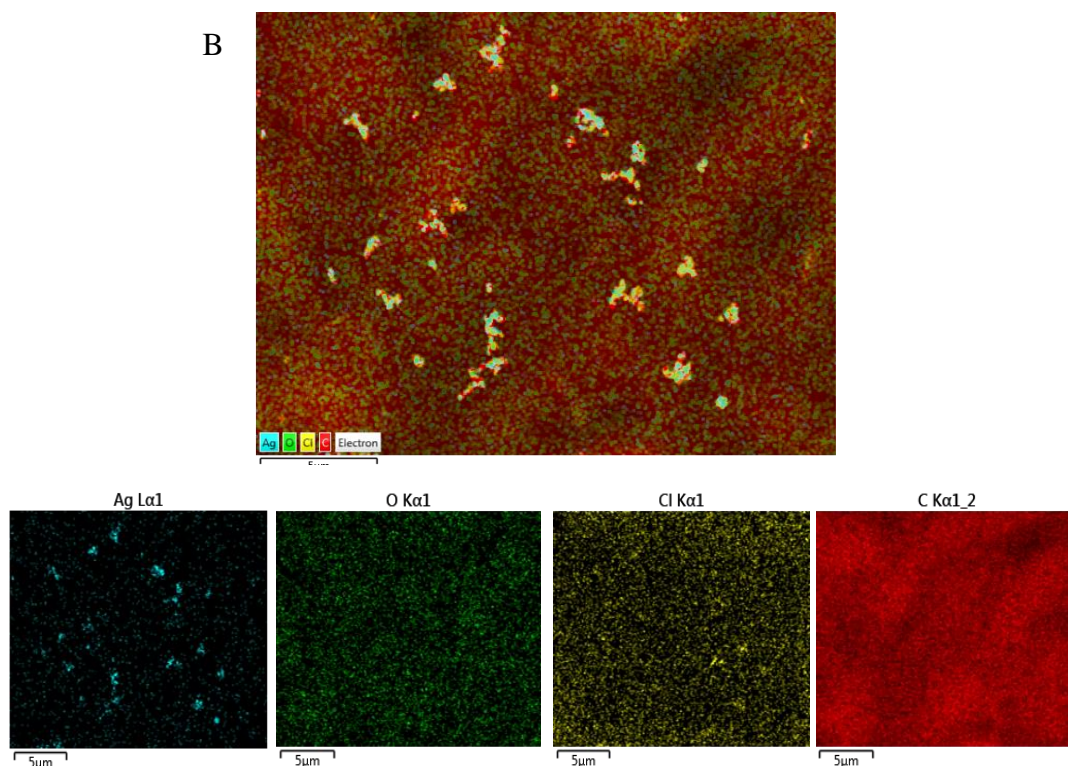


**Figure 4.30 EDS (A) spectrum and (B) mapping of the SPCE/rGO-AgNPs (continued)**

#### 4.3.1.4 SEM of the SPCE/rGO-AgNPs

The surface morphologies of the different modified electrodes were analyzed by scanning electron microscope (SEM) (experiment 3.5.3.4). As shown in Figure 4.31. The surface of SPCE were consisted of flake like structures of carbon. A thin wrinkling sheet-like stacked layers structure was observed after GO is electrochemically reduced and covered on the electrode surface. A globular structure of AgNPs with an average diameter about 150 nm was appeared after AgNPs was electrochemically deposited. Moreover, Sharma and et al. [198] reported that a wrinkled surface due to electrodeposition of GO and a spherical structure of AgNPs were observed on the electrode modified with rGO-AgNPs composite. After immobilization of ACP enzyme, the changes on morphology of the modified electrode was noticeably observed, which is the evidence of successful enzyme immobilization.

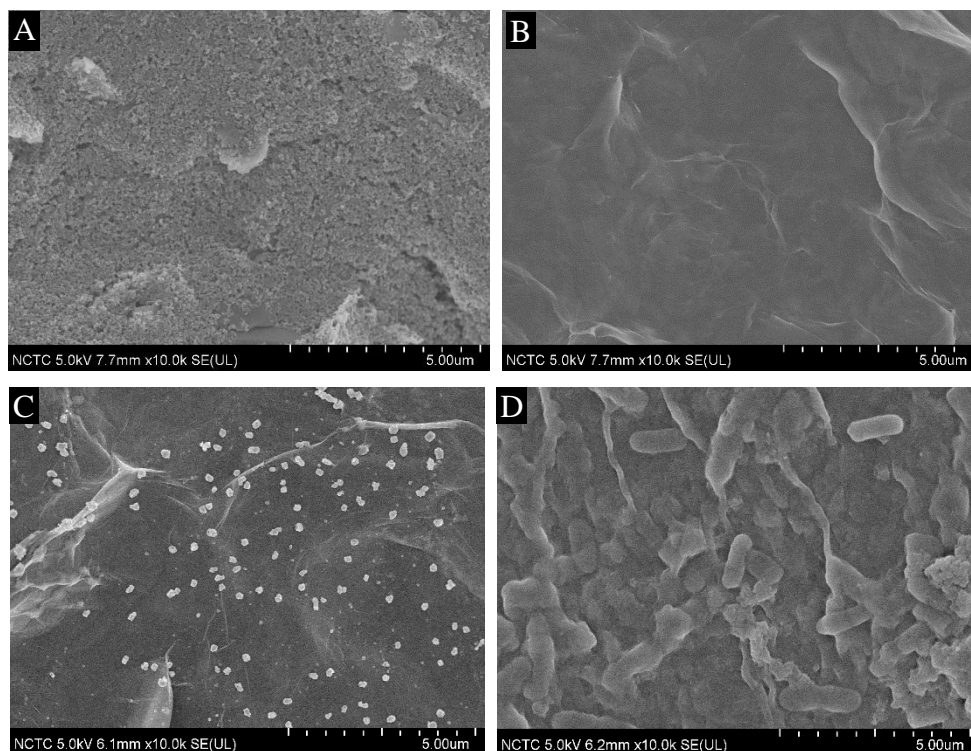


**Figure 4.31 SEM of (A) SPCE, (B) SPCE/rGO, (C) SPCE/rGO-AgNPs, and (D) SPCE/rGO-AgNPs/ACP at a magnification of 10,000x**

### 4.3.2 Electrochemical characterization results of the enzymatic biosensor

#### 4.3.2.1 CV and EIS of the SPCE/rGO-AgNPs

The cyclic voltammetry (CV) and electrochemical impedance spectroscopy (EIS) measurements were performed to investigate characteristic properties of the modified electrode in 5 mM  $\text{Fe}(\text{CN})_6^{3-/4-}$  (experiment 3.5.4.1). Figure 4.32(A) displays the CV of unmodified and modified SPCE with AgNPs, rGO and rGO-AgNPs. A pair of well defined quasi-reversible one-electron redox peaks of  $\text{Fe}(\text{CN})_6^{3-/4-}$  was observed on the bare SPCE. After the electrode had been modified with AgNPs or rGO, the current signal increased and the peak to peak separation ( $\Delta E_p$ ) decreased compared to the bare SPCE, indicating that AgNPs and rGO enhanced electrical conductivity and possessed electron-transfer properties of the SPCE. In the presence of both nanomaterials, a well-defined and highest enhanced redox peaks was obtained, which could be attributed to the synergistic effects from AgNPs and rGO. Moreover, Jin and et al. [199] also reported that the peak current intensity of rGO-AgNPs modified electrode was higher than that of rGO modified electrode and

unmodified electrode due to synergist effects from rGO and AgNPs to promote conductivity, and to increase surface areas for electron transfer.

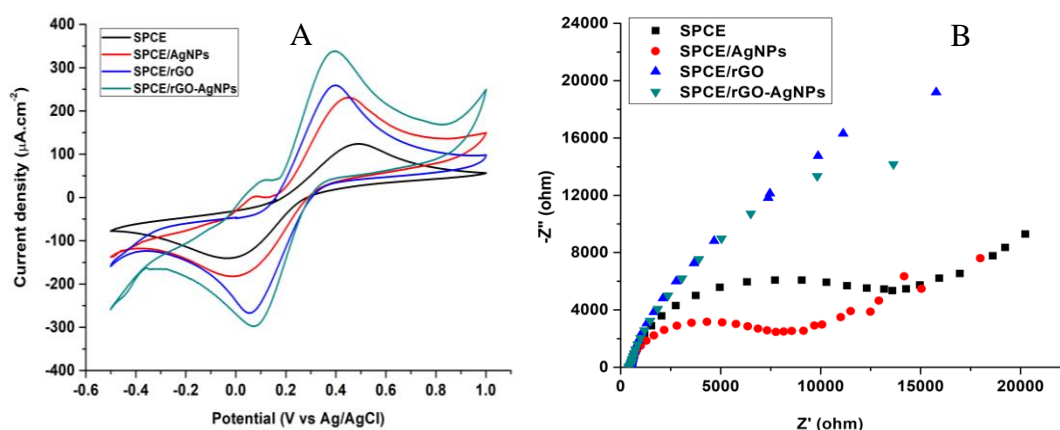


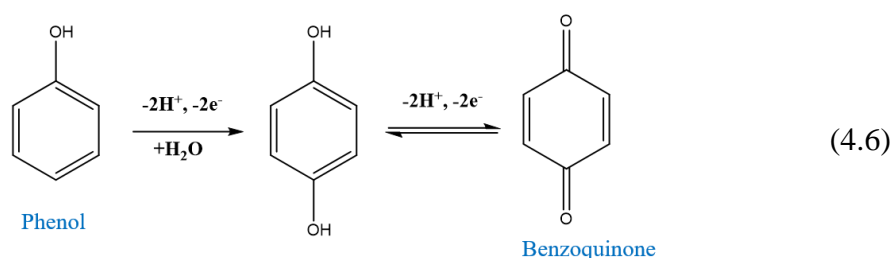
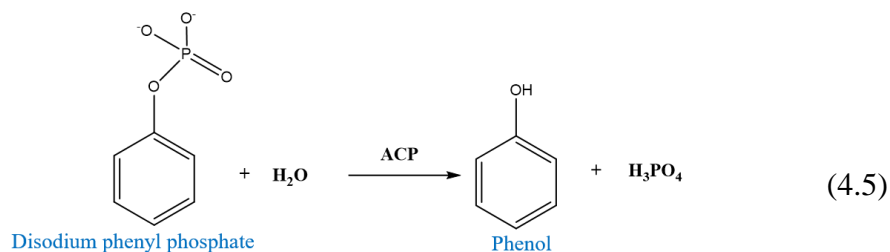
**Figure 4.32 (A) CV and (B) EIS of different electrodes in 1 mM  $\text{Fe}(\text{CN})_6^{3-/4-}$**

For further characterization, the SPCE/rGO-AgNPs was investigated by EIS (Figure 4.32(B)). After modification of the electrode with AgNPs, a decrease electron transfer impedance was observed compared with the bare SPCE, indicating that AgNPs could promote electron transfer between the electrochemical probe and the electrode surface. The impedance was dramatically decreased with the rGO modified electrode, owing to good electrical conductivity and fast electron transfer ability of the rGO films. By combining with the advantages of AgNPs and rGO, the lowest impedance was obtained suggesting that the rGO-AgNPs composites are facile for the electrode modification. Li and et al. [107] also revealed that the charge transfer resistance is obviously decreased after modification of the electrode with rGO-AgNPs nanocomposite.

#### 4.3.2.2 CV of the SPCE/rGO-AgNPs in phenol solution

The SPCE/rGO-AgNPs was applied for fabrication of the enzymatic biosensor for indirect detection of glyphosate herbicide based on inhibition measurement. Acid phosphatase (ACP) was used as an enzyme bioreceptor and disodium phenyl phosphate was employed as an enzyme substrate. In principle, ACP enzyme converts disodium phenyl phosphate substrate into phosphoric acid and phenol (Equation 4.5). The obtained phenol product is irreversibly oxidized to benzoquinone

(Equation 4.6) at a potential higher than 0.75 V (versus Ag/AgCl) by electrochemical methods. As a result, the oxidation peak can be measured, which is directly proportional to the enzyme substrate concentration.



To evaluate electrochemical performance of the SPCE/rGO-AgNPs for further fabrication of the enzymatic biosensor, the signal responses of the different electrodes were studied in 5 mg/L phenol solution by CV method (experiment 3.5.4.2). Figure 4.33(A) shows CV of the bare SPCE and SPCE modified with rGO, AgNPs, and rGO-AgNPs composite in buffer solution with absence and presence of phenol. It can be seen that no oxidation peak was observed in the absence of phenol, while a small oxidation peak at 0.76 V with current response of  $5.32 \mu\text{A}.\text{cm}^{-2}$  was occurred on the bare SPCE, as shown in Figure 4.33(B). This result confirms that the obtained signal is due to oxidation reaction of phenol. In the case of SPCE/rGO, the peak current is slightly increased in comparison to the bare and AgNPs modified SPCE. In addition, a shift in the peak potential to less positive potential is significantly noticed. The reason probably due to rGO sheet enhanced electrocatalytic behavior and electron transport for phenol oxidation. The highest signal response is found when both modifiers are presented at the electrode surface, indicating that the rGO-AgNPs nanocomposites can effectively catalyze the electrochemical oxidation of phenol due to its outstanding electrocatalytic activity, high electrical conductivity and very good electron transfer activity owing to

synergistic activity of the rGO and AgNPs. Sharma and et al. [198] also found that the electrode modified with rGO-AgNPs exhibited the maximum response for the electrochemical detection of amikacin. Zheng and et al. [200] reported that a much larger reduction peak current towards  $\text{H}_2\text{O}_2$  detection and a clear lowering shift of a peak potential were observed at the rGO-AgNPs modified glassy carbon electrode.

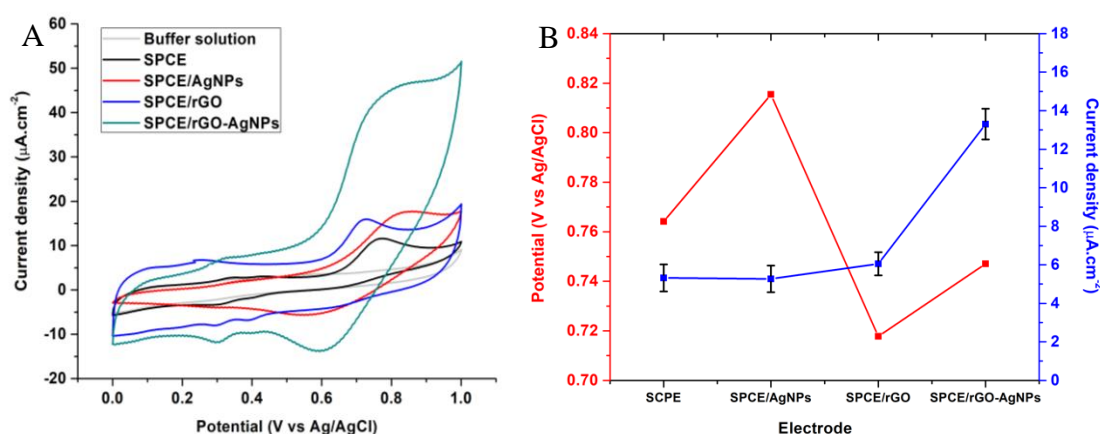


**Figure 4.33 (A) CV of different modified electrodes in buffer solution with absence and presence of 5 mg/L phenol and (B) its corresponding results**

#### 4.3.2.3 CV of the SPCE/rGO-AgNPs at different scan rate

In order to better understand the electrochemical process on the responses of SPCE/rGO-AgNPs, CV was further applied to investigate a possible kinetic mechanism with different scan rates of 0.01 to 0.10 V/s in 1 mM  $\text{Fe}(\text{CN})_6^{3-/4-}$  (experiment 3.5.4.3). The redox peak currents increased accordingly with the increase of scan rate (Figure 4.34(A)). The linear relationships of peak currents dependence on the square root of scan rates was established with two linear regression equations, as can be seen in Figure 4.34(B). According to Randles-Sevcik equation (Equation 4.2), this indicated that the kinetic reaction of  $\text{Fe}(\text{CN})_6^{3-/4-}$  probe on the surface of the SPCE/rGO-AgNPs is a diffusion-controlled process. In addition, the kinetic process for the oxidation of phenol at the SPCE/rGO-AgNPs was investigated with different scan rates of 0.002-0.020 V/s (Figure 4.34(C)). The anodic current density is also increased linearly with the square root of scan rate (Figure 4.34(D)). Therefore, it can be concluded that the



electrochemical behavior of the SPCE/rGO-AgNPs is a typical diffusion-controlled process. Moreover, this behavior was also reported by Jamil and co-worker. [201]

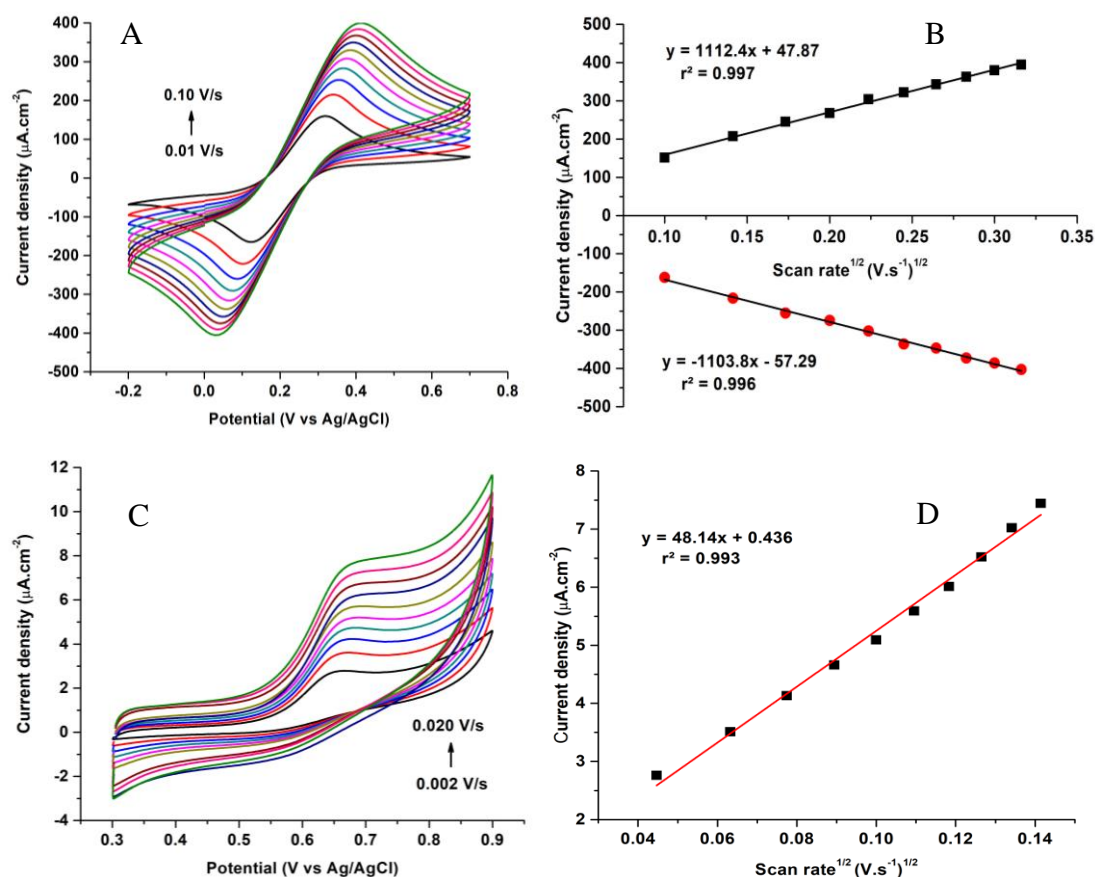


**Figure 4.34** (A) CV at different scan rates on the SPCE/rGO-AgNPs in 1 mM  $\text{Fe(CN)}_6^{3-/4-}$  and (B) its corresponding result; (C) CV at different scan rates in 5 mg/L phenol solution and (D) its corresponding data

#### 4.3.2.4 CV of the SPCE/rGO-AgNPs/ACP biosensor

The SPCE/rGO-AgNPs/ACP biosensor was applied for indirect detection of glyphosate herbicide based on enzyme inhibition. Therefore, the inhibition effect of glyphosate on ACP activity was evaluated by CV (experiment 3.5.4.4). Figure 4.35 describes the CV of SPCE/rGO-AgNPs/ACP in 0.1 M acetate buffer solution (pH 7.0) before (black line) and after introducing 10 g/L disodium phenyl phosphate without (red line) and with 50 mg/L glyphosate herbicide (blue line). No peak is observed when the biosensor was placed in buffer solution. On the other hand, in the presence of

disodium phenyl phosphate, an irreversible oxidation peak at 0.62 V was observed. Obviously, this peak occurred from the oxidation of phenol, product from catalytic reaction of the immobilized ACP enzyme on disodium phenyl phosphate substrate. This anodic peak current is proportional to the activity of ACP and concentration of disodium phenyl phosphate. The mechanism is already described in Equation 4.5 and 4.6. However, in the presence of glyphosate, the anodic peak current is decreased due to the decrease of phenol product resulted from the inhibition of ACP activity by the herbicide. The decreased current response is related to the inhibitory effect of glyphosate on the ACP activity and proportional to its concentration. This result evidences that ACP enzyme can be used as a bioreceptor for glyphosate detection based on enzyme inhibition. Moreover, Mazzei and et al. [202] presented an amperometric enzymatic biosensor for the determination of organophosphorus pesticide based on the reversible inhibition of ACP. Additionally, the electrochemical biosensor for the determination of organophosphorus pesticides by enzyme inhibition of alkaline phosphatase was reported by Mazzei and et al. [203]

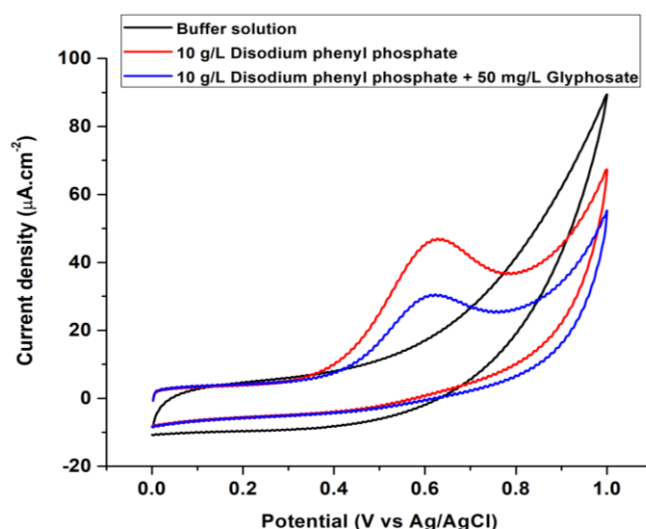


**Figure 4.35 CV of the SPCE/rGO-AgNPs/ACP for determination of inhibition effect of glyphosate on ACP activity**



### 4.3.3 Optimization of the SPCE/rGO-AgNPs/ACP

#### 4.3.3.1 Effect of potential apply

The operating potential is a crucial parameter that directly affects the sensitivity, detection limit and stability of the biosensor in hydrodynamic amperometry. Therefore, the influence of applied potential on the amperometric detection of glyphosate based on enzyme inhibition was investigated using the SPCE/rGO-AgNPs/ACP in 0.1 M acetate buffer solution containing 10 g/L disodium phenyl phosphate as enzyme substrate (experiment 3.5.5.1). The current signals obtained by chronoamperometry were analyzed by NOVA program version 1.11, as can be seen in Figure B.3 (Appendix B.3). A high steady-state current owing to catalytic reaction of the immobilized ACP enzyme on disodium phenyl phosphate substrate is recorded as  $I_0$ . Then, the decreased current response owing to inhibition of ACP activity by the glyphosate herbicide is recorded as  $I_1$ . The inhibited response was determined using the peak heights before and after introduction of glyphosate ( $\Delta I = I_0 - I_1$ ) and then the graph relationship between the  $\Delta I$  and applied potential was plotted as illustrated in Figure 4.36 (Table B.27, Appendix B. 3). When applied potential more than +0.2 V, the inhibited signals gradually increased with the increasing of potential because of rapidly oxidation of phenol at higher potential. However, +0.4 V was selected for further studies in order to avoid some chemical species expected to be present in samples are oxidized at such a high potential. [204]

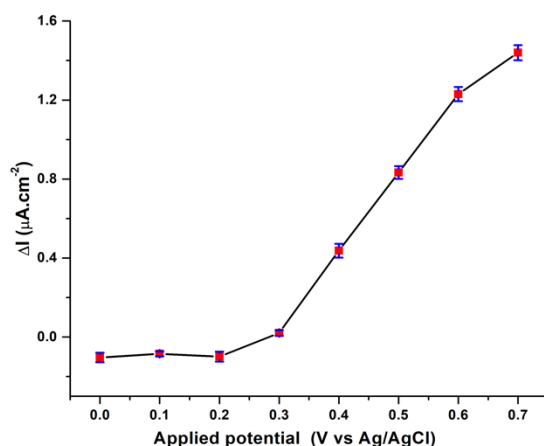


**Figure 4.36** Effect of potential on the detection of 0.2 mg/mL glyphosate

#### 4.3.3.2 Effect of amount of rGO and AgNPs

The parameters influence on the fabrication of the enzymatic biosensor, including amount of rGO and AgNPs on the electrode surface are investigated sequentially (experiment 3.5.5.2). The amount of rGO deposited on the SPCE was investigated from 0.0 to 12.5  $\mu\text{g.cm}^{-2}$ . The biosensor response increased continuously from 0.0 to 5.0  $\mu\text{g.cm}^{-2}$ , and then decreased afterward, as shown in Figure 4.37(A) and Table B.28 (Appendix B.3). The decrease of the signal response with higher loadings implies that a thick film of rGO partly block the active electrode surface and hinder the diffusion of electrochemically active substance to the electrode surface. Therefore, 5.0  $\mu\text{g.cm}^{-2}$  of rGO was chosen as the optimum amount for electrode modification. Moreover, da Silva and et al. [205] also reported that an increase of the rGO materials could block the electron-transfer process through the interface between electrode and electrolyte, resulting in decreasing the signal response.

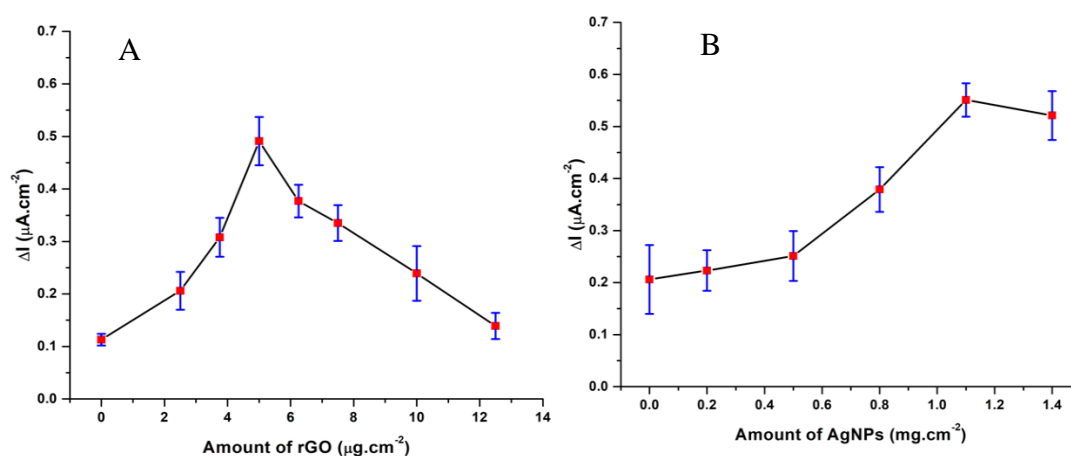


**Figure 4.37** Effect of amount of (A) rGO and (B) AgNPs deposited on the SPCE on the detection of 0.2 mg/mL glyphosate

Besides, the amount of AgNPs deposited on the rGO film was investigated from 0.0 to 1.4  $\text{mg.cm}^{-2}$ . As seen in Figure 4.37(B) and Table B.29 (Appendix B.3), the response increased gradually from 0.0 to 1.1  $\text{mg.cm}^{-2}$ , whereas it decreased slightly beyond. The enhanced response is mainly attributed to an improved electrocatalytic performance of the AgNPs. However, excessive nanoparticles could cause a strong aggregation of AgNPs on the electrode surface. As a result, an accessible

active surface area for the appropriated diffusion of analytes are limited and consequently reduced electrocatalytic activity. Therefore,  $1.1 \text{ mg.cm}^{-2}$  of AgNPs was deposited on the rGO film for electrode modification. Additionally, Satyanarayana and et al. [193] studied amount of AgNPs for preparing biosensor and they found that the current intensity increased with increasing AgNPs amount, and significantly decreased with further increasing the AgNPs.

#### 4.3.3.3 Amount of ACP and concentration of enzyme substrate

Since the enzyme concentration is an important factor for the biosensor fabrication, the effect of the ACP loading within the range from 0.00 to  $0.18 \text{ unit.cm}^{-2}$  on the sensitivity of the SPCE/rGO-AgNPs/ACP biosensor for indirect detection of glyphosate was evaluated (experiment 3.5.5.3). As showed in Figure 4.38(A) and Table B.30 (Appendix B.3), the signal response increased sharply with increase of the ACP concentration until reaching  $0.09 \text{ unit.cm}^{-2}$ , and then the signal remains almost constant owing to the saturated amount of the enzyme on the modified electrode surface. Thus, the ACP of  $0.15 \text{ unit.cm}^{-2}$  was referred as the optimum concentration of ACP for the enzymatic biosensor construction. The result is similar to the research of Jiang and et al. [206] who found that the response current of the biosensor was increased with the increase of enzyme loading, and then remained stable with the enzyme loading increased.

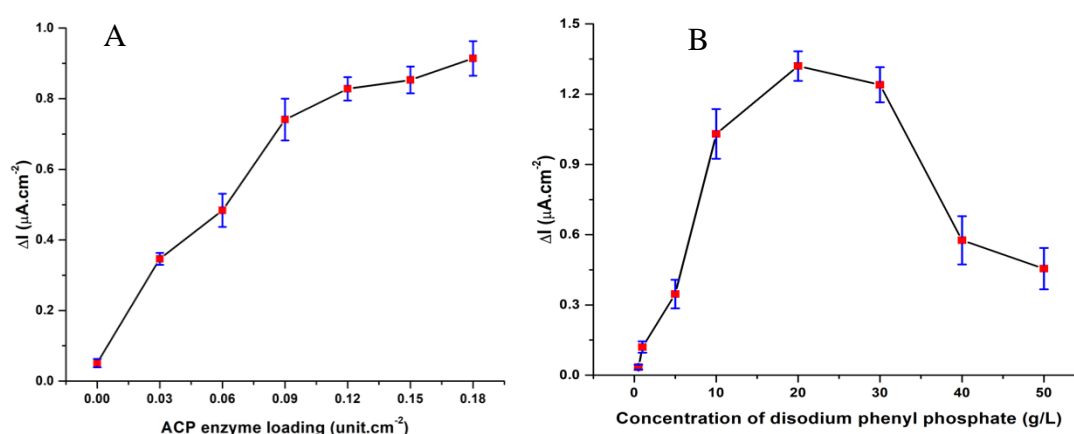


**Figure 4.38** Effect of (A) ACP enzyme loading and (B) concentration of disodium phenyl phosphate on the detection of 0.2 mg/mL glyphosate

The concentration of enzyme substrate is another important factor related to the performance of the biosensor. To enhance the sensitivity of the biosensor, the concentration of disodium phenyl phosphate was optimized (experiment 3.5.5.3). Figure 4.38(B) and Table B.31 (Appendix B.3) display the plot of the inhibited response of the SPCE/rGO-AgNPs/ACP versus the disodium phenyl phosphate concentrations. With the increasing of substrate concentration, the response increased dramatically and reached the maximal value at 20 g/L. This could be attributed to more catalytic reaction between enzyme and its substrate would be occurred and more phenol product would be generated. As a result, the beginning signal current was largely obtained and accordingly lead to increase in the apparent inhibited signal. However, with the increasing of substrate concentration, the response was gradually decreased. This might be due to the substrate would compete with glyphosate to occupy the active site of enzyme. Thus, 20 g/L of disodium phenyl phosphate was selected for indirect detection of glyphosate. This observation is similar to research of Song and co-worker [207] who reported that the response of the biosensor increased with the increasing of enzyme substrate and then declined afterward.

#### 4.3.3.4 Effect of pH solution on the detection of glyphosate

As the bioactivity of enzyme and biosensor sensitivity are greatly depended on the pH value of buffer solution and extreme pH conditions cause enzyme denaturation, pH of acetate buffer solution was studied over the range from 3.0-8.0 (experiment 3.5.5.4). As shown in Figure 4.39 and Table B.32 (Appendix B.3), the highest activity was achieved at pH of 7.0. This value is the normal pH in human body and higher acidity or basicity resulted in the loss of activity. [129] Hence, the acetate buffer at pH 7.0 is suitable for the indirect enzymatic measurement. As reported, the optimum pH values for ACP was in a low-pH environment (4.0-7.0) and the optimal ability for catalytic hydrolysis of ACP was also observed at pH of 6.2 by Qu and et al. [208]

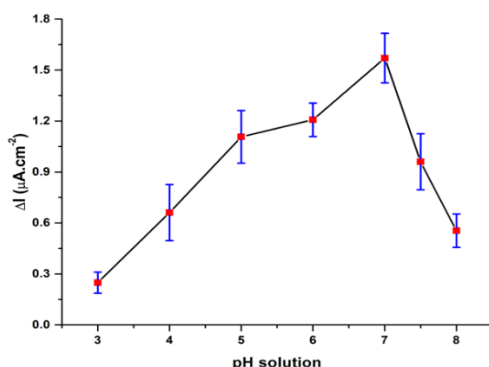


**Figure 4.39** Effect of pH value on the detection of 0.2 mg/mL glyphosate

In summary, the optimum conditions for fabrication of the enzymatic biosensor and indirect detection of glyphosate was as follow: applied potential of 0.4 V,  $5.0 \mu g.cm^{-2}$  of rGO and  $1.1 mg.cm^{-2}$  of AgNPs modified on the electrode surface,  $0.15 unit.cm^{-2}$  ACP enzyme loading, 20 g/L of disodium phenyl phosphate as enzyme substrate, and pH solution of 7.0. Under optimum condition, the enzyme kinetics and analytical performances of the biosensor were evaluated and the results are discussed in the next part.

#### 4.3.4 Enzyme kinetics

To study the kinetics of enzyme and type of inhibition, the response of the biosensor to various concentrations of disodium phenyl phosphate (50 to 500 mg/L) was investigated by chronoamperometry under optimum conditions (experiment 3.5.6). The typical amperometric current-time response for the SPCE/rGO-AgNPs/ACP biosensor in absence and presence of 1 mg/L glyphosate were illustrated in Figure 4.40(A) and (B), respectively. In the absence of glyphosate, the biosensor exhibited a rapid and sensitive oxidation current with the addition of disodium phenyl phosphate. Meanwhile, lower current values were recorded in the presence of glyphosate. Based on these results, Lineweaver-Burk plot for the enzymatic reaction was plotted between  $1/I$  versus  $1/C$ , as shown in Figure 4.40(C). The apparent kinetic constants ( $K_m$  and  $V_{max}$ ) were then calculated by fitting a linear function and analyzing the slope and intercept in the Lineweaver-Burk plot, as described in section 2.3.2 (Chapter 2). From the data in Table B.33 (Appendix B.3), the values of  $K_m$  and  $I_{max}$  in case of without glyphosate were calculated to be 3.79 mM and  $7.46 \mu A.cm^{-2}$ , respectively. The low  $K_m$  value proved that

the SPCE/rGO-AgNPs/ACP biosensor exhibited a high affinity for disodium phenyl phosphate. Moreover, the obtained  $K_m$  value is close to the value (3.5 mM) reported by Zhang and et al. [209] In the presence of glyphosate, the  $K_m$  and  $I_{max}$  values were calculated to be 4.72 mM and 7.63  $\mu A.cm^{-2}$ , respectively. This observation shows that the inhibition by glyphosate increase in the  $K_m$  value, whilst the  $I_{max}$  value remained almost the same with or without glyphosate. Therefore, it could be concluded that the inhibition of ACP enzyme by glyphosate is a reversible competitive type. As described in section 2.3.3 (Chapter 2), the reversible competitive inhibition increases  $K_m$  but does not change  $I_{max}$  because the inhibitor is close resemblance to substrate structure and it can competitively bind to active site of enzyme. Furthermore, Sanllorente-Méndez and et al. [210] also reported that the kind of inhibitory effect of As(V) ions on the response of the acid phosphatase biosensors was the competitive inhibition process.

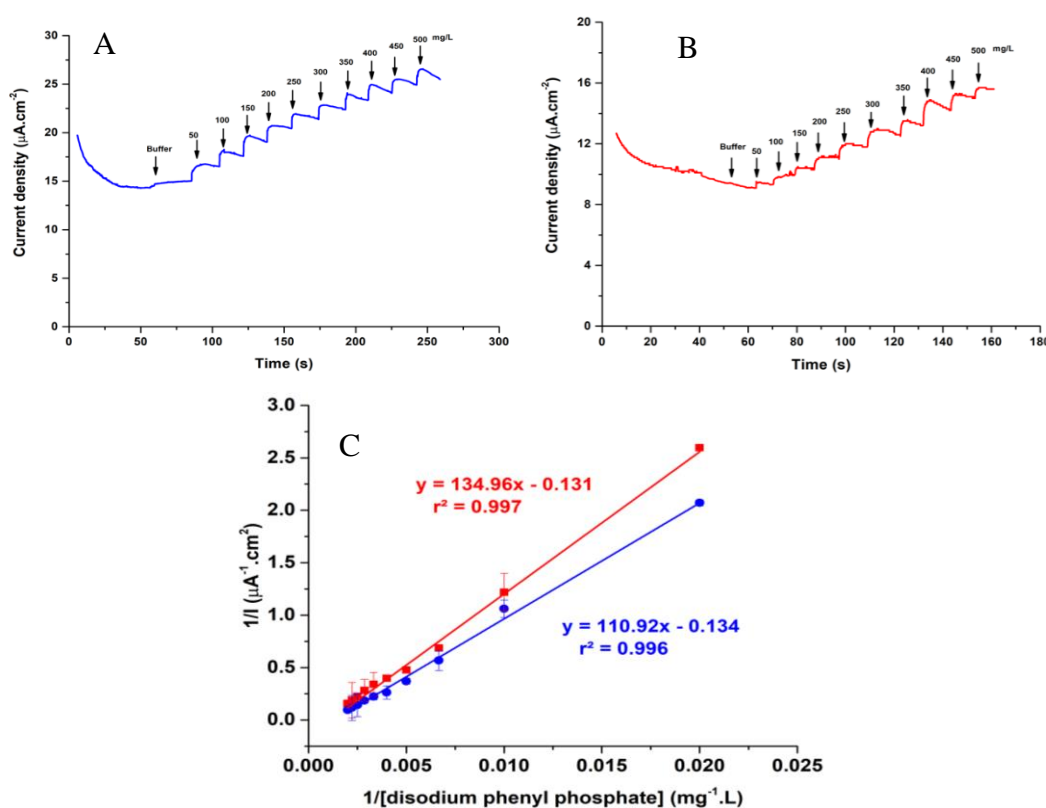


**Figure 4.40** Amperometric response of the SPCE/rGO-AgNPs/ACP to successive injections of 50-500 mg/L disodium phenyl phosphate in acetate buffer (pH 7.0) in the (A) absence and (B) presence of 1 mg/L glyphosate, and (C) its corresponding Lineweaver Burk plots

### 4.3.5 Interaction of enzyme-substrate and enzyme-glyphosate complexes

The structures of modelled substrates, including disodium phenyl phosphate and glyphosate, bound in the ACP enzyme structure were studied for better understanding the accommodation of these two substrates in the catalytic site of the enzyme. Therefore, the two compounds were docked into the active site of the ACP enzyme from red kidney bean (PDB code 4KBP) by *AutoDock Vina* [211] (experiment 3.5.7). There are not any previous reports revealing the X-ray structure of ACP from wheat germ, specifically. Thereafter, the crystal structure from red kidney bean (PDB entry 4KBP) has been representatively studied in this work since the ACP from wheat and red kidney bean are both classified in the same group of ACP family. [212] Figure 4.41(A) revealed that the X-ray structures of ACP from red kidney bean comprises of two sandwiched  $\beta\alpha\beta\alpha\beta$  motifs which form the core unit of metal coordinating. The dimeric protein containing Fe(III) and Zn(II) complexed is presumably represented the catalytic site in wheat germ in this study. [213, 214] Docking study of phenyl phosphate into the X-ray structure of ACP is showed in Figure 4.41(B). It is found that one oxygen atom of phosphate group is assumingly in covalent bonding distance to Zn ion (2.3 Å). Two oxygen atoms of phosphate form hydrogen bond with His202 and His296 with the distances of 2.9 Å and 2.8 Å, respectively. The side chain of His296 is in hydrogen bonding distance of 3.2 Å with an esterified oxygen atom proposed as the leaving group for the hydrolysis of enzyme. The selected conformation of phenyl phosphate had a binding free energy of -4.7 kcal/mol.

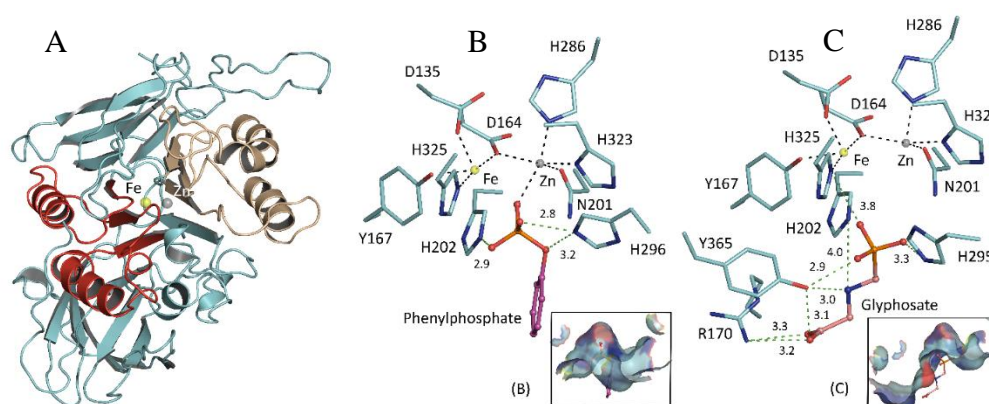


**Figure 4.41 (A) The overall structure of ACP from red kidney bean (PDB entry 4KBP) (B) Phenyl phosphate docked and (C) Glyphosate docked**

From the docking studies of glyphosate (Figure 4.41(C)), three oxygen atoms of phosphate group assumingly form hydrogen bond with His295, His325 and Tyr365 with the distances of 3.3 Å, 3.8 Å and 2.9 Å, respectively. Nitrogen atom of glyphosate is in hydrogen bonding distance (4.0 Å) with the side chain of His202 and the distance of 3.0 Å with the side chain of Tyr365. Moreover, two carboxylate groups assumingly form hydrogen bonds with side chain of Arg170 (3.2 Å and 3.3 Å). Importantly, one carboxylate of bound glyphosate orients to form hydrogen bond with the distance of 3.1 Å with Tyr365 located in the active site of enzyme. Moreover, the selected conformation of glyphosate yields a binding free energy of -4.9 kcal/mol, which is lower than the value of phenyl phosphate. Therefore, this result confirms that glyphosate is capable of interaction with the active site of ACP and it is able to inhibit the ACP activity efficiently in the presence of phenyl phosphate.

#### **4.3.6 Analytical performance of the SPCE/rGO-AgNPs/ACP**

##### **4.3.6.1 Linear range, LOD and LOQ of the SPCE/rGO-AgNPs/ACP**

The performance of the SPCE/rGO-AgNPs/ACP biosensor for indirect determination of glyphosate herbicide was studied by chronoamperometry under optimum conditions (experiment 3.5.8.1). As shown in Figure 4.42(A) and Table B.34 (Appendix B.3), the amperometric current-time curve of the biosensor is successively reduced in series with the adding glyphosate at different concentrations. This is resulted from the decrease in enzyme activity caused by the reversible binding between the herbicide and the active sites of the ACP enzyme. The calibration plot (Figure 4.42(B)) showed that the inhibited signals increased linearly with the glyphosate concentration in which two linear ranges were obtained from 0.05 to 0.5 mg/L (Figure 4.42(C)) and 0.5 to 22.0 mg/L (Figure 4.42(D)). The detection limit (LOD) and quantification limit (LOQ) were calculated on a basis of 3SD/slope and 10SD/slope, according to Equation 4.3 and 4.4, respectively. Where SD is standard deviation of glyphosate detected at the lowest concentration of the linear range and slope was obtained from the calibration curve. As can be seen in Table B.35 (Appendix B.3), the SD for glyphosate detection at 0.05 mg/L is 0.041. Thus, the LOD and LOQ were calculated to be 16 µg/L and 55 µg/L, respectively.



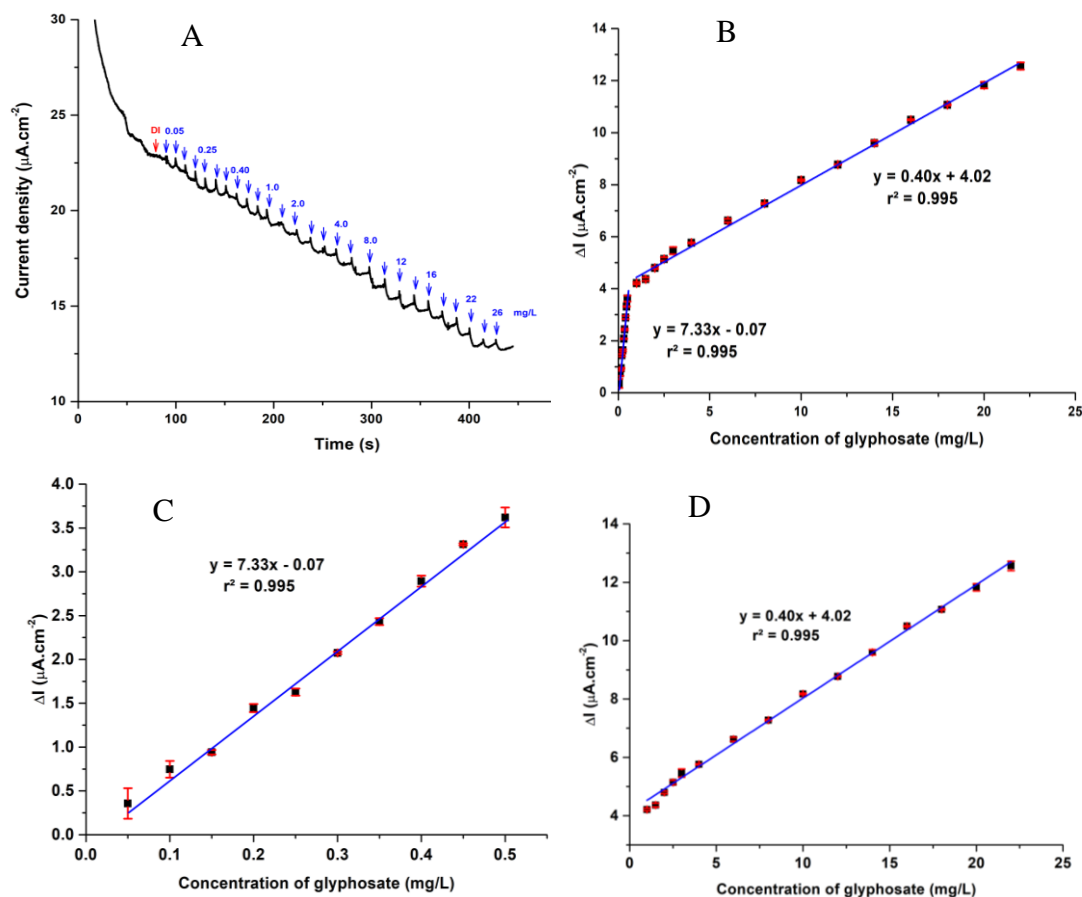


**Figure 4.42 (A) Amperometric response of the biosensor for glyphosate detection under optimum conditions and (B) its calibration plots. Linear range from (C) 0.05 to 0.5 mg/L and (D) 0.5 to 22.0 mg/L**

The LOD of the proposed biosensor is below a maximum contaminant level of glyphosate in drinking water (0.7 mg/L) and soil (2 mg/kg) set by the U.S. national primary. [94] The LOD is also lower than MRLs of glyphosate in crops (0.1-5.0 mg/kg) listed by the United Nations Food and Agricultural Organization. Furthermore, the SPCE/rGO-AgNPs/ACP possessed higher sensitivity than the developed sensor based on nanoclay modified APTES-ODA/MWCNTs and atemoya peroxidase [133] (Table 2.6).

#### 4.3.6.2 Reproducibility of the SPCE/rGO-AgNPs/ACP

Reproducibility is important parameter to evaluate the performance of the enzymatic biosensor. Thus, the intra-day and inter-days reproducibility of the SPCE/rGO-AgNPs/ACP were evaluated by using five different electrodes (n=5) for

detection of 0.2 mg/L glyphosate under optimum conditions (experiment 3.5.8.2). As shown in Table B.36 (Appendix B.3), the relative standard deviation (RSD) was found to be 5.21% and 5.46% for intra-day and inter-days tests, respectively. These results indicated a satisfactory reproducibility of the SPCE/rGO-AgNPs/ACP biosensor.

#### 4.3.6.3 Stability of the SPCE/rGO-AgNPs/ACP

To investigate stability of the biosensor, the amperometric responses of the biosensor for detection of 0.2 mg/L glyphosate were recorded for 5 consecutive days (experiment 3.5.8.3). When the biosensor was not in use, it was stored at 4 °C in a refrigerator. In the first 5 days storage, the signal response of the SPCE/rGO-AgNPs/ACP remained more than 81.9% of its initial signal (Figure 4.43 and Table B.37 (Appendix B.3)). After a week of storage, the rapidly decrease in signals were observed, which could be resulted from the reduction of enzyme activity and denaturation of ACP during the long-time storage. [206]

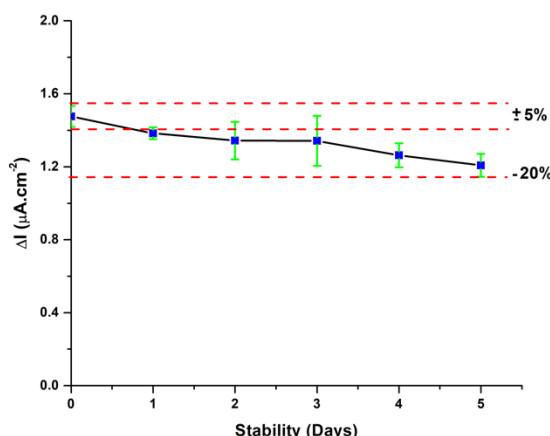


**Figure 4.43** Stability of the SPCE/rGO-AgNPs/ACP on glyphosate detection

#### 4.3.6.4 Selectivity of the SPCE/rGO-AgNPs/ACP

In order to demonstrate the selectivity of the SPCE/rGO-AgNPs/ACP, amperometric experiments were carried out with 0.1 M acetate buffer solution (pH 7.0) containing 20 g/L disodium phenyl phosphate toward the detection of 0.2 mg/L glyphosate without and with the interfering species (experiment 3.5.8.4). Firstly, polyethoxylated tallow amine (POEA), an original formulation of glyphosate herbicide, and glycine which is a precursor for glyphosate production, were examined

at a concentration of 0.2 mg/L. In addition, other categories of pesticides, such as organophosphorus (chlorpyrifos), organochlorine (paraquat) and carbamate (carbaryl, carbendazim) pesticides, were also investigated at a same concentration level. As displayed in Figure 4.44 and Table B.38 (Appendix B.3), no apparent change in the inhibited response was observed with the co-existence of those compounds in glyphosate solution compared to the signal of pure glyphosate. Therefore, it can be concluded that POEA, glycine, chlorpyrifos, paraquat, carbaryl, and carbendazim did not interfere glyphosate detection at the same concentration level. Apart from that, common inorganic ions normally found in environmental samples, such as  $\text{Mg}^{2+}$ ,  $\text{Zn}^{2+}$ ,  $\text{PO}_4^{2-}$ ,  $\text{SO}_4^{2-}$ ,  $\text{CO}_3^{2-}$ ,  $\text{NO}_3^-$ ,  $\text{Cl}^-$ ,  $\text{K}^+$ ,  $\text{Na}^+$ ,  $\text{Ca}^{2+}$ ,  $\text{Cu}^{2+}$ , and  $\text{Cd}^{2+}$ , were also evaluated. The results revealed that almost negligible changes in the signals were detected among the presence of 0.2 mg/L of  $\text{Mg}^{2+}$  and  $\text{Zn}^{2+}$ ,  $\text{PO}_4^{2-}$  and  $\text{SO}_4^{2-}$  at a concentration 10-fold higher, and 100-fold concentration of  $\text{CO}_3^{2-}$ ,  $\text{NO}_3^-$ ,  $\text{Cl}^-$ ,  $\text{K}^+$ ,  $\text{Na}^+$ ,  $\text{Ca}^{2+}$ ,  $\text{Cu}^{2+}$ , and  $\text{Cd}^{2+}$ . To summary, the inhibition of ACP by glyphosate co-existed in all those interferences had changed less than  $\pm 5\%$  over the standard response of glyphosate. Therefore, it can be proposed that the SPCE/rGO-AgNPs/ACP exhibited acceptable selectivity towards glyphosate detection.

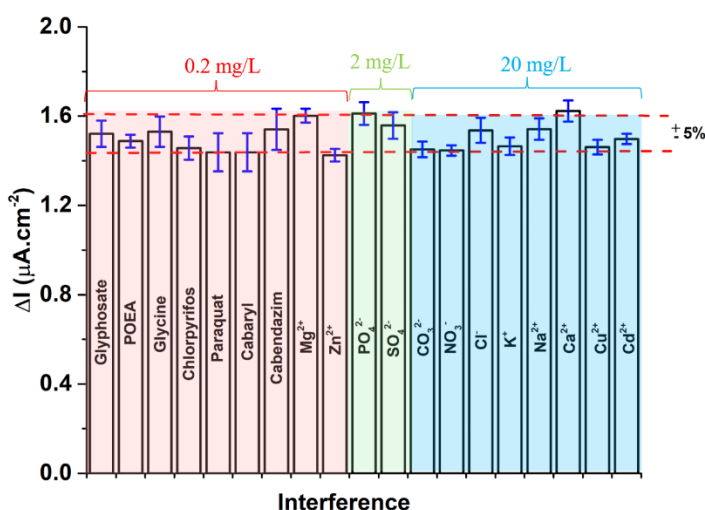


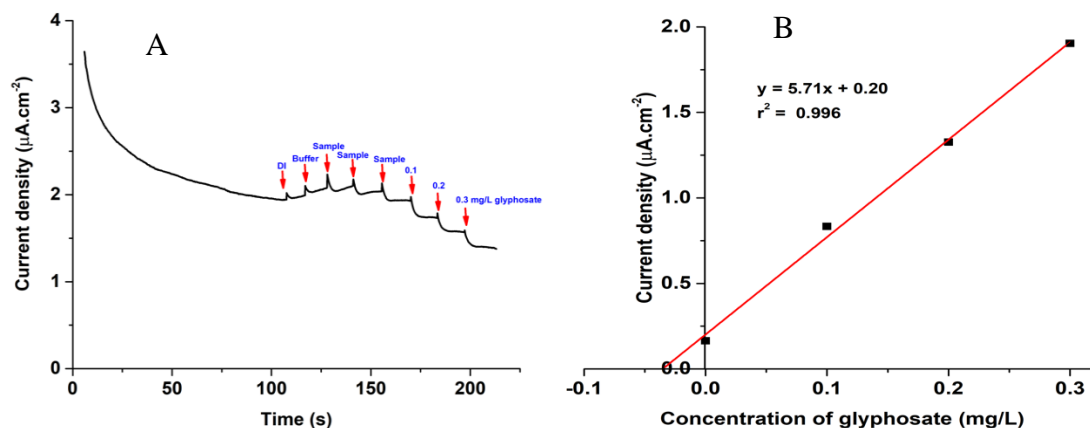
**Figure 4.44** Effect of interferences on the response of the SPCE/rGO-AgNPs/ACP biosensor

#### 4.3.7 Results of glyphosate determination in real samples

Glyphosate is a broad-spectrum herbicide mostly used in agriculture globally and it is used primarily before and after planting of traditional agricultural crops. Glyphosate herbicides represent a high toxicity to target species but it can be also toxic to non-target species, such as aquatic life and human beings. As a result, herbicide can cause both negative direct and indirect effects on human health. In 2015, the world health organization (WHO) have classified the glyphosate herbicide as probably carcinogenic to humans. Therefore, the amount of glyphosate contaminated in environmental waters and soils were determined by the developed SPCE/rGO-AgNPs/ACP biosensor and UHPLC as a standard method. Moreover, standard glyphosate solution (0.5 and 1.0 mg/L for water, 2 and 4 mg/kg for soil) were added into those sample solutions in order to check accuracy of the methods.

##### 4.3.7.1 Results of glyphosate determination by the enzymatic biosensor

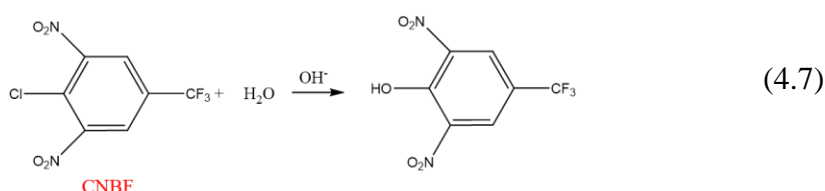
A certain volume of sample and spiked sample solutions was dropped on the biosensor surface containing disodium phenyl phosphate as an enzyme substrate (experiment 3.5.9.1). The current signal from enzymatic reaction between ACP and its substrate was detected by chronoamperometry at the potential of +0.4V under optimized conditions. In the presence of glyphosate, a decreased current signal was detected and the inhibited response was determined using the peak heights before and after introduction of glyphosate. The concentration of glyphosate was analyzed in triplicate by the standard addition method in the range from 0 to 0.3 mg/L, as showed in Figure 4.45 and Table B.39 (Appendix B.3). As a result, glyphosate at the concentration of  $0.65 \pm 0.11$  mg/L was found in the soil sample A using SPCE/rGO-AgNPs/ACP as the biosensor, as shown in Table 4.3. However, the detected concentration was below a maximum contaminant level of glyphosate in soil (2 mg/kg) set by the U.S. national primary. [94] Furthermore, accuracy of the biosensor was investigated by recovery measurements. The average recoveries of the spiked water and spiked soils were in the range of 95.6-104.7%. These results indicated that the developed SPCE/rGO-AgNPs/ACP biosensor was reliable for detection of glyphosate herbicide in environmental samples.

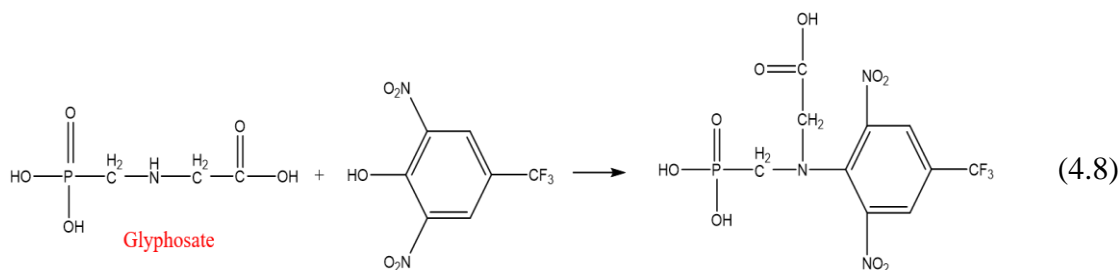


**Figure 4.45 (A) Amperometric response of SPCE/rGO-AgNPs/ACP for glyphosate determination in real samples by standard addition method and (B) its corresponding standard addition curve**

#### 4.3.7.2 Results of glyphosate determination by UHPLC

The concentration of glyphosate contaminated in environmental waters and soils was also analyzed by ultra-high performance liquid chromatography (UHPLC) as a standard method. UHPLC measurements were carried out with external calibration method after derivatization of standard glyphosate solutions and sample solutions with 4-chloro-3,5-dinitrobenzotrifluoride (CNBF) (experiment 3.5.1.12). CNBF was used as chemical derivatization because it can react to primary and secondary amines under basic condition to produce *N*-substituted-2,6-dinitro-4-(trifluoromethyl)-benzamine, which were satisfactory ultraviolet absorption. [215, 216] The reaction of CNBF with secondary amines on glyphosate under base condition is demonstrated in Equations 4.7 and 4.8.





The experiment was performed on C18 column (2.1×50 mm, 1.8 μm) as stationary phase and a gradient elution of a mixture between acetonitrile and 0.2% formic acid as a mobile phase (experiment 3.5.9.2). Figure 4.46 shows that the peak area increased linearly with the increasing of derivative glyphosate concentration in the range from 0.1 to 10 mg/L with a linear regression of  $A [\text{mAU} \cdot \text{min}] = 3.386 [\text{mg/L}] - 0.519$  ( $r^2 = 0.999$ ). The concentration of glyphosate in samples and spiked samples were analyzed by UHPLC in triplicate using this calibration plot, as shown in Table B.40 (Appendix B.3). The results are in very good agreement with the results obtained by the electrochemical biosensor and the recoveries of 95.9-103.8% upon spiking were received, as displayed in Table 4.3. Statistical analysis by a paired T-test at a confidence interval of 95% probability was verified to compare the analytical data between UHPLC and electrochemical biosensor. It was demonstrated that the two methods provided results which are not statistically significantly different due to the t-value is smaller than the tabulated critical value at a degree of freedom of 2.

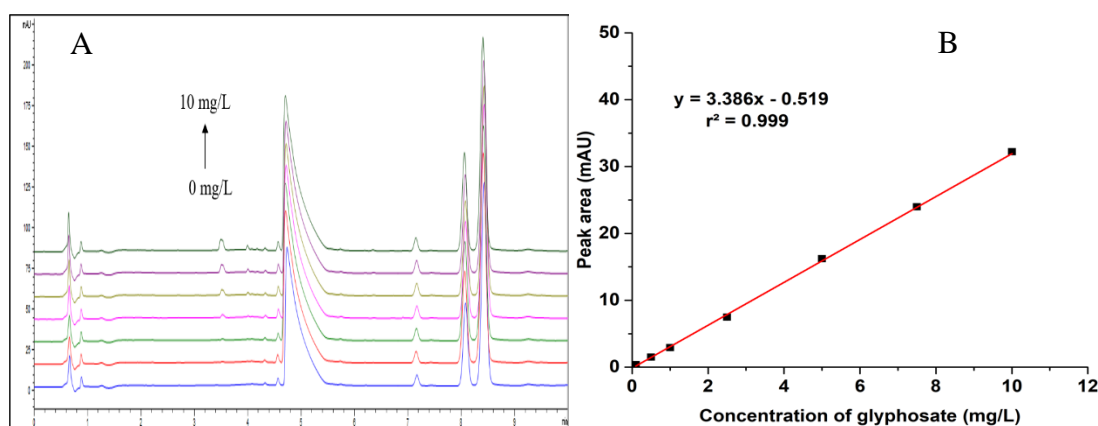


**Figure 4.46 (A) Chromatograms of glyphosate standards in the range from 0.1-10 mg/L and (B) calibration plots of peak area versus concentration**

**Table 4.3 Determination of glyphosate in environmental waters and soils by the biosensor and UHPLC ( $n=3$ )**

Sample	Added		Determined by biosensor		Determined by UHPLC			t-test <sup>b</sup>	
			Measured		Recovery	Measured			Recovery
	(mg.Kg <sup>-1</sup> )	(mg.L <sup>-1</sup> )	(mg.Kg <sup>-1</sup> )	(mg.L <sup>-1</sup> )		(mg.Kg <sup>-1</sup> )	(mg.L <sup>-1</sup> )		
Water A		-	n.d. <sup>a</sup>		-	n.d.	-	-	
		0.5	0.50 ± 0.05		100.1	0.52 ± 0.01	103.4	0.7	
		1.0	1.04 ± 0.12		104.0	1.04 ± 0.03	103.8	0.1	
Water B		-	n.d.		-	n.d.	-	-	
		0.5	0.51 ± 0.03		102.4	0.52 ± 0.01	103.2	0.2	
		1.0	1.02 ± 0.07		102.1	0.96 ± 0.03	96.1	2.1	
Water C		-	n.d.		-	n.d.	-	-	
		0.5	0.50 ± 0.03		100.8	0.49 ± 0.01	98.4	0.9	
		1.0	1.05 ± 0.12		104.7	0.96 ± 0.03	95.9	1.0	
Soil A	0		0.66 ± 0.06		-	0.79 ± 0.01	-	2.1	
	2.0		2.64 ± 0.24		99.3	2.76 ± 0.10	98.6	0.5	
	4.0		4.48 ± 0.32		95.6	4.74 ± 0.16	98.7	0.9	
Soil B	-		n.d.		-	n.d.	-	-	
	2.0		2.08 ± 0.10		104.0	2.05 ± 0.09	102.6	0.3	
	4.0		4.05 ± 0.20		101.3	4.13 ± 0.16	103.1	0.5	
Soil C	-		n.d.		-	n.d.	-	-	
	2.0		2.08 ± 0.06		104.1	2.00 ± 0.06	100.2	0.4	
	4.0		3.89 ± 0.27		97.2	4.01 ± 0.08	100.3	0.6	

<sup>a</sup> n.d. means “not detectable”<sup>b</sup> t-test at a confidence level of 95% probability and degree of freedom of 2

#### **4.4 Carbon composite nanomaterials-based sensor: SERS-based sensor for detection of glyphosate herbicide**

In this SERS-based sensor, the analytical method for determination of glyphosate herbicide in environments was also designed based on surface enhanced Raman spectroscopy (SERS). Titanium dioxide nanotube arrays (TiO<sub>2</sub> NTs) modified with silver nanoparticles (AgNPs) and reduced graphene oxide (rGO) were fabricated as a SERS substrate in order to obtain high-performance SERS activity for glyphosate detection. TiO<sub>2</sub> NTs were employed because self-cleaning function of the TiO<sub>2</sub> semiconductor, making the SERS substrate could be recyclable under ultra-violet irradiation. [217] The TiO<sub>2</sub> NTs were decorated with AgNPs because Ag nanomaterial exhibits a great surface plasmonic property that can amplify the electromagnetic enhancement mechanism in SERS system and also provides a charge transfer channel at the metal-semiconductor interface. [218] In addition, the transferring rGO onto the surface of TiO<sub>2</sub> NTs/AgNPs could be attributed remarkable improvement of Raman signals because the charge transfer between analytes and graphene materials lead to enhancing the chemical enhancement mechanism. [219] Thus, the TiO<sub>2</sub> NTs/AgNPs-rGO was fabricated as the sensor for glyphosate determination in environmental waters and soils based on SERS measurement. The optical and physical properties of the sensor was firstly characterized. Then, parameters influence on the Raman measurements and preparation conditions affect the structure of TiO<sub>2</sub> NTs/AgNPs-rGO were optimized by using methylene blue (MB) as a probe molecule. Next, analytical performance of the sensor for detection of MB and glyphosate were sequentially investigated. Finally, applications of the TiO<sub>2</sub> NTs/AgNPs-rGO for glyphosate determination in water and soil samples were discussed and compared with ultra-high-performance liquid chromatography (UHPLC) as a standard reference method.

##### **4.4.1 Characterization results of the TiO<sub>2</sub> NTs/AgNPs-rGO**

###### **4.4.1.1 Optical characterization of the TiO<sub>2</sub> NTs/AgNPs-rGO**

The optical property of the TiO<sub>2</sub> NTs/AgNPs-rGO was characterized by UV-visible spectrophotometer in the wavelength ranging from 200 to 800 nm, in comparison to a Ti sheet, TiO<sub>2</sub> NTs, and TiO<sub>2</sub> NTs/AgNPs (experiment 3.6.3.1). The UV-visible absorption spectra of different nanomaterials are presented in Figure 4.47. In comparison to Ti, the TiO<sub>2</sub> NTs shows very strong spectral absorption



due to electron transition between the valence band and conduction band of the TiO<sub>2</sub> semiconductor. A strong maximum absorption peak at 363 nm was observed, corresponding to a band gap energy of 3.41 eV. Energy band gap of the materials can be calculated by the formula as shown in Equation 4.9.

$$E = \frac{h.c}{\lambda} \quad (4.9)$$

where  $h$  is Planck's constant ( $6.62 \times 10^{-34}$  J.s),  $c$  is the velocity of light ( $3 \times 10^8$  m.s<sup>-1</sup>) and  $\lambda$  is the wavelength of maximum absorbance. Therefore, the band gap energy of the synthesized TiO<sub>2</sub> NTs is calculated to be 3.41 eV, in which  $1.6 \times 10^{-19}$  J = 1 eV. Moreover, this result indicates that crystalline structure of the synthesized TiO<sub>2</sub> NTs is anatase phase because band gap energy for the anatase phase have been reported in the literatures from 3.2 to 3.4 eV. [220] Furthermore, the absorption peak around 200 nm is attributed to the electronic transitions from  $e_g$  ( $\sigma$ ) orbital of O 2p electronic states to  $t_{2g}^*$  ( $\pi^*$ ) orbital of the Ti 3d. [221, 222] After deposition of AgNPs, the shift of the ultraviolet light absorption peak is occurred due to electron clouds on the surface of AgNPs transferring to the TiO<sub>2</sub> conduction band, leading to change of the surrounding dielectric property TiO<sub>2</sub>. [223] The maximum absorption peak is appeared at about 348 nm, which is attributed to the inter-band absorption energy of Ag (3.56 eV). [224] This sharp absorption peak also indicates that more electron excitations are accelerated resulted from surface plasmon resonance of Ag material. With the addition of rGO, almost the same absorption peak position as that of the TiO<sub>2</sub> NTs/AgNPs was observed, indicating that the rGO films does not change the band gap of TiO<sub>2</sub> NTs/AgNPs. Furthermore, a broad absorption peak in the visible light region at around 508 nm is appeared, which is attributed to the surface oxygen remaining groups and the interfacial electron transfer between the TiO<sub>2</sub> NTs/AgNPs and rGO. [225]

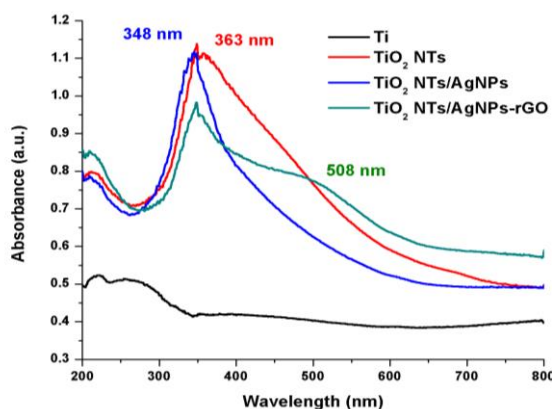


**Figure 4.47** UV-visible absorption spectra of different nanomaterials

#### 4.4.1.2 Electrochemical characterization of the TiO<sub>2</sub> NTs/AgNPs-rGO

The electrochemical method was employed to construct TiO<sub>2</sub> NTs and deposit rGO film. Therefore, electrochemical property of the prepared substrate was characterized by measuring the interfacial impedance between the substrate surface and the electrolyte using electrical impedance spectroscopy (EIS). Nyquist plots of the different prepared substrates, including Ti, TiO<sub>2</sub> NTs, TiO<sub>2</sub> NTs/rGO, TiO<sub>2</sub> NTs/AgNPs, and TiO<sub>2</sub> NTs/AgNPs-rGO, measured by the EIS technique in 5 mM Fe(CN)<sub>6</sub><sup>3-/4-</sup> as a redox probe are displayed Figure 4.48 (experiment 3.6.3.2). It can be seen that the semicircle diameter correlated with the electron transfer resistance ( $R_{ct}$ ) of the TiO<sub>2</sub> NTs ( $R_{ct} = 21.8 \text{ k}\Omega$ ) is larger than Ti sheet ( $R_{ct} = 13.1 \text{ k}\Omega$ ), indicating that electron transfer barrier is occurred from the oxide layer formation. After modification of the TiO<sub>2</sub> NTs with AgNPs and rGO, the  $R_{ct}$  value is reduced due to high electrocatalytic activity and excellent conductivity of rGO and AgNPs materials. [226] Furthermore, the  $R_{ct}$  value decreased dramatically to 8.9 k $\Omega$  after the TiO<sub>2</sub> NTs was modified with AgNPs-rGO hybrid nanomaterials compared to TiO<sub>2</sub> NTs/rGO (14.5 k $\Omega$ ) and TiO<sub>2</sub> NTs/AgNPs (12.5 k $\Omega$ ). This could be attributed to the synergistic effect of AgNPs-rGO nanocomposites that can facilitate charge transport and reduce resistance significantly. [227] The decrease in  $R_{ct}$  value is also attributed to the decreasing double-layer impedance at the substrate-electrolyte interfaces as a result of rapid electron mobility on the surface of conductive TiO<sub>2</sub> NTs/AgNPs-rGO. The correlation between SERS and EIS have been proved that the ideal nanostructure for SERS application that

possesses the largest Raman enhancement factor (EF) will provide the lowest double-layer impedance. [228] This can be explained from the fact that Raman scattering is obtained from the electromagnetic waves that propagate along the conductive material surface. The responding free electrons have been collected by oscillating in resonance with the light waves which constitutes the surface plasmon property and gives rise to the light scattering. Thus, it can be implied that higher intense Raman signals are received on nanostructured conducting materials. Since the introduction of AgNPs and rGO can improve the conductivity and promote charge transfer of the TiO<sub>2</sub> NTs, therefore the proposed TiO<sub>2</sub> NTs/AgNPs-rGO substrate serves as the best nanocomposite material for SERS measurement.

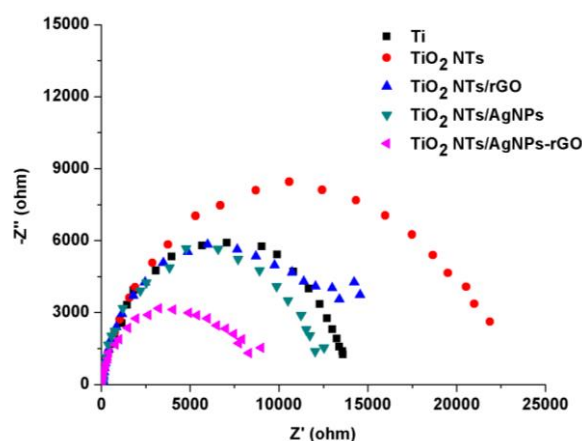


**Figure 4.48** EIS in a 5 mM Fe(CN)<sub>6</sub><sup>3-/4-</sup> solution of Ti, TiO<sub>2</sub> NTs, TiO<sub>2</sub> NTs/rGO, TiO<sub>2</sub> NTs/AgNPs, and TiO<sub>2</sub> NTs/AgNPs-rGO

#### 4.4.1.3 XRD of the TiO<sub>2</sub> NTs/AgNPs-rGO

The crystal structure of the TiO<sub>2</sub> NTs/AgNPs-rGO was characterized compared to Ti, TiO<sub>2</sub> NTs, TiO<sub>2</sub> NTs/AgNPs, TiO<sub>2</sub> NTs/rGO by X-ray diffraction spectroscopy (XRD) (experiment 4.6.3.3). XRD pattern of Ti foil shows the diffraction peaks at 38.9°, 40.3°, 53.1°, 63.1°, 70.8° and 76.4° (Figure 4.49). According to database of Ti foil, these peaks correspond to the lattice planes of (0 0 2), (1 0 1), (1 0 2), (1 1 0), (1 0 3) and (1 1 2), respectively. [229] After anodization and annealing, some new peaks belonging to TiO<sub>2</sub> anatase appeared at 25.4° and 48.2°, which can be assigned to the lattice planes of (1 0 1) and (2 0 0), respectively (JCPDS No. 21-1272). After deposition of AgNPs, two more diffraction peaks at 38.2° and 43.3° are observed,

which are originated from the lattice planes of (1 1 1) and (2 0 0) of face centered cubic of Ag (JCPDS No. 65-2871). Moreover, the main characteristic (002) diffraction peak of rGO (JCPDS No. 41-1487) is detected at around  $26.0^\circ$  in the  $\text{TiO}_2$  NTs/rGO and  $\text{TiO}_2$  NTs/AgNPs-rGO. These results are well consistent with previous works. For instance, Liu and et al. [230] presented the XRD results of  $\text{TiO}_2$  NTs-Ag composite and shown seven obvious diffraction peaks at  $2\theta = 25.6^\circ, 38.4^\circ, 48.7^\circ, 54.6^\circ, 63.7^\circ, 70.4^\circ$  and  $74.8^\circ$  corresponding to the reflection planes of anatase structure  $\text{TiO}_2$  as well as two main diffraction peaks of Ag appeared at  $2\theta = 38.1^\circ$  and  $44.2^\circ$ . Lu and et al. [225] revealed that  $\text{TiO}_2$  showed six characteristic planes of anatase  $\text{TiO}_2$  at  $2\theta$  about  $26^\circ, 38^\circ, 48^\circ, 55^\circ, 63^\circ$ , and  $75^\circ$  while the characteristic (002) diffraction peak of graphene is detected at  $26.0^\circ$ .

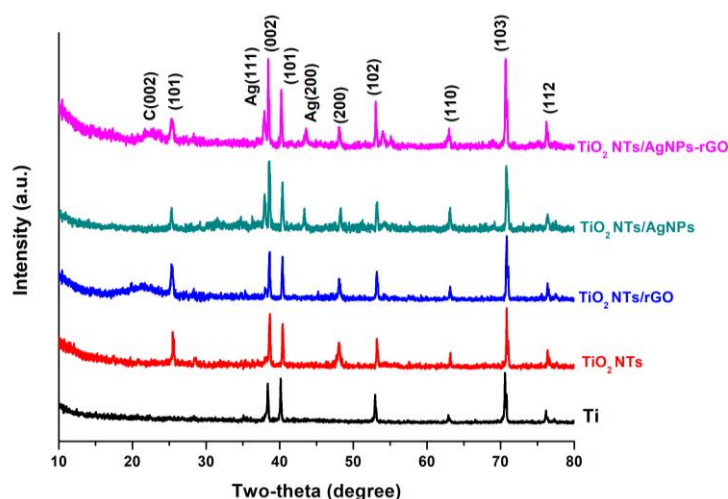


**Figure 4.49 XRD spectra of different nanomaterials**

#### 4.4.1.4 Raman spectra of the $\text{TiO}_2$ NTs/AgNPs-rGO

Raman spectroscopy is an effective characterization method for studying the nanostructures of  $\text{TiO}_2$  NTs and carbon-based materials. Therefore,  $\text{TiO}_2$  NTs/AgNPs-rGO was characterized by Raman spectroscopy compared to a Ti,  $\text{TiO}_2$  NTs,  $\text{TiO}_2$  NTs/GO, and  $\text{TiO}_2$  NTs/rGO (experiment 4.6.3.4). As can be seen in Figure 4.50, all the samples except Ti show three important peaks centered at 408, 528, and  $647\text{ cm}^{-1}$ , which are corresponded to  $B_{1g}$ ,  $A_{1g}$ , and  $E_g$  vibration modes in tetragonal structure of anatase phase of  $\text{TiO}_2$  NTs. This result also well corresponded with UV-vis

spectra and XRD patterns indicating that crystalline structure of the synthesized  $\text{TiO}_2$  NTs is anatase phase. The  $B_{1g}$ ,  $A_{1g}$ , and  $E_g$  are contributed by the symmetric bending vibration, the anti-symmetric bending vibration, and the symmetric stretching vibration of O-Ti-O in  $\text{TiO}_2$  NTs, respectively. [231] In the presence of GO or rGO, two peaks at  $1361$  and  $1603\text{ cm}^{-1}$  are observed, which are assigned to disorder carbon (D band) and graphite carbon (G band), respectively. [232] The D band is mainly originated from local defects and disorder of carbon within the hexagonal graphitic structure, while G band is related to the  $\text{sp}^2$  hybridized carbon atoms. It is clearly seen that the D peak is presented in all graphene-based substrates because of laser induced damage during Raman measurement. [233] However, this experiment is performed under the same conditions. The intensity ratio of the D band to the G band ( $I_D/I_G$ ) is widely used to characterize the defect quantity in carbon. [234] The  $I_D/I_G$  value of the  $\text{TiO}_2$  NTs/GO is 1.04, while the  $I_D/I_G$  ratio had increased to 1.28 and 1.11 in case of  $\text{TiO}_2$  NTs/rGO and  $\text{TiO}_2$  NTs/AgNPs-rGO, respectively. This indicates that more defects in the graphitized structures are formed after electrochemical reduction of GO material. The result is in accordance with Harraz and et al. [235] who revealed that the  $I_D/I_G$  ratio of rGO was slightly larger than GO due to a size decrease of  $\text{sp}^2$  carbon atoms domains upon the reduction of the GO, suggesting the formation of rGO during the reduction reaction. Furthermore, another Raman feature at around  $2700\text{ cm}^{-1}$  named 2D band was also observed in graphene-based samples. This 2D band is usually used for determination of number of layers of graphene. [236] The  $I_{2D}/I_G$  ratio of the  $\text{TiO}_2$  NTs/AgNPs-rGO was calculated to be 0.89, indicating a few layers of rGO covered on the  $\text{TiO}_2$  NTs/AgNPs. Moreover, an additional disorder related peaks, including D+G and 2G at about  $2950\text{ cm}^{-1}$  and  $3220\text{ cm}^{-1}$ , were observed. The D+G peak is a combination scattering mode of D and G peak, while the 2G peak is an overtone of G modes as a result of second order Raman scattering in the graphene material. [237]

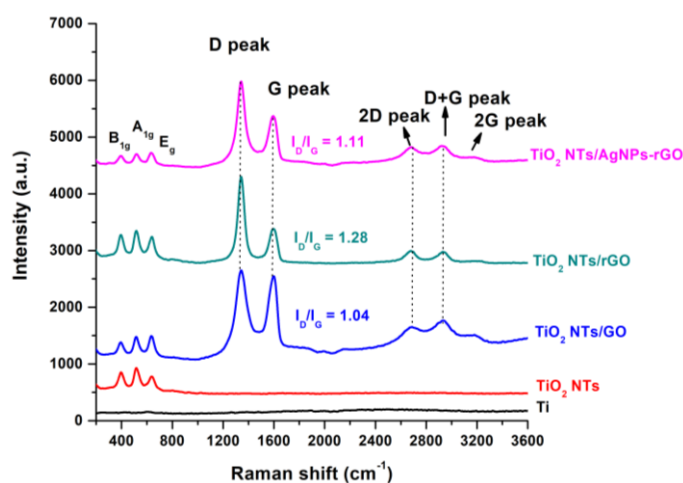


**Figure 4.50 Raman spectra of different nanomaterials**

#### 4.4.1.5 XPS of the TiO<sub>2</sub> NTs/AgNPs-rGO

To characterize chemical compositions and bonding environments in the TiO<sub>2</sub> NTs/AgNPs-rGO material, X-ray photoelectron spectroscopy (XPS) analysis was performed (experiment 3.6.3.5). The chemical states information and the full scan XPS of the TiO<sub>2</sub> NTs/AgNPs-rGO was demonstrated in Figure 4.51(A). There are no impurity elements presented in the prepared material and there are only desired elements including Ti, O, Ag, and C were detected. The high-resolution Ti 2p XPS spectrum (Figure 4.51(B)) shows two binding energy peaks at 459.9 eV (2p<sub>3/2</sub>) and 465.5 eV (2p<sub>1/2</sub>). The difference of 5.6 eV between the Ti 2p spin doublets revealed that Ti<sup>4+</sup> oxidation state was presented in the TiO<sub>2</sub> NTs. [238] The additional duplex shoulder peaks at higher binding energy (472.3 eV and 477.9 eV) were considered as satellite features of TiO<sub>2</sub>. [239] Figure 4.51(C) illustrates the deconvoluted XPS data for the O 1s electrons. A major binding energy peak at 530.1 eV was assigned to the lattice oxygen species in TiO<sub>2</sub> NTs (Ti-O bands), and a minor binding energy peak at 532.0 eV was corresponded to the surface hydroxyl oxygen. [240] Figure 4.51(D) shows that the TiO<sub>2</sub> NTs/AgNPs-rGO contains two binding energy peaks at 374.8 eV and 368.8 eV, corresponding to Ag 3d<sub>3/2</sub> and Ag 3d<sub>5/2</sub> of metallic silver with spin separation of 6.0, respectively. [241] In addition, no other peaks such as AgO (spin separation of 5.9) or Ag<sub>2</sub>O (spin separation of 6.1) are observed, indicating that Ag exists only in its metallic state (Ag<sup>0</sup>). [242] The similar results were observed by Dong and et al. [241] and Huang

and co-worker. [243] They revealed that the binding energy at 374.8 and 368.8 eV were corresponded to Ag 3d<sub>3/2</sub> and Ag 3d<sub>5/2</sub> of the Ag<sup>0</sup> state in pure Ag material, respectively. The deconvoluted C 1s spectra (Figure 4.51(E)) displays four peaks at the position of 285.0 eV, 286.7 eV, 289.0 eV, and 290.9 eV. The binding energy at 285.0 eV is assigned to C-C band from sp<sup>2</sup> hybridized carbon of rGO. Two peaks at 286.7 eV and 289.0 eV are attributed to the C-O and C=O, respectively. The fitted peak at 290.9 eV is corresponded to O-C=O bond, proving that the interaction is formed at the interface of rGO and TiO<sub>2</sub> NTs. [244]

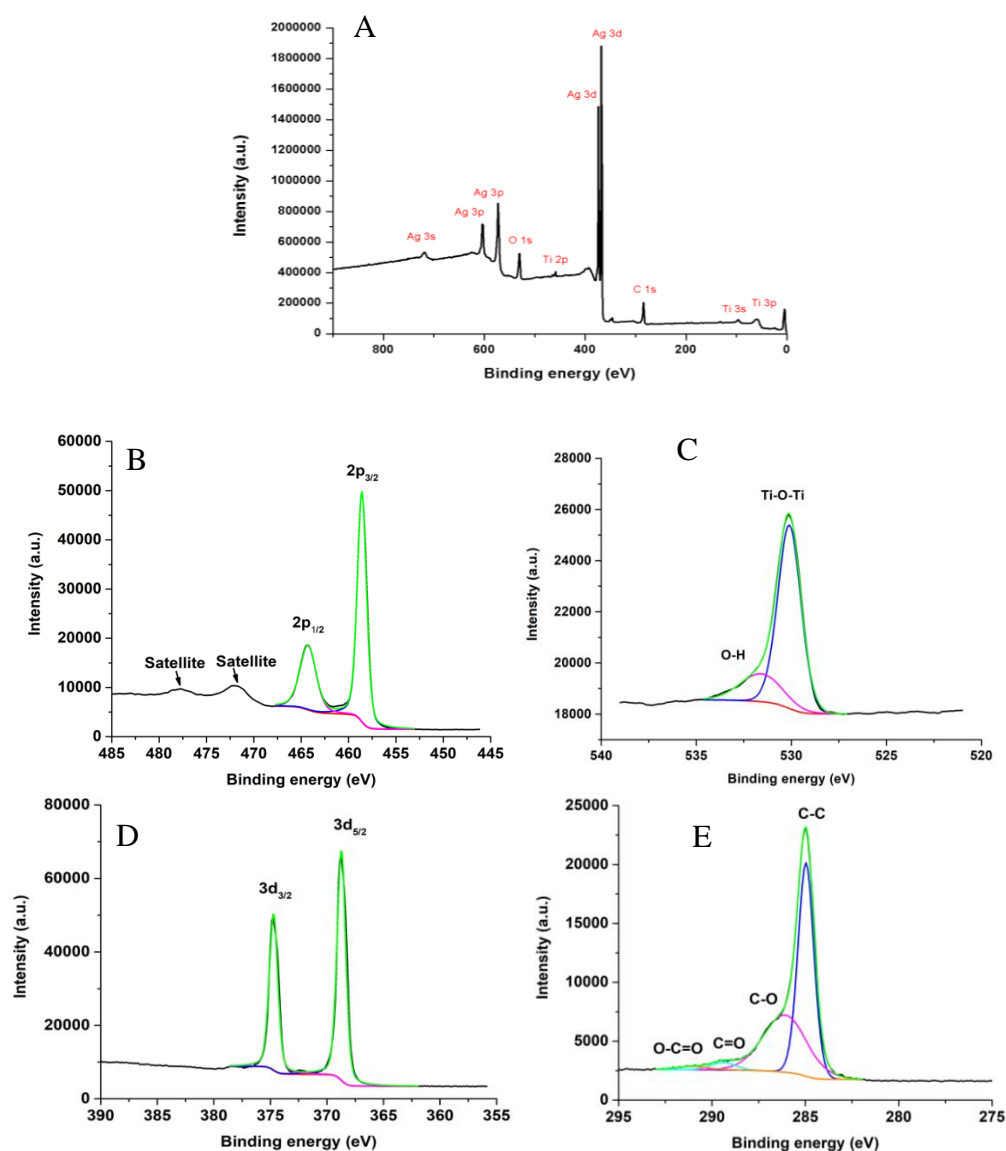


**Figure 4.51** XPS of (A) TiO<sub>2</sub> NTs/AgNPs-rGO and high resolution XPS analysis of (B) Ti 2p (C) O 1s (D) Ag 3d and (E) C 1s components (continued)

#### 4.4.1.6 EDS of the TiO<sub>2</sub> NTs/AgNPs-rGO

The overall elemental composition of the TiO<sub>2</sub> NTs/AgNPs-rGO was determined by an energy dispersive X-ray (EDS) analysis (experiment 3.6.3.6) and the EDS spectrum is displayed in Figure 4.52. The clear peaks of Ti, C, O, and Ag are presented in the spectrum, which are corresponded well to the element of individual nanomaterials. This result indicates the successful synthesis of the TiO<sub>2</sub> NTs/AgNPs-rGO nanostructure, which are made up of O (31.7 %wt), Ti (60.2 %wt), Ag (4.2 %wt), and C (3.8 %wt). These weight percentage is relative to absolute concentration of element in the sample. Moreover, number of atoms of each element can be calculated from the element weight percentage by dividing weight percentage by its atomic weight. Then, the number of atoms of that element is divided by the total number of atoms in the sample multiplied by 100 in order to obtain atomic percentage. The chemical formula of titanium dioxide is TiO<sub>2</sub>, which means that it consists of one Ti atom and two O atoms. Therefore, the stoichiometric ratio of O/Ti should be 2. However, the result shows the O/Ti atomic ratio of 1.6. The decreasing in O proportion might be due to a replacement of oxide just above the top of the TiO<sub>2</sub> surface as a result of physisorption between AgNPs and TiO<sub>2</sub> semiconductor. [245]

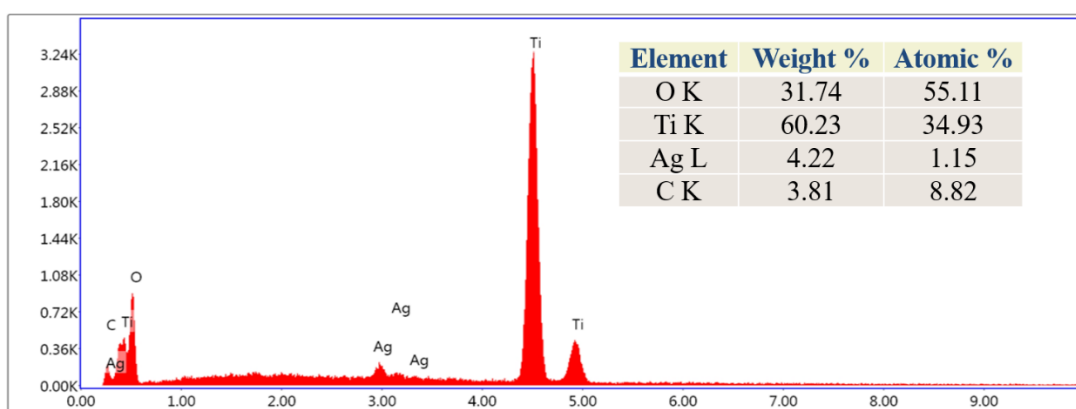


**Figure 4.52 EDS spectrum of TiO<sub>2</sub> NTs/AgNPs-rGO**

#### 4.4.2 Optimization of Raman parameters

The conditions influence on the SERS measurements such as laser excitation wavelengths, objective lens, acquisition times and number of accumulations were investigated by using Raman active molecule. Generally, Raman active molecule would



be a species that have a center of symmetry and the molecular vibration must cause a change in polarizability. [246] In the work, methylene blue (MB) is used as a probe molecule because it is an organic dye model that have been generally employed in a field of SERS and it provides strong Raman signals. [247] The relatively intense characteristic peaks of Raman active MB were obtained in the region from 200 to 2000  $\text{cm}^{-1}$  (Figure 4.53). MB is a heterocyclic aromatic substance consisting a thiazine ring and its characteristic peaks at 437  $\text{cm}^{-1}$  is attributed to the C-N-C skeletal deformation mode. In-plane bending mode of C-H is observed at 761  $\text{cm}^{-1}$  and 893  $\text{cm}^{-1}$ , while in-plane ring deformation mode of C-H is at 1142  $\text{cm}^{-1}$ . Two prominent peaks at around 1385 and 1435  $\text{cm}^{-1}$  were assigned to the symmetric and asymmetric C-N stretching, respectively. [248] To estimate the enhancement ability, the intensity of the 1624  $\text{cm}^{-1}$  peak in Raman spectrum correlated to C-C ring stretching is employed.

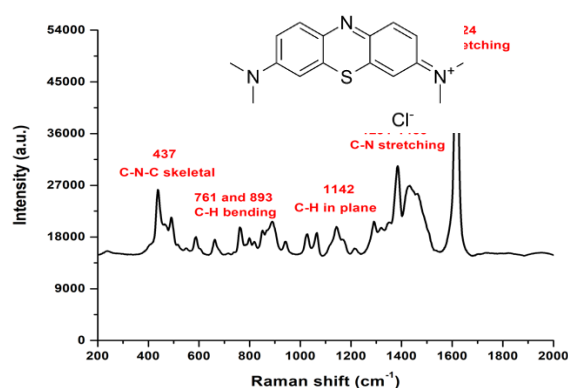


**Figure 4.53 Raman spectra and chemical structure of methylene blue**

#### 4.4.2.1 Laser excitation wavelength and objective lens

A variable and suitable excitation laser sources is primarily aimed to provide a sensitive Raman system with desired flexibility toward the suppression of unwanted fluorescence. Therefore, four different wavelengths of laser sources, including 325 nm, 532 nm, 633 nm, and 785 nm, were investigated (experiment 3.6.4.1). The choice of wavelength depends heavily on the specific applications and surface metals. It is found that laser excitation at 532, 633, and 785 nm yielded reasonably structured Raman fingerprints of MB with almost negligible fluorescence, as can be

seen in Figure 4.54(A). It is clearly observed that pattern of the Raman shifts and intensities of the Raman peaks show a remarkable difference at various excitation wavelengths. At 325 nm, it is difficult to discern the MB signals since the sample is burned after a few milliseconds because of extremely high energy. [249] Under 532 nm excitation laser, multiple Raman bands between 437 and 1617  $\text{cm}^{-1}$  are clearly seen and the Raman peak correlated to C-C ring stretching at 1624  $\text{cm}^{-1}$  is distinguished. By contrast, most of the Raman bands are strongly enhanced, especially for the Raman peak related to C-N-C skeletal deformation at 437  $\text{cm}^{-1}$  and asymmetric C-N stretching at 1291-1460  $\text{cm}^{-1}$ , at the excitation wavelength of 633 nm. This indicates that resonance effect of Raman active molecule is contributed to the enhancement effect due to the maximum absorption peak of MB molecules is about 668 nm. [250] At a longer excitation wavelength of 785 nm, the Raman bands are hardly to see in the low wavenumber range ( $<600 \text{ cm}^{-1}$ ), which probably due to the laser photon does not have enough energy to excite skeletal part. [251]

Even though 633 nm laser provides rich fingerprint peaks of MB, it is not suitable to use as an excitation wavelength because MB can be excited in the wavelength ranging from 550-700 nm, with an emission centered around 690 nm. [252] Therefore, background fluorescence may be easily detected. As a result, the choice of 532 nm and 785 nm laser wavelength can avoid exciting fluorescence. In this case, the wavelength of 532 nm offers the best response on the MB detection by using  $\text{TiO}_2$  NTs/AgNPs-rGO substrate, according to the Raman peak of 1624  $\text{cm}^{-1}$ , and the result is noticeable seen on the detection of 1 nM MB (Figure 4.54(B) and Table B.41 (Appendix B.4)). This can be explained from the fact that the SERS activity can be efficiently increased when the surface plasmon resonance of the substrate matched with the excitation wavelength of laser and probe molecules [253, 254] and the surface plasmon resonance of the  $\text{TiO}_2$  NTs/AgNPs-rGO have reported at about 500 nm. [255] Moreover, this result is well consistent with optical characterization as described in the part 4.4.1.1. The absorption spectrum of the  $\text{TiO}_2$  NTs/AgNPs-rGO showed maximum absorption peak at 363 nm and 508 nm. Thus, 532 nm is selected as the laser excitation. Moreover, some previous works employed a wavelength of 532 nm for SERS measurement based on using  $\text{TiO}_2$  NTs, AgNPs, and/or rGO as the SERS substrate. [156, 162]

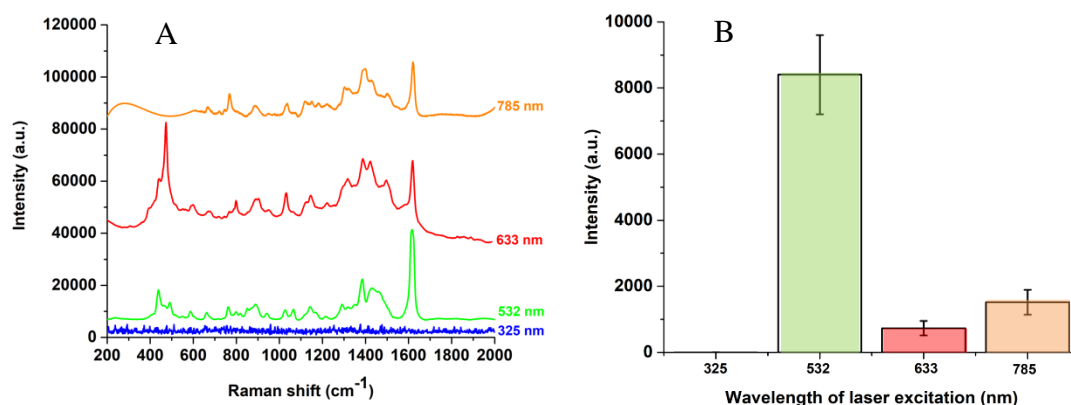


**Figure 4.54** The influences of laser excitation wavelengths on the detection of (A) 1 mM MB and (B) 1 nM MB

The size of objective lens is one of the parameters that effects on the SERS performance due to the peak intensity and resolution of Raman bands depends on the microscope objective lens. [256] Therefore, the microscope objectives were evaluated by three different magnifications, including 10x, 50x and 100x, for the detection of 1 nM MB (experiment 3.6.4.1). It was observed that 50x objective provided the best efficiency for green light collection on the TiO<sub>2</sub> NTs/AgNPs-rGO substrate Table B.42 (Appendix B.4). This can be clarified from the working distance between the SERS substrate and objective, and the numerical aperture (NA). To avoid sample burning, usually a long working distance objective needs to be employed and the distance decreases with the increasing of objective magnification. [257] In contrast, the highest collection efficiency was obtained by using a high NA objective and the NA value increase with the increasing of objective size. [256] Thus, the 50x objective was the best compromise to equip with Raman spectrometer for further study.

#### 4.4.2.2 Acquisition times and number of accumulations

The acquisition times for SERS analysis were tested from 1 to 15 second (experiment 3.6.4.2) and the results are displayed in Table B.43 (Appendix B.4). A better SERS signals were obtained with higher acquisition time. However, 10 second was employed as the optimized acquisition time to avoid sample degradation or burning and to reduce measurement time. Moreover, to enhance the sensitivity of the SERS measurement and to reduce the random noise inherent in Raman spectrum, the

accumulation number was further optimized (experiment 3.6.4.2). As can be seen in Table B.44 (Appendix B.4), the Raman intensity increased greatly with an increase of the accumulation number and it levelled off after 5 cycles. This indicated that coaddition of successive spectra for 5 times could provide an appropriate intensity of MB detection on the TiO<sub>2</sub> NTs/AgNPs-rGO substrate. Thus, accumulation for 5 cycles were applied for collection of the SERS signal.

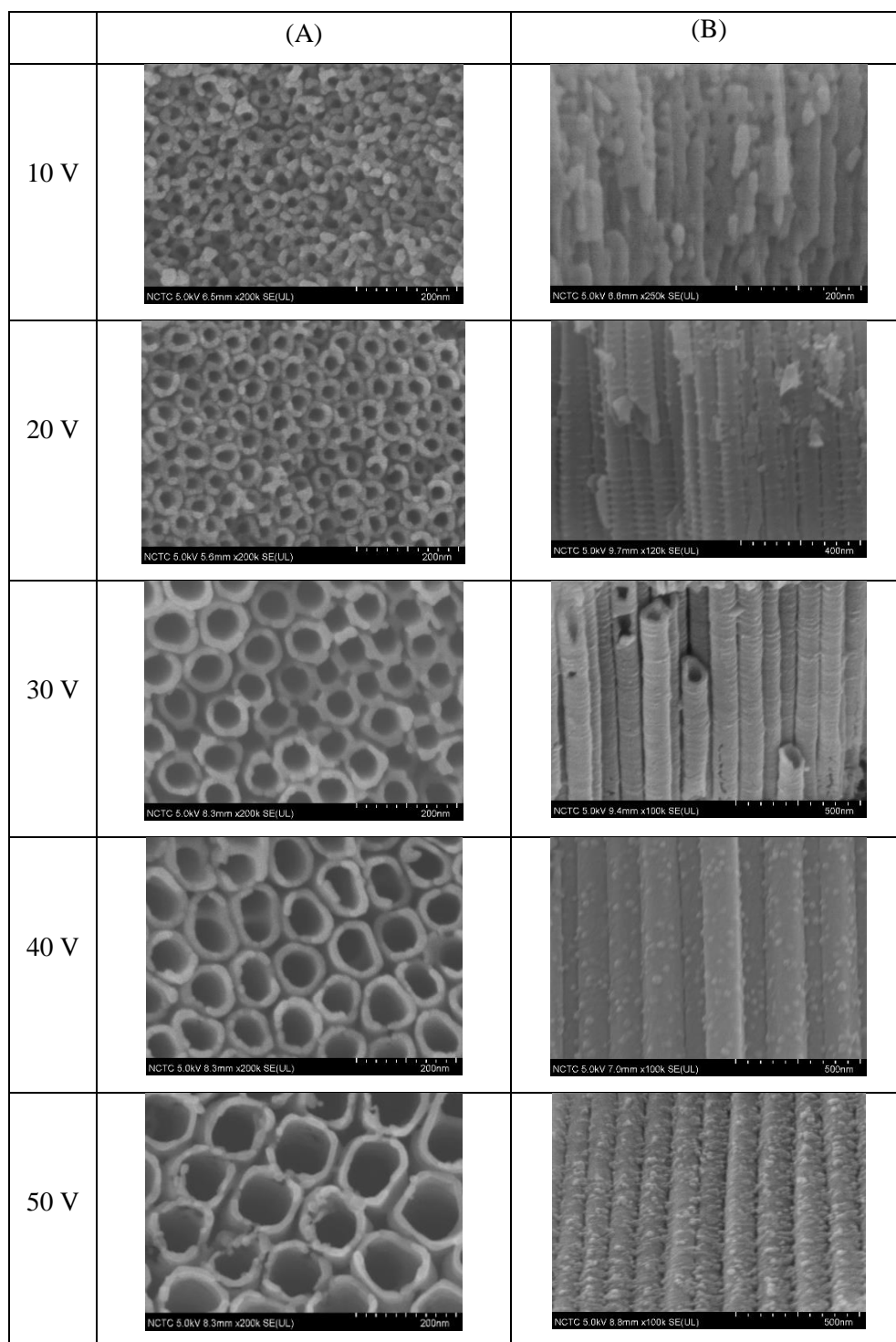
### 4.4.3 Optimization of SERS substrate structure

#### 4.4.3.1 Effect of anodization potential for TiO<sub>2</sub> NTs construction

The TiO<sub>2</sub> NTs was fabricated by electrochemical anodization method, in which the formation of nanotubular TiO<sub>2</sub> on Ti sheet was based on a competition between anodic oxide formation of insoluble TiO<sub>2</sub> and chemical dissolution of soluble [TiF<sub>6</sub>]<sup>2-</sup>, respectively. [258] The oxide formation is a consequence of the metal oxidation and water dissociation at metal complex-water interface as Equation 4.10 and 4.11, respectively. Then, the oxidized Ti<sup>4+</sup> react with O<sup>2-</sup> ions, resulting in TiO<sub>2</sub> are formed (Equation 4.12). The electric field within the oxide is progressively reduced by the increasing oxide thickness, leading to self-limiting process. [259] As a result, the oxides were etched and then complexed with fluoride ions presented in the electrolyte as Equation 4.13. The dissolution [TiF<sub>6</sub>]<sup>2-</sup> complex lead to pore formation and the individual pores begin to interfere with each other. During anodization, continual growth of oxide layers and chemical reaction of the oxide occurs simultaneously. Steady state was established when the oxide growth rate is equal to the dissociation rate of oxide film. [242, 260]



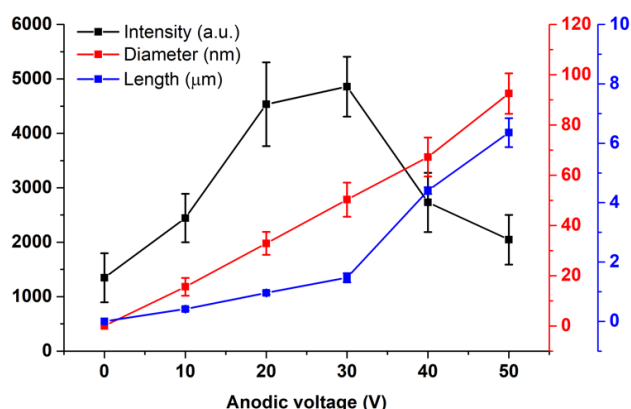
The growth and structure of  $\text{TiO}_2$  NTs could be controlled by adjusting anodization parameters. The anodic voltage is one of the parameters that affects size and structure of the  $\text{TiO}_2$  NT. Therefore, the different potentials (0, 10, 20, 30, 40, and 50 V) were investigated for anodization of the  $\text{TiO}_2$  NTs (experiment 3.6.5.1). Firstly, effect of voltage on morphologies of the  $\text{TiO}_2$  NTs was studied. The top surface and cross-sectional microstructure of the  $\text{TiO}_2$  NTs were measured by scanning electron microscope (SEM). As shown in Figure 4.55(A), the anodic voltage has a significant influence on the pore size of the  $\text{TiO}_2$  NTs and the inner diameter of the nanotubes increased with increasing voltage. The reason is that the anodic voltage defines the strength of electric field. [261] Therefore, the migration of  $\text{F}^-$  through the anodic oxide layer are more accelerated at higher voltage because of high electric field strength. The average inner diameter of the  $\text{TiO}_2$  NTs is approximately  $15.6 \pm 3.5$  nm,  $32.9 \pm 4.6$  nm,  $50.3 \pm 6.8$  nm,  $67.2 \pm 7.7$  nm, and  $92.5 \pm 8.1$  nm at the voltage of 10 V, 20 V, 30 V, 40 V, and 50 V, respectively (Figure 4.56 (red line)). Some previous researches were also revealed that there was a large effect of anodic voltage on the tube diameter, in which this dependence is approximately linear. [262, 263] The cross-section images of the  $\text{TiO}_2$  NTs are displayed in Figure 4.55(B). It is observed that the nanotube arrays appear imperfect in shape at the anodic potential of 10V, whilst the tubular morphology of the  $\text{TiO}_2$  NTs is clearly seen at the potential is higher than 20V. This is due to the strength of electric field which it is quite low under the voltage less than 20V, resulting in fluoride ions are difficult to transport across the oxide layer. As a result, the chemical dissolution reaction is imperfect and the disordered  $\text{TiO}_2$  NTs is created. Moreover, length of the  $\text{TiO}_2$  NTs is also depended on the applied voltage, in which nanotube length increased with increasing of voltage, as shown in Figure 4.56 (blue line). This is due to high electric field encourage a simultaneous formation and dissolution of the oxide layer, resulting in the rate of nanotubular creation is faster. The average length of the  $\text{TiO}_2$  NTs was obtained as  $0.4 \pm 0.1$   $\mu\text{m}$ ,  $1.0 \pm 0.1$   $\mu\text{m}$ ,  $1.5 \pm 0.2$   $\mu\text{m}$ ,  $4.4 \pm 0.1$   $\mu\text{m}$ , and  $6.4 \pm 0.5$   $\mu\text{m}$  for 10 V, 20 V, 30 V, 40 V, and 50 V, respectively. In summary, the anodization voltage had a significant influence on the diameter and length of the  $\text{TiO}_2$  NTs.



**Figure 4.55 SEM images of (A) top surface and (B) cross-sectional microstructure of the TiO<sub>2</sub> NTs as a function of voltage and a fixed time of 30 min**

Since, the TiO<sub>2</sub> NTs were used as building blocks for further loading of plasmonic AgNPs. Therefore, the effect of anodic voltage on SERS performances

were investigated and the results are showed in Figure 4.56 (black line) and Table B.45 (Appendix B.4). In comparison to silver deposited flat  $\text{TiO}_2$  film (0 V), silver top-decorated  $\text{TiO}_2$  NTs showed larger intensities in Raman scattering. This can be explained from the theory that SERS effect could be extended by introducing a nanoscale surface roughness because the surface roughness was capable of sustaining hot spots responsible for the Raman signal enhancement. [264] Since nanotubular  $\text{TiO}_2$  had more roughness than that of the flat surface, therefore the high value of the electromagnetic field intensity was produced and resulted in high Raman signal measured in the  $\text{TiO}_2$  NTs. Moreover, Macias and et al. [264] reported that rough SERS substrate exhibited enhancement factors (EF) up to two orders of magnitude higher than the EF exhibited by similar smooth material. In comparison between  $\text{TiO}_2$  NTs prepared at different potentials, the SERS intensity increased with increasing of voltage up to 30V and decreased afterward. Therefore, it could be assumed that the greater enhancement was achieved by using the  $\text{TiO}_2$  NTs with the diameter and length of about 50 nm and 1.5  $\mu\text{m}$ , which possess an aspect ratio of length to diameter of 30. This could be explained by the fact that suitability of the nanotubular size could effectively enhance SERS activity because optimal diameter and length of the  $\text{TiO}_2$  NTs could promote the coupling of AgNP and possessed a suitable electronic structure of AgNPs arranged on the nanotubular surface. [265, 266] Furthermore, Ling and et al. [262] noticed that differences in Raman intensities were observed in nanotubes with different anodization voltages and the highest enhancement was observed on the  $\text{TiO}_2$  NTs/AgNPs prepared at anodic voltage of 30V.

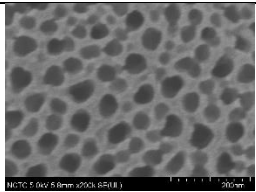
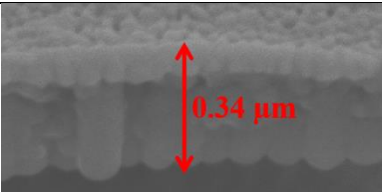
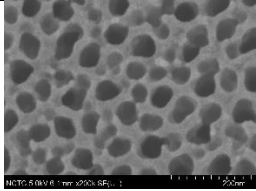
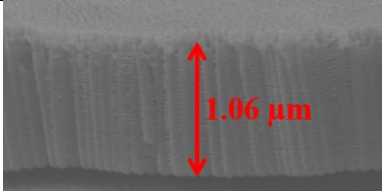
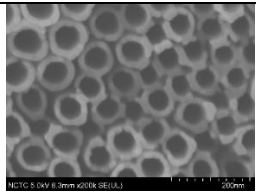
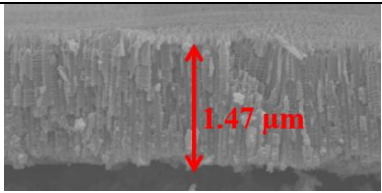
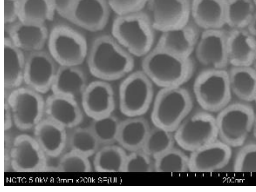
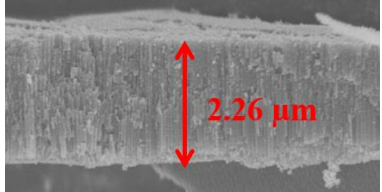
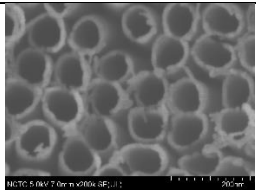
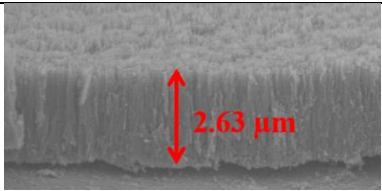
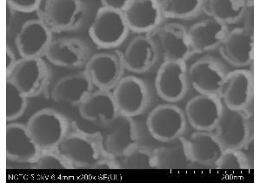
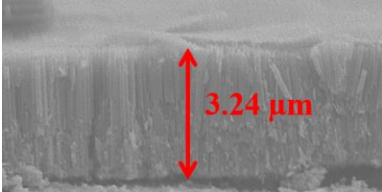
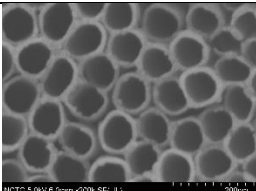
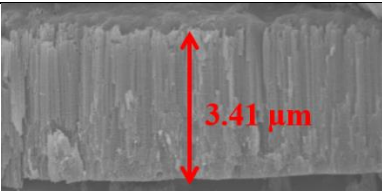


**Figure 4.56** SERS response on the detection of 1 nM MB of the TiO<sub>2</sub> NTs prepared at different voltages and covered with 5 nm AgNPs (black line) and the effect of the anodic voltage on tube diameter (red line) and length (blue line)

#### 4.4.3.2 Effect of anodization time for TiO<sub>2</sub> NTs fabrication

Another majority of anodizing experiments that influences on the formation and structure of the TiO<sub>2</sub> NTs is anodic time. Therefore, the effect of anodizing time was detailed investigated from 10 to 180 minutes (experiment 3.6.5.2). It was observed that the average inner diameter of the TiO<sub>2</sub> NTs gradually increased with increasing of anodic time because the amount of oxide on the top surface was continuously etched over time. [267] As shown in Figure 4.57(A) and Figure 4.58 (red line), the diameter was calculated to be  $42.2 \pm 7.1$  nm,  $49.3 \pm 7.7$  nm,  $50.3 \pm 6.8$  nm,  $62.0 \pm 10.5$  nm,  $63.1 \pm 7.5$  nm,  $65.5 \pm 10.0$  nm,  $72.2 \pm 9.0$  nm, and  $77.7 \pm 10.6$  nm for anodic time of 10, 20, 30, 60, 90, 120, 150, and 180 minutes, respectively. Moreover, length of the nanotubes increased obviously with the increasing of time because chemical etching process of nanotube continuously take place with time. As shown in Figure 4.57(B) and Figure 4.58 (blue line), length of TiO<sub>2</sub> NTs was measured to be  $0.3 \pm 0.01$  μm,  $1.1 \pm 0.01$  μm,  $1.5 \pm 0.02$  μm,  $2.3 \pm 0.02$  μm,  $2.6 \pm 0.01$  μm,  $3.2 \pm 0.02$  μm,  $3.4 \pm 0.02$  μm, and  $4.4 \pm 0.02$  μm for 10, 20, 30, 60, 90, 120, 150, and 180 minutes, respectively. This result confirms that anodic time was one of the parameters that influenced on diameter and length of the TiO<sub>2</sub> NTs.



	(A)	(B)
10 mins		
20 mins		
30 mins		
60 mins		
90 mins		
120 mins		
150 mins		

**Figure 4.57 SEM images of (A) top surface and (B) cross-sectional microstructure of the TiO<sub>2</sub> NTs as a function of time and a fixed voltage of 30 V**

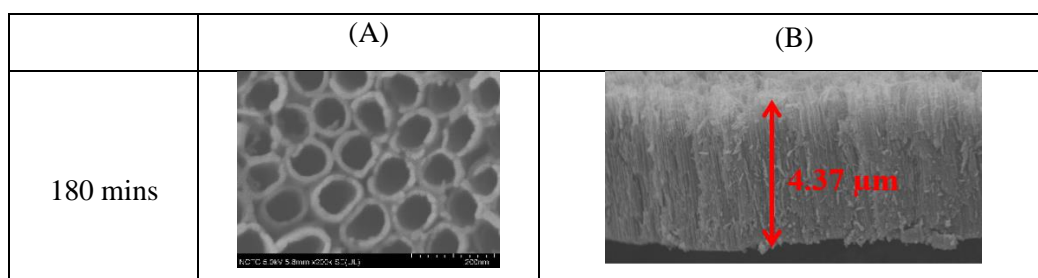


**Figure 4.57 SEM images of (A) top surface and (B) cross-sectional microstructure of the TiO<sub>2</sub> NTs as a function of time and a fixed voltage of 30 V (continued)**

The SERS performance of the TiO<sub>2</sub> NTs prepared at different anodic times from 10 to 180 minutes was investigated on the detection of 1 nM MB. As can be seen in Figure 4.58 (black line) and Table B.46 (Appendix B.4), the Raman scattering signals trend to stable in the range from 10 to 30 minutes, which might be due to the same self-organization degree of the TiO<sub>2</sub> NTs. [268] Then, the signals gradually decreased with the increase of anodic time. The decrease in signal is attributed to charge transfer mechanism limited owing to the oscillating electrons by surface plasmon resonance on AgNPs. It is hard to transfer along the longer nanotube and reach the bottom Ti substrate. [269, 270] Another reason is that long pores of nanotubes ( $\geq 2 \mu\text{m}$ ) lead to light trapping effect occurring. [271] As a consequence, the light scattering was lost and the SERS signals of the long TiO<sub>2</sub> NTs were reduced. Furthermore, Yang and et al. [271] revealed that the SERS intensity decreased when the height of silicon nanowires (SiNWs) is larger than  $1 \mu\text{m}$ . This result confirms that TiO<sub>2</sub> NTs with the diameter of 50 nm and length of  $1.5 \mu\text{m}$  (aspect ratio of 30) is the most suitable platform for using as building blocks to be further combined with the plasmonic AgNPs and rGO films.

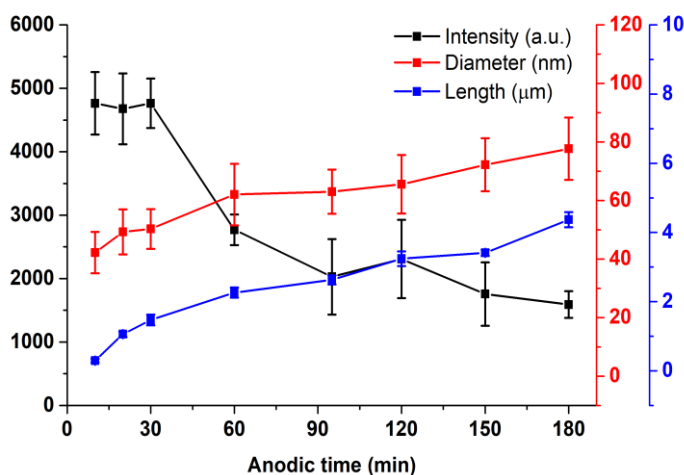


**Figure 4.58** SERS response on the detection of 1 nM MB of the TiO<sub>2</sub> NTs prepared at different anodic times and covered with 5 nm AgNPs (black line) and the effect of the anodic time on tube diameter (red line) and length (blue line)

#### 4.4.3.3 Effect of AgNPs thickness loaded on the TiO<sub>2</sub> NTs

The amount of AgNPs loaded on the TiO<sub>2</sub> NTs is a crucial factor to obtain highly sensitive SERS substrate with excellent uniformity. Thus, conditions for AgNPs deposition by DC magnetron sputtering were studied in a term of thickness from 3 nm to 17 nm (experiment 3.6.5.3). The Ag thickness was recorded by Direct current magnetron sputtering (EMACE600, Leica). Moreover, the real thickness of AgNPs was also investigated by atomic force microscopy (AFM), which was determined by deposition of Ag on a cleaned silicon wafer that attached partly with a tape. Before measurement, the tape was removed and then the thickness was determined from the height of the step that was operated by the tape. For example, the thickness calculation of AgNPs deposited at a condition of 11 nm recorded by the Leica is displayed in Figure 4.59. It is found that the height of the Si/AgNPs is 22.4 nm (Z2), while the height of 12.1 nm (Z1) was determined at the position that the tape was eliminated. Therefore, it could be calculated that the real thickness of AgNPs was 10.3 nm, which was different from the value obtained by the Leica about 0.7 nm. However, this very small deviations (less than 1 nm) indicated that the value reported by the Leica is reliable.

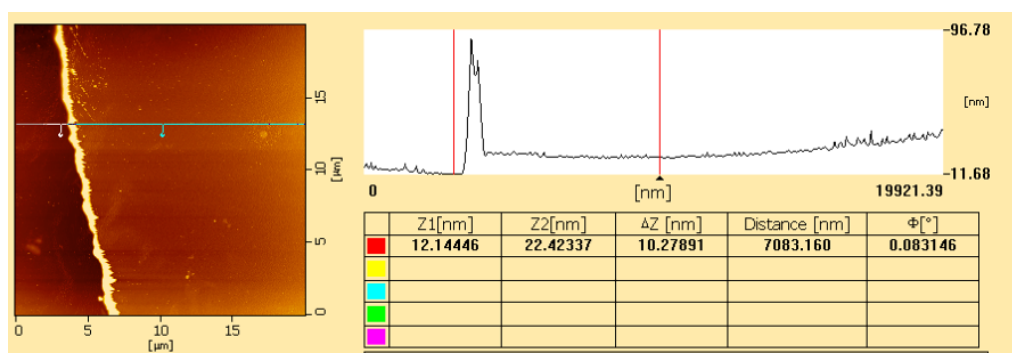


**Figure 4.59** AFM image and the thickness of AgNPs deposited on a Si substrate

The morphology of AgNPs with different thicknesses on the top of TiO<sub>2</sub> NTs was investigated by SEM, as shown in Figure 4.60. It is found that the TiO<sub>2</sub> NTs covered with 3-9 nm of AgNPs exhibited quite same morphology because AgNPs were deposited in the form of ring at the top edges of the nanotubes. The average diameter of single nanoparticles of Ag in case of 3 nm and 5 nm thickness was calculated to be  $17.3 \pm 3.3$  nm and  $21.9 \pm 3.1$  nm, respectively. Meanwhile, the agglomerated AgNPs with the average diameter of  $31.2 \pm 5.2$  nm and  $32.3 \pm 5.0$  nm were obtained in case of 7 nm and 9 nm, respectively. On the other hand, the morphology of the TiO<sub>2</sub> NTs covered with 11-17 nm was similar due to not only single layer of doughnut-like AgNPs formation on the edge of the TiO<sub>2</sub> NTs but also double layer of AgNPs cluster distributed on the Ag interconnected layer. The average diameter of secondary spherical AgNPs were calculated as  $52.0 \pm 8.1$  nm,  $54.8 \pm 7.5$  nm,  $60.2 \pm 12.1$  nm, and  $97.9 \pm 19.1$  nm for thickness of 11, 13, 15, and 17, respectively. Therefore, it can be concluded that the morphology of AgNPs deposited on the TiO<sub>2</sub> NTs is deposition condition-dependent.

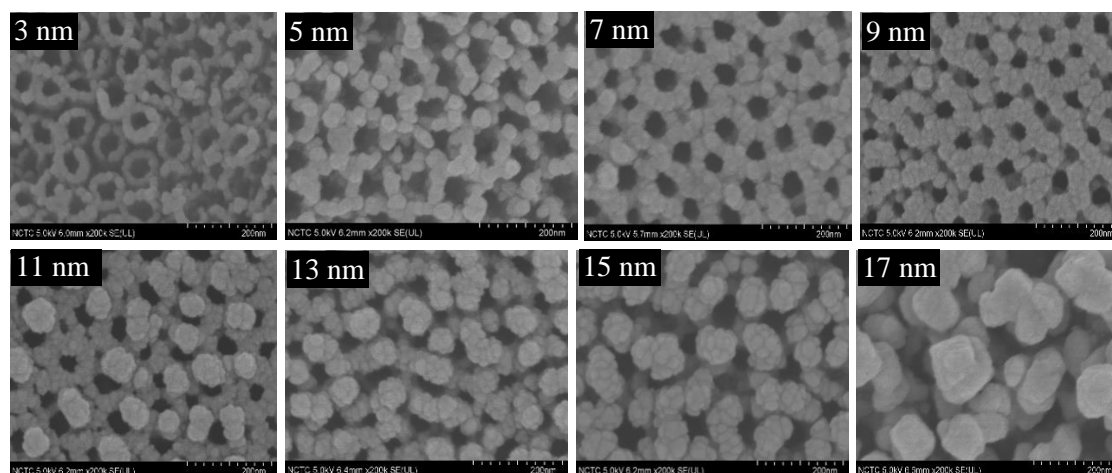


**Figure 4.60** SEM images of a  $\text{TiO}_2$  NTs covered with different thickness of AgNPs

In order to investigate effect of AgNPs amount on SERS performance, Raman intensity of 1 nM MB on the  $\text{TiO}_2$  NTs loaded with different thickness of AgNPs was measured, as can be seen in Figure 4.61 and Table B.47 (Appendix B.4). The results revealed that SERS activity is not proportional to the AgNPs thickness and the greater enhancement were observed on the  $\text{TiO}_2$  NTs covered with 5 nm, 11 nm, 13 nm, and 15 nm thickness of AgNPs. The differences in the SERS intensity could be explained by the geometric configuration of AgNPs coated on the  $\text{TiO}_2$  NTs because the SERS enhancement depends on size, shape, morphology, distribution and  $\text{TiO}_2$  NTs/AgNPs contact surface, which were related to AgNPs deposition conditions. [272] Based on the SEM results, effect of AgNPs thickness could be explained by separation into two groups, which are 3-9 nm and 11-17 nm thickness. In the first group, Raman intensity trends to increase with the increasing thickness of AgNPs, except in case of 5 nm. This is due to smaller inner diameter of nanotubes can promote the electromagnetic field coupling [139] and it is clearly seen that the nanotube diameter is reduced sequentially as the AgNPs thickness increased. By contrast, the highest SERS signal was obtained with the  $\text{TiO}_2$  NTs/AgNPs-5nm because a lot of interspaces between AgNPs created hot spots for SERS more than the others. In the latter group, the Raman scattering signals of double layer AgNPs (11-17 nm) is higher than a single layer (3-9 nm) due to smaller interparticle connection and larger dense plasmonic hot-spots were created in the top secondary layer of AgNPs. Consequently,

local electromagnetic fields were concentrated more significantly, which resulted in stronger SERS enhancement. [273-275] Moreover, many recent works have been proved that multilayer-based SERS substrates demonstrated significant enhancements over comparable single layer substrates. For example, Tang and co-worker [276] presented that the stacked dual-layer metal porous films showed prominent Raman enhancement and ultrasensitive SERS sensing capability than single layer films. However, a reduction of Raman intensity signal was observed in case of the TiO<sub>2</sub> NTs/AgNPs-17nm due to the AgNPs are strongly agglomerated, leading to lower hot-spots. Additionally, the size of AgNPs is not uniform, resulted in larger variation of signal intensity on SERS substrate. In summary, the maximum intensity together with the lowest variations was achieved by using the TiO<sub>2</sub> NTs/AgNPs at 11 nm and this condition provided suitable Ag particle density. Therefore, 11 nm thickness of AgNPs was selected for further measurements.

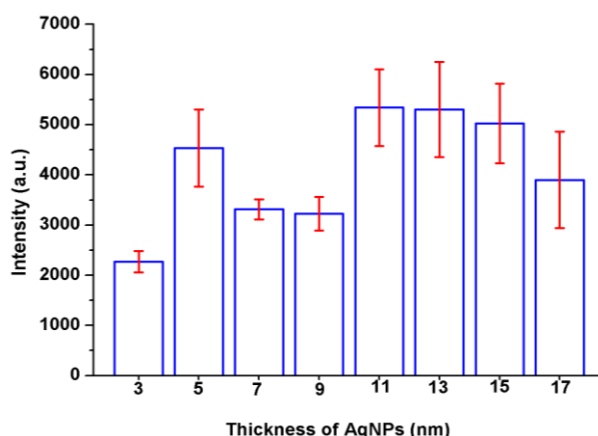


**Figure 4.61 SERS response of the TiO<sub>2</sub> NTs/AgNPs on the detection of 1 nM MB**

#### 4.4.3.4 Effect of rGO amount on the TiO<sub>2</sub> NTs/AgNPs

A rGO film was transferred to cover on the surface of TiO<sub>2</sub> NTs/AgNPs array via electrodeposition method using cyclic voltammetry performed in 0.1 M phosphate buffer solution pH 9.32 containing GO suspension under magnetic stirring. Therefore, the optimum conditions for rGO wrapping were investigated, including concentration of GO and cycles for electrodeposition (experiment 3.6.5.4). The concentration of GO was firstly studied in a range from 0.0 mg/mL to 0.3 mg/mL

and the relationship between the SERS intensity and the GO concentration is displayed Figure 4.62(A) and Table B.48 (Appendix B.4). Raman scattering signal was increased with the increase of GO concentration up to 0.1 mg/mL and decreased afterward. At this condition, the TiO<sub>2</sub> NTs/AgNPs-rGO showed ~2.0 times more enhancement than the TiO<sub>2</sub> NTs/AgNPs because high absorption ability of rGO film could act as an excellent anchor for probe molecules. Furthermore, rGO could promote charge transfer between analytes and the SERS substrate owing to  $\pi$ - $\pi$  delocalization in graphene materials, resulting in enhancing the chemical enhancement mechanism. [277] However, the SERS response of the TiO<sub>2</sub> NTs/AgNPs-rGO was lower than the TiO<sub>2</sub> NTs/AgNPs in case of deposition of 0.3 mg/mL GO because irreversible agglomerates through strong  $\pi$ - $\pi$  restacking and *Van der waals* interactions is easily occurred at higher concentration. As a consequence, the graphene surface supports ineffective adsorption of the MB molecule. [278] Therefore, 0.1 mg/mL of GO was referred as the optimal concentration for the SERS substrate construction.

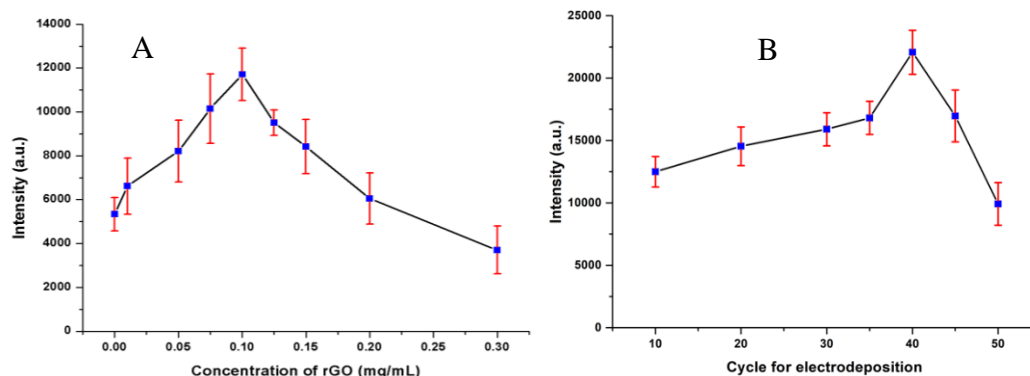


**Figure 4.62 Effects of (A) GO concentration and (B) cycles for electrodeposition of rGO on the TiO<sub>2</sub> NTs/AgNPs on the detection of 1 nM MB**

Next, the effect of cycle numbers for electrodeposition of rGO on the TiO<sub>2</sub> NTs/AgNPs was investigated between 10 and 50 cycles because thickness of rGO film can be controlled by this condition. Figure 4.62(B) and Table B.49 (Appendix B.4) showed correlation between the peak intensity and cycles for GO electrodeposition. It was obviously seen that the maximum SERS intensity was obtained by electrodeposition of rGO for 40 cycles. This result can be explained by SEM images, as

can be seen in Figure 4.63. The  $\text{TiO}_2$  NTs/AgNPs was thoroughly covered by a smooth rGO film in case of deposition for 10 to 35 cycles. Meanwhile, a wrinkled structure of rGO was observed by electrodeposition for 40 to 50 cycles because the rGO film was formed from stacked individual layers of ultra-thin rGO that was created after every single cycle. [279] Therefore, a wrinkled stack of rGO could be observed when the cycle number of electrochemical reductions increased. This means that a wrinkled surface of rGO sheets provided more effective SERS enhancement because it has a higher surface area and provided more contact points between the rGO and MB molecules compared to a smooth surface. [280] Moreover, Sun and et al. [151] revealed that the 3D crumpled graphene hybrid structure showed higher SERS sensitivity than flat hybrid structure. However, the SERS intensity decreased in case of electrodeposition of rGO for 45 and 50 cycles, which was attributed to a thick layer of rGO hindered electromagnetic enhancements of plasmonic AgNPs. [281, 282]

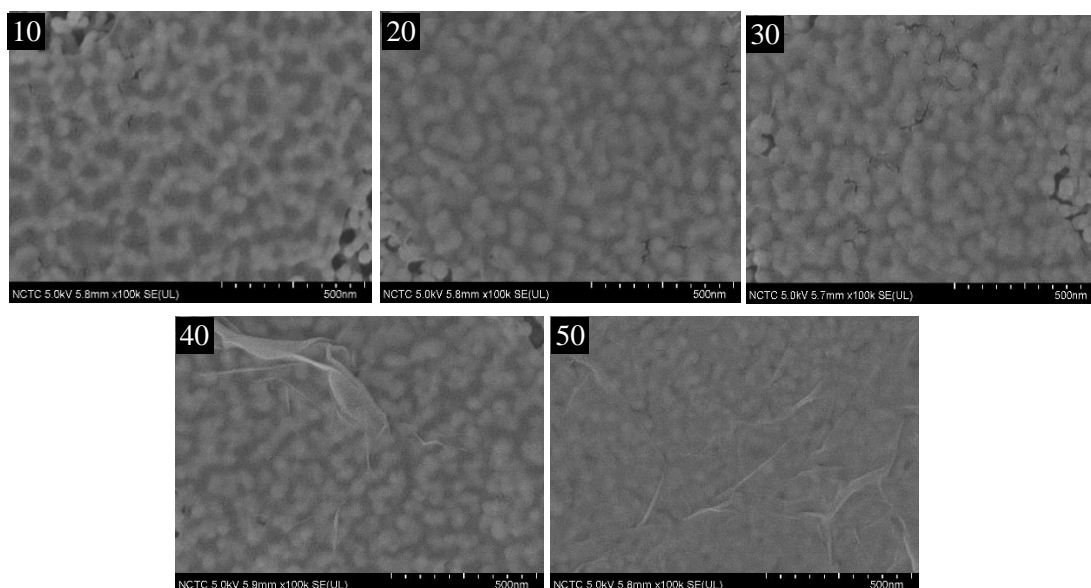


**Figure 4.63 SEM of  $\text{TiO}_2$  NTs/AgNPs-rGO prepared at different electrochemical deposition cycles**

#### 4.4.4 Analytical performance of the $\text{TiO}_2$ NTs/AgNPs-rGO

##### 4.4.4.1 Performance of the $\text{TiO}_2$ NTs/AgNPs-rGO

In order to confirm that the  $\text{TiO}_2$  NTs/AgNPs-rGO possesses the best SERS performance, the Raman signal obtained from the  $\text{TiO}_2$  NTs/AgNPs-rGO



substrate was compared to the TiO<sub>2</sub> film, TiO<sub>2</sub> NTs, TiO<sub>2</sub> film/rGO, TiO<sub>2</sub> NTs/rGO, TiO<sub>2</sub> film/AgNPs, TiO<sub>2</sub> NTs/AgNPs, and TiO<sub>2</sub> film/AgNPs-rGO substrates (experiment 3.6.6.1). Figure 4.64 and Table B.50 (Appendix B.4) showed the Raman scattering intensity of 1 mM MB on the different substrates. It is found that Raman signal of MB can be observed on the TiO<sub>2</sub> film substrate, indicating that the TiO<sub>2</sub> semiconductor could contribute Raman enhancement. This can be ascribed to charge transfer mechanism between TiO<sub>2</sub> semiconductor and MB molecule, in which electrons in the valence band of TiO<sub>2</sub> are excited to the conduction band by incident light and then injected into the LUMO of the adsorbed molecules. [152] Additionally, it is observed that MB molecule exhibits a larger SERS enhancement on TiO<sub>2</sub> NTs substrate compared to the TiO<sub>2</sub> film. This improvement is due to the tubular morphology of the TiO<sub>2</sub> allows a specific arrangement of AgNPs that creates many SERS hot-spots. [283] Moreover, the strong coupling of electromagnetic field can be occurred at the gaps between closely neighboring nanotubes. [284] Overall, the highest SERS activity is achieved on the TiO<sub>2</sub> NTs/AgNPs-rGO substrate. This behavior could be explained from the fact that MB molecule is effectively absorbed on the substrate because of a large specific surface area and excellent absorption capacity of rGO film. Moreover, rGO can promote chemical enhancement based on charge transfer mechanism between the substrate and the target molecules owing to the large  $\pi$ - $\pi$  conjugations in graphene structure. Meanwhile, AgNPs improve the SERS activity markedly due to surface plasmonic property of Ag material which is amplifier the electromagnetic mechanism in SERS system. Additionally, double layers of AgNPs decorated on the TiO<sub>2</sub> NTs provide a pretty rough surface and appropriate interparticle gap that would create higher density SERS hot-spots. Therefore, this is an evident demonstrated that the TiO<sub>2</sub> NTs/AgNPs-rGO substrate boosts significant enhanced SERS intensity, which is originated from the chemical enhancement as a result of introducing TiO<sub>2</sub> NTs array and rGO sheets, and electromagnetic enhancement generated from plasmonic AgNPs. Moreover, Wang and et al. [158] presented that SERS performance of the substrate was significantly improved due to the dominant contribution of chemical enhancement of rGO and TiO<sub>2</sub> nanorod array, and electromagnetic enhancement of Ag nanomaterials.

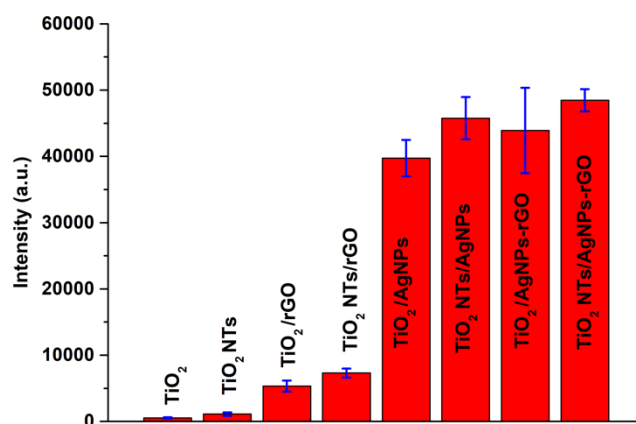


**Figure 4.64 SERS responses of the different substrates on 1 mM MB detection**

#### 4.4.4.2 Linear range and detection limit of the TiO<sub>2</sub> NTs/AgNPs-rGO

The SERS enhancement performance of the TiO<sub>2</sub> NTs/AgNPs-rGO substrate was verified by measuring MB probe molecule at different concentration from  $10^{-1}$  to  $10^{-13}$  M (experiment 3.6.6.2). The Raman characteristic peak located at  $1624\text{ cm}^{-1}$ , which correlated to C-C ring stretching in the MB structure, was employed for investigation. It is found that the Raman intensities gradually decreased with the decreasing concentration of MB (Figure 4.65(A)), suggesting that the intensity is directly proportional to the amount of probe molecules. At lower concentrations, the D ( $1361\text{ cm}^{-1}$ ) and G ( $1603\text{ cm}^{-1}$ ) Raman bands of rGO was observable. However, this rGO background signal didn't limit the performance of the substrate. As shown in Figure 4.65(B) and Table B.51 (Appendix B.4), a good linear relationship between the SERS intensities and the logarithms of MB concentration is obtained in the range from  $10^{-2}$  to  $10^{-12}$  M. According to the linear fitting lines, the fitted equation is expressed by  $I_{1624} = 4303.4 \log C + 59381.0$  with  $R^2$  of 0.991. In order to investigate the detection limit (LOD) of MB, the Raman signals of background are detected for 20 repetitions ( $n=20$ ). Then, the LOD is calculated based on the definition of the international union of pure and applied chemistry (IUPAC), as can be seen the detailed information below the Table 4.11 (Appendix B.4). Here, LOD of the TiO<sub>2</sub> NTs/AgNPs-rGO substrate for MB detection is obtained as low as  $10^{-14}$  M. The proposed SERS-based sensor exhibited higher sensitivity for detection of dye molecules than the previous researches listed in Table 2.7.

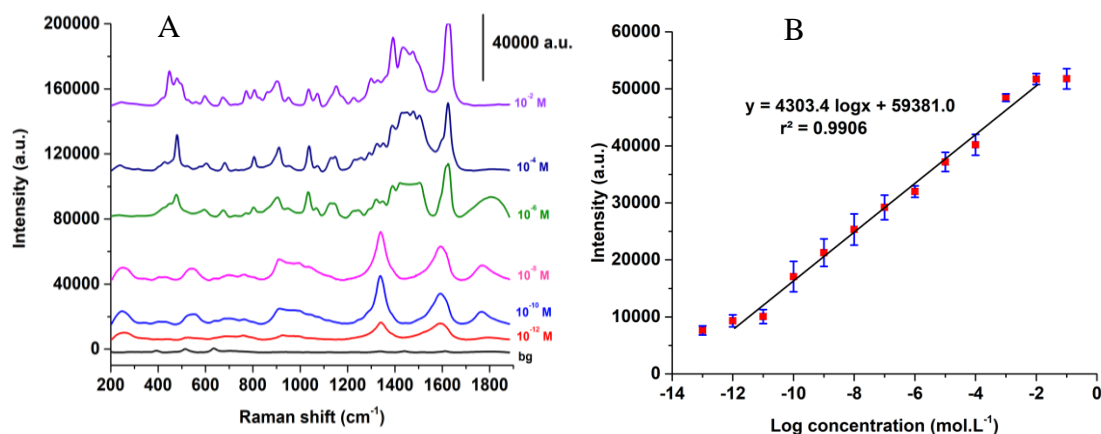


**Figure 4.65 (A) SERS spectra of MB with different concentrations on the TiO<sub>2</sub> NTs/AgNPs-rGO and (B) its corresponding calibration curve**

#### 4.4.4.3 Enhancement factor

The enhancement ability of the TiO<sub>2</sub> NTs/AgNPs-rGO is evaluated by calculating the analytical enhancement factor (AEF). The AEF values can be estimated by using the Equation 4.14. Where  $I_{\text{SERS}}$  and  $I_{\text{NRS}}$  are the Raman intensities at 1624 cm<sup>-1</sup> of MB deposited onto TiO<sub>2</sub> NTs/AgNPs-rGO and bare Ti substrates, respectively.  $C_{\text{SERS}}$  and  $C_{\text{NRS}}$  is the corresponding concentration of MB deposited, which is 1 nM for SERS substrate and 0.1 M for bare Ti substrate.

$$\text{AEF} = \frac{I_{\text{SERS}}}{I_{\text{NRS}}} \times \frac{C_{\text{NRS}}}{C_{\text{SERS}}} \quad (4.14)$$

The calculated AEF value of the TiO<sub>2</sub> NTs/AgNPs-rGO was found to be  $7.1 \times 10^8$  (Table B.52 (Appendix B.4)), which is lower than most of the previous works presented in Table 2.7. However, the Raman enhancement factor of this presented substrate is lower than the substrates fabricated by Xiao and et al. (sulfonated-rGO/AgNPs). [147] The enhancement factor of the sulfonated-rGO/AgNPs was calculated to be as large as  $10^9$ . The extremely high SERS enhancement was resulted from closely-packed AgNPs are assembled on the wrinkled sulfonated-rGO thin film surface. Therefore, larger dense plasmonic hot-spots were created on the sulfonated-rGO/AgNPs substrate than the designed TiO<sub>2</sub> NTs/AgNPs-rGO.

#### 4.4.4.4 Repeatability and reproducibility of the TiO<sub>2</sub> NTs/AgNPs-rGO

The repeatability and reproducibility of the TiO<sub>2</sub> NTs/AgNPs-rGO for detection of 1 mM MB were evaluated by both spot-to-spot and batch-to-batch (experiment 3.6.6.4 and Table B.53 (Appendix B.4)). The repeatability of the TiO<sub>2</sub> NTs/AgNPs-rGO was tested by calculating the relative standard deviation (RSD) of the SERS signals collected from twenty different positions ( $n=20$ ) in an area of  $30\times 30\text{ }\mu\text{m}$  on the same substrate. As shown in Figure 4.66(A), the profiles of the Raman spectra obtained from different spots are very similar and the RSD value of a characteristic peak at  $1624\text{ cm}^{-1}$  is calculated to be 4.4%, indicating a well homogenous property of the TiO<sub>2</sub> NTs/AgNPs-rGO. Meanwhile, reproducibility of the SERS substrate was evaluated on the different TiO<sub>2</sub> NTs/AgNPs-rGO substrates in ten batches ( $n=10$ ). The RSD value was obtained as 2.0% according to the Raman intensity distribution of the band at  $1624\text{ cm}^{-1}$  (Figure 4.66(B)), confirming that the TiO<sub>2</sub> NTs/AgNPs-rGO substrate possesses a good reproducibility because a good value should be less than 5%. The excellent precision of the proposed SERS substrate is resulted from a well-ordered array of the TiO<sub>2</sub> NTs induces a highly uniform arrangement of AgNPs. Moreover, precision of the TiO<sub>2</sub> NTs/AgNPs-rGO is better than the sulfonated-rGO/AgNPs substrate (repeatability of 7.9% and reproducibility of 3.4%), [147] even if the enhancement factor of our sensor is lower.

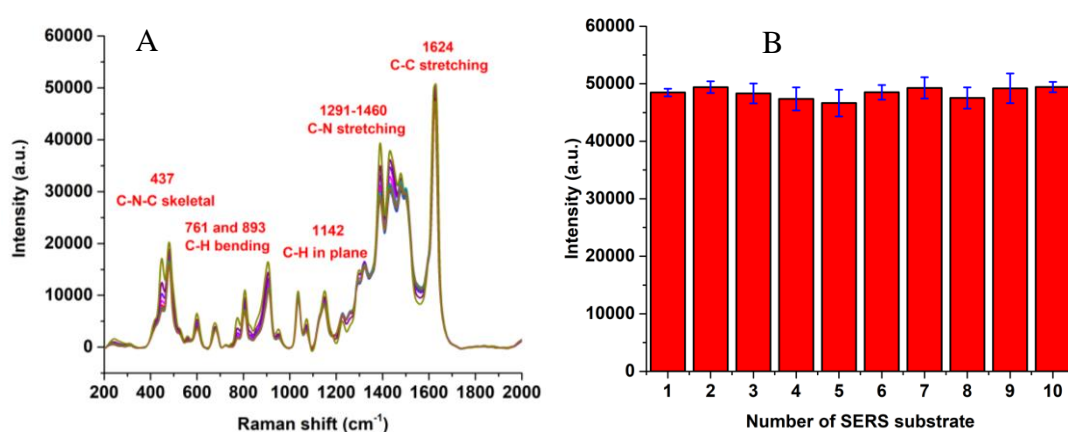


**Figure 4.66** (A) SERS spectra collected from twenty different positions of 1 mM MB on the same TiO<sub>2</sub> NTs/AgNPs-rGO substrate and (B) SERS intensity at  $1624\text{ cm}^{-1}$  band obtained from ten different substrates

#### 4.4.4.5 Stability of the TiO<sub>2</sub> NTs/AgNPs-rGO

An important requirement for SERS based sensor is stability. Generally, Ag nanomaterials can be easily oxidized in air, leading to the Raman signal is reduced and the application of Ag-based SERS substrate for long-time analysis is limited. [138] In order to confirm that the storage stability of the TiO<sub>2</sub> NTs/AgNPs-rGO substrate is improved because of the introduction of rGO on the top layer above AgNPs, a time-dependent SERS measurement of the TiO<sub>2</sub> NTs/AgNPs-rGO was investigated within 30 days compared to TiO<sub>2</sub> NTs/AgNPs (experiment 3.6.6.5). These substrates were kept under air ambient condition without any light or moisture protection when not in use. Figure 4.67(A) and Table B.54 (Appendix B.4) show the Raman intensity of 1 mM MB at a characteristic peak of 1624 cm<sup>-1</sup> obtained from the TiO<sub>2</sub> NTs/AgNPs and TiO<sub>2</sub> NTs/AgNPs-rGO. It is found that SERS intensities of MB detected on the TiO<sub>2</sub> NTs/AgNPs substrate had dramatically decreased with time, which is reduced by 55.1% after exposure to the common air environment for 30 days. In contrast, the SERS intensities of MB on the TiO<sub>2</sub> NTs/AgNPs-rGO have varied less than 6.0 %RSD (bath-to-bath) after 30 days of storage. This is an evident proved that rGO is very effective materials that can protect the oxidation of AgNPs. Additionally, long-term stability of the TiO<sub>2</sub> NTs/AgNPs-rGO substrate was further tested and the results revealed that the SERS signals decreased 8.1% after 180 days (Figure 4.67(B)), indicating that the TiO<sub>2</sub> NTs/AgNPs-rGO is very stable. The utilization of graphene materials as the protective layer to maintain the stability of the develop SERS-active platforms has been reported so far. For example, Jiang and et al. [138] presented that the Raman intensity measured on AgNPs decreased to 97% while that one measured in GO-AgNPs substrate has decreased by 15% after 240 days. Lu and et al. [285] demonstrated that the covered GO film not only provide an additional enhancement for the SERS signal from chemical enhancement mechanism, but also ensure the stability of the GO-AgNPs hybrids from the oxidation. They found that the detection limit of the GO-AgNPs could be down to 10<sup>-14</sup> M, which is one order of magnitude lower than that of the AgNPs substrate and the SERS signals on the AgNPs substrate was dropped by 44.7%, while the decrease of the Raman intensity on the GO-AgNPs was only 8.4% under the exposure to the common air environment for 15 days.

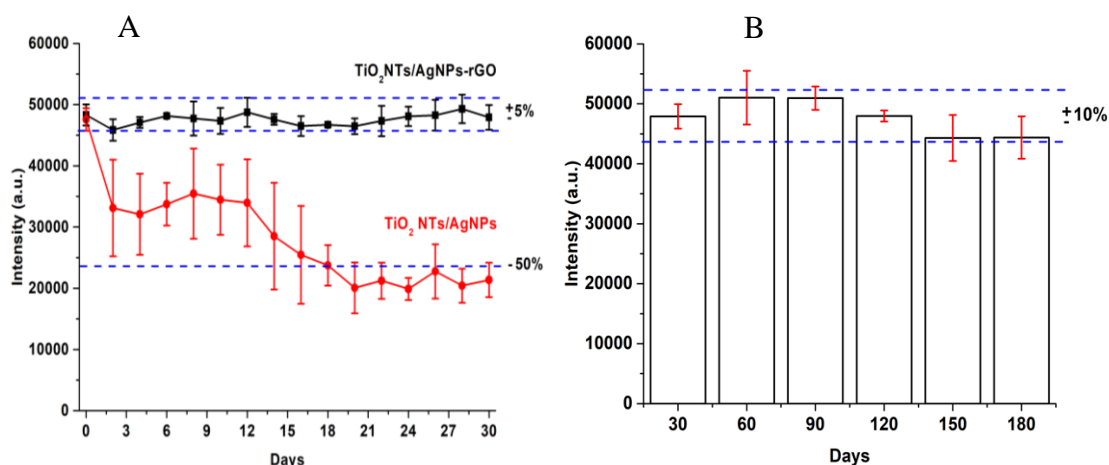


**Figure 4.67 (A) Stability of the TiO<sub>2</sub> NTs/AgNPs and TiO<sub>2</sub> NTs/AgNPs-rGO and (B) long-term stability of the TiO<sub>2</sub> NTs/AgNPs-rGO on 1 mM MB detection**

#### 4.4.4.6 Reusability of the TiO<sub>2</sub> NTs/AgNPs-rGO

TiO<sub>2</sub> semiconductor material was selected as a building blocks for construction of SERS substrate due to its large bandgap that provides an excellent photocatalyst activity. [286] As a result, the TiO<sub>2</sub> based SERS substrate normally exhibits recyclability for reuse because of photodegradation process. Herein, the recyclability of the TiO<sub>2</sub> NTs/AgNPs-rGO after detection of 1 mM MB was investigated by irradiation with Xenon arc lamp for 120 minutes (experiment 3.6.6.6). The SERS signal of MB was completely degraded to be small molecules [287, 288] (Figure 4.69(C)) after visible light illumination within 120 minutes while three main Raman characteristic peaks of anatase TiO<sub>2</sub> (408, 528, and 647 cm<sup>-1</sup>) and two characteristic bands of rGO (D and G peak), which is similar to the background of freshly prepared TiO<sub>2</sub> NTs/AgNPs-rGO, were preserved (Figure 4.68(A) and Table B.55 (Appendix B.4)). After each self-cleaning, the SERS signals corresponding to MB could be recovered, in which the signal intensities of each test are almost the same to the new substrate. This means that the MB molecules are decomposed during the recycle process and this cleaned SERS substrate can be successfully reused. The recyclable efficiency was calculated as 96.4% after recycle for 3 times using the intensities of the characteristic peak at 1624 cm<sup>-1</sup>. The intensity reduction after reuse for 2-3 cycles is due

to the decrease of SERS hot-spots caused by the aggregation of AgNPs, as can be seen in the SEM images (Figure 4.68(B)), because the SERS substrate was immersed into water during photodegradation process and the AgNPs were deposited on the TiO<sub>2</sub> NTs by physical method. Consequently, the prepared AgNPs will be dispersed and easily aggregated in the wetting condition. Furthermore, Tang and et al. [289] revealed that a removal efficiency of almost 100% was obtained after 160 minutes UV-irradiation on the TiO<sub>2</sub> NTs/rGO-AgNPs and this substrate exhibited much higher degradation efficiency of 2,4- D herbicide than both TiO<sub>2</sub> NTs/rGO and TiO<sub>2</sub> NTs/AgNPs because of a synergetic effect between rGO and AgNPs, which was benefited from high charge separation of rGO and light-harvesting property of AgNPs.

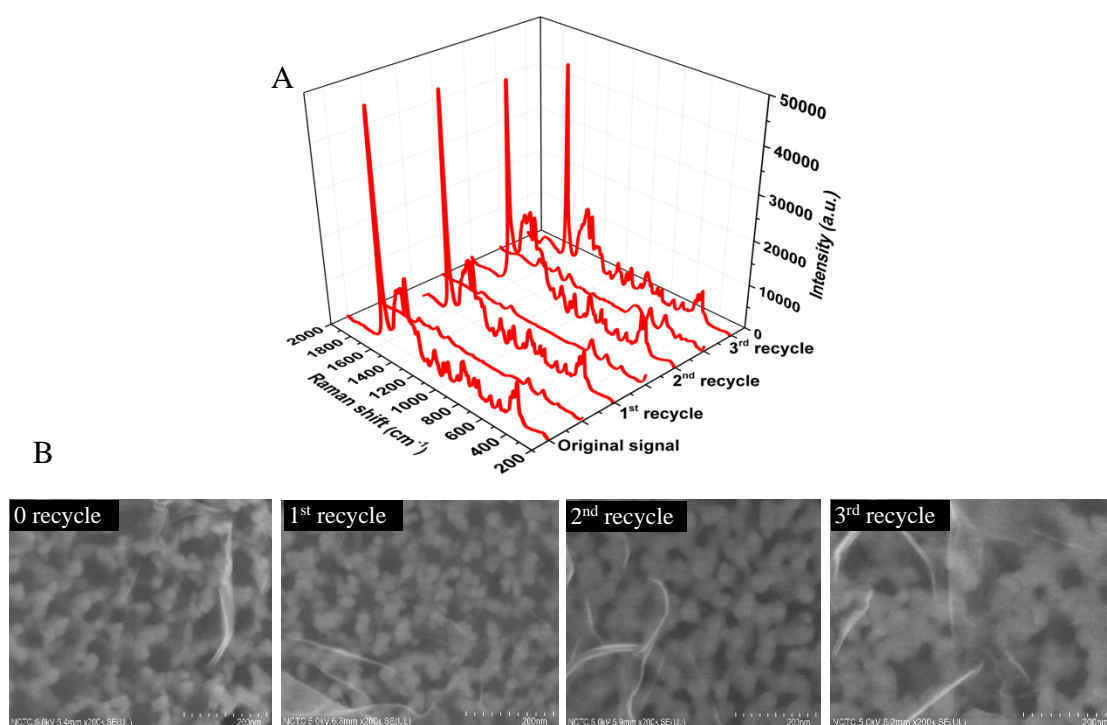


**Figure 4.68** (A) SERS spectra of MB (1 mM) adsorbed on the TiO<sub>2</sub> NTs/AgNPs-rGO and (B) SEM images of the TiO<sub>2</sub> NTs/AgNPs-rGO surface before and after Xenon arc lamp irradiation by repeating for 3 cycles

The mechanism of the photocatalytic activity of the TiO<sub>2</sub> NTs/AgNPs-rGO could be explained based on the Schottky barriers and energy band diagram, as can be seen in Figure 4.69(A). Firstly, the TiO<sub>2</sub> NTs adsorbs photon and

produces electrons ( $e^-$ ) and holes ( $h^+$ ) under visible light irradiation. The photogenerated electrons transfer from the  $\text{TiO}_2$  NTs/Ti conduction band to AgNPs due to the work function of Ag materials (4.26 eV) is higher than the conduction band of the  $\text{TiO}_2$  semiconductor (4.20 eV). [290] Then, the electrons move through the  $\text{TiO}_2$  NTs/AgNPs interface to rGO due to higher work function of rGO nanomaterials (4.40 eV). [291] After that, those electrons are accumulated on the top layer surface of rGO and subsequently captured by dissolved oxygens, resulting in superoxide radical anions ( $\text{O}_2^{\bullet-}$ ) formation. Then, the produced radical interacts to water in applied condition, producing hydroxyl radicals ( $\bullet\text{OH}$  and  $\bullet\text{OH}_2$ ) and hydrogen peroxide ( $\text{H}_2\text{O}_2$ ). Meanwhile, adsorbed water ( $\text{H}_2\text{O}$ ) or hydroxy ions ( $\text{OH}^-$ ) interacts with the corresponding holes at the valence band of the  $\text{TiO}_2$  semiconductor, resulting in  $\bullet\text{OH}$  production. The generated  $\bullet\text{OH}$  radicals are very powerful oxidizing agents that can facilitate the oxidative degradation of MB. [158, 290] Figure 4.69(B) demonstrates the detailed reaction mechanisms of the photocatalytic activity of the  $\text{TiO}_2$  NTs/AgNPs-rGO. [289]

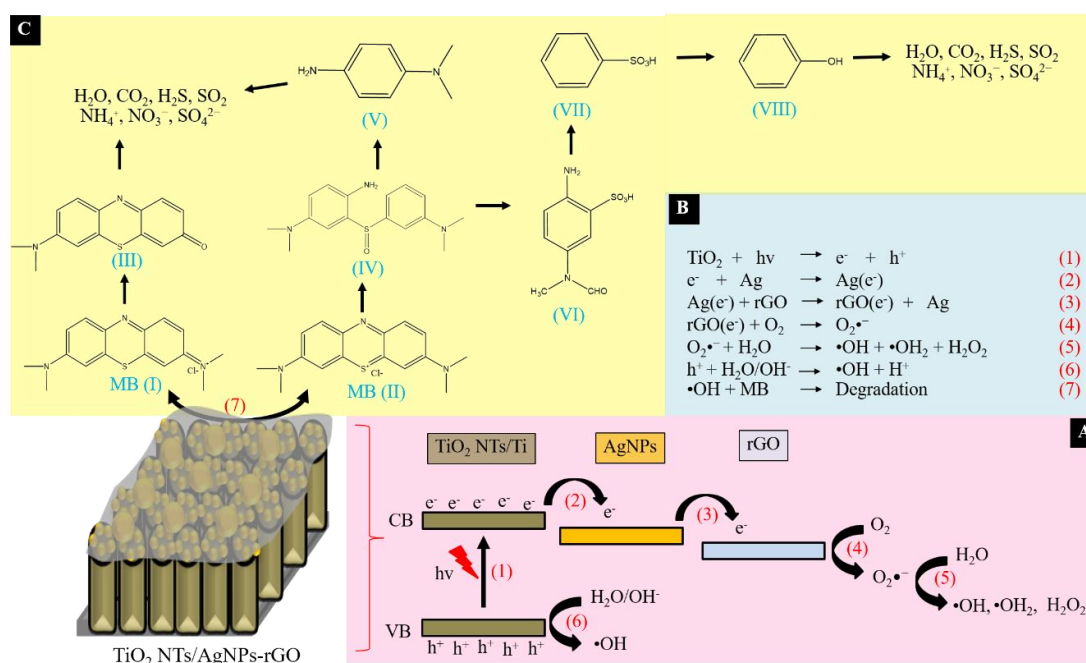


**Figure 4.69** (A) Diagrams of electron and hole transfer in the  $\text{TiO}_2$  NTs/AgNPs-rGO and (B) its reaction mechanisms; (C) possible degradation mechanism of MB under visible light irradiation



Two possible mechanisms for MB degradation could be occurred via interchangeable forms of MB (MB I and MB II), as displayed in Figure 4.69(C). [287, 288] Referring to the MB I form, the active super oxide radicals catalyze oxidation reaction of MB via attacking the  $\text{CH}_3\text{-N}^+\text{-CH}_3$  functional group. As a result, the MB I compound is transformed to methylene violet (III) and then subsequently degraded into small molecules. All the processes produce water ( $\text{H}_2\text{O}$ ), gaseous ( $\text{CO}_2$ ,  $\text{H}_2\text{S}$ ,  $\text{SO}_2$ ) and inorganic ions ( $\text{NH}_4^+$ ,  $\text{NO}_3^-$ ,  $\text{SO}_4^{2-}$ ). According to the MB II form, the active radicals interacts to the  $\text{C-S}^+=\text{C}$  functional group, leading to the central aromatic ring is opened and 3-(3-(dimethylamino)phenylsulfinyl)- $\text{N}^1, \text{N}^1$ -dimethylbenzene-1,4-diamine (IV) was obtained. Then, this (IV) compound could be oxidized to N,N-dimethyl-p-phenylenediamine (V), which is subsequently degraded to small molecules, or 2-amino-5-(N-methylformamido) benzenesulfonic acid (VI), which is sequentially oxidized to benzene sulfonic acid (VII) and phenol (VIII). All the decomposed steps generate those small molecules. Since the small molecules have weak Raman signals and can be removed easily from the substrate by washing, therefore the SERS signals are disappeared after irradiation to visible light.

#### 4.4.4.7 Commercial SERS substrates comparison

Performances of the  $\text{TiO}_2$  NTs/AgNPs-rGO included enhancement factor (EF), repeatability (spot-to-spot), reproducibility (batch-to-batch), and stability were compared to the commercial SERS substrates. Three SERS substrates were purchased from ATOID<sup>TM</sup>, Ocean optics, and Hamamatsu company. MB (1 mM) was employed as a Raman active molecule to investigate performances of the prepared  $\text{TiO}_2$  NTs/AgNPs-rGO and the three commercial substrates (experiment 3.6.6.7). In order to compare the enhancement ability, enhancement factor (EF) was calculated according the Equation 4.15. Where  $I_{\text{SERS}}$  and  $I_{\text{NRS}}$  are the Raman intensities at  $1624\text{ cm}^{-1}$  of MB deposited on the SERS substrate and bare silicon wafer, respectively.  $N_{\text{SERS}}$  is the number of the single-layer molecules covering the SERS substrate under the laser spot (laser spot area of  $0.9\text{ }\mu\text{m}^2$ ), which was calculated by the Equation 4.16. Referring to the literature reviews. [292, 293] the area of a single molecule of MB was calculated to be approximately  $2\text{ nm}^2$ . Therefore, the  $N_{\text{SERS}}$  value was estimated as  $0.45 \times 10^6$ . The  $N_{\text{NRS}}$  is the number of MB molecules excited by laser on the surface of the silicon wafer substrate, which was calculated from the Equation 4.17. Where, the Avogadro's number,

molar concentration of MB, volume of MB solution, laser spot area, and surface area of MB molecules adsorbed on the silicon wafer are  $6.022 \times 10^{23}$  molecules,  $10^{-3}$  mol/L, 5  $\mu\text{L}$ ,  $0.9 \mu\text{m}^2$ , and  $3.14 \text{ mm}^2$ , respectively. Therefore, the  $N_{\text{NRS}}$  value is estimated as  $8.63 \times 10^8$ .

$$\text{AEF} = \frac{I_{\text{SERS}}}{I_{\text{NRS}}} \times \frac{N_{\text{NRS}}}{N_{\text{SERS}}} \quad (4.15)$$

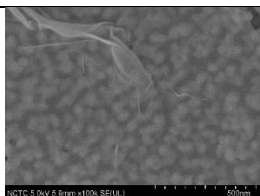
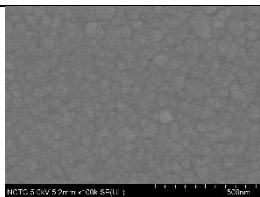
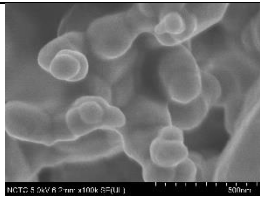
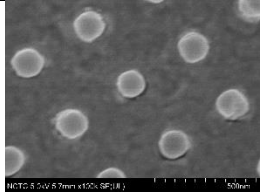
$$N_{\text{SERS}} = \frac{\text{Laser spot area}}{\text{MB monolayer}} \quad (4.16)$$

$$N_{\text{NRS}} = \frac{(\text{Avogadro's number})(\text{molar concentration})(\text{volume})(\text{Laser spot area})}{\text{surface area of MB molecules adsorbed on the substrate}} \quad (4.17)$$

The EF values of the  $\text{TiO}_2$  NTs/AgNPs-rGO and the three commercial SERS substrates are reported in Table 4.4 (Table B.56, Appendix B.4). It is observed that the EF value of the  $\text{TiO}_2$  NTs/AgNPs-rGO substrate is larger than the three commercial SERS substrates, which is attributed to a utilization of three nanomaterials. The strong enhancement arises from chemical enhancement produced by rGO and  $\text{TiO}_2$  NTs array, and electromagnetic enhancement from AgNPs. Moreover, it is clearly seen from the surface morphology measured by SEM that the plasmonic nanoparticles arranged more closely on the  $\text{TiO}_2$  NTs/AgNPs-rGO, resulting in a greater number of hot-spots were created over the  $\text{TiO}_2$  NTs/AgNPs-rGO. In term of precision, it is not surprised that the  $\text{TiO}_2$  NTs/AgNPs-rGO and ATOID<sup>TM</sup> SERS substrate had an excellent repeatability and reproducibility because of a uniformly packed AgNPs. By contrast, the SERS substrate fabricated by the Ocean optics offers a pretty poor precision both across a single substrate and between different substrate. This might be due to the AgNPs were prepared by chemical reduction method and then they are loaded on the paper platform by drop-casting method. Therefore, the distribution of AgNPs on the paper surface is uncontrollable. In case of Hamamatsu SERS substrate, the RSD value for repeatability study is almost 10%. This might be due to a gap between nanoparticles is too large, leading to a significant fluctuation on randomly selected positions is easily obtained. On the other hand, the reproducibility of the Hamamatsu SERS substrate is very good, which is better than the designed  $\text{TiO}_2$  NTs/AgNPs-rGO.

This can be explained from the fact that Au nanostructure is formed by highly uniform nanoimprinted technology. Additionally, Hamamatsu SERS substrate is prepared in just one step, while there are three steps to fabricate the TiO<sub>2</sub> NTs/AgNPs-rGO substrate.

**Table 4.4 Comparison of EF, repeatability, reproducibility, and stability between the prepared TiO<sub>2</sub> NTs/AgNPs-rGO and commercial substrates**

Substrate	Surface morphology	EF	Precision (%RSD)	Stability (%retained for 30 days)
TiO <sub>2</sub> NTs/ AgNPs-rGO		$3.8 \times 10^5$	4.4% (spot-to-spot) 2.0% (batch-to-batch)	99.2%
Silicate glass/ AgNPs (AtoID™)		$2.4 \times 10^5$	4.9% (spot-to-spot) 2.1% (batch-to-batch)	97.6%
Paper/AgNPs (Ocean optics)		$7.2 \times 10^4$	10.2% (spot-to-spot) 11.3% (batch-to-batch)	84.8%
Polypropylene/ AuNPs (Hamamatsu)		$1.2 \times 10^5$	9.6% (spot-to-spot) 1.3% (batch-to-batch)	99.7%

Furthermore, stability of the prepared TiO<sub>2</sub> NTs/AgNPs-rGO substrate was also compared to the commercial substrates. It is found that SERS signals for MB molecules on the AtoID™ and Ocean optics were decreased obviously after 30 days because AgNPs could be easily oxidized. On the contrary, the SERS activity decreased by only 0.3% on the Hamamatsu SERS substrate because Au nanomaterial is

much more oxidation-resistant than Ag material. [294] Meanwhile, the TiO<sub>2</sub> NTs/AgNPs-rGO offers a pretty well stability because of a utilization of rGO as already described in the part 4.4.4.5.

#### **4.4.5 Analytical performance of the SERS sensor for glyphosate detection**

##### **4.4.5.1 Linear range and detection limit for glyphosate detection**

The analytical performance of the TiO<sub>2</sub> NTs/AgNPs-rGO substrate for determination of glyphosate herbicide, including linearity and LOD, were evaluated (experiment 3.6.7.1). Figure 4.70(A) shows that the SERS intensities at a characteristic peak of 920 cm<sup>-1</sup>, which was assigned to the symmetric stretching of PO<sub>2</sub>, [295] increased with the increasing of glyphosate concentrations. The SERS signal exhibited a good linear relation with the glyphosate concentration in the range from 0.1 to 100 mg/L (Figure 4.70(B) and Table B.57 (Appendix B.4)). Additionally, the LOD for detection of glyphosate using the TiO<sub>2</sub> NTs/AgNPs-rGO sensor was obtained as 0.05 mg/L, which was calculated based on signal-to-noise (3S/N) (Table B.58, Appendix B.4). This LOD is well below than a maximum contaminant level of glyphosate in drinking water (0.7 mg/L) and soil (2 mg/kg) set by the U.S. national primary, and a maximum residue limits (MRL) in crops (0.1-5.0 mg/kg) as reported by the United Nations Food and Agricultural Organization. [94] Furthermore, the designed SERS sensor possessed higher sensitivity than the previous developed SERS sensors for detection of glyphosate. For example, Sharma and et al. [159] proposed that the SERS sensor based on Cu-grids modified Ag dendrites provided the LOD for glyphosate detection as 0.85 mg/L. Xu and et al. [160] reported that the LOD of SERS sensor-based on AgNPs for indirect detection of glyphosate based on ninhydrin reaction was obtained as 2.41 mg/L. Therefore, it can be concluded that the designed TiO<sub>2</sub> NTs/AgNPs-rGO based SERS sensor is effective for sensitive detection of glyphosate herbicide.

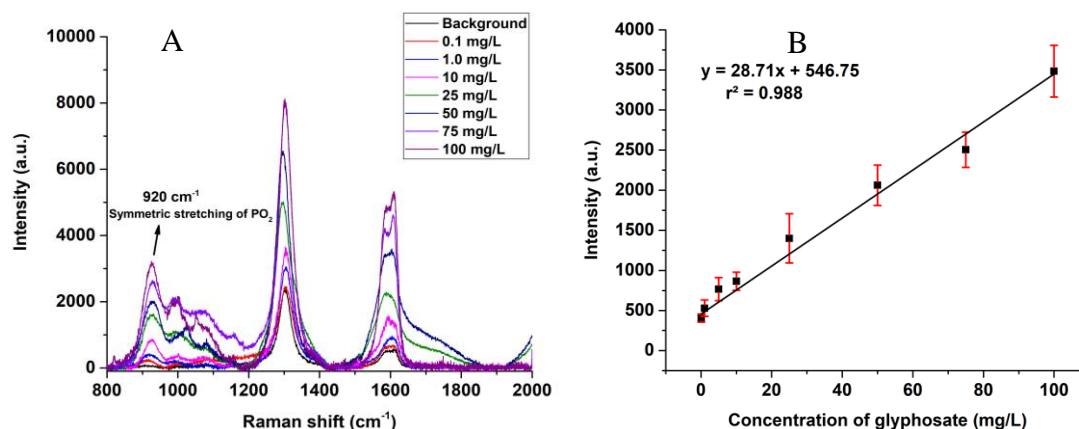


**Figure 4.70 (A) SERS spectra of glyphosate with different concentrations and (B) its corresponding calibration curve**

#### 4.4.5.2 Selectivity of the TiO<sub>2</sub> NTs/AgNPs-rGO based SERS sensor

Effect of interferences on the detection of glyphosate (10 mg/L) using the TiO<sub>2</sub> NTs/AgNPs-rGO substrate were investigated (experiment 3.6.7.2). Formulation of glyphosate herbicide (POEA), precursor for glyphosate production (glycine), and other categories of pesticides, such as organophosphorus (chlorpyrifos), organochlorine (paraquat), and carbamate (carbaryl, carbendazim) pesticides, were tested at the same concentration level with glyphosate (10 mg/L). Moreover, common inorganic compounds normally found in environmental samples, such as KPO<sub>4</sub>, NaSO<sub>4</sub>, MgSO<sub>4</sub>, CuSO<sub>4</sub>, KNO<sub>3</sub>, NaNO<sub>3</sub>, ZnNO<sub>3</sub>, CaCO<sub>3</sub>, KCl, NaCl, and CaCl<sub>2</sub>, were investigated at different concentrations (50 and 100 mg/L). The SERS signal toward the detection of standard pure glyphosate was compared to the signals of glyphosate co-existed with interferent compounds, as showed in Figure 4.71 and Table B.59 (Appendix B.4). It is found that the SERS intensities had changed less than  $\pm 5\%$  after the co-presence of 1-fold concentration of POEA, glycine, chlorpyrifos, paraquat, carbaryl, and carbendazim. Meanwhile, KPO<sub>4</sub> substance did not interfere glyphosate detection at the 5-fold concentration higher and almost negligible changes in the SERS intensities were detected among the co-presence of 100 mg/L NaSO<sub>4</sub>, MgSO<sub>4</sub>, CuSO<sub>4</sub>, KNO<sub>3</sub>, NaNO<sub>3</sub>, ZnNO<sub>3</sub>, CaCO<sub>3</sub>, KCl, NaCl, and CaCl<sub>2</sub>. This can be summarized that the designed SERS sensor exhibited acceptable selectivity towards glyphosate detection and can be applied for glyphosate determination in environments.

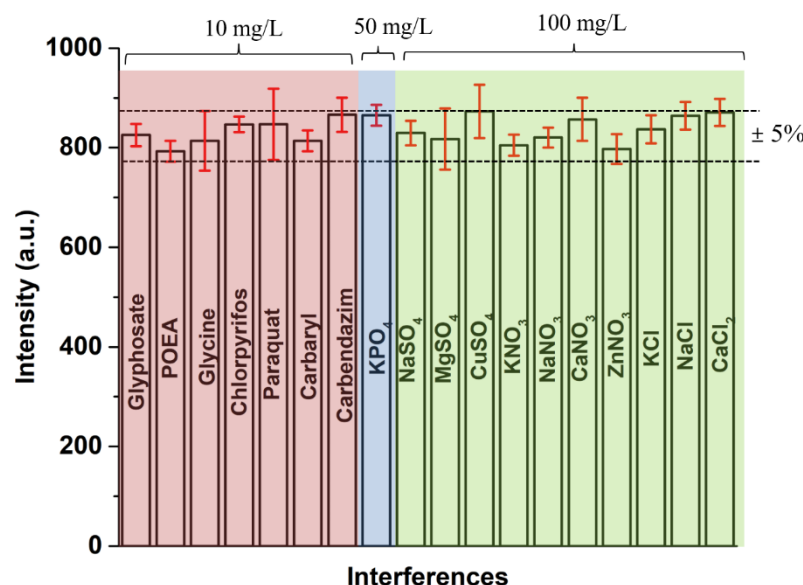


**Figure 4.71** Effect of interferences on the response of the TiO<sub>2</sub> NTs/AgNPs-rGO

#### 4.4.6 Determination of glyphosate in real samples by the SERS based sensor

In order to demonstrate the application of the SERS-based sensor for glyphosate detection in the real samples. The proposed TiO<sub>2</sub> NTs/AgNPs-rGO substrate was applied for the determination of glyphosate in environmental waters and soils by external calibration method (experiment 3.6.8). The SERS signals of glyphosate in real samples are analyzed in triplicate using the calibration plot, as shown in Figure 4.69. It is found that  $1.65 \pm 0.17$  mg/kg glyphosate was determined in the soil sample A. However, the detected concentration is below a maximum contaminant level of glyphosate in soil (2 mg/kg) set by the U.S. national primary. [94] Furthermore, the collected water and soil samples were spiked with varying concentrations of glyphosate (0.5 and 1.0 mg/L for water, 2 and 4 mg/kg for soil) in order to evaluate accuracy of the SERS-based sensor. The results are presented in Table 4.5 and Table B.60 (Appendix B.4). The recoveries of both water and soil samples varied from 94.0% to 108.2%, suggesting that the proposed method was applicable and capable for glyphosate analysis in real environmental samples. Additionally, feasibility of the proposed SERS sensor was tested by comparing the results with standard values obtained from ultra-high performance liquid chromatography (UHPLC) method (experiment 3.5.8.2). The results obtained by the designed sensor are well consistent with that derived from UHPLC

method, as can be seen in the part 4.3.6.2 and Table B.3.14 (Appendix B.3). Therefore, it can be concluded that the designed SERS sensor based on  $\text{TiO}_2$  NTs/AgNPs-rGO provided results that are not statistically significantly different from standard UHPLC method verified by a paired T-test at a confidence interval of 95% probability.

**Table 4.5 Determination of glyphosate in environmental waters and soils by the SERS-based sensor and UHPLC (*n*=3)**

Sample	Added		Determined by SERS sensor			Determined by UHPLC			t-test <sup>b</sup>
			Measured		Recovery	Measured		Recovery	
	(mg.Kg <sup>-1</sup> )	(mg.L <sup>-1</sup> )	(mg.Kg <sup>-1</sup> )	(mg.L <sup>-1</sup> )	(%)	(mg.Kg <sup>-1</sup> )	(mg.L <sup>-1</sup> )	(%)	
Water A		-	n.d. <sup>a</sup>		-		n.d. <sup>a</sup>	-	-
		0.5	0.54 ± 0.03		108.2		0.52 ± 0.01	103.4	2.5
		1.0	1.05 ± 0.01		105.3		1.04 ± 0.03	103.8	1.3
Water B		-	n.d.		-		n.d.	-	-
		0.5	0.52 ± 0.03		104.3		0.52 ± 0.01	103.2	0.3
		1.0	1.02 ± 0.06		101.7		0.96 ± 0.03	96.1	1.9
Water C		-	n.d.		-		n.d.	-	-
		0.5	0.54 ± 0.06		107.9		0.49 ± 0.01	98.4	1.3
		1.0	0.98 ± 0.09		98.1		0.96 ± 0.03	95.9	0.3
Soil A	0		1.65 ± 0.27		-	0.79 ± 0.01		-	3.1
	2.0		3.53 ± 0.17		94.0	2.76 ± 0.10		98.6	0.7
	4.0		5.57 ± 0.03		97.8	4.74 ± 0.16		98.7	0.1
Soil B	-		n.d.		-	n.d.		-	-
	2.0		2.13 ± 0.18		106.7	2.05 ± 0.09		102.6	0.8
	4.0		4.17 ± 0.20		104.3	4.13 ± 0.16		103.1	0.3
Soil C	-		n.d.		-	n.d.		-	-
	2.0		2.11 ± 0.08		105.6	2.00 ± 0.06		100.2	0.7
	4.0		3.96 ± 0.20		99.0	4.01 ± 0.08		100.3	0.7

<sup>a</sup> n.d. means “not detectable”

<sup>b</sup> t-test at a confidence level of 95% probability and degree of freedom of 2





## CHAPTER 5

### CONCLUSIONS

This work focused on the development and designment of sensors and biosensors based on nanomaterials using electrochemical method and surface enhanced Raman spectroscopy (SERS) as the detection methods for food, environmental, and clinical applications. Consequently, all the results are concluded separated into 4 parts.

(1) An electrochemical sensor for food application was fabricated based on glassy carbon paste electrode modified with graphene nanoplatelets functionalized with ionic liquid (GCPE/GNP-IL). The sensor was applied for detection of bisphenol A (BPA) and performed by differential pulse voltammetry (DPV). Scanning electron microscopy (SEM) and Fourier transform infrared spectroscopy (FTIR) were employed to confirm successfully fabricated sensor. Then, electrochemical behavior of the sensor was investigated by cyclic voltammetry (CV), electrochemical impedance spectroscopy (EIS), and DPV. It is proved that a synergistic between GNP and IL nanomaterials could improve conductivity and promote electron transfer process of the GCPE. Next, conditions for preparation of the GCPE/GNP-IL and parameters for DPV measurement are optimized, as shown in Table 5.1.

**Table 5.1 Conditions for GCPE/GNP-IL construction and DPV measurement**

Instrument	Conditions	Sub-conditions	Optimal value
Potentiostat/Galvanostat Autolab	GCPE/GNP-IL	IL amount	0.4 mg.cm <sup>-2</sup>
		GNP-IL composite	28 µg.cm <sup>-2</sup>
	Buffer solution	pH value	8.0
	DPV parameters	Pulse potential	150 mV
		Step potential	30 mV
		Scan rate	50 mV/s

Moreover, analytical performance (Table 5.2), interferent effects, and practical application of the developed GCPE/GNP-IL sensor was sequentially evaluated. The result showed that phenolic compounds (phenol, 1-naphthol, and 4-nitrophenol), organic compounds (glucose and sucrose), and inorganic ions ( $\text{Na}^+$ ,  $\text{Ca}^{2+}$ ,  $\text{Mg}^{2+}$ ,  $\text{Al}^{3+}$ ,  $\text{Zn}^{2+}$ ,  $\text{Cu}^{2+}$ ,  $\text{Fe}^{2+}$ ,  $\text{Pb}^{2+}$ , and  $\text{Cd}^{2+}$ ) had no obvious influence on BPA determination at the tested concentration level. Furthermore, the sensor was successfully applied to the determination of BPA in water samples in contact with plastic materials. The results are satisfactory and in agreement with reference values from a high-performance liquid chromatography (HPLC) method.

**Table 5.2 Analytical performance of the sensor for BPA detection**

Figure of merit	Results
1. Linear range	0.02-5.0 $\mu\text{M}$
2. Detection limit	6.4 nM
3. Quantification limit	0.02 $\mu\text{M}$
4. Repeatability	3.3% (n=5)
5. Reproducibility	3.8% (n=5)
6. Stability	14 days

Additionally, a comparison of various different electrochemical methods for the determination of BPA is also presented in Table 5.3.

**Table 5.3 Electrochemical sensing assays for the determination of BPA**

Modified electrode	Linear range ( $\mu\text{M}$ )	LOD (nM)	Reference
GCE/MWCNT/ZnO	0.002-700	9.0	[100]
GCE/MWCNT/AuNPs	0.01-0.7	4.0	[101]
GCE/MWCNT/PDDA/AuPd	0.18-18	60.0	[102]
GCE/MWCNT/PtNPs/GN	0.06-10	42.0	[103]
CPE/GN/PME	9.0-1000	10.5	[104]
GCE/GN/AuPd	0.05-10	8.0	[105]

**Table 5.3 Electrochemical sensing assays for the determination of BPA**  
(continued)

Modified electrode	Linear range ( $\mu\text{M}$ )	LOD (nM)	Reference
GCE/rGO/SiO <sub>2</sub> /AuNPs	0.03-120	4.0	[108]
GCE/SGrNF/AuNPs	0.08-250	35.0	[110]
GCE/GNR/Au-Cu@BSA	0.01-70	4.0	[111]
GCPE/GNP-IL	0.02-5.0	6.4	This work

MWCNT: multi-walled carbon nanotubes, GN: graphene, SGrNF: stacked graphene nanofibers, GNR: graphene nanoribbons, PME: poly(melamine), PDDA: poly (diallyldimethylammonium chloride), BSA: bovine serum albumin, NPs: nanoparticles, GCE: glassy carbon electrode, CPE: carbon paste electrode

(2) An electrochemical biosensor for clinical application was designed based on CEA antibody (anti-CEA) anchored with core shell Fe<sub>3</sub>O<sub>4</sub>@Au nanoparticles which were immobilized on a screen-printed carbon electrode modified with manganese dioxide decorating on graphene nanoplatelets (SPCE/GNP-MnO<sub>2</sub>). The prepared biosensor was applied for detection of carcinoembryonic antigen (CEA), which was monitored in a 5 mM Fe(CN)<sub>6</sub><sup>3-/4-</sup> solution using linear sweep voltammetry (LSV) and EIS. Physical property of the GNP-MnO<sub>2</sub> and Fe<sub>3</sub>O<sub>4</sub>@Au nanomaterials were characterized by SEM, X-ray diffraction spectroscopy (XRD), and FTIR technique. According to electrochemical characterization, GNP-MnO<sub>2</sub> composite could improve sensitivity and electrocatalytic activity of the biosensor, while core shell Fe<sub>3</sub>O<sub>4</sub>@Au nanoparticles could serve as an immune sensing platform for immobilizing antibody. Then, optimum conditions for biosensor construction and CEA determination were investigated, as displayed in Table 5.4.

**Table 5.4 Optimum conditions for biosensor construction and CEA analysis**

Instrument	Conditions	Sub-conditions	Optimal value
Potentiostat/ Galvanostat Autolab	SPCE/GNP-MnO <sub>2</sub>	GNP amount	5.0 mg.cm <sup>-2</sup>
		Ratio of GNP:Mn	1:0.1 (mg:mg)
	Fe <sub>3</sub> O <sub>4</sub> @Au/antiCEA	Concentration of CEA antibody	200 µg/mL
	Buffer solution	pH value	7.4
	Incubation	Temperature	37°C
		Time for antibody	120 min
		Time for antigen	120 min

Under optimized conditions, analytical performances of the biosensor were evaluated and the results is presented in Table 5.5. The fabricated biosensor possessed very high selectivity because no apparent signal change took place in comparison between signal of pure CEA solution and signal of CEA mixed with 500-fold higher concentration interferent compounds, including prostate-specific antigen (PSA), human serum albumin (HSA), human immunoglobulin (IgG), bovine serum albumin (BSA), cholesterol, glucose, sucrose, cysteine, ascorbic acid, and uric acid. Furthermore, the applicability of the biosensor was verified by well-corresponding determination of CEA in diluted human serums by electrochemiluminescence (ECL) immunoassay.

**Table 5.5 Analytical performance of the biosensor for CEA analysis**

Figure of merit	Results
1. Linear range	0.001-100 ng/mL
2. Detection limit	0.10 pg/mL (LSV) and 0.30 pg/mL (EIS)
3. Repeatability (n=5)	3.3% for LSV and 2.3% for EIS
4. Reproducibility (n=5)	4.9% for LSV and 4.5% for EIS
5. Stability	7 days

Additionally, a comparison of various different electrochemical methods for the determination of CEA is also displayed in Table 5.6.

**Table 5.6 Electrochemical biosensing immunoassays for the determination of CEA**

<b>Modified electrode</b>	<b>Linear range (ng/mL)</b>	<b>LOD (pg/mL)</b>	<b>Reference</b>
GCE/PEDOT/AuNPs	0.05-40	0.01	[117]
GCE/PEDOT/AuNPs/GN	0.0004-40	0.1	[119]
GCE/Chitosan/Pd-Ir bimetallic NPs	0.05-50	0.017	[120]
GCE/AuNPs/thionine/MoS <sub>2</sub>	0.001-10	0.52	[123]
GCE/rGO/Nile blue/AuNPs	0.001-40	0.45	[127]
GCE/Sulfonated GN/thionine/chitosan nanotubular mesoporous PdCu	0.01–12	4.86	[128]
SPCE/GNP-MnO <sub>2</sub> /Fe <sub>3</sub> O <sub>4</sub> @Au	0.001-100	0.1 and 0.3	This work

GN: graphene, rGO: reduced graphene oxide, NPs: nanoparticles, PEDOT: poly(3,4-ethylenedioxythiophene), GCE: glassy carbon electrode,

(3) An electrochemical biosensor for environmental application was fabricated based on SPCE modified with reduced graphene oxide (rGO) and silver nanoparticles (AgNPs). The biosensor was applied for indirect detection of glyphosate herbicide, which was relied on inhibition of acid phosphatase enzyme (ACP) immobilized on the SPCE/rGO-AgNPs surface. The current signal owing to the enzymatic reaction of ACP to its substrate, disodium phenyl phosphate, was measured by chronoamperometry. Surface morphology, crystalline nature, and overall elemental composition of the SPCE/rGO-AgNPs were confirmed by XRD, SEM, and energy dispersive spectroscopy (EDS), respectively. Furthermore, Raman spectroscopy was used for analysis of carbon-based nanomaterials. The electrochemical behavior of the modified electrode and SPCE/rGO-AgNPs/ACP biosensor was characterized by CV and EIS. Then, optimum conditions for biosensor preparation and for glyphosate detection were investigated, as shown in Table 5.7.

**Table 5.7 Optimum conditions of enzymatic biosensor for glyphosate detection**

Instrument	Conditions	Sub-conditions	Optimal value
Potentiostat/ Galvanostat Autolab	Amperometry	Applied potential	0.4 V
	SPCE/rGO-AgNPs/ ACP	rGO amount	5.0 $\mu\text{g.cm}^{-2}$
		AgNPs amount	1.1 $\text{mg.cm}^{-2}$
		ACP loading	0.15 $\text{unit.cm}^{-2}$
	Enzyme substrate	Concentration of disodium phenyl phosphate	20 g/L
	Buffer solution	pH value	7.0

For enzyme kinetic study, the apparent kinetic constants ( $K_m$  and  $V_{\max}$ ) of ACP immobilized on the SPCE/rGO-AgNPs was calculated to be 3.79 mM and  $7.46 \mu\text{A.cm}^{-2}$ , respectively. Moreover, type of inhibition was investigated and it was found that inhibition of ACP enzyme by glyphosate is a reversible competitive type. Table 5.8 shows analytical performance of the SPCE/rGO-AgNPs/ACP biosensor. Additionally, selectivity of the biosensor was studied by testing effect of interference, including polyethoxylated tallow amine (POEA), glycine, chlorpyrifos, paraquat, carbaryl, carbendazim,  $\text{Mg}^{2+}$ ,  $\text{Zn}^{2+}$ ,  $\text{PO}_4^{2-}$ ,  $\text{SO}_4^{2-}$ ,  $\text{CO}_3^{2-}$ ,  $\text{NO}_3^-$ ,  $\text{Cl}^-$ ,  $\text{K}^+$ ,  $\text{Na}^+$ ,  $\text{Ca}^{2+}$ ,  $\text{Cu}^{2+}$ , and  $\text{Cd}^{2+}$ . The proposed biosensor was successfully applied for determination of glyphosate in water and soil samples, and the results are well accordance with ultra-high performance liquid chromatography (UHPLC) method.

**Table 5.8 Analytical performance of the biosensor for glyphosate detection**

Figure of merit	Results
1. Linear range	0.05 to 0.5 mg/L and 0.5 to 22.0 mg/L
2. Detection limit	16 $\mu\text{g/L}$
3. Quantification limit	55 $\mu\text{g/L}$
4. Reproducibility	5.21% (intra-day, n=5) 5.46% (inter-days, n=5)
5. Stability	5 days

Additionally, a comparison of various different electrochemical methods for the determination of glyphosate herbicide is also demonstrated in Table 5.9.

**Table 5.9 Electrochemical methods for the determination of glyphosate**

Modified electrode	Linear range (mg/L)	LOD ( $\mu\text{g/L}$ )	Reference
Au electrode/PDMA-PSS/HRP	0.25-14.0	1.7	[133]
Pt electrode/NiAl-LDH	0.15-1.69	0.16	[134]
CPE/Nanoclay modified APTES-ODA/MWCNTs/ atemoya peroxidase	0.10-4.55	30.0	[135]
PEG/MWCNT-IL/CuO NPs	0.0085-0.19	0.22	[136]
PEG/AuNPs- MAC/MWCNTs/MIP	0.004-0.176	0.35	[94]
SPCE/rGO-AgNPs/ACP	0.05-0.5 and 0.5-22.0	16.0	This work

MWCNTs: multiwalled carbon nanotubes, IL: ionic liquid, PMDA: poly(2,5-dimethoxyani-line), PSS: poly(4-styrenesulfonic acid), LDH: layered double hydroxide, APTES: aminopropyltriethoxysilane, ODA: octadecylamine, MAC: N-methacryloyl-L-cysteine, NPs: nanoparticles, CPE: carbon paste electrode, PEG: pencil graphite electrode, HRP: horseradish peroxidase, MIP: molecular imprinted polymer

(4) An analytical sensor based on surface enhanced Raman spectroscopy (SERS) was designed for detection of glyphosate in environmental samples. Vertical heterostructure composed of titanium dioxide nanotube arrays ( $\text{TiO}_2$  NTs), AgNPs and rGO was constructed and served as a SERS-based sensor. Optical property, surface morphology, and crystalline nature of the  $\text{TiO}_2$  NTs/AgNPs-rGO substrate were characterized by UV-visible spectroscopy, SEM, and XRD, respectively. Furthermore, composition of the prepared SERS substrate was confirmed by Raman spectroscopy, EDS, and X-ray photoelectron spectroscopy (XPS). Then, parameters influence on SERS measurements and conditions for fabrication of the  $\text{TiO}_2$  NTs/AgNPs-rGO were optimized, as depicted in Table 5.10.



**Table 5.10 Conditions for SERS measurement and SERS substrate construction**

Instruments	Conditions	Sub-conditions	Optimal value
Raman spectrophotometer	Raman parameters	Laser excitation	532 nm
		Objective lens	50x
		Acquisition time	10 second
		Accumulation	5
DC power supply	TiO <sub>2</sub> NTs	Anodization voltage	30 V
		Anodization time	30 mins
DC sputtering	AgNPs	Thickness of AgNPs	11 nm
Potentiostat/ Galvanostat Autolab	rGO	GO concentration	0.1 mg/mL
		Cycles for electrodeposition	40

Under optimum conditions, the TiO<sub>2</sub> NTs/AgNPs-rGO surface exhibited high SERS activity for detection of methylene blue (MB) as probe molecule. The analytical performances of the SERS-based sensor are demonstrated in Table 5.11.

**Table 5.11 Analytical performance of the TiO<sub>2</sub> NTs/AgNPs-rGO SERS substrate**

Figure of merit	Results
1. Linear range	10 <sup>-2</sup> to 10 <sup>-12</sup> M
2. Detection limit	10 <sup>-14</sup> M
3. Enhancement factor	7.1 × 10 <sup>8</sup>
4. Repeatability	4.4% (n=20)
5. Reproducibility	2.0% (n=10)
6. Stability	180 days
7. Reusability	3 times

Moreover, analytical performances of various different SERS substrates for the detection of Raman active molecule where compared with this work, as shown in Table 5.12.

**Table 5.12 Comparison of analytical performance from different SERS substrates**

SERS substrate	Probe molecule	EF	LOD (M)	Reference
rGO/AgNPs	MB	$4.6 \times 10^5$	$10^{-7}$	[144]
Sulfonated-rGO/AgNPs	MG	$1.0 \times 10^9$	$10^{-6}$	[149]
GN/AgNPs	R6G	$3.4 \times 10^7$	$10^{-13}$	[151]
3D wrinkled-GN/AgNPs	R6G	$1.6 \times 10^5$	$10^{-9}$	[153]
TiO <sub>2</sub> NFs/AgNPs	MB	$4.4 \times 10^5$	$10^{-8}$	[157]
TiO <sub>2</sub> nanotree/AgNPs	R6G	$5.3 \times 10^5$	$10^{-12}$	[158]
TiO <sub>2</sub> NRs/GO-AgNPs	R6G	$5.9 \times 10^5$	$10^{-12}$	[160]
TiO <sub>2</sub> NTs/AgNPs-rGO	MB	$7.1 \times 10^8$	$10^{-14}$	This work

rGO: reduced graphene oxide, GN: graphene, NPs: nanoparticles, NFs: nanofibers, NRs: nanorods, NTs: nanotubes, MG: malachite green, R6G: rhodamine 6G

Furthermore, the designed SERS sensor was successfully applied for glyphosate detection in the range from 0.1 to 100 mg/L and the detection limit as 0.05 mg/L was achieved. The practical applications on glyphosate determination in environmental waters and soils were investigated and the results are in good agreement with those UHPLC standard method. Additionally, a comparison of various different SERS substrates for the determination of glyphosate is also presented in Table 5.13.

**Table 5.13 Comparison of glyphosate detection from different SERS substrates**

SERS substrate	Linear range (mg/L)	LOD (mg/L)	Reference
Cu-grids/Ag dendrites	1-100	0.85	[296]
MPB-AuNRs conjugates	1-1,200	0.10	[297]
AgNPs based on ninhydrin reaction	0.017-16.9	0.002	[298]
Metal carbonyl-AuNPs conjugates	0.001-0.25	0.0001	[299]
TiO <sub>2</sub> NTs/AgNPs-rGO	0.1-100	0.05	This work

MPB: 4-mercaptophenylboronic acid, NPs: nanoparticles, NRs: nanorods

## REFERENCES

## REFERENCES

- [1] Connor, T. H. and Smith, J. P. “New approaches to wipe sampling methods for antineoplastic and other hazardous drugs in healthcare settings”, **Pharmaceutical Technology in Hospital Pharmacy**. 1(3): 107-114; September, 2016.
- [2] Rotariu, L. and et al. “Electrochemical biosensors for fast detection of food contaminants-trends and perspective”, **TrAC Trends in Analytical Chemistry**. 79: 80-87; May, 2016.
- [3] Arduini, F. and et al. “Electrochemical biosensors based on nanomodified screen-printed electrodes: Recent applications in clinical analysis”, **TrAC Trends in Analytical Chemistry**. 79: 114-126; May, 2016.
- [4] Maduraiveeran, G., Sasidharan, M. and Ganesan, V. “Electrochemical sensor and biosensor platforms based on advanced nanomaterials for biological and biomedical applications”, **Biosensors and Bioelectronics**. 103: 113-129; April, 2018.
- [5] Huang, X. and et al. “Nanotechnology-enhanced no-wash biosensors for in vitro diagnostics of cancer”, **ACS Nano**. 11(6): 5238-5292; June, 2017.
- [6] Cialla, D. and et al. “Surface-enhanced Raman spectroscopy (SERS): progress and trends”, **Analytical and Bioanalytical Chemistry**. 403: 27-54; April, 2012.
- [7] Zhang, Y. and et al. “Surface-enhanced Raman spectroscopy (SERS) combined techniques for high-performance detection and characterization”, **TrAC Trends in Analytical Chemistry**. 90: 1-13; May, 2017.
- [8] Adams, F. C. and Barbante. C. “Nanoscience, nanotechnology and spectrometry”, **Spectrochimica Acta Part B: Atomic Spectroscopy**. 86: 3-13; August, 2013.
- [9] Patil, P. O. and et al. “Graphene-based nanocomposites for sensitivity enhancement of surface plasmon resonance sensor for biological and chemical sensing: A review”, **Biosensors and Bioelectronics**. 139: 111324; August, 2019.

## REFERENCES (CONTINUED)

- [10] Li, Y. and et al. “Nanoparticle-based sensors for food contaminants”, **TrAC Trends in Analytical Chemistry**. 113: 74-83; April, 2019.
- [11] Liu, B. and Liu, J. “Sensors and biosensors based on metal oxide nanomaterials”, **TrAC Trends in Analytical Chemistry**. 121: 115690-115738; December, 2019.
- [12] Banica, F. G. **Chemical Sensors and Biosensors: Fundamentals and Applications**. England: John Wiley & Sons, 2012.
- [13] Gooding, J. J. and Hall E. A. “A fill-and-flow biosensor”, **Analytical chemistry**. 70(15): 3131-3136; June, 1998.
- [14] Mikkelsen, S. R. and Cortón, E. **Bioanalytical Chemistry**. England: John Wiley & Sons, 2016.
- [15] Shen, W. C. and Louie, S. G. **Immunology for Pharmacy Students**. Florida: CRC Press, 1999.
- [16] Davies, D. R. and Metzger, H. “Structural basis of antibody function”, **Annual Review of Immunology**. 1(1): 87-115; April, 1983.
- [17] Miller, G. E. and Cohen, S. “Psychological interventions and the immune system: A meta-analytic review and critique”, **Health Psychology**. 20(1): 47; August, 2001.
- [18] Kim, S. D., Shin, K. R. and Zhang, B. T. “Molecular immunocomputing with application to alphabetical pattern recognition mimics the characterization of ABO blood type”, In **The 2003 Congress on Evolutionary Computation**. p.2549-2556. Canberra: IEEE Conferences, 2003.
- [19] Hawcroft, D., Hector, T. and Rowell, F. **Quantitative Bioassay**. England: John Wiley & Sons, 2008.
- [20] Mohanty, D. “Introduction to Blood Transfusion Technology-ISBT Science series”, **Asian Journal of Transfusion Science**. 3(2): 112-112; June, 2009.
- [21] O'Leary, W. M. **Practical Handbook of Microbiology**. Florida: CRC Press, 1989.
- [22] Weir, D. M. **Handbook of Experimental Immunology in Four Volumes**. Boston: Blackwell Scientific, 1986.

## REFERENCES (CONTINUED)

- [23] Sonawane, M. D. and Nimse, S. B. “Surface modification chemistries of materials used in diagnostic platforms with biomolecules”, **Journal of Chemistry**. 9241378-9241397: May, 2016.
- [24] Ullman, E. F. and Maggio, E. T. “Principles of homogeneous enzyme-immunoassay”, In **Enzyme Immunoassay**. Edward T. Maggio Editor. p.105-134. Florida: CRC Press, 1980.
- [25] Zane, H. D. **Immunology: Theoretical & Practical Concepts in Laboratory Medicine**. Philadelphia: WB Saunders Company, 2001.
- [26] Okuno, J. and et al. “Label-free immunosensor for prostate-specific antigen based on single-walled carbon nanotube array-modified microelectrodes”, **Biosensors and Bioelectronics**. 22(9-10): 2377-2381; April, 2007.
- [27] Wang, Y. and et al. “Label-free electrochemical immunosensor based on flower-like Ag/MoS<sub>2</sub>/rGO nanocomposites for ultrasensitive detection of carcinoembryonic antigen”, **Sensors and Actuators B: Chemical**. 255: 125-132; February, 2018.
- [28] Robinson, P. K. “Enzymes: principles and biotechnological applications”, **Essays in Biochemistry**. 59: 1-41; October, 2015.
- [29] Amine, A. and et al. “Recent advances in biosensors based on enzyme inhibition”, **Biosensors and Bioelectronics**. 76: 180-194; February, 2016.
- [30] Seager, S. L. and Slabaugh, M. R. **Chemistry for Today: General, Organic, and Biochemistry**. Boston: Cengage Learning, 2013.
- [31] Steehler, J. K. “Bioanalytical Chemistry”, **Journal of Chemical Education**. 81(9): 1270; September, 2004.
- [32] Leskovac, V. **Comprehensive Enzyme Kinetics**. Berlin: Springer Science & Business Media, 2003.
- [33] Bisswanger, H. **Enzyme Kinetics**. Weinheim: Wiley-Vch, 2001.
- [34] Bugg, T. D. **Introduction to Enzyme and Coenzyme Chemistry**. England: John Wiley & Sons, 2012.

## REFERENCES (CONTINUED)

- [35] Amine, A. and et al. “Enzyme inhibition-based biosensors for food safety and environmental monitoring”, **Biosensors and Bioelectronics**. 21(8): 1405-1423; February, 2006.
- [36] Marques, P. R. B. D. O. and Yamanaka, H. “Biosensors based on the enzymatic inhibition process”, **Química Nova**. 31(7): 1791-1799; April, 2008.
- [37] Bachan Upadhyay, L. S. and Verma, N. “Enzyme inhibition-based biosensors: A review”, **Analytical Letters**. 46(2): 225-241; July, 2013.
- [38] Bull, H. and et al. “Acid phosphatases”, **Molecular Pathology**. 55(2): 65-72; April, 2002.
- [39] Henneberry, M. O., Engel, G. and Grayhack, J. T. “Acid phosphatase”, **The Urologic clinics of North America**. 6(3): 629-641; October, 1979.
- [40] Monk, P. M. **Fundamentals of Electroanalytical Chemistry**. England: John Wiley & Sons, 2008.
- [41] Westbroek, P., Priniotakis, G., and Kiekens, P. **Analytical Electrochemistry in Textiles**. Amsterdam: Elsevier, 2005.
- [42] Rani, S. and et al. “Integrated circuit design of 3 electrode sensing system using two-stage operational amplifier”, **Materials Science and Engineering**. 340(1): 12017-12025; August, 2018.
- [43] Compton, R. G. and Sanders, G. H. **Electrode Potentials**. Oxford: Oxford University Press, 1996.
- [44] Randelović, M. S. and et al. “Electrocatalytic behaviour of serpentinite modified carbon paste electrode”, **Journal of Electroanalytical Chemistry**. 801: 338-344; September, 2017.
- [45] Kalambate, P. K. and et al. “Highly sensitive and selective determination of methylergometrine maleate using carbon nanofibers/silver nanoparticles composite modified carbon paste electrode”, **Materials Science and Engineering: C**. 69: 453-461; December, 2016.
- [46] Honeychurch, K. C. and Hart, J. P. “Screen-printed electrochemical sensors for monitoring metal pollutants”, **TrAC Trends in Analytical Chemistry**. 22(7): 456-469; August, 2003.

## REFERENCES (CONTINUED)

- [47] Vassos, B. H. and Ewing, G. W. **Electroanalytical Chemistry**. England: John Wiley & Sons, 1983.
- [48] Galus, Z. **Fundamentals of Electrochemical Analysis**. New York: Halsted Press, 1977.
- [49] Kissinger, P. T. and Heineman, W. R. "Cyclic voltammetry", **Journal of Chemical Education**. 60(9): 702-759; September, 1983.
- [50] Pletcher, D. and et al. **Instrumental Methods in Electrochemistry**. Amsterdam: Elsevier, 2001.
- [51] Mansfeld, F. "Use of electrochemical impedance spectroscopy for the study of corrosion protection by polymer coatings", **Journal of Applied Electrochemistry**. 25(3): 187-202; March, 1995.
- [52] Turrell, G., Gardiner, D. J., and Graves, P. R. **Practical Raman Spectroscopy**. Berlin: Springer, 1989.
- [53] Lopez-Lopez, M. and Garcia-Ruiz, C. "Infrared and Raman spectroscopy techniques applied to identification of explosives", **TrAC Trends in Analytical Chemistry**. 54: 36-44; February, 2014.
- [54] Smith, E. and Dent, G. **Modern Raman Spectroscopy: A Practical Approach**. New Jersey: Wiley Online Library, 2019.
- [55] Butler, H. J. and et al. "Using Raman spectroscopy to characterize biological materials", **Nature Protocols**. 11(4): 664-687; March, 2016.
- [56] Sitarski, A. M. "Development of spectroscopic methods for dynamic cellular level study of biochemical kinetics and disease progression", **The University of Maine**. 25(3): 2652-2694; March, 2017.
- [57] Notingher, I. "Raman spectroscopy cell-based biosensors", **Sensors**. 7(8): 1343-1358; July, 2007.
- [58] Pieczonka, N. P. and Aroca, R. F. "Single molecule analysis by surfaced-enhanced Raman scattering", **Chemical Society Reviews**. 37(5): 946-954; February, 2008.
- [59] Stiles, P. L. and et al. "Surface-enhanced Raman spectroscopy", **Annual Review of Analytical Chemistry**. 1: 601-626; July, 2008.



## REFERENCES (CONTINUED)

- [60] Zheng, J. and He, L. “Surface-enhanced Raman spectroscopy for the chemical analysis of food”, **Comprehensive Reviews in Food Science and Food Safety**. 13(3): 317-328; May, 2014.
- [62] Hildebrandt, P. and Stockburger, M. “Surface-enhanced resonance Raman spectroscopy of Rhodamine 6G adsorbed on colloidal silver”, **The Journal of Physical Chemistry**. 88(24): 5935-5944; November, 1984.
- [63] Kneipp, K. and et al. “Single molecule detection using surface-enhanced Raman scattering (SERS)”, **Physical review letters**. 78(9): 1667; March, 1997.
- [64] Burstein, E. and et al. “Raman scattering by adsorbed molecules on metal surfaces”, **Solid State Communications**. 29(8): 567-570; February, 1979.
- [65] Maier, S. A. **Plasmonics: fundamentals and applications**. Berlin: Springer Science & Business Media, 2007.
- [66] Ding, S. Y. and et al. “Electromagnetic theories of surface-enhanced Raman spectroscopy”, **Chemical Society Reviews**. 46(13): 4042-4076; Jun, 2017.
- [67] Willets, K. A. and Van Duyne, R. P. “Localized surface plasmon resonance spectroscopy and sensing”, **Annual Review of Analytical Chemistry**. 58: 267-297; May, 2007.
- [68] Tian, Z. Q. and et al. “SERS from transition metals and excited by ultraviolet light”, **Springer**. 103: 125-146; January, 2006.
- [69] Naik, G. V., Shalae, V. M., and Boltasseva, A. “Alternative plasmonic materials: beyond gold and silver”, **Advanced Materials**. 25: 3264-3294; May, 2013.
- [70] Le Ru, E. and Etchegoin, P. **Principles of Surface-Enhanced Raman Spectroscopy: and related plasmonic effects**. Amsterdam: Elsevier, 2008.
- [71] Lu, C. H. and et al. “A graphene platform for sensing biomolecules”, **Angewandte Chemie International Edition**. 48(26): 4785-4787; June, 2009.
- [72] Prasad, G. L. “Biomedical applications of nanoparticles”, **Springer**. 20: 89-109: October, 2009.

## REFERENCES (CONTINUED)

- [73] Liu, Z., Kiessling, F. and Gätjens, J. “Advanced nanomaterials in multimodal imaging: design, functionalization, and biomedical applications”, **Journal of Nanomaterials**. 2010: 51-66; January, 2010.
- [74] Immanuel, S., Aparna, T. K. and Sivasubramanian, R. “Graphene-Metal Oxide Nanocomposite Modified Electrochemical Sensors”, **Elsevier**. 1: 113-138; October, 2019.
- [75] Galiński, M., Lewandowski, A. and Stępnia, I. “Ionic liquids as electrolytes”, **Electrochimica Acta**. 51(26): 5567-5580; August, 2006.
- [76] Wang, X. and Hao, J. “Recent advances in ionic liquid-based electrochemical biosensors”, **Science Bulletin**. 61(16): 1281-1295; July, 2016.
- [77] Brady, J. B. and Boardman, S. J. “Introducing mineralogy students to x-ray diffraction through optical diffraction experiments using lasers”, **Journal of Geological Education**. 43(5): 471-476; February, 1995.
- [78] Bragg, W. H. and Bragg, W. L. “The reflection of X-rays by crystals”, **Proceedings of the Royal Society of London**. 88(605): 428-438; January, 1913.
- [79] Turner, D. W. and Jobory, M. A. “Determination of ionization potentials by photoelectron energy measurement”, **The Journal of Chemical Physics**. 37(12): 3007-3008; July, 1962.
- [80] Ray, S. and Shard, A. G. “Quantitative analysis of adsorbed proteins by X-ray photoelectron spectroscopy”, **Analytical Chemistry**. 83(22): 8659-8666; October, 2011.
- [81] Ebnesajjad, S. “Surface and material characterization techniques”, **Handbook of Adhesives and Surface Preparation**. 5: 31-48; January, 2011.
- [82] Perkins, W. D. “Fourier transform-infrared spectroscopy: Part I. Instrumentation”, **Journal of Chemical Education**. 63(1): 45-51; January, 1986.
- [83] Goldstein, J. I. and et al. **Scanning Electron Microscopy and X-ray Microanalysis**. Berlin: Springer, 2017.

## REFERENCES (CONTINUED)

- [84] Lozano-Sánchez, J. and et al. “Chromatographic Technique: High-Performance Liquid Chromatography (HPLC)”, **Modern Techniques for Food Authentication**. 18: 459-526; November, 2018.
- [85] Karger, B. L. “HPLC: Early and recent perspectives”, **Journal of Chemical Education**. 74(1): 45-49; January, 1997.
- [86] Leventis, N. **Electrogenerated Chemiluminescence**. New York: Marcel Dekker Inc., 2005.
- [87] Wei, H. and Wang, E. “Electrochemiluminescence of tris (2, 2'-bipyridyl) ruthenium and its applications in bioanalysis: a review”, **Luminescence**. 26(2): 77-85; March, 2011.
- [88] Landolfi, A. and et al. “Bisphenol A glucuronidation in patients with Parkinson's disease”, **Neurotoxicology**. 63: 90-96; December, 2017.
- [89] Ragavan, K. V., Rastogi, Navin K. and Thakur, M. S. “Sensors and biosensors for analysis of bisphenol-A”, **TrAC Trends in Analytical Chemistry**. 52: 248-260; December, 2013.
- [90] Wu, L. and Qu, X. “Cancer biomarker detection: recent achievements and challenges”, **Chemical Society Reviews**. 44(10): 2963-2997; March, 2015.
- [91] Li, X. and et al. “A sensor for detection of carcinoembryonic antigen based on the polyaniline-Au nanoparticles and gap-based interdigitated electrode”, **Sensors and Actuators B: Chemical**. 239: 874-882; February, 2017.
- [92] Han, J. and et al. “A novel sandwich-type immunosensor for detection of carcino-embryonic antigen using silver hybrid multiwalled carbon nanotubes/manganese dioxide”, **Journal of Electroanalytical Chemistry**. 786: 112-119; February, 2017.
- [93] Portier, C. J. and et al. “Differences in the carcinogenic evaluation of glyphosate between the International Agency for Research on Cancer (IARC) and the European Food Safety Authority (EFSA)”, **Journal of Epidemiology and Community Health**. 70(8): 741-745; April, 2016.

## REFERENCES (CONTINUED)

- [94] Prasad, B. B., Jauhari, D. and Tiwari, M. P. “Doubly imprinted polymer nanofilm-modified electrochemical sensor for ultra-trace simultaneous analysis of glyphosate and glufosinate”, **Biosensors and Bioelectronics**. 59: 81-88; September, 2014.
- [95] Zhang, Y. and et al. “Sensitive determination of bisphenol A base on arginine functionalized nanocomposite graphene film”, **Electrochimica Acta**. 80: 77-83; October, 2012.
- [96] Wang, Q. and et al. “Voltammetric detection of bisphenol a by a chitosan–graphene composite modified carbon ionic liquid electrode”, **Thin Solid Films**. 520(13): 4459-4464; April, 2012.
- [97] Li, Y. and et al. “Electrochemical determination of bisphenol A at ordered mesoporous carbon modified nano-carbon ionic liquid paste electrode”, **Talanta**. 148: 362-369; February, 2016.
- [98] Li, J. and et al. “Voltammetric determination of bisphenol A in food package by a glassy carbon electrode modified with carboxylated multi-walled carbon nanotubes”, **Microchimica Acta**. 172(3-4): 379-386; March, 2011.
- [99] Bolat, G., Yaman, Y. T. and Abaci, S. “Highly sensitive electrochemical assay for Bisphenol A detection based on poly (CTAB)/MWCNTs modified pencil graphite electrodes”, **Sensors and Actuators B: Chemical**. 255: 140-148; February, 2018.
- [100] Najafi, M., Khalilzadeh, M. A. and Karimi-Maleh, H. “A new strategy for determination of bisphenol A in the presence of Sudan I using a ZnO/CNTs/ ionic liquid paste electrode in food samples”, **Food Chemistry**. 158: 125-131; September, 2014.
- [101] Messaoud, N. B. and et al. “Electrochemical sensor based on multiwalled carbon nanotube and gold nanoparticle modified electrode for the sensitive detection of bisphenol A”, **Sensors and Actuators B: Chemical**. 253: 513-522; December, 2017.

## REFERENCES (CONTINUED)

- [102] Mo, F. and et al. "A sensitive electrochemical sensor for bisphenol A on the basis of the AuPd incorporated carboxylic multi-walled carbon nanotubes", **Food Chemistry**. 292: 253-259; September, 2019.
- [103] Zheng, Z. and et al. "Pt/graphene-CNTs nanocomposite based electrochemical sensors for the determination of endocrine disruptor bisphenol A in thermal printing papers", **Analyst**. 138(2): 693-701; November, 2013.
- [104] Peng, J. and et al. "Simultaneous determination of bisphenol A and hydroquinone using a poly (melamine) coated graphene doped carbon paste electrode", **Microchimica Acta**. 183(7): 2289-2296; July, 2016.
- [105] Su, B. et al. "A sensitive bisphenol A voltammetric sensor relying on AuPd nanoparticles/graphene composites modified glassy carbon electrode", **Talanta**. 166: 126-132; May, 2017.
- [106] Tian, C. and et al. "Electrochemical bisphenol A sensor based on nanoporous PtFe alloy and graphene modified glassy carbon electrode", **Journal of Electroanalytical Chemistry**. 830: 27-33; December, 2018.
- [107] Li, Y. and et al. "An electrochemical sensor for the determination of bisphenol A using glassy carbon electrode modified with reduced graphene oxide-silver/poly-L-lysine nanocomposites", **Journal of Electroanalytical Chemistry**. 805: 39-46; November, 2017.
- [108] Liu, E. and Zhang, X. "Electrochemical sensor for endocrine disruptor bisphenol A based on a glassy carbon electrode modified with silica and nanocomposite prepared from reduced graphene oxide and gold nanoparticles", **Analytical Methods**. 6(21): 8604-8612; September, 2014.
- [109] Canevari, T. C., Rossi, M. V. and Alexiou, A. D. "Development of an electrochemical sensor of endocrine disruptor bisphenol A by reduced graphene oxide for incorporation of spherical carbon nanoparticles", **Journal of Electroanalytical Chemistry**. 832: 24-30; January, 2019.
- [110] Niu, X. and et al. "A novel electrochemical sensor of bisphenol A based on stacked graphene nanofibers/gold nanoparticles composite modified glassy carbon electrode", **Electrochimica Acta**. 98: 167-175; May, 2013.

## REFERENCES (CONTINUED)

- [111] Mahmoudi, E. and et al. “A novel platform based on graphene nanoribbons/protein capped Au-Cu bimetallic nanoclusters: Application to the sensitive electrochemical determination of bisphenol A”, **Microchemical Journal**. 145: 242-251; March, 2019.
- [112] Kumar, S. and et al. “Reduced graphene oxide modified smart conducting paper for cancer biosensor”, **Biosensors and Bioelectronics**. 73: 114-122; November, 2015.
- [113] Lin, C. W. and et al. “A reusable magnetic graphene oxide-modified biosensor for vascular endothelial growth factor detection in cancer diagnosis”, **Biosensors and Bioelectronics**. 67: 431-437; May, 2015.
- [114] Pang, P. and et al. “Ultrasensitive enzyme-free electrochemical immunosensor for microcystin using molybdenum disulfide/gold nanoclusters nanocomposites as platform and Au@Pt core-shell nanoparticles as signal enhancer”, **Sensors and Actuators B: Chemical**. 266: 400-407; August, 2018.
- [115] Yang, T. and et al. “Three-dimensional gold nanoparticles/prussian blue-poly (3, 4-ethylenedioxythiophene) nanocomposite as novel redox matrix for label-free electrochemical immunoassay of carcinoembryonic antigen”, **Sensors and Actuators B: Chemical**. 239: 76-84; February, 2017.
- [116] Wang, J. and Hui, N. “Zwitterionic poly (carboxybetaine) functionalized conducting polymer polyaniline nanowires for the electrochemical detection of carcinoembryonic antigen in undiluted blood serum”, **Bioelectrochemistry**. 125: 90-96; February, 2019.
- [117] Gao, Y. S. and et al. “A label-free electrochemical immunosensor for carcinoembryonic antigen detection on a graphene platform doped with poly (3, 4-ethylenedioxythiophene)/Au nanoparticles”, **RSC Advances**. 5(106): 86910-86918; October, 2015.
- [118] Zheng, L. and et al. “A Label-Free Immunosensor for CEA based on Pd-Ir bimetallic nanoparticles”, **Journal of Nanoscience and Nanotechnology**. 16(6): 5984-5990; June, 2016.

## REFERENCES (CONTINUED)

- [119] Huang, J. Y. and et al. “A high-sensitivity electrochemical aptasensor of carcinoembryonic antigen based on graphene quantum dots-ionic liquid-nafion nanomatrix and DNAzyme-assisted signal amplification strategy”, **Biosensors and Bioelectronics**. 99: 28-33; January, 2018.
- [120] Samanman, S. and et al. “Highly-sensitive label-free electrochemical carcinoembryonic antigen immunosensor based on a novel Au nanoparticles-graphene-chitosan nanocomposite cryogel electrode”, **Analytica Chimica Acta**. 853: 521-532; January, 2015.
- [121] Su, S. and et al. “Shape-controlled gold nanoparticles supported on MoS<sub>2</sub> nanosheets: synergistic effect of thionine and MoS<sub>2</sub> and their application for electrochemical label-free immunosensing”, **Nanoscale**. 7(45): 19129-19135; October, 2015.
- [122] Rizwan, M. and et al. “AuNPs/CNOs/SWCNTs/chitosan-nanocomposite modified electrochemical sensor for the label-free detection of carcinoembryonic antigen”, **Biosensors and Bioelectronics**. 107: 211-217; January, 2018.
- [123] Aslan, S. and Anik, U. “Development of TiO<sub>2</sub> and Au nanocomposite electrode as CEA immunosensor transducer”, **Electroanalysis**. 26(6): 1373-1381; April, 2014.
- [124] Han, J., Ma, J. and Ma, Z. “One-step synthesis of graphene oxide-thionine-Au nanocomposites and its application for electrochemical immunosensing”, **Biosensors and Bioelectronics**. 47: 243-247; September, 2013.
- [125] Gao, Y. S. and et al. “Label-free electrochemical immunosensor based on Nile blue A-reduced graphene oxide nanocomposites for carcinoembryonic antigen detection”, **Analytical Biochemistry**. 500: 80-87; May, 2016.
- [126] Cai, Y. and et al. “Electrochemical immunoassay for carcinoembryonic antigen based on signal amplification strategy of nanotubular mesoporous PdCu alloy”, **Biosensors and Bioelectronics**. 36(1): 6-11; July, 2012.

## REFERENCES (CONTINUED)

- [127] Wang, Y. and et al. “A novel label-free microfluidic paper-based immunosensor for highly sensitive electrochemical detection of carcinoembryonic antigen”, **Biosensors and Bioelectronics**. 83: 319-326; September, 2016.
- [128] Zhang, P. and et al. “A sensitive amperometric AChE-biosensor for organophosphate pesticides detection based on conjugated polymer and Ag-rGO-NH<sub>2</sub> nanocomposite”, **Bioelectrochemistry**. 127: 163-170; June, 2019.
- [129] Zhou, L. and et al. “Acetylcholinesterase/chitosan-transition metal carbides nanocomposites-based biosensor for the organophosphate pesticides detection”, **Biochemical Engineering Journal**. 128: 243-249; December, 2017.
- [130] Pabbi, M. and et al. “A surface expressed alkaline phosphatase biosensor modified with flower shaped ZnO for the detection of chlorpyrifos”, **Sensors and Actuators B: Chemical**. 258: 215-227; April, 2018.
- [131] Songa, E. A. and et al. “Electrochemical detection of glyphosate herbicide using horseradish peroxidase immobilized on sulfonated polymer matrix”, **Bioelectrochemistry**. 75(2): 117-123; June, 2009.
- [132] Khenifi, A. and et al. “Glyphosate and glufosinate detection at electrogenerated NiAl-LDH thin films”, **Analytica Chimica Acta**. 654(2): 97-102; November, 2009.
- [133] Oliveira, G. C. and et al. “Biosensor based on atemoya peroxidase immobilised on modified nanoclay for glyphosate biomonitoring”, **Talanta**. 98: 130-136; August, 2012.
- [134] Gholivand, M. B., Akbari, A. and Norouzi, L. “Development of a novel hollow fiber-pencil graphite modified electrochemical sensor for the ultra-trace analysis of glyphosate”, **Sensors and Actuators B: Chemical**. 272: 415-424; November, 2018.
- [135] Cao, Y. and et al. “An electrochemical sensor on the hierarchically porous Cu-BTC MOF platform for glyphosate determination”, **Sensors and Actuators B: Chemical**. 283: 487-494; March, 2019.



## REFERENCES (CONTINUED)

- [136] Zouaoui, F. and et al. “Electrochemical impedance spectroscopy determination of glyphosate using a molecularly imprinted chitosan”, **Sensors and Actuators B: Chemical**. 309: 127753-127774; April, 2020.
- [137] Gu, C. and et al. “Ultrasensitive non-enzymatic pesticide electrochemical sensor based on HKUST-1-derived copper oxide@mesoporous carbon composite”, **Sensors and Actuators B: Chemical**. 305: 127478; February, 2020.
- [138] Jiang, Y. and et al. “Highly durable graphene-mediated surface enhanced Raman scattering (G-SERS) nanocomposites for molecular detection”, **Applied Surface Science**. 450: 451-460; August, 2018.
- [139] Sun, Y. and et al. “Parameter optimization for Ag-coated TiO<sub>2</sub> nanotube arrays as recyclable SERS substrates”, **Applied Surface Science**. 443: 613-618; June, 2018.
- [140] Fang, H. and et al. “Recyclable three-dimensional Ag nanoparticle-decorated TiO<sub>2</sub> nanorod arrays for surface-enhanced Raman scattering”, **Biosensors and Bioelectronics**. 64: 434-441; 2015.
- [141] Yang, L. and et al. “Improved SERS performance of single-crystalline TiO<sub>2</sub> nanosheet arrays with co-exposed {001} and {101} facets decorated with Ag nanoparticles”. **Sensors and Actuators B: Chemical**. 242: 932-939; April, 2017.
- [142] Chettri, P. and et al. “Green synthesis of silver nanoparticle-reduced graphene oxide using *Psidium guajava* and its application in SERS for the detection of methylene blue”, **Applied Surface Science**. 406: 312-318; June, 2017.
- [143] Wadhwa, H. and et al. “Microwave assisted facile synthesis of reduced graphene oxide-silver (RGO-Ag) nanocomposite and their application as active SERS substrate”, **Materials Chemistry and Physics**. 194: 274-282; June, 2017.
- [144] Naqvi, T. K. and et al. “Silver nanoparticles decorated reduced graphene oxide (rGO) SERS sensor for multiple analytes”, **Applied Surface Science**. 478: 887-895; June, 2019.

## REFERENCES (CONTINUED)

- [145] Han, B. and et al. “Direct laser scribing of AgNPs@RGO biochip as a reusable SERS sensor for DNA detection”, **Sensors and Actuators B: Chemical**. 270: 500-507; October, 2018.
- [146] Chen, L. and et al. “SERS effect on the presence and absence of rGO for Ag@Cu<sub>2</sub>O core-shell”, **Materials Science in Semiconductor Processing**. 91: 290-295; March, 2019.
- [147] Xiao, G. and et al. “Highly sensitive, reproducible and stable SERS substrate based on reduced graphene oxide/silver nanoparticles coated weighing paper”, **Applied Surface Science**. 404: 334-341; May, 2017.
- [148] Cheng, Y. W. and et al. “Manipulated interparticle gaps of silver nanoparticles by dendron-exfoliated reduced graphene oxide nanohybrids for SERS detection”, **Applied Surface Science**. 469: 887-895; March, 2019.
- [149] Zhou, Y. and et al. “Ecofriendly and environment-friendly synthesis of size-controlled silver nanoparticles/graphene composites for antimicrobial and SERS actions”, **Applied Surface Science**. 457: 1000-1008; November, 2018.
- [150] Zhu, C., Hu, X. and Wang, X. “Silver nanocubes/graphene oxide hybrid film on a hydrophobic surface for effective molecule concentration and sensitive SERS detection”, **Applied Surface Science**. 470: 423-429; March, 2019.
- [151] Sun, H., Liu, H. and Wu, Y. “Three-dimensional (3D) crumpled graphene-silver hybrid nanostructures on shape memory polymers for surface-enhanced Raman scattering”, **Applied Surface Science**. 467: 554-560; February, 2019.
- [152] Jiang, X. and et al. “Revealing interfacial charge transfer in TiO<sub>2</sub>/reduced graphene oxide nanocomposite by surface-enhanced Raman scattering (SERS): Simultaneous a superior SERS-active substrate”, **Applied Surface Science**. 487: 938-944; September, 2019.

## REFERENCES (CONTINUED)

- [153] Chong, X. and, et al. “Photocatalytic degradation of rhodamine 6G on Ag modified TiO<sub>2</sub> nanotubes: surface-enhanced Raman scattering study on catalytic kinetics and substrate recyclability”, **Colloids and Surfaces A: Physicochemical and Engineering Aspects**. 481: 7-12; September, 2015.
- [154] Zhao, X. and et al. “Sensitive surface-enhanced Raman scattering of TiO<sub>2</sub>/Ag nanowires induced by photogenerated charge transfer”, **Journal of Colloid and Interface Science**. 507: 370-377; December, 2017.
- [155] Karagoz, S. and et al. “Synthesis of Ag and TiO<sub>2</sub> modified polycaprolactone electrospun nanofibers (PCL/TiO<sub>2</sub>-Ag NFs) as a multifunctional material for SERS, photocatalysis and antibacterial applications”, **Ecotoxicology and Environmental Safety**. 188: 109856; January, 2020.
- [156] Wang, X. and, et al. “Three-dimensional hierarchical anatase@ rutile TiO<sub>2</sub> nanotree array films decorated by silver nanoparticles as ultrasensitive recyclable surface-enhanced Raman scattering substrates”, **Journal of Alloys and Compounds**. 725: 1166-1174; November, 2017.
- [157] Guo, T. L. and et al. “Photocatalytic growth of Ag nanocrystals on hydrothermally synthesized multiphasic TiO<sub>2</sub>/reduced graphene oxide (rGO) nanocomposites and their SERS performance”, **Applied Surface Science**. 423: 1-12; November, 2017.
- [158] Wang, Y. and et al. “Facile fabrication of Ag/graphene oxide/TiO<sub>2</sub> nanorod array as a powerful substrate for photocatalytic degradation and surface-enhanced Raman scattering detection”, **Applied Catalysis B: Environmental**. 252: 174-186; September, 2019.
- [159] Sharma, H. S., Carmichael, E. and McCall, D. “Fabrication of SERS substrate for the detection of rhodamine 6G, glyphosate, melamine and salicylic acid”, **Vibrational Spectroscopy**. 83: 159-169; March, 2016.
- [160] Xu, M. L. et al. “Indirect glyphosate detection based on ninhydrin reaction and surface-enhanced Raman scattering spectroscopy”, **Spectrochimica Acta Part A: Molecular and Biomolecular Spectroscopy**. 197: 78-82; May, 2018.

## REFERENCES (CONTINUED)

- [161] Jiao, A. and et al. “Construction of pure worm-like AuAg nanochains for ultrasensitive SERS detection of pesticide residues on apple surfaces”, **Spectrochimica Acta Part A: Molecular and Biomolecular Spectroscopy**. 209: 241-247; February, 2019.
- [162] Wang, X. and et al. “Highly sensitive surface-enhanced Raman scattering detection of organic pesticides based on Ag-nanoplate decorated graphene-sheets”, **Applied Surface Science**. 486: 405-410; August, 2019.
- [163] Jing, P. and et al. “Electrochemical sensing of bisphenol A by graphene-1-butyl-3-methylimidazolium hexafluorophosphate modified electrode”, **Talanta**. 141: 41-46; August, 2015.
- [164] Gong, Q., Wang, Y. and Yang, H. “A sensitive impedimetric DNA biosensor for the determination of the HIV gene based on graphene-Nafion composite film”, **Biosensors and Bioelectronics**. 89: 565-569; March, 2017.
- [165] Sun, W. and et al. “Synthesis of magnetic graphene nanocomposites decorated with ionic liquids for fast lead ion removal”, **International Journal of Biological Macromolecules**. 85: 246-251; August, 2016.
- [166] Chaiyo, S. and et al. “Electrochemical sensors for the simultaneous determination of zinc, cadmium and lead using a Nafion/ionic liquid/graphene composite modified screen-printed carbon electrode”, **Analytica Chimica Acta**. 918: 26-34; March, 2016.
- [167] Santos, A. M., Wong, A. and Fatibello-Filho, O. “Simultaneous determination of salbutamol and propranolol in biological fluid samples using an electrochemical sensor based on functionalized-graphene, ionic liquid and silver nanoparticles”, **Journal of Electroanalytical Chemistry**. 824: 1-8; July, 2018.
- [168] Hou, K. and et al. “A bisphenol A sensor based on novel self-assembly of zinc phthalocyanine tetrasulfonic acid-functionalized graphene nanocomposites”, **Materials Science and Engineering: C**. 49: 640-647; January, 2015.

## REFERENCES (CONTINUED)

- [169] Wong, A. and et al. “Electrochemical sensor based on graphene oxide and ionic liquid for ofloxacin determination at nanomolar levels”, **Talanta**. 161: 333-341; December, 2016.
- [170] Zhang, H., Bo, X. and Guo, L. “Electrochemical preparation of Pt nanoparticles supported on porous graphene with ionic liquids: Electrocatalyst for both methanol oxidation and H<sub>2</sub>O<sub>2</sub> reduction”, **Electrochimica Acta**. 201: 117-124; May, 2016.
- [171] Jemmeli, D. and et al. “Highly sensitive paper-based electrochemical sensor for a reagent free detection of bisphenol A”, **Talanta**. 216: 120924-120931; March, 2020.
- [172] Fan, H. and et al. “Electrochemical bisphenol A sensor based on N-doped graphene sheets”, **Analytica Chimica Acta**. 711: 24-28; November, 2011.
- [173] Wu, L. and et al. “Nanographene-based tyrosinase biosensor for rapid detection of bisphenol A”, **Biosensors and Bioelectronics**. 35: 193-199; May, 2012.
- [174] Vukojević, V. and et al. “Enzymatic glucose biosensor based on manganese dioxide nanoparticles decorated on graphene nanoribbons”, **Journal of Electroanalytical Chemistry**. 823: 610-616; August, 2018.
- [175] Izadiyan, Z. and et al. “Green fabrication of biologically active magnetic core-shell Fe<sub>3</sub>O<sub>4</sub>/Au nanoparticles and their potential anticancer effect”, **Materials Science and Engineering: C**. 96: 51-57; March, 2019.
- [176] El-Deen, S.E.S. and et al. “Evaluation of CNTs/MnO<sub>2</sub> composite for adsorption of 60Co (II), 65Zn (II) and Cd (II) ions from aqueous solutions”, **Radiochimica Acta**. 105: 43-55; April, 2017.
- [177] Ángeles-Pascual, A. and et al. “Structure, magnetic and cytotoxic behaviour of solvothermally grown Fe<sub>3</sub>O<sub>4</sub>@ Au core-shell nanoparticles”, **Materials Characterization**. 142: 237-244; August, 2018.
- [178] Rout, S. and et al. “Enhanced energy recovery by manganese oxide/reduced graphene oxide nanocomposite as an air-cathode electrode in the single-chambered microbial fuel cell”, **Journal of Electroanalytical Chemistry**. 815: 1-7; April, 2018.

## REFERENCES (CONTINUED)

- [179] Mahmoudi-Badiki, T. and et al. "A performance evaluation of  $\text{Fe}_3\text{O}_4/\text{Au}$  and  $\gamma\text{-Fe}_2\text{O}_3/\text{Au}$  nanoparticles in an electrochemical DNA bioassay", **Journal of Electroanalytical Chemistry**. 788: 210-216; March, 2017.
- [180] Hasanzadeh, M. and et al. "Nanomaterials for use in immunosensing of carcinoembryonic antigen (CEA): Recent advances", **TrAC Trends in Analytical Chemistry**. 86: 185-205; January, 2017.
- [181] He, Q. and et al. "Manganese dioxide Nanorods/electrochemically reduced graphene oxide nanocomposites modified electrodes for cost-effective and ultrasensitive detection of Amaranth", **Colloids and Surfaces B: Biointerfaces**. 172: 565-572; December, 2018.
- [182] Singhal, C. and et al. "Paper based DNA biosensor for detection of chikungunya virus using gold shells coated magnetic nanocubes", **Process Biochemistry**. 74: 35-42; November, 2018.
- [183] Wen, G.L. and et al. "N-doped reduced graphene oxide/ $\text{MnO}_2$  nanocomposite for electrochemical detection of  $\text{Hg}^{2+}$  by square wave stripping voltammetry", **Electrochimica Acta**. 291: 95-102; November, 2018.
- [184] Wang, X. and et al. "Highly selective and sensitive electrochemical sensor for L-cysteine detection based on graphene oxide/multiwalled carbon nanotube/manganese dioxide/gold nanoparticles composite", **Journal of Electroanalytical Chemistry**. 757: 100-106; November, 2015.
- [185] Zhang, C. and et al. "Sandwich-type electrochemical immunosensor for sensitive detection of CEA based on the enhanced effects of AgNPs@CS spaced Hemin/rGO", **Biosensors and Bioelectronics**. 126: 785-791; February, 2019.
- [186] Ensafi, A.A., Nasr-Esfahani, P. and Rezaei, B. "Metronidazole determination with an extremely sensitive and selective electrochemical sensor based on graphene nanoplatelets and molecularly imprinted polymers on graphene quantum dots", **Sensors and Actuators B: Chemical**. 270: 192-199; October, 2018.

## REFERENCES (CONTINUED)

- [187] Gu, X. and et al. “Electrochemical detection of carcinoembryonic antigen”, **Biosensors and Bioelectronics**. 102: 610-616; April, 2018.
- [188] Wang, R. and et al. “A label-free electrochemical immunosensor based on AgPt nanorings supported on reduced graphene oxide for ultrasensitive analysis of tumor marker”, **Sensors and Actuators B: Chemical**. 254: 1174-1181; January, 2018.
- [189] Zhou, J. and et al. “An ultrasensitive electrochemical immunosensor for carcinoembryonic antigen detection based on staphylococcal protein A-Au nanoparticle modified gold electrode”, **Sensors and Actuators B: Chemical**. 197: 220-227; July, 2014.
- [190] Fassel, V. A. “International Union of Pure and Applied Chemistry (IUPAC)”, **Pure and Applied Chemistry**. 45: 99-103; January, 1976.
- [191] Atacan, K. “CuFe<sub>2</sub>O<sub>4</sub>/reduced graphene oxide nanocomposite decorated with gold nanoparticles as a new electrochemical sensor material for L-cysteine detection”, **Journal of Alloys and Compounds**. 791: 391-401; June, 2019.
- [192] Oghli, A. H. and Soleymanpour, A. “Polyoxometalate/reduced graphene oxide modified pencil graphite sensor for the electrochemical trace determination of paroxetine in biological and pharmaceutical media”, **Materials Science and Engineering: C**. 108: 110407-110442; March, 2020.
- [193] Satyanarayana, M. and et al. “Silver nanoparticles impregnated chitosan layered carbon nanotube as sensor interface for electrochemical detection of clopidogrel in-vitro”, **Materials Science and Engineering: C**. 101: 103-110; August, 2019.
- [194] Nazarpour, S., Hajian, R. and Sabzvari, M. H. “A Novel Nanocomposite Electrochemical Sensor based on Green Synthesis of Reduced Graphene Oxide/Gold Nanoparticles Modified Screen Printed Electrode for Determination of Tryptophan using Response Surface methodology Approach”, **Microchemical Journal**. 154: 104634-104641; January, 2020.

## REFERENCES (CONTINUED)

- [195] Moreira, L. F. P. P., Buffon, E. and Stradiotto, N. R. “Electrochemical sensor based on reduced graphene oxide and molecularly imprinted poly (phenol) for d-xylose determination”, **Talanta**. 208: 120379-120388; September, 2020.
- [196] Wan, H. and et al. “High sensitive reduced graphene oxide-based room temperature ionic liquid electrochemical gas sensor with carbon-gold nanocomposites amplification”, **Sensors and Actuators B: Chemical**. 299: 126952-126959; August, 2019.
- [197] Lin, J. C., Huang, B. R. and Lin, T. C. “Hybrid structure of graphene sheets/ZnO nanorods for enhancing electron field emission properties”, **Applied surface science**. 289: 384-387; January, 2014.
- [198] Sharma, N., Selvam, S. P. and Yun, K. “Electrochemical detection of amikacin sulphate using reduced graphene oxide and silver nanoparticles nanocomposite”, **Applied Surface Science**. 512: 145742-145751; February, 2020.
- [199] Jin, H. and et al. “Selective and sensitive electrochemical sensing of gastrodin based on nickel foam modified with reduced graphene oxide/silver nanoparticles complex-encapsulated molecularly imprinted polymers”, **Sensors and Actuators B: Chemical**. 277: 14-21; December, 2017.
- [200] Zheng, Y. and et al. “Hydrothermal preparation of reduced graphene oxide-silver nanocomposite using *Plectranthus amboinicus* leaf extract and its electrochemical performance”, **Enzyme and Microbial Technology**. 95: 112-117; May, 2016.
- [201] Jamil, A. and et al. “Preparation and characterization of silver nanoparticles-reduced graphene oxide on ITO for immunosensing platform”, **Sensors and Actuators B: Chemical**. 221: 1423-1432; August, 2015.
- [202] Mazzei, F., Botrè, F. and Botrè, C. “Acid phosphatase/glucose oxidase-based biosensors for the determination of pesticides”, **Analytica Chimica Acta**. 336(1-3): 67-75; August, 1996.



## REFERENCES (CONTINUED)

- [203] Mazzei, F. and et al. “Alkaline phosphatase inhibition based electrochemical sensors for the detection of pesticides”, **Journal of Electroanalytical Chemistry**. 574(1): 95-100; August, 2004.
- [204] Apetrei, C., Rodríguez-Méndez, M. L. and De Saja, J. A. “Amperometric tyrosinase based biosensor using an electropolymerized phosphate-doped polypyrrole film as an immobilization support: Application for detection of phenolic compounds”, **Electrochimica Acta**. 56: 8919-8925; August, 2011.
- [205] da Silva, M. K. L. and et al. “Determination of carbamate pesticide in food using a biosensor based on reduced graphene oxide and acetylcholinesterase enzyme”, **Sensors and Actuators B: Chemical**. 277: 555-561; September, 2018.
- [206] Jiang, Y. and et al. “Silver nanoparticles modified two-dimensional transition metal carbides as nanocarriers to fabricate acetylcholinesterase-based electrochemical biosensor”, **Chemical Engineering Journal**. 339: 547-556; January, 2018.
- [207] Song, Y. and et al. “A simple electrochemical biosensor based on AuNPs/MPS/Au electrode sensing layer for monitoring carbamate pesticides in real samples”, **Journal of Hazardous Materials**. 304: 103-109; October, 2016.
- [208] Qu, Z. and et al. “A novel fluorescence biosensor for sensitivity detection of tyrosinase and acid phosphatase based on nitrogen-doped graphene quantum dots”, **Analytica Chimica Acta**. 997: 52-59; October, 2018.
- [209] Zhang, J. and et al. “Detecting acid phosphatase enzymatic activity with phenol as a chemical exchange saturation transfer magnetic resonance imaging contrast agent (PhenolCEST MRI)”, **Biosensors and Bioelectronics**. 141: 111442-111448; June, 2019.
- [210] Sanllorente-Méndez, S., Domínguez-Renedo, O. and Arcos-Martínez, M. J. “Development of acid phosphatase based amperometric biosensors for the inhibitive determination of As(V)”, **Talanta**. 93: 301-306; February, 2012.

## REFERENCES (CONTINUED)

- [211] Trott, O. and Olson, A. J. “AutoDock Vina: improving the speed and accuracy of docking with a new scoring function, efficient optimization, and multithreading”, **Journal of Computational Chemistry**. 31(2), 455-461; June, 2010.
- [212] Zhu, S. and et al. “Characterization of purple acid phosphatase family and functional analysis of GmPAP7a/7b involved in extracellular ATP utilization in soybean”, **Frontiers in Plant Science**. 11, 661-676, June, 2020.
- [213] Klabunde, T. and et al. “Mechanism of Fe (III)-Zn (II) purple acid phosphatase based on crystal structures”, **Journal of Molecular Biology**. 259(4): 737-748; June, 1996.
- [214] Schenk, G. and et al. “Crystal structures of a purple acid phosphatase, representing different steps of this enzyme's catalytic cycle”, **BMC Structural Biology**. 8(1): 6-19; January, 2008.
- [215] Wang, L. and et al. “Facile, green and clean one-step synthesis of carbon dots from wool: application as a sensor for glyphosate detection based on the inner filter effect”, **Talanta**. 160: 268-275; July, 2016.
- [216] Qian, K. and et al. “Residue determination of glyphosate in environmental water samples with high-performance liquid chromatography and UV detection after derivatization with 4-chloro-3, 5-dinitrobenzotrifluoride”, **Analytica Chimica Acta**. 635(2): 222-226; January, 2009.
- [217] Yamada, H., and Yamamoto, Y. “Surface enhanced Raman scattering (SERS) of chemisorbed species on various kinds of metals and semiconductors”, **Surface Science**. 134(1): 71-90; November, 1983.
- [218] Li, J. F. and et al. “Shell-isolated nanoparticle-enhanced Raman spectroscopy”, **Nature**. 464(7287): 392; March, 2010.
- [219] Zhang, C. and et al. “SERS detection of R6G based on a novel graphene oxide/silver nanoparticles/silicon pyramid arrays structure”, **Optics Express**. 23(19): 24811-24821; September, 2015.

## REFERENCES (CONTINUED)

- [220] Islam, M. A. and et al. “Optical and structural characterization of TiO<sub>2</sub> nanoparticles”, **Journal of Electrical and Electronics Engineering**. 3(2): 18-24; November, 2012.
- [221] Komaguchi, K. and et al. “Electron-transfer reaction of oxygen species on TiO<sub>2</sub> nanoparticles induced by sub-band-gap illumination”, **The Journal of Physical Chemistry C**. 114(2): 1240-1245; December, 2010.
- [222] Sério, S. and et al. “Spectroscopic studies of anatase TiO<sub>2</sub> thin films prepared by DC reactive magnetron sputtering”, **Chemical Physics Letters**. 508(1-3): 71-75; May, 2011.
- [223] Wang, Y. and et al. “Charge transfer tuned by the surrounding dielectrics in TiO<sub>2</sub>-Ag composite”, **Nanomaterials**. 8(12): 1019-1028; December, 2018.
- [224] Ehrenreich, H. R. P. H. and Philipp, H. R. “Optical properties of Ag and Cu”, **Physical Review**. 128(4): 1622-1634; November, 1962.
- [225] Lu, X. and et al. “Synergetic effect of graphene and Co(OH)<sub>2</sub> as cocatalysts of TiO<sub>2</sub> nanotubes for enhanced photogenerated cathodic protection”, **Journal of Materials Science & Technology**. 37: 55-63; January, 2020.
- [226] Guo, W. and et al. “A novel electrochemical determination platform of uranyl ion based on silver nanodendrites-reduced graphene oxide”, **Microchemical Journal**. 158: 105134-105150; November, 2020.
- [227] Tao, B., He, J. and Miao, F. “A hybrid sandwich structure of TiO<sub>2</sub>/N-graphene/Ag supported by ordered silicon nanowires and its application as lithium-ion battery electrodes”, **Materials Letters**. 262: 127046-127055; March, 2020.
- [228] Zong, X., Zhu, R. and Guo, X. “Nanostructured gold microelectrodes for SERS and EIS measurements by incorporating ZnO nanorod growth with electroplating”, **Scientific Reports**. 5: 16454-16472; November, 2015.
- [229] Yang, J. H. and et al. “The effect of dye-sensitized solar cell based on the composite layer by anodic TiO<sub>2</sub> nanotubes”, **Nanoscale Research Letters**. 9(1): 671-689; December, 2014.

## REFERENCES (CONTINUED)

- [230] Liu, C. and et al. “Silver nanoparticle modified TiO<sub>2</sub> nanotubes with enhanced the efficiency of dye-sensitized solar cells”, **Microporous and Mesoporous Materials**. 287: 228-233; June, 2019.
- [231] Ohsaka, T., Izumi, F. and Fujiki, Y. “Raman spectrum of anatase, TiO<sub>2</sub>”, **Journal of Raman spectroscopy**. 7(6): 321-324; December, 1978.
- [232] Lei, D. and et al. “Enhanced field emission from titanium dioxide nanotube arrays decorated with graphene sheets and silver nanoparticles”, **Vacuum**. 126: 29-33; January, 2016.
- [233] Childres, I. and et al. “Raman spectroscopy of graphene and related materials”, **New Developments in Photon and Materials Research**. 1: 1-20; August, 2013.
- [234] Kuang, L. and Zhang, W. “Enhanced hydrogen production by carbon-doped TiO<sub>2</sub> decorated with reduced graphene oxide (rGO) under visible light irradiation”, **RSC Advances**. 6(3): 2479-2488; December, 2016.
- [235] Harraz, F. A. and et al. “TiO<sub>2</sub>/reduced graphene oxide nanocomposite as efficient ascorbic acid amperometric sensor”, **Journal of Electroanalytical Chemistry**. 832: 225-232; January, 2019.
- [236] Pandey, S. and et al. “Improved electron field emission from morphologically disordered monolayer graphene”, **Applied Physics Letters**. 100(4): 43104-43123; January, 2012.
- [237] Hong, J. and et al. “Origin of new broad Raman D and G peaks in annealed graphene”, **Scientific Reports**. 3: 2700-2711; September, 2013.
- [238] Dong, P. and et al. “The green synthesis of Ag-loaded photocatalyst via DBD cold plasma assisted deposition of Ag nanoparticles on N-doped TiO<sub>2</sub> nanotubes”, **Journal of Photochemistry and Photobiology A: Chemistry**. 382: 111971-11990; September, 2019.
- [239] Konstantinova, E. and et al. “Unveiling point defects in titania mesocrystals: a combined EPR and XPS study”, **New Journal of Chemistry**. 42(18): 15184-15189; August, 2018.

## REFERENCES (CONTINUED)

- [240] Niu, X. and et al. “Synthesis of Nb doped TiO<sub>2</sub> nanotube/reduced graphene oxide heterostructure photocatalyst with high visible light photocatalytic activity”, **Applied Surface Science**. 440: 804-813; May, 2018.
- [241] Dong, P. and et al. “The green synthesis of Ag-loaded photocatalyst via DBD cold plasma assisted deposition of Ag nanoparticles on N-doped TiO<sub>2</sub> nanotubes”, **Journal of Photochemistry and Photobiology A: Chemistry**. 382: 111971; July, 2019.
- [242] Van V. P. and et al. “Silver nanoparticle loaded TiO<sub>2</sub> nanotubes with high photocatalytic and antibacterial activity synthesized by photoreduction method”, **Journal of Photochemistry and Photobiology A: Chemistry**. 352: 106-112; 2018.
- [243] Huang, J. and et al. “Efficient silver modification of TiO<sub>2</sub> nanotubes with enhanced photocatalytic activity”, **Solid State Sciences**. 80: 116-122; June, 2018.
- [244] Zhang, Y. and et al. “Calcination of reduced graphene oxide decorated TiO<sub>2</sub> composites for recovery and reuse in photocatalytic applications”, **Ceramics International**. 43(1): 1150-1159; January, 2017.
- [245] Gomes, J. and et al. “N-TiO<sub>2</sub> photocatalysts: a review of their characteristics and capacity for emerging contaminants removal”, **Water**. 11(2): 373-385; February, 2019.
- [246] Smith, E. and Dent, G. **Modern Raman Spectroscopy: A Practical Approach**. New Jersey: Wiley Online Library, 2005.
- [247] del Pilar Rodríguez-Torres, M., Díaz-Torres, L. A. and Romero-Servin, S. “Heparin assisted photochemical synthesis of gold nanoparticles and their performance as SERS substrates”, **International Journal of Molecular Sciences**. 15(10): 19239-19252; October, 2014.
- [248] Li, C. and et al. “Analysis of trace methylene blue in fish muscles using ultra-sensitive surface-enhanced Raman spectroscopy”, **Food Control**. 65: 99-105; July, 2016.

## REFERENCES (CONTINUED)

- [249] Forato, F. and et al. “Functionalized core-shell Ag@TiO<sub>2</sub> nanoparticles for enhanced Raman spectroscopy: a sensitive detection method for Cu (ii) ions”, **Physical Chemistry Chemical Physics**. 21(6): 3066-3072; January, 2019.
- [250] Whang, T.-J. and et al. “Laser-induced silver nanoparticles on titanium oxide for photocatalytic degradation of methylene blue”, **International Journal of Molecular Sciences**. 10(11): 4707-4718; October, 2009.
- [251] Horiba, J. Y. **Raman Application Note: Raman Spectroscopy for Analysis and Monitoring**. New Jersey: Horiba, 2015.
- [252] DSouza, A. V. and et al. “Review of fluorescence guided surgery systems: identification of key performance capabilities beyond indocyanine green imaging”, **Journal of Biomedical Optics**. 21(8): 80901-80921; August, 2016.
- [253] Jackson, J. B. and N. J. Halas. “Surface-enhanced Raman scattering on tunable plasmonic nanoparticle substrates”, **Proceedings of the National Academy of Sciences**. 101(52): 17930-17935; December, 2004.
- [254] Hsiao, W.-H. and et al. “Surface-enhanced Raman scattering imaging of a single molecule on urchin-like silver nanowires”, **ACS Applied Materials & Interfaces**. 3(9): 3280-3284; July, 2011.
- [255] Dai, Z. and et al. “Obviously angular, cuboid-shaped TiO<sub>2</sub> nanowire arrays decorated with Ag nanoparticle as ultrasensitive 3D surface-enhanced Raman scattering substrates”, **The Journal of Physical Chemistry C**. 118(39): 22711-22718; September, 2014.
- [256] Tuschel, D. “The effect of microscope objectives on the Raman spectra of crystals”, **Spectroscopy**. 32: 14-23; September, 2017.
- [257] Tian, Y. and et al. “Efficiency enhancement of Raman spectroscopy at long working distance by parabolic reflector”, **Biomedical Optics Express**. 8(11): 5243-5252; November, 2017.
- [258] Grimes, C. A. and Mor, G. K. **TiO<sub>2</sub> nanotube arrays: synthesis, properties, and applications**. Berlin: Springer Science & Business Media, 2009.

## REFERENCES (CONTINUED)

- [259] Berger, S. and et al. “Self-organized TiO<sub>2</sub> nanotubes: Factors affecting their morphology and properties”, **Physica Status Solid.** 247(10): 2424-2435; October, 2010.
- [260] Giorgi, L. and et al. “Titania nanotubes self-assembled by electrochemical anodization: Semiconducting and electrochemical properties”, **Thin Solid Films.** 601: 28-34; February, 2016.
- [261] Kapusta-Kołodziej, J. and et al. “Effects of anodizing potential and temperature on the growth of anodic TiO<sub>2</sub> and its photo-electrochemical properties”, **Applied Surface Science.** 396: 1119-1129; February, 2017.
- [262] Ling, Y. and et al. “Using Ag-embedded TiO<sub>2</sub> nanotubes array as recyclable SERS substrate”, **Applied Surface Science.** 388: 169-173; December, 2016.
- [263] Shin, D. H. and et al. “Wettability changes of TiO<sub>2</sub> nanotube surfaces”, **Nanotechnology.** 22(31): 315704-315718; November, 2011.
- [264] Macias, G. and et al. “Surface roughness boosts the SERS performance of imprinted plasmonic architectures”, **Journal of Materials Chemistry C.** 4(18): 3970-3975; January, 2016.
- [265] Kodama, A. and et al. “Bioactivation of titanium surfaces using coatings of TiO<sub>2</sub> nanotubes rapidly pre-loaded with synthetic hydroxyapatite”, **Acta Biomaterialia.** 5(6): 2322-2330; July, 2009.
- [266] Pisarek, M. and et al. “The role of Ag particles deposited on TiO<sub>2</sub> or Al<sub>2</sub>O<sub>3</sub> self-organized nanoporous layers in their behavior as SERS-active and biomedical substrates”, **Materials Chemistry and Physics.** 139(1): 55-65; April, 2013.
- [267] Marien, C. B. and et al. “TiO<sub>2</sub> nanotube arrays: influence of tube length on the photocatalytic degradation of paraquat”, **Applied Catalysis B: Environmental.** 194: 1-6; October, 2016.
- [268] Marchezini, E. and et al. “Controlling morphological parameters of a nanotubular TiO<sub>2</sub> coating layer prepared by anodic oxidation”, **Materials Research Express.** 7(2): 25017-25028; February, 2020.

## REFERENCES (CONTINUED)

- [269] Zhang, G. and et al. “A facile strategy to fabricate Au/TiO<sub>2</sub> nanotubes photoelectrode with excellent photoelectrocatalytic properties”, **Applied Surface Science**. 391: 345-352; January, 2017.
- [270] Hyam, R.S. and et al. “Plasmonic-Photonic Interference Coupling in Submicrometer Amorphous TiO<sub>2</sub>-Ag Nanoarchitectures”, **Langmuir**. 33(43): 12398-12403; October, 2017.
- [271] Yang, J. and et al. “High aspect ratio SiNW arrays with Ag nanoparticles decoration for strong SERS detection”, **Nanotechnology**. 25(46): 465707; October, 2014.
- [272] Huang, Y. and et al. “SERS study of Ag nanoparticles electrodeposited on patterned TiO<sub>2</sub> nanotube films”, **Journal of Raman Spectroscopy**. 42(5): 986-991; November, 2011.
- [273] Li, H. and et al. “Multilayer enhanced gold film over nanostructure surface-enhanced Raman substrates”, **Applied Spectroscopy**. 60: 1377-1385; June, 2006.
- [274] Zhan, Y. and et al. “Electrochemically Synthesized Porous Ag Double Layers for Surface-Enhanced Raman Spectroscopy Applications”, **Langmuir**. 35(19): 6340-6345; April, 2019.
- [275] Zhao, C. and et al. “Multi-layer nanoarrays sandwiched by anodized aluminium oxide membranes: an approach to an inexpensive, reproducible, highly sensitive SERS substrate”, **Nanoscale**. 10(34): 16278-16283; August, 2018.
- [276] Tang, L. and et al. “A novel SERS substrate platform: Spatially stacking plasmonic hotspots films”, **Nanoscale Research Letters**. 14: 94-115; March, 2019.
- [277] Ouyang, L. and et al. “A reusable laser wrapped graphene-Ag array-based SERS sensor for trace detection of genomic DNA methylation”, **Biosensors and Bioelectronics**. 92: 755-762; September, 2017.
- [278] Dutta, S. and et al. “Silver nanoparticle decorated reduced graphene oxide (rGO) nanosheet: a platform for SERS based low-level detection of uranyl ion”, **ACS Applied Materials & Interfaces**. 5: 8724-8732; August, 2013.



## REFERENCES (CONTINUED)

- [279] Basirun, W. J. and et al. “Solid-phase electrochemical reduction of graphene oxide films in alkaline solution”, **Nanoscale Research Letters**. 8(1): 397-410; September, 2013.
- [280] Kumar, S. and Parekh, S. H. “Linking graphene-based material physicochemical properties with molecular adsorption, structure and cell fate”, **Communications Chemistry**. 3(1): 1-11; January, 2020.
- [281] Liu, X. and et al. “Thickness dependent Raman spectra and interfacial interaction between Ag and epitaxial graphene on 6H-SiC (0001)”, **Physical Chemistry Chemical Physics**. 20(8): 5964-5974; February, 2018.
- [282] Wang, X. and et al. “Preparation of graphene-Ag nanoparticles hybrids and their SERS activities”, **Applied Surface Science**. 387: 707-719; November, 2016.
- [283] Ambroziak, R. and et al. “Cubic silver nanoparticles fixed on TiO<sub>2</sub> nanotubes as simple and efficient substrates for surface enhanced Raman scattering”, **Materials**. 12(20): 3373-3388; October, 2019.
- [284] Chen, Y. and et al. “In situ controlled growth of well-dispersed gold nanoparticles in TiO<sub>2</sub> nanotube arrays as recyclable substrates for surface-enhanced Raman scattering”, **Dalton Transactions**. 41(3): 1020-1026; 2012.
- [285] Lu, Z. and et al. “A novel natural surface-enhanced Raman spectroscopy (SERS) substrate based on graphene oxide-Ag nanoparticles-Mytilus coruscus hybrid system”, **Sensors and Actuators B: Chemical**. 261: 1-10; January, 2018.
- [286] Li, X. and et al. “Multifunctional Au-coated TiO<sub>2</sub> nanotube arrays as recyclable SERS substrates for multifold organic pollutants detection”, **Advanced Functional Materials**. 20(17): 2815-2824; September, 2010.
- [287] Houas, A. and et al. “Photocatalytic degradation pathway of methylene blue in water”, **Applied Catalysis B: Environmental**. 31(2): 145-157; May, 2001.

## REFERENCES (CONTINUED)

- [288] Wang, Y. and et al. “Enhanced photoelectric catalytic degradation of methylene blue via TiO<sub>2</sub> nanotube arrays hybridized with graphite-like carbon”, **Journal of Molecular Catalysis A: Chemical**. 349(1-2): 13-19; October, 2011.
- [289] Tang, Y. and et al. “Efficient removal of herbicide 2, 4-dichlorophenoxyacetic acid from water using Ag/reduced graphene oxide co-decorated TiO<sub>2</sub> nanotube arrays”, **Journal of Hazardous Materials**. 241: 323-330; September, 2012.
- [290] Wen, Y. Ding, H. and Shan, Y. “Preparation and visible light photocatalytic activity of Ag/TiO<sub>2</sub>/graphene nanocomposite”, **Nanoscale**. 3(10): 4411-4417; August, 2011.
- [291] Faraji, M. and Mohaghegh, N. “Ag/TiO<sub>2</sub>-nanotube plates coated with reduced graphene oxide as photocatalysts”, **Surface and Coatings Technology**. 288: 144-150; January, 2016.
- [292] Wong-Ek, K. and et al. “Silver nanoparticles deposited on anodic aluminum oxide template using magnetron sputtering for surface-enhanced Raman scattering substrate”, **Thin Solid Films**. 518(23): 7128-7132; September, 2010.
- [293] Samransuksamer, B. and et al. “Facile method for decorations of Au nanoparticles on TiO<sub>2</sub> nanorod arrays toward high-performance recyclable SERS substrates”, **Sensors and Actuators B: Chemical**. 277: 102-113; August, 2018.
- [294] Li, X. and et al. “Ordered array of gold semishells on TiO<sub>2</sub> spheres: an ultrasensitive and recyclable SERS substrate”, **ACS Applied Materials & Interfaces**. 4(4): 2180-2185; April, 2012.
- [295] Costa, J. C and et al. “Surface-enhanced Raman spectroscopy studies of organophosphorous model molecules and pesticides”, **Physical Chemistry Chemical Physics**. 14(45): 15645-15651; September, 2012.

**REFERENCES (CONTINUED)**

- [296] Sharma, H. S. Carmichael, E. and McCall, D. “Fabrication of SERS substrate for the detection of rhodamine 6G, glyphosate, melamine and salicylic acid”, **Vibrational Spectroscopy**. 83: 159-169; February, 2016.
- [297] Torul, H., Boyaci, I. H. and Tamer, U. “Attomole detection of glyphosate by surface-enhanced Raman spectroscopy using gold nanorods”, **FABAD Journal of Pharmaceutical Sciences**. 35: 179-184; September, 2010.
- [298] Xu, M. L. and et al. “Indirect glyphosate detection based on ninhydrin reaction and surface-enhanced Raman scattering spectroscopy”, **Spectrochimica Acta Part A: Molecular and Biomolecular Spectroscopy**. 197: 78-82; May, 2018.
- [299] Tan, M. J. and et al. “Metal carbonyl-gold nanoparticle conjugates for highly sensitive SERS detection of organophosphorus pesticides”, **Biosensors and Bioelectronics**. 96: 167-172; May, 2017.

## **APPENDICES**

## **APPENDIX A**

### **EXPERIMENTAL DETAILS**



### A.1 Glassy carbon paste electrode and its set up

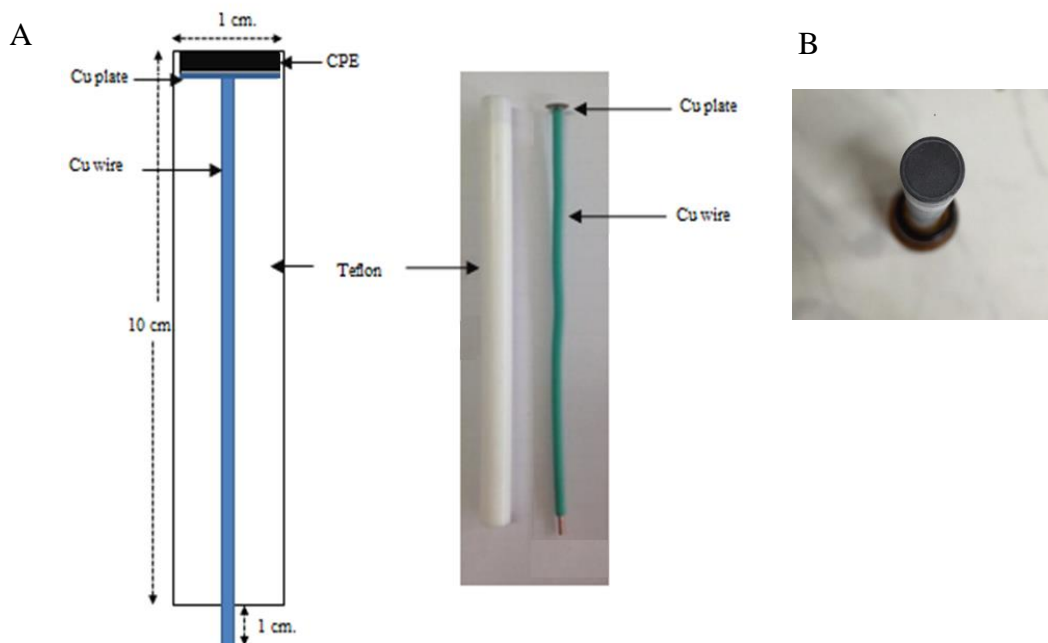


Figure A.1 (A) Electrode composition and (B) electrode surface

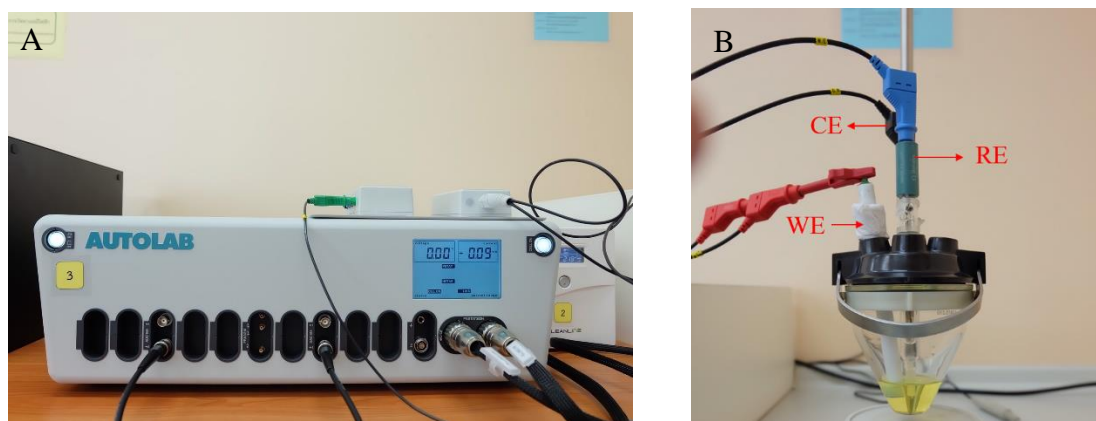
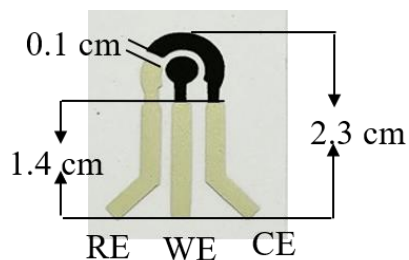
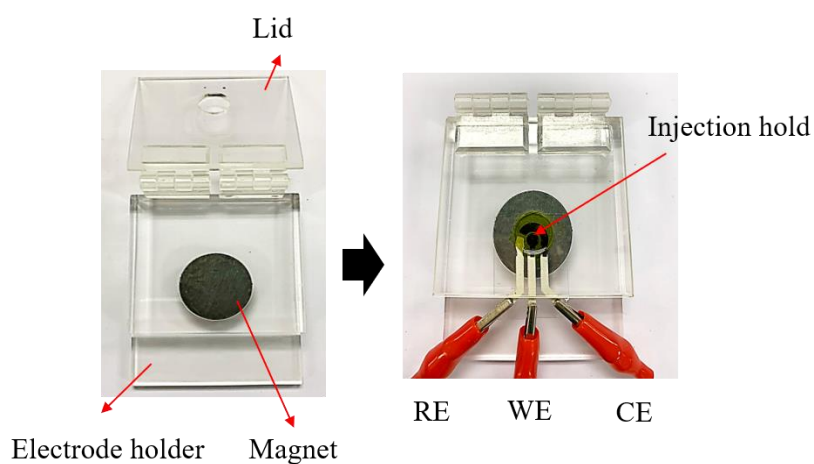


Figure A.2 (A) Potentiostat/Galvanostat and (B) three-electrode system

## A.2 Screen-printed carbon electrode and its set up



**Figure A.3** Screen printed carbon electrode



**Figure A.4** Electrode holder for fixing of the screen-printed carbon electrode

## A.3 SERS substrate and its set up

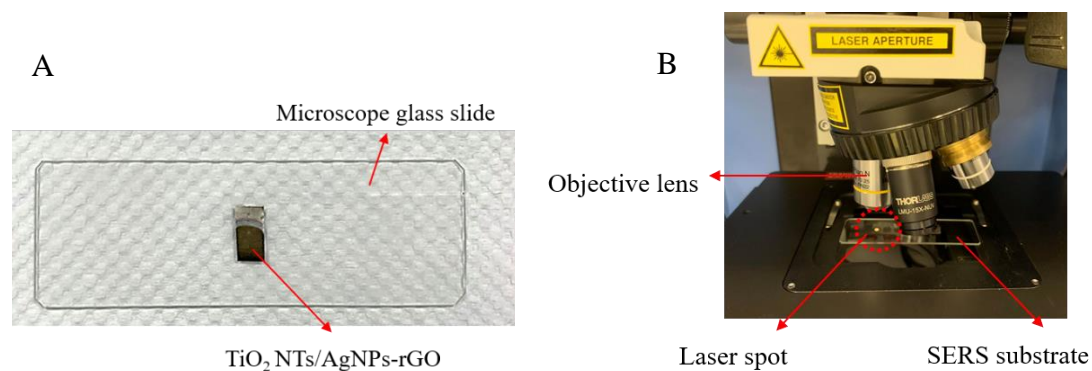


**Figure A.5** (A) SERS substrate, (B) Raman analysis part, and (C) instrumentation





**Figure A.5 (A) SERS substrate, (B) Raman analysis part, and (C) instrumentation (continued)**

#### A.4 Solar simulator and its set up

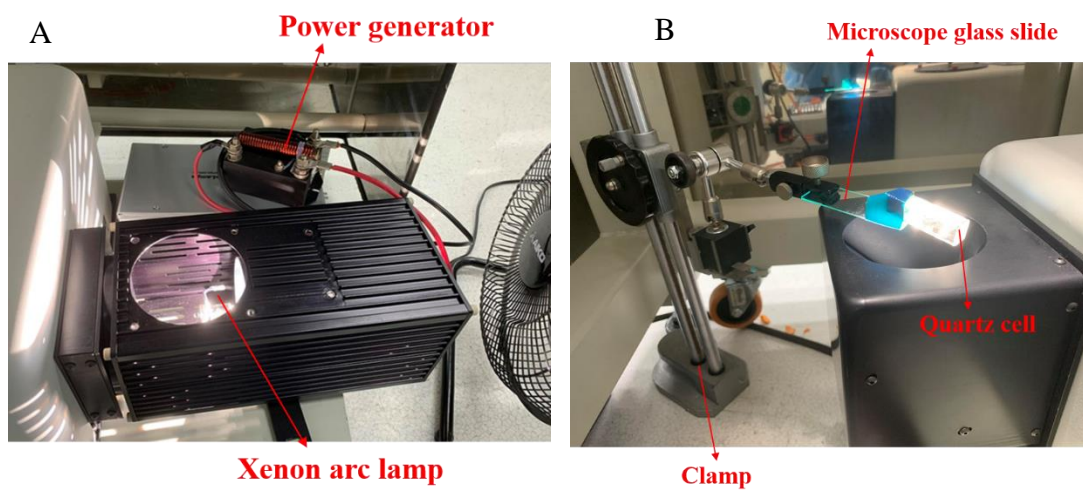


**Figure A.6 (A) Xenon arc lamp equipped with a solar simulator and (B) the set-up of SERS substrate for recyclable study**



**APPENDIX B**  
**THE RESULTS OF ANALYSIS**



### B.1 Carbon composite nanomaterials-based sensor: electrochemical sensor

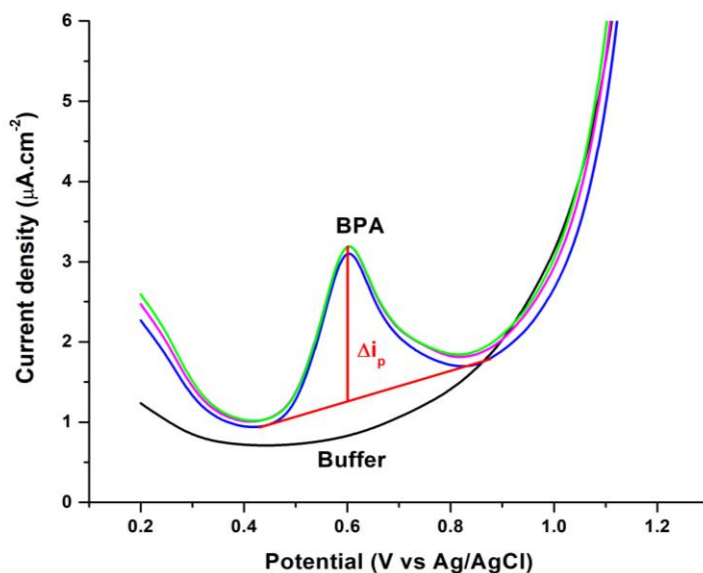


**Figure B.1** Current responses on the GCPE/GNP-IL measured by DPV in 0.1 M phosphate buffer solution containing 1  $\mu$ M BPA solution

**Table B.1** The current of GCPE/GNP-IL on the amount of IL

Amount of IL (mg.cm <sup>-2</sup> )	Average current ( $\mu$ A.cm <sup>-2</sup> )			
	1	2	3	Mean $\pm$ SD
0.0	1.66	1.68	1.67	1.67 $\pm$ 0.01
0.1	2.25	2.15	2.24	2.22 $\pm$ 0.06
0.2	2.48	2.40	2.29	2.39 $\pm$ 0.09
0.3	2.40	2.48	2.48	2.45 $\pm$ 0.05
0.4	2.75	3.00	2.78	2.83 $\pm$ 0.11
0.5	2.41	2.64	2.55	2.53 $\pm$ 0.11

**Table B.2 The current of GCPE/GNP-IL on the amount of GNP-IL**

Amount of GNP-IL ( $\mu\text{g.cm}^{-2}$ )	Average current ( $\mu\text{A.cm}^{-2}$ )			
	1	2	3	Mean $\pm$ SD
8	1.19	1.06	1.18	$1.14 \pm 0.07$
16	1.22	1.37	1.33	$1.31 \pm 0.08$
20	1.89	1.99	2.11	$1.99 \pm 0.13$
24	2.00	2.12	2.03	$2.05 \pm 0.06$
28	2.87	2.61	2.81	$2.77 \pm 0.14$
32	2.03	1.84	1.82	$1.90 \pm 0.11$
40	1.59	1.53	1.98	$1.70 \pm 0.24$

**Table B.3 The peak current and peak potential of GCPE/GNP-IL on pH solution**

pH solution	Average current ( $\mu\text{A.cm}^{-2}$ )				Peak potential (V vs Ag/AgCl)
	1	2	3	Mean $\pm$ SD	
5	1.05	1.08	1.10	$1.08 \pm 0.02$	0.72
6	2.26	2.32	2.27	$2.28 \pm 0.03$	0.65
7	2.42	3.13	2.72	$2.76 \pm 0.36$	0.57
8	3.38	3.11	3.22	$3.24 \pm 0.14$	0.50
9	1.66	1.51	2.38	$1.85 \pm 0.47$	0.45

**Table B.4 The current of GCPE/GNP-IL on the pulse potential**

Pulse potential	Average current ( $\mu\text{A.cm}^{-2}$ )			
	1	2	3	Mean $\pm$ SD
25	0.63	0.87	0.74	$0.75 \pm 0.12$
50	2.52	2.88	2.41	$2.60 \pm 0.24$
75	3.46	3.39	3.33	$3.39 \pm 0.06$
100	3.61	3.32	3.40	$3.44 \pm 0.15$
125	3.66	3.65	3.61	$3.64 \pm 0.02$
150	4.73	4.65	4.81	$4.73 \pm 0.08$

**Table B.4 The current of GCPE/GNP-IL on the pulse potential (continued)**

Pulse potential	Average current ( $\mu\text{A.cm}^{-2}$ )			
	1	2	3	Mean $\pm$ SD
175	2.42	2.47	2.36	$2.42 \pm 0.05$
200	1.79	2.03	1.92	$1.92 \pm 0.11$

**Table B.5 The current of GCPE/GNP-IL on the step potential**

Step potential	Average current ( $\mu\text{A.cm}^{-2}$ )			
	1	2	3	Mean $\pm$ SD
10	2.46	2.58	2.00	$2.35 \pm 0.30$
20	3.95	3.28	3.36	$3.53 \pm 0.36$
30	4.82	4.17	4.71	$4.50 \pm 0.24$
40	3.18	2.97	3.09	$3.08 \pm 0.10$
50	2.79	3.14	3.20	$3.04 \pm 0.22$
60	3.18	3.10	2.70	$2.99 \pm 0.25$

**Table B.6 The current of GCPE/GNP-IL on the scan rate**

Scan rate	Average current ( $\mu\text{A.cm}^{-2}$ )			
	1	2	3	Mean $\pm$ SD
10	3.10	2.77	2.79	$2.89 \pm 0.19$
25	3.35	3.58	4.03	$3.66 \pm 0.34$
50	4.33	3.97	4.24	$4.18 \pm 0.19$
75	2.58	3.04	2.36	$2.66 \pm 0.34$
100	2.82	2.26	2.47	$2.52 \pm 0.29$
125	2.12	2.34	2.49	$2.32 \pm 0.18$

**Table B.7 The current of different modified electrodes on BPA determination**

[BPA] ( $\mu\text{M}$ )	Average current ( $\mu\text{A.cm}^{-2}$ ) $\pm$ SD			[BPA] ( $\mu\text{M}$ )	Average current ( $\mu\text{A.cm}^{-2}$ ) $\pm$ SD
	GCPE	GPCE/IL	GCPE/GNP		
0.05	$0.12 \pm 0.01$	$0.07 \pm 0.01$	$0.09 \pm 0.02$	0.02	$0.18 \pm 0.01$
0.10	$0.27 \pm 0.01$	$0.22 \pm 0.01$	$0.20 \pm 0.01$	0.10	$0.30 \pm 0.03$
0.15	$0.45 \pm 0.02$	$0.38 \pm 0.02$	$0.32 \pm 0.02$	0.20	$0.72 \pm 0.08$
0.20	$0.60 \pm 0.01$	$0.48 \pm 0.03$	$0.58 \pm 0.07$	0.40	$2.65 \pm 0.34$
0.25	$0.78 \pm 0.01$	$0.70 \pm 0.03$	$0.62 \pm 0.06$	0.80	$6.21 \pm 0.34$
0.30	$0.91 \pm 0.01$	$0.80 \pm 0.02$	$0.80 \pm 0.09$	1.20	$9.16 \pm 0.08$
0.35	$1.06 \pm 0.02$	$0.93 \pm 0.03$	$0.93 \pm 0.09$	1.60	$10.66 \pm 0.33$
0.40	$1.19 \pm 0.02$	$1.11 \pm 0.01$	$1.12 \pm 0.10$	2.00	$14.59 \pm 0.30$
0.80	$2.94 \pm 0.16$	$3.02 \pm 0.28$	$3.05 \pm 0.35$	2.50	$16.76 \pm 0.39$
1.20	$4.50 \pm 0.19$	$4.85 \pm 0.36$	$5.68 \pm 0.40$	3.00	$20.66 \pm 0.80$
1.60	-	$6.29 \pm 0.39$	$7.09 \pm 0.30$	3.50	$23.26 \pm 0.67$
2.00	-	$7.64 \pm 0.35$	$8.46 \pm 0.18$	4.00	$25.06 \pm 0.43$
2.40	-	-	$9.69 \pm 0.31$	4.50	$28.37 \pm 0.90$
2.80	-	-	-	5.00	$32.50 \pm 0.73$

**Table B.8 The current response on the detection of 0.02  $\mu\text{M}$  BPA**

Number	Average current ( $\mu\text{A.cm}^{-2}$ )
1	0.184
2	0.176
3	0.186
4	0.188
5	0.199
6	0.205
7	0.160
8	0.199
9	0.184



**Table B.8 The current response on the detection of 0.02  $\mu\text{M}$  BPA (continued)**

Number	Average current ( $\mu\text{A.cm}^{-2}$ )
10	0.207
<b>Average <math>\pm</math> SD</b>	$0.189 \pm 0.014$

**Table B.9 The response for repeatability and reproducibility study**

Number	Average current ( $\mu\text{A.cm}^{-2}$ )	
	Repeatability	Reproducibility
1	4.852	4.902
2	5.132	5.337
3	5.004	5.195
4	5.226	5.149
5	4.850	4.889
<b>Average</b>	5.013	5.094
<b>SD</b>	0.167	0.194
<b>%RSD</b>	3.33	3.81

**Table B.10 The response for the GCPE/GNP-IL on its stability**

Days	Average current ( $\mu\text{A.cm}^{-2}$ )				Relative current density (%)
	1	2	3	Mean $\pm$ SD	
1	5.81	5.51	5.77	$5.70 \pm 0.08$	100.00
2	5.74	5.84	5.22	$5.60 \pm 0.17$	98.35
3	5.55	5.73	5.31	$5.53 \pm 0.11$	97.05
4	5.56	5.23	4.91	$5.24 \pm 0.16$	91.95
5	4.95	5.22	5.05	$5.07 \pm 0.07$	89.07
6	5.21	4.80	4.93	$4.98 \pm 0.10$	87.43
7	4.99	4.61	4.53	$4.71 \pm 0.12$	82.71
8	4.70	5.11	4.80	$4.87 \pm 0.11$	85.52
9	5.01	4.42	5.05	$4.83 \pm 0.18$	84.71

**Table B.10 The response for the GCPE/GNP-IL on its stability (continued)**

Days	Average current ( $\mu\text{A.cm}^{-2}$ )				Relative current density (%)
	1	2	3	Mean $\pm$ SD	
10	4.83	4.96	4.82	$4.87 \pm 0.04$	85.48
11	4.53	4.62	4.67	$4.61 \pm 0.04$	80.84
12	4.98	4.83	4.69	$4.84 \pm 0.07$	84.88
13	4.89	4.75	4.39	$4.68 \pm 0.13$	82.14
14	5.31	4.53	3.86	$4.56 \pm 0.36$	80.13

**Table B.11 The response for the GCPE/GNP-IL on its selectivity (n=3)**

Substances	Concentration ( $\mu\text{M}$ )	Average current ( $\mu\text{A.cm}^{-2}$ )	Relative current density (%)
BPA	1	$3.99 \pm 0.07$	100.00
Phenol	1	$3.99 \pm 0.13$	100.03
1-naphthol	1	$3.75 \pm 0.13$	93.99
4-nitrophenol	10	$3.96 \pm 0.28$	99.31
Glucose	100	$3.68 \pm 0.14$	92.42
Sucrose	100	$3.80 \pm 0.13$	95.47
$\text{Na}^+$	100	$3.76 \pm 0.15$	94.25
$\text{Ca}^{2+}$	100	$3.69 \pm 0.04$	92.69
$\text{Mg}^{2+}$	100	$3.74 \pm 0.14$	93.89
$\text{Al}^{3+}$	100	$3.84 \pm 0.05$	96.32
$\text{Zn}^{2+}$	100	$4.04 \pm 0.37$	101.41
$\text{Cu}^{2+}$	100	$3.89 \pm 0.16$	97.57
$\text{Fe}^{2+}$	100	$4.09 \pm 0.20$	102.74
$\text{Pb}^{2+}$	100	$4.23 \pm 0.29$	106.24
$\text{Cd}^{2+}$	100	$3.84 \pm 0.15$	96.25

**Table B.12 The linear regression for BPA determination by the GCPE/GNP-IL using standard addition method and concentration of BPA found in the samples**

Samples	Linear regression ( $y = mx + c$ )	$r^2$	BPA in sample
Plastic A	$y = 8.78x + 0.59$	0.999	3.23 mg/kg
	$y = 8.06x + 0.63$	0.999	3.76 mg/kg
	$y = 7.26x + 0.52$	0.992	3.45 mg/kg
Plastic B	$y = 12.15x + 0.64$	0.997	2.52 mg/kg
	$y = 12.26x + 0.65$	0.999	2.52 mg/kg
	$y = 11.08x + 0.61$	0.998	2.64 mg/kg
Plastic C	$y = 9.75x + 0.43$	0.999	2.08 mg/kg
	$y = 9.17x + 0.41$	0.999	2.13 mg/kg
	$y = 7.99x + 0.29$	0.997	1.75 mg/kg
Spiked plastic A	$y = 9.99x + 1.58$	0.992	7.61 mg/kg
	$y = 9.74x + 1.51$	0.999	7.42 mg/kg
	$y = 9.58x + 1.56$	0.998	7.82 mg/kg
Spiked plastic B	$y = 10.07x + 1.36$	0.996	6.46 mg/kg
	$y = 8.99x + 1.09$	0.992	5.83 mg/kg
	$y = 8.56x + 1.25$	0.995	7.02 mg/kg
Spiked plastic C	$y = 10.60x + 1.36$	0.999	6.16 mg/kg
	$y = 9.88x + 1.26$	0.996	6.13 mg/kg
	$y = 9.17x + 1.18$	0.994	6.18 mg/kg
Spiked water in plastic A	$y = 7.53x + 1.49$	0.993	0.95 mg/L
	$y = 7.41x + 1.43$	0.997	0.93 mg/L
	$y = 7.06x + 1.45$	0.996	0.98 mg/L
Spiked water in plastic B	$y = 10.07x + 2.10$	0.999	1.00 mg/L
	$y = 9.99x + 2.06$	0.995	0.99 mg/L
	$y = 9.77x + 1.96$	0.998	0.96 mg/L

**Table B.12 The linear regression for BPA determination by the GCPE/GNP-IL using standard addition method and concentration of BPA found in the samples (continued)**

Samples	Linear regression ( $y = mx + c$ )	$r^2$	BPA in sample
Spiked water in plastic C	$y = 11.98x + 2.47$	0.997	0.99 mg/L
	$y = 11.34x + 2.29$	0.992	0.97 mg/L
	$y = 11.37 + 2.25$	0.997	0.95 mg/L

#### Plastic and spiked plastic sample calculation

For plastic samples preparation, 1.00 g of plastic powder are added to 20 mL of acetonitrile. After extraction and filtration, the liquid phase is concentrated by a rotary evaporator and adjusted the final volume to 2 mL. After that, the obtained samples are diluted 2 times and only 0.5 mL are injected into the electrochemical cell (6 mL total volume). Therefore, the concentration of BPA can be calculated as follow.

For example, plastic B provided the linear regression of  $y = 11.08x + 0.61$ .

In stead of  $y = 0$ ;

$$0 = 11.08x + 0.61$$

$$x = \frac{0.61}{11.08} = 0.055 \text{ mg/L}$$

Thus, the concentration of BPA in the electrochemical cell is 0.055 mg/L.

From

$$C_1V_1 = C_2V_2$$

$$C_1 (0.5 \text{ mL}) = (0.055 \text{ mg/L})(6 \text{ mL})$$

$$C_1 = 0.66 \text{ mg/L} \times 2 \text{ dilution factor} = 1.32 \text{ mg/L}$$

Thus, the concentration of BPA in the 2 mL-volumetric flasks is 1.32 mg/L.

$$\begin{array}{llll}
 \text{In } 1000 \text{ mL} & \text{there is BPA} & 1.32 \text{ mg} & \\
 \text{In } 2 \text{ mL} & \text{there is BPA} & \frac{(1.32 \text{ mg})(2 \text{ mL})}{1000 \text{ mL}} = 2.64 \mu\text{g} & \\
 \\ 
 \text{In } 1.0012 \text{ g} & \text{there is BPA} & 2.64 \mu\text{g} & \\
 \text{In } 1000 \text{ g} & \text{there is BPA} & \frac{(2.64 \mu\text{g})(1000 \text{ g})}{1.0012 \text{ g}} = 2.64 \text{ mg/kg} & 
 \end{array}$$

Thus, the concentration of BPA in the plastic sample B is 2.64 mg/kg.

### Spiked water in plastic sample calculation

For water sample preparation, 100 mL of drinking water sample from the three plastic bottles are extracted and made the final volume to 2 mL. After that, 0.1 mL of the obtained samples are diluted with acetonitrile in 2-mL volumetric flask and only 0.5 mL are injected into the electrochemical cell (6 mL total volume). Therefore, the concentration of BPA can be calculated as follow.

For example, spiked water sample in plastic B provided  $y = 10.07x + 2.10$ .

In stead of  $y = 0$ ;

$$\begin{aligned}
 0 &= 10.07x + 2.10 \\
 x &= \frac{2.10}{10.07} = 0.21 \text{ mg/L}
 \end{aligned}$$

Thus, the concentration of BPA in electrochemical cell is 0.21 mg/L.

$$\begin{aligned}
 \text{From } C_1V_1 &= C_2V_2 \\
 C_1(0.5 \text{ mL}) &= (0.21 \text{ mg/L})(6 \text{ mL}) \\
 C_1 &= 2.52 \text{ mg/L}
 \end{aligned}$$

$$\begin{aligned}
 \text{From } C_1V_1 &= C_2V_2 \\
 C_1(0.1 \text{ mL}) &= (2.52 \text{ mg/L})(2 \text{ mL}) \\
 C_1 &= 50.4 \text{ mg/L}
 \end{aligned}$$

Thus, the concentration of BPA in the 2 mL-volumetric flasks is 50.4 mg/L.

In 1000 mL there is BPA 50.4 mg

In 2 mL there is BPA  $\frac{(50.4 \text{ mg})(2 \text{ mL})}{1000 \text{ mL}} = 0.10 \text{ mg}$

In 100 mL there is BPA 0.10 mg

In 1000 mL there is BPA  $\frac{(0.10 \text{ mg})(1000 \text{ g})}{100 \text{ mL}} = 1.00 \text{ mg/L}$

Thus, the concentration of BPA in spiked water sample in plastic B is 1.00 mg/L.

**Table B.13 The peak area, retention time, and concentration of BPA found in the samples using external calibration method**

Samples	Peak area	Retention time	BPA in sample
Plastic A	0.516	4.933	3.44 mg/kg
	0.520	4.930	3.47 mg/kg
	0.512	4.927	3.41 mg/kg
Plastic B	0.389	4.920	2.59 mg/kg
	0.381	4.920	2.53 mg/kg
	0.399	4.917	2.65 mg/kg
Plastic C	0.284	4.927	1.88 mg/kg
	0.289	4.927	1.92 mg/kg
	0.290	4.927	1.92 mg/kg
Spiked plastic A	1.101	5.010	7.35 mg/kg
	1.136	5.007	7.58 mg/kg
	1.015	5.010	6.77 mg/kg
Spiked plastic B	1.056	5.000	7.04 mg/kg
	0.998	5.007	6.65 mg/kg
	0.890	5.003	5.93 mg/kg

**Table B.13 The peak area, retention time, and concentration of BPA found in the samples using external calibration method (continued)**

Samples	Peak area	Retention time	BPA in sample
Spiked plastic C	0.872	5.010	5.81 mg/kg
	0.941	5.007	6.27 mg/kg
	0.893	5.007	6.95 mg/kg
Spiked water in plastic A	1.505	4.997	1.01 mg/L
	1.503	4.993	1.00 mg/L
	1.438	4.993	0.95 mg/L
Spiked water in plastic B	1.546	4.997	1.03 mg/L
	1.543	4.997	1.030 mg/L
	1.559	4.997	1.040 mg/L
Spiked water in plastic C	1.536	5.003	1.026 mg/L
	1.542	5.003	1.030 mg/L
	1.537	5.003	1.026 mg/L

#### **Plastic and spiked plastic sample calculation**

For plastic sample preparation, 1.00 g of plastic powder is added to 20 mL of acetonitrile. After extraction and filtration, the liquid phase is concentrated by a rotary evaporator and adjusted the final volume to 2 mL. After that, the obtained samples are diluted 2 times and injected into the HPLC system. Therefore, the concentration of BPA can be calculated as follow.

For example plastic A;

From the linear regression of  $y = 0.598x + 0.002$

$$\begin{aligned}
 y &= 0.598x + 0.002 \\
 0.520 &= 0.598x + 0.002 \\
 x &= \frac{0.520 - 0.002}{0.598} = 0.87 \text{ mg/L}
 \end{aligned}$$

Thus, the concentration of BPA in vial is 0.866 mg/L and the concentration of BPA in the 2 mL-volumetric flasks is  $0.87 \text{ mg/L} \times 2 \text{ dilution factor} = 1.73 \text{ mg/L}$ .

$$\begin{array}{llll}
 \text{In } 1000 \text{ mL} & \text{there is BPA} & 1.73 \text{ mg} & \\
 \text{In } 2 \text{ mL} & \text{there is BPA} & \frac{(1.73 \text{ mg})(2 \text{ mL})}{1000 \text{ mL}} = 3.47 \mu\text{g} & \\
 \\ 
 \text{In } 1.0012 \text{ g} & \text{there is BPA} & 3.47 \mu\text{g} & \\
 \text{In } 1000 \text{ g} & \text{there is BPA} & \frac{(3.47 \mu\text{g})(1000 \text{ g})}{1.0012 \text{ g}} = 3.47 \text{ mg/kg} & 
 \end{array}$$

Thus, the concentration of BPA in the plastic sample A is 3.47 mg/kg.

### Spiked water in plastic sample calculation

For water sample preparation, 100 mL of drinking water sample from the three plastic bottles are extracted and made the final volume to 2 mL. After that, 0.1 mL of the obtained samples are diluted with acetonitrile in 2-mL volumetric flask. Then, the sample solutions are injected into the HPLC system. Therefore, the concentration of BPA can be calculated as follow.

For example, spiked water sample in plastic A;

From the linear regression of  $y = 0.598x + 0.002$

$$\begin{aligned}
 y &= 0.598x + 0.002 \\
 1.505 &= 0.598x + 0.002 \\
 x &= \frac{1.505 - 0.002}{0.598} = 2.51 \text{ mg/L}
 \end{aligned}$$

Thus, the concentration of BPA in vial is 2.51 mg/L.

$$\begin{aligned}
 \text{From } C_1V_1 &= C_2V_2 \\
 C_1(0.1 \text{ mL}) &= (2.51 \text{ mg/L})(2 \text{ mL}) \\
 C_1 &= 50.20 \text{ mg/L}
 \end{aligned}$$



Thus, the concentration of BPA in the 2 mL-volumetric flasks is 50.20 mg/L.

In	1000 mL	there is BPA	50.20 mg	
In	2 mL	there is BPA	$\frac{(50.20 \text{ mg})(2 \text{ mL})}{1000 \text{ mL}}$	$= 0.10 \text{ mg}$
In	100 mL	there is BPA	0.10 mg	
In	1000 mL	there is BPA	$\frac{(0.10 \text{ mg})(1000 \text{ mL})}{100 \text{ mL}}$	$= 1.01 \text{ mg/L}$

Thus, concentration of BPA in the spiked water sample in plastic A is 1.01 mg/L.

## B.2 Carbon composite nanomaterials-based biosensor: electrochemical biosensor based on immunoassay

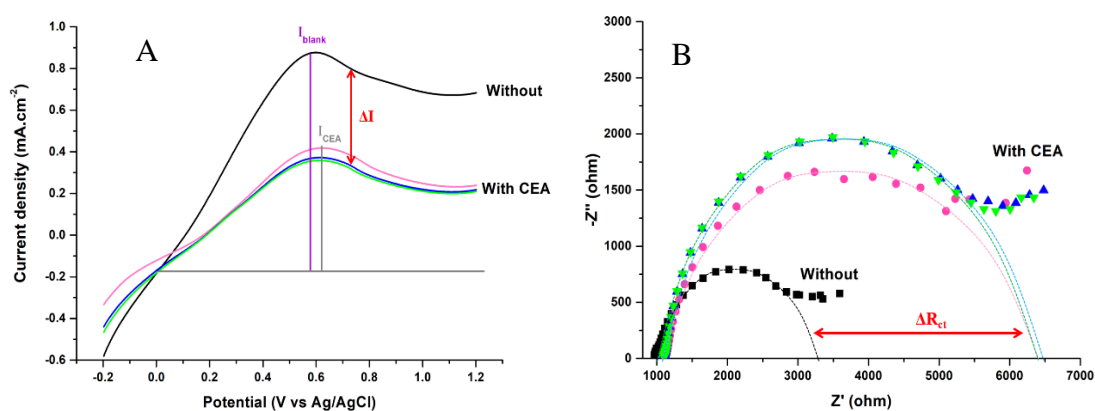


**Figure B.2** (A) LSV and (B) EIS responses of the SPCE/GNP-MnO<sub>2</sub>/Fe<sub>3</sub>O<sub>4</sub>@Au biosensor toward 10 ng/mL CEA detected in phosphate buffer solution containing 5 mM Fe(CN)<sub>6</sub><sup>3-/4-</sup>

**Table B.14 The response of the biosensor on the amount of GNP (n=3)**

<b>Amount of GNP (mg.cm<sup>-2</sup>)</b>	<b><math>\Delta I</math> (mA.cm<sup>-2</sup>)</b>	<b><math>\Delta R_{ct}</math> (k<math>\Omega</math>)</b>
2.50	0.11 $\pm$ 0.01	2.14 $\pm$ 0.19
2.75	0.16 $\pm$ 0.01	2.61 $\pm$ 0.21
5.00	0.22 $\pm$ 0.01	3.29 $\pm$ 0.13
6.25	0.18 $\pm$ 0.01	3.20 $\pm$ 0.14
7.50	0.17 $\pm$ 0.01	2.45 $\pm$ 0.13
10.00	0.13 $\pm$ 0.01	2.47 $\pm$ 0.19
12.50	0.03 $\pm$ 0.02	2.41 $\pm$ 0.19

**Table B.15 The response of the biosensor on the amount of MnO<sub>2</sub> (n=3)**

<b>Ratio of GNP:MnO<sub>2</sub> (mg:mg)</b>	<b><math>\Delta I</math> (mA.cm<sup>-2</sup>)</b>	<b><math>\Delta R_{ct}</math> (k<math>\Omega</math>)</b>
1:0.00	0.18 $\pm$ 0.02	2.17 $\pm$ 0.12
1:0.05	0.20 $\pm$ 0.01	3.04 $\pm$ 0.17
1:0.10	0.27 $\pm$ 0.02	3.65 $\pm$ 0.14
1:0.15	0.20 $\pm$ 0.01	2.77 $\pm$ 0.23
1:0.20	0.17 $\pm$ 0.01	2.38 $\pm$ 0.15
1:0.40	0.18 $\pm$ 0.02	2.28 $\pm$ 0.13
1:1.10	0.18 $\pm$ 0.02	1.53 $\pm$ 0.15

**Table B.16 The response of the biosensor on the concentration of antibody (n=3)**

<b>CEA antibody concentration (<math>\mu</math>g/mL)</b>	<b><math>\Delta I</math> (mA.cm<sup>-2</sup>)</b>	<b><math>\Delta R_{ct}</math> (k<math>\Omega</math>)</b>
50	0.19 $\pm$ 0.01	2.91 $\pm$ 0.26
100	0.24 $\pm$ 0.01	3.40 $\pm$ 0.25
150	0.30 $\pm$ 0.02	3.93 $\pm$ 0.28
200	0.36 $\pm$ 0.01	4.36 $\pm$ 0.29

**Table B.16 The response of the biosensor on the concentration of antibody (continued)**

<b>CEA antibody concentration (<math>\mu\text{g/mL}</math>)</b>	<b><math>\Delta I</math> (<math>\text{mA}\cdot\text{cm}^{-2}</math>)</b>	<b><math>\Delta R_{\text{ct}}</math> (<math>\text{k}\Omega</math>)</b>
250	$0.38 \pm 0.01$	$4.37 \pm 0.19$
300	$0.38 \pm 0.01$	$4.32 \pm 0.25$

**Table B.17 The response of the biosensor on the pH solution (n=3)**

<b>pH value</b>	<b><math>\Delta I</math> (<math>\text{mA}\cdot\text{cm}^{-2}</math>)</b>	<b><math>\Delta R_{\text{ct}}</math> (<math>\text{k}\Omega</math>)</b>
5.0	$0.11 \pm 0.02$	$3.08 \pm 0.20$
6.0	$0.20 \pm 0.02$	$3.66 \pm 0.26$
7.0	$0.32 \pm 0.01$	$4.21 \pm 0.13$
7.4	$0.36 \pm 0.01$	$4.33 \pm 0.12$
8.0	$0.30 \pm 0.01$	$3.98 \pm 0.17$
8.5	$0.24 \pm 0.01$	$3.38 \pm 0.29$
9.0	$0.15 \pm 0.01$	$2.24 \pm 0.26$

**Table B.18 The response of biosensor on the temperature (n=3)**

<b>Temperature (<math>^{\circ}\text{C}</math>)</b>	<b><math>\Delta I</math> (<math>\text{mA}\cdot\text{cm}^{-2}</math>)</b>	<b><math>\Delta R_{\text{ct}}</math> (<math>\text{k}\Omega</math>)</b>
25	$0.09 \pm 0.01$	$0.49 \pm 0.05$
30	$0.16 \pm 0.07$	$1.33 \pm 0.58$
35	$0.31 \pm 0.06$	$4.14 \pm 0.15$
37	$0.38 \pm 0.04$	$4.52 \pm 0.35$
40	$0.34 \pm 0.04$	$4.40 \pm 0.06$
45	$0.21 \pm 0.01$	$2.26 \pm 0.28$
50	$0.09 \pm 0.01$	$0.39 \pm 0.13$

**Table B.19 The response of the biosensor on the incubation time (n=3)**

Incubation time (min)	$\Delta I$ (mA.cm <sup>-2</sup> )	$\Delta R_{ct}$ (k $\Omega$ )
30	0.08 $\pm$ 0.01	0.54 $\pm$ 0.25
60	0.25 $\pm$ 0.03	3.10 $\pm$ 0.23
80	0.28 $\pm$ 0.04	3.81 $\pm$ 0.17
100	0.30 $\pm$ 0.01	4.63 $\pm$ 0.26
120	0.33 $\pm$ 0.01	4.71 $\pm$ 0.11
140	0.35 $\pm$ 0.06	4.54 $\pm$ 0.18
160	0.32 $\pm$ 0.02	4.44 $\pm$ 0.20
180	0.32 $\pm$ 0.02	4.51 $\pm$ 0.44
200	0.33 $\pm$ 0.02	4.25 $\pm$ 0.31

**Table B.20 The response of the biosensor on the reaction time (n=3)**

Reaction time (min)	$\Delta I$ (mA.cm <sup>-2</sup> )	$\Delta R_{ct}$ (k $\Omega$ )
30	0.20 $\pm$ 0.01	2.55 $\pm$ 0.32
45	0.21 $\pm$ 0.03	3.16 $\pm$ 0.02
60	0.27 $\pm$ 0.02	3.40 $\pm$ 0.26
75	0.27 $\pm$ 0.02	4.16 $\pm$ 0.23
90	0.31 $\pm$ 0.01	4.33 $\pm$ 0.29
105	0.31 $\pm$ 0.01	4.30 $\pm$ 0.30
120	0.35 $\pm$ 0.02	4.83 $\pm$ 0.26
135	0.36 $\pm$ 0.01	4.80 $\pm$ 0.57
150	0.35 $\pm$ 0.03	4.83 $\pm$ 0.16

**Table B.21 The LSV and EIS response of the biosensor on CEA determination**

Concentration (ng/mL)	Log concentration (ng/mL)	$\Delta I$ (mA.cm <sup>-2</sup> )	$\Delta R_{ct}$ (k $\Omega$ )
0.001	-3	$0.11 \pm 0.02$	$1.52 \pm 0.16$
0.01	-2	$0.20 \pm 0.03$	$2.28 \pm 0.21$
0.1	-1	$0.26 \pm 0.03$	$3.11 \pm 0.29$
1	0	$0.31 \pm 0.02$	$3.51 \pm 0.12$
10	1	$0.37 \pm 0.03$	$4.23 \pm 0.26$
100	2	$0.46 \pm 0.02$	$4.91 \pm 0.15$

**Table B.22 The LSV and EIS response on the detection of blank (buffer solution)**

Number	$\Delta I$ (mA.cm <sup>-2</sup> )	$\Delta R_{ct}$ (k $\Omega$ )
1	0.010	0.247
2	0.020	0.539
3	0.010	0.050
4	0.010	0.722
5	0.030	0.342
6	0.030	0.183
7	0.040	0.098
8	0.040	0.177
9	0.010	0.440
10	0.010	0.573
<b>Average</b>	0.019	0.232
<b>SD</b>	0.015	0.342

The LOD is calculated as explained follow. Firstly, the smallest measure ( $X_L$ ) is calculated by using a mean ( $x_{b1}$ ) and standard deviation ( $s_{b1}$ ) of the blank measures according to Equation B.1. A value of 3 for  $k$  is a numerical factor chosen according to the confidence level of 90% in a practical sense.

$$X_L = X_{b1} + kSb_1 \quad (\text{B.1})$$

### For LSV measurement

After making ten measurements of blank, the  $X_{b1} = 0.019$  and  $Sb_1 = 0.015$  are obtained.

$$\begin{aligned} \text{Therefore} \quad X_L &= X_{b1} + kSb_1 \\ &= 0.019 + (3 \times 0.015) \\ &= 0.064 \end{aligned}$$

The calibration plot of this proposed biosensor is  $\Delta I = 0.068 \log C + 0.317$ .

$$\begin{aligned} \text{Therefore} \quad C &= 10^{(\Delta I - 0.317)/0.068} \\ \text{Instead of } \Delta I = X_L = 0.064; \quad &= 10^{(0.064 - 0.317)/0.068} \\ &= 10^{-3.72} = 0.0001 \text{ ng/mL} \end{aligned}$$

Thus, the LOD for detection of CEA based on LSV measurement is 0.1 pg/mL.

### For EIS measurement

After making ten measurements of blank, the  $X_{b1} = 0.232$  and  $Sb_1 = 0.342$  are obtained.

$$\begin{aligned} \text{Therefore} \quad X_L &= X_{b1} + kSb_1 \\ &= 0.232 + (3 \times 0.342) \\ &= 1.258 \end{aligned}$$

The calibration plot of this proposed biosensor is  $\Delta R = 0.663 \log C + 3.591$ .

$$\begin{aligned} \text{Therefore} \quad C &= 10^{(\Delta R - 3.591)/0.663} \\ \text{Instead of } \Delta R = X_L = 1.258; \quad &= 10^{(1.258 - 3.591)/0.663} \\ &= 10^{-3.52} = 0.0003 \text{ ng/mL} \end{aligned}$$

Thus, the LOD for detection of CEA based on EIS measurement is 0.3 pg/mL.

**Table B.23 The response of the biosensor on repeatability and reproducibility**

Number	$\Delta I$ (mA.cm <sup>-2</sup> )		$\Delta R_{ct}$ (k $\Omega$ )	
	Repeatability	Reproducibility	Repeatability	Reproducibility
1	0.316	0.280	4.079	3.260
2	0.335	0.267	3.899	3.058
3	0.329	0.257	3.983	3.331
4	0.336	0.250	4.051	3.423
5	0.313	0.279	4.146	3.408
<b>Average</b>	0.326	0.268	4.032	3.292
<b>SD</b>	0.011	0.013	0.094	0.149
<b>%RSD</b>	3.3	4.9	2.3	4.5

**Table B.24 The response of the biosensor on stability**

Days	$\Delta I$ (mA.cm <sup>-2</sup> )	Relative current (%)	$\Delta R_{ct}$ (k $\Omega$ )	Relative impedance (%)
0	0.51 $\pm$ 0.01	100.00	7.75 $\pm$ 0.13	100.00
1	0.50 $\pm$ 0.02	98.04	7.69 $\pm$ 0.26	99.23
2	0.44 $\pm$ 0.03	86.27	8.03 $\pm$ 0.09	103.61
3	0.43 $\pm$ 0.03	84.31	8.06 $\pm$ 0.35	104.00
4	0.43 $\pm$ 0.01	84.31	8.10 $\pm$ 0.17	104.52
5	0.42 $\pm$ 0.04	82.35	8.45 $\pm$ 0.35	109.03
6	0.42 $\pm$ 0.01	82.35	9.03 $\pm$ 0.12	116.52
7	0.41 $\pm$ 0.01	80.39	9.19 $\pm$ 0.21	118.58

**Table B.25 The response of the biosensor on selectivity**

Substances	Concentration (ng/mL)	$\Delta I$ (mA.cm <sup>-2</sup> )	$\Delta R_{ct}$ (k $\Omega$ )
CEA	1	0.31 $\pm$ 0.01	3.54 $\pm$ 0.13
Blank	0	0.03 $\pm$ 0.01	0.30 $\pm$ 0.27
PSA	500	0.04 $\pm$ 0.01	0.52 $\pm$ 0.12

**Table B.25 The response of the biosensor on selectivity (continued)**

Substances	Concentration (ng/mL)	$\Delta I$ (mA.cm <sup>-2</sup> )	$\Delta R_{ct}$ (k $\Omega$ )
HAS	500	0.04 $\pm$ 0.01	0.37 $\pm$ 0.14
IgG	500	0.04 $\pm$ 0.01	0.45 $\pm$ 0.19
BSA	500	0.03 $\pm$ 0.01	0.38 $\pm$ 0.14
Cholesterol	500	0.02 $\pm$ 0.01	0.55 $\pm$ 0.13
Glucose	500	0.03 $\pm$ 0.01	0.52 $\pm$ 0.16
Sucrose	500	0.01 $\pm$ 0.02	0.50 $\pm$ 0.08
Cysteine	500	0.06 $\pm$ 0.01	0.38 $\pm$ 0.16
Ascorbic acid	500	0.02 $\pm$ 0.01	0.08 $\pm$ 0.17
Uric acid	500	0.06 $\pm$ 0.01	0.44 $\pm$ 0.18
Mixed interferences	500 ng/mL interferences + 1 ng/mL CEA	0.32 $\pm$ 0.01	3.43 $\pm$ 0.13

**Table B. 26 The EIS and LSV response of the SPCE/GNP-MnO<sub>2</sub>/Fe<sub>3</sub>O<sub>4</sub>@Au biosensor for CEA determination in diluted serum samples**

Serum dilution	Add (ng/mL)	$\Delta I$ (mA.cm <sup>-2</sup> )	$\Delta R_{ct}$ (k $\Omega$ )
10x	0	0.046 $\pm$ 0.010	0.351 $\pm$ 0.087
	1	0.318 $\pm$ 0.013	3.606 $\pm$ 0.125
	10	0.379 $\pm$ 0.010	4.280 $\pm$ 0.162
	50	0.436 $\pm$ 0.004	4.747 $\pm$ 0.130
100x	0	0.029 $\pm$ 0.011	0.322 $\pm$ 0.015
	1	0.311 $\pm$ 0.005	3.553 $\pm$ 0.129
	10	0.383 $\pm$ 0.005	4.254 $\pm$ 0.061
	50	0.427 $\pm$ 0.006	4.711 $\pm$ 0.078

**Calculation based on LSV measurement**

The signal from the 10x diluted sample spiked with 1 ng/mL is 0.318 mA.cm<sup>-2</sup>.

Linear regression of  $\Delta I = 0.068 \log C + 0.317$



Therefore,  $0.318 = 0.068 \log C + 0.317$

$$\log C = \frac{0.318 - 0.317}{0.068}$$

$$\log C = 0.0147$$

$$C = 10^{0.0147} = 1.03 \text{ ng/mL}$$

Thus, concentration of CEA in 10x-diluted serum spiked with 1 ng/mL is 1.03 ng/mL detected by LSV method.

### **Calculation based on LSV measurement**

The signal from the 10x diluted sample spiked with 1 ng/mL is 3.606 kΩ.

Linear regression of  $\Delta R = 0.663 \log C + 3.591$

Therefore,  $3.606 = 0.663 \log C + 3.591$

$$\log C = \frac{3.606 - 3.591}{0.663}$$

$$\log C = 0.0226$$

$$C = 10^{0.0226} = 1.05 \text{ ng/mL}$$

Thus, concentration of CEA in 10x-diluted serum spiked with 1 ng/mL is 1.05 ng/mL detected by EIS method.

### B.3 Carbon composite nanomaterials-based biosensor: electrochemical biosensor based on enzymatic reaction

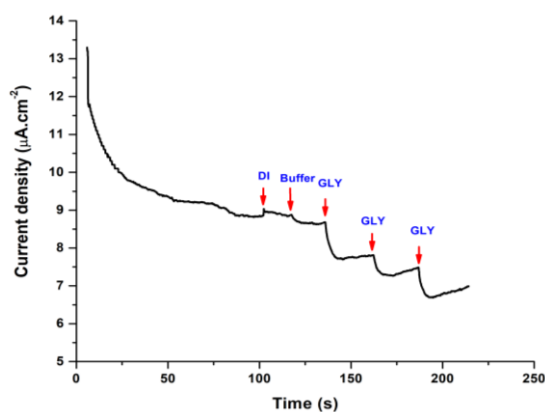


**Figure B.3** Amperometric responses on the SPCE/rGO-AgNPs/ACP at potential of 0.4 V in 0.1 M acetate buffer solution containing 20 g/L disodium phenyl phosphate and 0.2 mg/L glyphosate

**Table B.27** The current of SPCE/rGO-AgNPs/ACP on the potential apply

Potential (V)	Inhibited current ( $\mu\text{A}\cdot\text{cm}^{-2}$ )			
	1	2	3	Mean $\pm$ SD
0.0	0.12	0.11	0.07	$0.10 \pm 0.02$
0.1	0.10	0.07	0.09	$0.09 \pm 0.01$
0.2	0.12	0.07	0.11	$0.10 \pm 0.03$
0.3	0.02	0.04	0.03	$0.03 \pm 0.01$
0.4	0.44	0.40	0.48	$0.44 \pm 0.04$
0.5	0.87	0.84	0.80	$0.83 \pm 0.03$
0.6	1.04	0.97	0.78	$0.93 \pm 0.04$
0.7	1.45	1.48	1.40	$1.44 \pm 0.04$

**Table B.28 The current of SPCE/rGO-AgNPs/ACP on the amount of rGO**

Amount of rGO ( $\mu\text{g.cm}^{-2}$ )	Inhibited current ( $\mu\text{A.cm}^{-2}$ )			
	1	2	3	Mean $\pm$ SD
0.00	0.11	0.13	0.10	$0.11 \pm 0.01$
2.50	0.20	0.25	0.18	$0.21 \pm 0.04$
3.75	0.35	0.31	0.27	$0.31 \pm 0.04$
5.00	0.56	0.49	0.43	$0.49 \pm 0.05$
6.25	0.37	0.37	0.39	$0.38 \pm 0.01$
7.50	0.35	0.38	0.30	$0.34 \pm 0.03$
10.00	0.27	0.27	0.18	$0.24 \pm 0.05$
12.50	0.11	0.14	0.16	$0.14 \pm 0.03$

**Table B.29 The current of SPCE/rGO-AgNPs/ACP on the amount of AgNPs**

Amount of AgNPs ( $\text{mg.cm}^{-2}$ )	Inhibited current ( $\mu\text{A.cm}^{-2}$ )			
	1	2	3	Mean $\pm$ SD
0.0	0.28	0.17	0.16	$0.21 \pm 0.07$
0.2	0.22	0.20	0.24	$0.22 \pm 0.02$
0.5	0.31	0.23	0.22	$0.25 \pm 0.05$
0.8	0.41	0.33	0.39	$0.38 \pm 0.04$
1.1	0.54	0.53	0.58	$0.55 \pm 0.03$
1.4	0.57	0.51	0.49	$0.52 \pm 0.05$

**Table B.30 The current of SPCE/rGO-AgNPs/ACP on the amount of enzyme**

Amount of ACP ( $\text{unit.cm}^{-2}$ )	Inhibited current ( $\mu\text{A.cm}^{-2}$ )			
	1	2	3	Mean $\pm$ SD
0.00	0.06	0.05	0.04	$0.05 \pm 0.01$
0.03	0.37	0.35	0.34	$0.35 \pm 0.02$
0.06	0.52	0.43	0.50	$0.48 \pm 0.05$
0.09	0.69	0.72	0.80	$0.74 \pm 0.06$

**Table B.30 The current of SPCE/rGO-AgNPs/ACP on the amount of enzyme (continued)**

Amount of ACP (unit.cm <sup>-2</sup> )	Inhibited current (μA.cm <sup>-2</sup> )			
	1	2	3	Mean ± SD
0.12	0.83	0.86	0.81	0.83 ± 0.03
0.15	0.87	0.80	0.89	0.85 ± 0.04
0.18	0.89	0.97	0.88	0.91 ± 0.05

**Table B.31 The current of enzymatic biosensor on the substrate concentration**

Concentration of substrate (g/L)	Inhibited current (μA.cm <sup>-2</sup> )			
	1	2	3	Mean ± SD
0.5	0.05	0.03	0.03	0.03 ± 0.01
1.0	0.10	0.11	0.15	0.12 ± 0.02
5.0	0.39	0.28	0.38	0.35 ± 0.06
10.0	0.09	1.10	1.21	1.03 ± 0.11
20.0	1.25	1.34	1.38	1.32 ± 0.06
30.0	1.32	1.16	1.25	1.24 ± 0.08
40.0	0.49	0.72	0.53	0.58 ± 0.11
50.0	0.51	0.50	0.35	0.46 ± 0.09

**Table B.32 The current of SPCE/rGO-AgNPs/ACP on pH value**

pH	Inhibited current (μA.cm <sup>-2</sup> )			
	1	2	3	Mean ± SD
3.0	0.26	0.18	0.31	0.25 ± 0.06
4.0	0.55	0.86	0.60	0.66 ± 0.17
5.0	1.23	1.25	0.98	1.12 ± 0.15
6.0	1.10	1.25	1.28	1.21 ± 0.10
7.0	1.52	1.46	1.73	1.57 ± 0.15
7.5	1.12	0.79	0.97	0.96 ± 0.16
8.0	0.61	0.44	0.61	0.55 ± 0.10

**Table B.33 The current of SPCE/rGO-AgNPs/ACP on enzyme kinetics (n=3)**

Concentration of substrate [S] (mg/L)	1/[S]	Enzyme-substrate		Enzyme-glyphosate	
		I ( $\mu\text{A.cm}^{-2}$ )	1/I	I ( $\mu\text{A.cm}^{-2}$ )	1/I
50	0.0200	$0.48 \pm 0.03$	2.07	$0.39 \pm 0.03$	2.60
100	0.0200	$0.94 \pm 0.08$	1.06	$0.82 \pm 0.18$	1.22
150	0.0067	$1.76 \pm 0.09$	0.57	$1.46 \pm 0.02$	0.69
200	0.0050	$2.71 \pm 0.03$	0.37	$2.09 \pm 0.03$	0.48
250	0.0040	$3.80 \pm 0.06$	0.26	$2.52 \pm 0.03$	0.40
300	0.0033	$4.46 \pm 0.03$	0.22	$2.94 \pm 0.11$	0.34
350	0.0029	$5.39 \pm 0.03$	0.19	$3.55 \pm 0.11$	0.28
400	0.0025	$7.02 \pm 0.11$	0.14	$4.46 \pm 0.02$	0.22
450	0.0022	$8.57 \pm 0.12$	0.12	$5.26 \pm 0.17$	0.19
500	0.0020	$10.40 \pm 0.02$	0.10	$6.37 \pm 0.03$	0.16

**Calculation of  $I_{\max}$  based on enzyme-substrate kinetic study**

$I_{\max}$  is obtained from y-intercept of the linear calibration curve.

The linear regression is  $y = 110.92x - 0.134$ .

From the Lineweaver-Burk plot; y-intercept =  $\frac{1}{I_{\max}}$

$$I_{\max} = \frac{1}{0.134} = 7.46 \mu\text{A.cm}^{-2}$$

Therefore,  $I_{\max}$  of enzymatic reaction between ACP and disodium phenyl phosphate is  $7.46 \mu\text{A.cm}^{-2}$ .

**Calculation of  $K_m$  based on enzyme-substrate kinetic study**

$K_m$  is obtained from slope of the linear calibration curve.

The linear regression is  $y = 110.92x - 0.134$ .

From the Lineweaver-Burk plot;  $\text{slope} = \frac{K_m}{V_{\max}}$

$$K_m = 110.92 \times 7.46 = 827.46 \text{ mg/L}$$

The molecular weight of disodium phenyl phosphate is 218.09 g/mol.

$$\text{Thus, } K_m = \frac{827.46 \text{ mg/L}}{218.09 \text{ g/mol}} = 3.79 \text{ mmol/L}$$

Therefore,  $K_m$  of enzymatic reaction between ACP and disodium phenyl phosphate is 3.79 mM.

**Table B.34 The current of SPCE/rGO-AgNPs/ACP on glyphosate determination**

Concentration (mg/L)	Inhibited current ( $\mu\text{A}\cdot\text{cm}^{-2}$ )			
	1	2	3	Mean $\pm$ SD
0.05	0.30	0.55	0.22	$0.36 \pm 0.17$
0.10	0.77	0.64	0.83	$0.75 \pm 0.10$
0.15	0.95	0.96	0.91	$0.94 \pm 0.03$
0.20	1.42	1.50	1.42	$1.44 \pm 0.05$
0.25	1.67	1.60	1.61	$1.63 \pm 0.04$
0.30	2.06	2.07	2.09	$2.07 \pm 0.01$
0.35	2.40	2.48	2.42	$2.43 \pm 0.04$
0.40	2.83	2.90	2.96	$2.89 \pm 0.06$
0.45	3.33	3.31	3.30	$3.31 \pm 0.01$
0.50	3.68	3.69	3.49	$3.62 \pm 0.11$
1.00	4.18	4.20	4.26	$4.21 \pm 0.04$
1.50	4.39	4.42	4.30	$4.37 \pm 0.06$
2.00	4.75	4.83	4.80	$4.80 \pm 0.04$
2.50	5.15	5.21	5.07	$5.14 \pm 0.07$
3.00	5.51	5.57	5.31	$5.46 \pm 0.14$
4.00	5.78	5.77	5.74	$5.76 \pm 0.02$
6.00	6.66	6.66	6.54	$6.62 \pm 0.07$

**Table B.34 The current of SPCE/rGO-AgNPs/ACP on glyphosate determination (continued)**

Concentration (mg/L)	Inhibited current ( $\mu\text{A}\cdot\text{cm}^{-2}$ )			
	1	2	3	Mean $\pm$ SD
8.00	7.26	7.27	7.30	$7.28 \pm 0.02$
10.00	8.17	8.15	8.20	$8.17 \pm 0.02$
12.00	8.76	8.77	8.79	$8.77 \pm 0.01$
14.00	9.61	9.50	9.68	$9.60 \pm 0.09$
16.00	10.48	10.52	10.49	$10.50 \pm 0.02$
18.00	11.06	11.10	11.05	$11.07 \pm 0.02$
20.00	11.77	11.74	11.97	$11.83 \pm 0.13$
22.00	12.34	12.51	12.60	$12.56 \pm 0.14$

**Table B.35 The current response on the detection of 0.05 mg/L glyphosate**

Number	Inhibited current ( $\mu\text{A}\cdot\text{cm}^{-2}$ )
1	0.397
2	0.325
3	0.435
4	0.441
5	0.383
6	0.427
7	0.387
8	0.418
9	0.326
10	0.394
<b>Average <math>\pm</math> SD</b>	$0.393 \pm 0.041$

**Table B.36** The response of enzymatic biosensor on reproducibility study

Number	Inhibited current ( $\mu\text{A.cm}^{-2}$ )	
	Intra-day	Inter-days
1	1.708	1.471
2	1.573	1.574
3	1.595	1.694
4	1.683	1.614
5	1.501	1.521
<b>Average <math>\pm</math> SD</b>	$1.612 \pm 0.084$	$1.575 \pm 0.086$
<b>%RSD</b>	5.21	5.46

**Table B.37** The response for the SPCE/rGO-AgNPs/ACP on its stability

Days	Inhibited current ( $\mu\text{A.cm}^{-2}$ )				Relative current signal (%)
	1	2	3	Mean $\pm$ SD	
0	1.54	1.43	1.46	$1.48 \pm 0.06$	100.00
1	1.42	1.37	1.36	$1.38 \pm 0.03$	93.73
2	1.37	1.23	1.43	$1.34 \pm 0.10$	91.02
3	1.50	1.25	1.28	$1.34 \pm 0.14$	90.93
4	1.32	1.19	1.28	$1.26 \pm 0.07$	85.55
5	1.21	1.27	1.14	$1.21 \pm 0.06$	81.85

**Table B.38** The response for the SPCE/rGO-AgNPs/ACP on its selectivity (n=3)

Substances	Concentration (mg/L)	Inhibited current ( $\mu\text{A.cm}^{-2}$ )	Relative current signal (%)
Glyphosate	0.2	$1.521 \pm 0.059$	100.00
POEA	0.2	$1.488 \pm 0.029$	97.83
Glycine	0.2	$1.530 \pm 0.068$	100.59
Chlorpyrifos	0.2	$1.457 \pm 0.052$	95.79
Paraquat	0.2	$1.430 \pm 0.061$	94.02



**Table B.38 The response for the SPCE/rGO-AgNPs/ACP on its selectivity (continued)**

Substances	Concentration (mg/L)	Inhibited current ( $\mu\text{A}\cdot\text{cm}^{-2}$ )	Relative current signal (%)
Carbaryl	0.2	$1.438 \pm 0.085$	94.54
Carbendazim	0.2	$1.541 \pm 0.092$	101.31
$\text{Mg}^{2+}$	0.2	$1.602 \pm 0.031$	105.32
$\text{Zn}^{2+}$	0.2	$1.425 \pm 0.028$	93.69
$\text{PO}_4^{2-}$	2.0	$1.612 \pm 0.051$	105.98
$\text{SO}_4^{2-}$	2.0	$1.558 \pm 0.059$	102.43
$\text{CO}_3^{2-}$	20.0	$1.451 \pm 0.035$	95.40
$\text{NO}_3^-$	20.0	$1.446 \pm 0.023$	95.07
$\text{Cl}^-$	20.0	$1.536 \pm 0.056$	100.98
$\text{K}^+$	20.0	$1.465 \pm 0.039$	96.32
$\text{Na}^+$	20.0	$1.542 \pm 0.048$	101.38
$\text{Ca}^{2+}$	20.0	$1.623 \pm 0.047$	106.71
$\text{Cu}^{2+}$	20.0	$1.461 \pm 0.033$	96.06
$\text{Cd}^{2+}$	20.0	$1.498 \pm 0.023$	98.49

**Table B.39 The linear regression for glyphosate detection by the SPCE/rGO-AgNPs/ACP using standard addition method and concentration of glyphosate found in the samples**

Samples	Linear regression ( $y = mx + c$ )	$r^2$	Glyphosate in sample
Spiked water A (0.5 mg/L)	$y = 0.53x + 0.06$	0.996	0.566 mg/L
	$y = 0.48x + 0.04$	0.995	0.451 mg/L
	$y = 0.46x + 0.04$	0.994	0.502 mg/L
Spiked water A (1.0 mg/L)	$y = 0.38x + 0.08$	0.985	1.139 mg/L
	$y = 0.39x + 0.07$	0.999	0.909 mg/L
	$y = 0.45x + 0.09$	0.990	1.072 mg/L

**Table B.39 The linear regression for glyphosate detection by the SPCE/rGO-AgNPs/ACP using standard addition method and concentration of glyphosate found in the samples (continued)**

<b>Samples</b>	<b>Linear regression (<math>y = mx + c</math>)</b>	<b><math>r^2</math></b>	<b>Glyphosate in sample</b>
Spiked water B (0.5 mg/L)	$y = 0.62x + 0.06$	0.992	0.487 mg/L
	$y = 0.45x + 0.04$	0.997	0.539 mg/L
	$y = 0.57x + 0.05$	0.993	0.510 mg/L
Spiked water B (1.0 mg/L)	$y = 0.40x + 0.07$	0.994	0.957 mg/L
	$y = 0.26x + 0.05$	0.987	1.088 mg/L
	$y = 0.44x + 0.08$	0.999	1.018 mg/L
Spiked water C (0.5 mg/L)	$y = 0.51x + 0.05$	0.997	0.475 mg/L
	$y = 0.50x + 0.05$	0.989	0.508 mg/L
	$y = 0.42x + 0.04$	0.999	0.530 mg/L
Spiked water C (1.0 mg/L)	$y = 0.35x + 0.08$	0.995	1.148 mg/L
	$y = 0.46x + 0.08$	0.992	0.908 mg/L
	$y = 0.41x + 0.09$	0.999	1.087 mg/L
Soil sample A	$y = 5.71x + 0.20$	0.996	0.701 mg/kg
	$y = 5.97x + 0.22$	0.996	0.727 mg/kg
	$y = 5.96x + 0.16$	0.994	0.537 mg/kg
Soil sample A (2 mg/kg)	$y = 4.10x + 0.47$	0.996	2.293 mg/kg
	$y = 4.06x + 0.54$	0.991	2.660 mg/kg
	$y = 5.12x + 0.76$	0.987	2.969 mg/kg
Soil sample A (4 mg/kg)	$y = 4.51x + 1.00$	0.987	4.434 mg/kg
	$y = 3.07x + 0.77$	0.996	5.016 mg/kg
	$y = 4.72x + 0.94$	0.983	3.983 mg/kg
Soil sample B (2 mg/kg)	$y = 5.09x + 0.56$	0.993	2.200 mg/kg
	$y = 3.94x + 0.40$	0.987	2.030 mg/kg
	$y = 3.88x + 0.39$	0.997	2.010 mg/kg

**Table B.39 The linear regression for glyphosate detection by the SPCE/rGO-AgNPs/ACP using standard addition method and concentration of glyphosate found in the samples (continued)**

Samples	Linear regression ( $y = mx + c$ )	$r^2$	Glyphosate in sample
Soil sample B (4 mg/kg)	$y = 3.27x + 0.63$	0.991	3.843 mg/kg
	$y = 3.42x + 0.73$	0.988	4.248 mg/kg
	$y = 3.63x + 0.74$	0.985	4.070 mg/kg
Soil sample C (2 mg/kg)	$y = 5.99x + 0.61$	0.996	2.024 mg/kg
	$y = 4.81x + 0.50$	0.993	2.071 mg/kg
	$y = 6.15x + 0.66$	0.995	2.150 mg/kg
Soil sample C (4 mg/kg)	$y = 4.34x + 0.85$	0.986	3.924 mg/kg
	$y = 3.92x + 0.81$	0.994	4.132 mg/kg
	$y = 3.67x + 0.66$	0.994	3.602 mg/kg

### Spiked water sample calculation

For water sample preparation, 50 mL of water samples are extracted and pre-concentrated for 10 times. Then, 2  $\mu$ L of the samples are injected onto the active surface of the biosensor containing 100  $\mu$ L of enzyme substrate. Therefore, the concentration of glyphosate can be calculated as follow.

For example, spiked glyphosate in water sample A provided  $y = 0.53x + 0.06$ .

In stead of  $y = 0$ ;

$$0 = 0.53x + 0.06$$

$$x = \frac{0.06}{0.53} = 0.113 \text{ mg/L}$$

$$\text{From } C_1V_1 = C_2V_2$$

$$C_1 (2 \mu\text{L}) = (0.113 \text{ mg/L})(100 \mu\text{L})$$

$$C_1 = 5.66 \text{ mg/L} \div 10 \text{ dilution factor} = 0.566 \text{ mg/L}$$

Thus, the concentration of glyphosate in the spiked water sample A is 0.566 mg/L.

### Soil sample and spiked soil calculation

For soil samples preparation, 25 g of the collected soils are added to 60 mL of NaOH. After extraction and filtration, the samples are diluted to 100 mL using DI-water and then pre-concentrated for 10-times. Then, 2  $\mu$ L of the samples are injected onto the active surface of the biosensor containing 100  $\mu$ L of enzyme substrate.

For example, soil sample A provided the linear regression of  $y = 5.71x + 0.20$ .

In stead of  $y = 0$ ;

$$0 = 5.71x + 0.20$$

$$x = \frac{0.20}{5.71} = 0.035 \text{ mg/L}$$

From

$$C_1V_1 = C_2V_2$$

$$C_1 (2 \mu\text{L}) = (0.035 \text{ mg/L})(100 \mu\text{L})$$

$$C_1 = 1.751 \text{ mg/L} \div 10 \text{ dilution factor} = 0.175 \text{ mg/L}$$

Thus, concentration of glyphosate in the 100 mL-volumetric flasks is 0.175 mg/L.

In 1000 mL there is glyphosate 0.175 mg

In 100 mL there is glyphosate  $\frac{(0.175 \text{ mg})(100 \text{ mL})}{1000 \text{ mL}} = 0.018 \text{ mg}$

In 25.0 g there is glyphosate 0.018 mg

In 1000 g there is glyphosate  $\frac{(0.018 \text{ mg})(1000 \text{ g})}{25.0 \text{ g}} = 0.701 \text{ mg/kg}$

Thus, the concentration of glyphosate in the soil sample A is 0.701 mg/kg.

**Table B.40 The peak area, retention time, and concentration of glyphosate found in the samples using external calibration method**

<b>Samples</b>	<b>Peak area (mAU)</b>	<b>Retention time (min)</b>	<b>Glyphosate in sample</b>
Spiked water A (0.5 mg/L)	1.264	3.534	0.526 mg/L
	1.257	3.535	0.524 mg/L
	1.178	3.537	0.501 mg/L
Spiked water A (1.0 mg/L)	2.965	3.531	1.028 mg/L
	3.106	3.532	1.070 mg/L
	2.923	3.537	1.016 mg/L
Spiked water B (0.5 mg/L)	1.230	3.533	0.516 mg/L
	1.245	3.533	0.520 mg/L
	1.217	3.535	0.512 mg/L
Spiked water B (1.0 mg/L)	2.630	3.530	0.930 mg/L
	2.806	3.529	0.981 mg/L
	2.778	3.533	0.973 mg/L
Spiked water C (0.5 mg/L)	1.137	3.532	0.489 mg/L
	1.131	3.554	0.487 mg/L
	1.177	3.533	0.500 mg/L
Spiked water C (1.0 mg/L)	2.650	3.525	0.935 mg/L
	2.842	3.527	0.992 mg/L
	2.704	3.534	0.951 mg/L
Soil sample A	0.160	3.522	0.799 mg/kg
	0.135	3.521	0.772 mg/kg
	0.153	3.525	0.793 mg/kg
Soil sample A (2 mg/kg)	1.894	3.526	2.850 mg/kg
	1.729	3.523	2.655 mg/kg
	1.831	3.534	2.776 mg/kg

**Table B.40 The peak area, retention time, and concentration of glyphosate found in the samples using external calibration method (continued)**

<b>Samples</b>	<b>Peak area (mAU)</b>	<b>Retention time (min)</b>	<b>Glyphosate in sample</b>
Soil sample A (4 mg/kg)	3.863	3.532	5.176 mg/kg
	3.520	3.530	4.771 mg/kg
	3.086	3.531	4.258 mg/kg
Soil sample B (2 mg/kg)	1.181	3.533	2.008 mg/kg
	1.167	3.537	1.991 mg/kg
	1.309	3.534	2.159 mg/kg
Soil sample B (4 mg/kg)	3.052	3.533	4.218 mg/kg
	3.050	3.533	4.216 mg/kg
	2.819	3.531	3.943 mg/kg
Soil sample C (2 mg/kg)	1.364	3.534	2.224 mg/kg
	1.232	3.530	2.068 mg/kg
	0.938	3.534	1.721 mg/kg
Soil sample C (4 mg/kg)	2.839	3.529	3.966 mg/kg
	2.839	3.531	3.966 mg/kg
	2.957	3.533	4.106 mg/kg

#### **Spiked water sample calculation**

For water sample preparation, 50 mL of water samples are extracted and pre-concentrated for 10 times. Then, 100  $\mu$ L of the samples are used for derivatization and the final volume is adjusted to 1 mL. Therefore, the concentration of glyphosate can be calculated as follow.

For example, spiked glyphosate (0.5 mg/L) in water sample A;

From the linear regression of  $y = 3.386x - 0.519$

$$y = 3.386x - 0.519$$

$$1.264 = 3.386x - 0.519$$

$$x = \frac{1.264+0.519}{3.386} = 0.526 \text{ mg/L}$$

From  $C_1V_1 = C_2V_2$

$$C_1 (0.1 \text{ mL}) = (0.526 \text{ mg/L})(1 \text{ mL})$$

$$C_1 = 5.26 \text{ mg/L} \div 10 \text{ dilution factor} = 0.526 \text{ mg/L}$$

Thus, the concentration of glyphosate in the spiked water sample A is 0.526 mg/L.

### Soil sample and spiked soil calculation

For soil samples preparation, 25 g of the collected soils are added to 60 mL of NaOH. After extraction and filtration, the samples are diluted to 100 mL using DI-water and then pre-concentrated for 10-times. Then, 100  $\mu$ L of the samples are used for derivatization and the final volume is adjusted to 1 mL.

For example, soil sample A;

From the linear regression of  $y = 3.386x - 0.519$

$$y = 3.386x - 0.519$$

$$0.160 = 3.386x - 0.519$$

$$x = \frac{0.160+0.519}{3.386} = 0.20 \text{ mg/L}$$

From  $C_1V_1 = C_2V_2$

$$C_1 (0.1 \text{ mL}) = (0.20 \text{ mg/L})(1 \text{ mL})$$

$$C_1 = 2.00 \text{ mg/L} \div 10 \text{ dilution factor} = 0.20 \text{ mg/L}$$

Thus, the concentration of glyphosate in the 100 mL-volumetric flasks is 0.20 mg/L.

In 1000 mL there is glyphosate 0.20 mg

$$\text{In } 100 \text{ mL there is glyphosate } \frac{(0.20 \text{ mg})(100 \text{ mL})}{1000 \text{ mL}} = 0.02 \text{ mg}$$

$$\begin{array}{l} \text{In } 25.00 \text{ g} \quad \text{there is glyphosate } 0.02 \text{ mg} \\ \text{In } 1000 \text{ g} \quad \text{there is glyphosate } \frac{(0.02 \text{ mg})(1000 \text{ g})}{25.00 \text{ g}} = 0.799 \text{ mg/kg} \end{array}$$

Thus, the concentration of glyphosate in the soil sample A is 0.799 mg/kg.

#### B.4 Carbon composite nanomaterials-based sensor: SERS sensor

**Table B.41 Raman intensity on laser excitation wavelength**

Wavelength (nm)	Average Raman intensity (a.u.)	SD. (n=20)	%RSD
325	0.00	0.00	0.00
532	8401.94	1199.61	14.28
633	728.10	221.57	30.43
785	1515.14	377.58	24.92

**Table B.42 Raman intensity of the TiO<sub>2</sub> NTs/AgNPs-rGO on objective lens**

Objective lens	Average Raman intensity (a.u.)	SD. (n=20)	%RSD
10x	1953.48	478.00	24.47
50x	9633.14	1015.08	10.54
100x	8334.89	2312.70	27.75

**Table B.43 Raman intensity of the TiO<sub>2</sub> NTs/AgNPs-rGO on acquisition time**

Time (second)	Average Raman intensity (a.u.)	SD. (n=20)	%RSD
1	1272.86	188.65	14.82
3	6270.34	1560.09	24.88
5	8445.22	1497.82	17.74
7	9352.20	1330.63	14.23
10	10970.86	1099.17	10.02
15	11005.50	1440.95	13.09



**Table B.44 Raman intensity of the TiO<sub>2</sub> NTs/AgNPs-rGO on accumulation**

Accumulation	Average Raman intensity (a.u.)	SD. (n=20)	%RSD
1	3972.36	770.46	19.40
3	6669.94	1167.16	17.50
5	9613.19	1283.81	13.35
7	8599.43	1123.95	13.07
10	7612.47	1066.29	14.01

**Table B.45 Raman intensity of the TiO<sub>2</sub> NTs/AgNPs on anodic potential**

Potential (V)	Average Raman intensity (a.u.) (n=20)	Diameter (nm) (n=300)	Length (μm) (n=100)
0	1348.86 ± 450.60	0	0
10	2444.58 ± 445.89	15.59 ± 3.50	0.42 ± 0.05
20	4534.97 ± 770.65	32.87 ± 4.55	0.96 ± 0.05
30	4857.85 ± 551.21	50.30 ± 6.80	1.47 ± 0.15
40	2730.89 ± 554.62	67.24 ± 7.74	4.41 ± 0.12
50	2046.12 ± 456.91	92.54 ± 8.06	6.36 ± 0.49

**Table B.46 Raman intensity of the TiO<sub>2</sub> NTs/AgNPs on anodic time**

Time (mins)	Average Raman intensity (a.u.) (n=20)	Diameter (nm) (n=300)	Length (μm) (n=100)
10	4763.24 ± 493.29	42.21 ± 7.08	0.30 ± 0.05
20	4677.21 ± 558.07	49.28 ± 7.73	1.06 ± 0.08
30	4764.02 ± 390.34	50.30 ± 6.80	1.47 ± 0.15
60	2769.67 ± 240.80	62.03 ± 10.51	2.26 ± 0.15
90	2027.41 ± 594.88	63.05 ± 7.54	2.63 ± 0.13
120	2307.80 ± 617.21	65.54 ± 10.00	3.24 ± 0.21
150	1756.22 ± 501.23	72.21 ± 9.03	3.41 ± 0.09
180	1591.08 ± 209.20	77.69 ± 10.63	4.37 ± 0.22

**Table B.47 Raman intensity of the TiO<sub>2</sub> NTs/AgNPs on AgNPs thickness**

<b>Thickness (nm)</b>	<b>Average Raman intensity (a.u.)</b>	<b>SD. (n=20)</b>	<b>%RSD</b>
3	2268.64	213.22	9.40
5	4534.97	769.65	16.97
7	3315.39	200.23	6.04
9	3228.03	336.70	10.40
11	5341.33	762.04	14.27
13	5303.29	950.65	17.93
15	5024.82	793.00	15.78
17	3898.26	959.23	24.61

**Table B.48 Raman intensity of the TiO<sub>2</sub> NTs/AgNPs-rGO on GO concentration**

<b>Concentration (mg/mL)</b>	<b>Average Raman intensity (a.u.)</b>	<b>SD. (n=20)</b>	<b>%RSD</b>
0.000	5341.33	762.04	14.27
0.010	6613.19	1283.81	19.41
0.050	8210.33	1415.40	17.24
0.075	10152.31	1580.05	15.56
0.100	11712.03	1191.02	10.17
0.125	9510.53	578.24	6.08
0.150	8421.67	1231.69	14.63
0.200	6052.35	1164.62	19.24
0.300	3705.02	1093.62	29.52

**Table B.49 Raman intensity of the TiO<sub>2</sub> NTs/AgNPs-rGO on deposition cycles**

<b>Cycles</b>	<b>Average Raman intensity (a.u.)</b>	<b>SD. (n=20)</b>	<b>%RSD</b>
10	12497.72	1217.60	9.74
20	14535.21	1539.02	10.59
30	15901.62	1329.64	8.36
35	16808.39	1330.07	7.91
40	22067.99	1763.43	7.99
45	16966.25	2071.73	12.21
50	9913.30	1713.57	17.29

**Table B.50 Raman intensity of the different substrates**

<b>Substrate</b>	<b>Average Raman intensity (a.u.)</b>	<b>SD. (n=20)</b>	<b>%RSD</b>
Ti	525.42	116.12	22.10
TiO <sub>2</sub> NTs	1107.39	247.81	22.38
Ti/rGO	5328.69	838.49	15.74
TiO <sub>2</sub> NTs/rGO	7310.44	677.73	9.13
Ti/AgNPs	39723.59	2757.96	6.94
TiO <sub>2</sub> NTs/AgNPs	45767.71	3186.05	6.96
Ti/AgNPs-rGO	43906.29	6452.72	14.70
TiO <sub>2</sub> NTs/AgNPs-rGO	48470.81	1656.19	3.42

**Table B.51 Raman intensity of the TiO<sub>2</sub> NTs/AgNPs-rGO on MB determination**

<b>Concentration (M)</b>	<b>Average Raman intensity (a.u.)</b>	<b>SD. (n=20)</b>	<b>%RSD</b>
10 <sup>-1</sup>	51767.02	1784.01	3.44
10 <sup>-2</sup>	51714.79	959.83	1.86
10 <sup>-3</sup>	48470.81	656.19	1.35

**Table B.51 Raman intensity of the TiO<sub>2</sub> NTs/AgNPs-rGO on MB determination (continued)**

Concentration (M)	Average Raman intensity (a.u.)	SD. (n=20)	%RSD
10 <sup>-4</sup>	40183.32	1824.72	4.54
10 <sup>-5</sup>	37181.99	1668.95	4.49
10 <sup>-6</sup>	31990.99	993.31	3.10
10 <sup>-7</sup>	29205.46	2155.06	7.38
10 <sup>-8</sup>	25335.56	2733.91	10.79
10 <sup>-9</sup>	21283.67	2412.61	11.33
10 <sup>-10</sup>	17068.60	2674.65	15.67
10 <sup>-11</sup>	10063.89	1226.44	12.19
10 <sup>-12</sup>	9324.17	1051.83	11.28
10 <sup>-13</sup>	7634.15	813.08	10.65
Background	674.59	103.89	15.40

The LOD is calculated based on the definition of IUPAC. Firstly, the smallest measure ( $X_L$ ) is calculated by using a mean ( $X_{b1}$ ) and standard deviation ( $S_{b1}$ ) of the background signal as following equation;  $X_L = X_{b1} + kS_{b1}$ . A value of 3 for  $k$  is a numerical factor chosen according to the confidence level of 90% in a practical sense. After making twenty measurements of background, the  $X_{b1} = 674.6$  and  $S_{b1} = 103.9$  are obtained.

$$\begin{aligned}
 \text{Therefore,} \quad X_L &= X_{b1} + kS_{b1} \\
 &= 674.6 + (3 \times 103.9) \\
 &= 986.3
 \end{aligned}$$

The calibration plot of this SERS sensor is  $I_{1624} = 4303.4 \log C + 59381.0$ .

$$\begin{aligned}
 \text{Therefore,} \quad C &= 10^{(I - 59381.0)/4303.4} \\
 \text{Instead of } I = X_L = 986.3; \quad &= 10^{(986.3 - 59381.0)/4303.4} \\
 &= 10^{-13.6} \approx 10^{-14} \text{ M}
 \end{aligned}$$

Thus, the LOD for detection of MB based on the TiO<sub>2</sub> NTs/AgNPs-rGO substrate is 10<sup>-14</sup> M.

**Table B.52 Raman intensity of 0.1 M MB on Ti sheet and 1 nM MB on the TiO<sub>2</sub> NTs/AgNPs-rGO substrate**

Substrate	Average Raman intensity (a.u.)	SD. (n=20)	%RSD
Ti	2978.95	424.38	14.25
TiO <sub>2</sub> NTs/AgNPs-rGO	21283.67	2412.61	11.34

**Table B.53 Raman intensity of TiO<sub>2</sub> NTs/AgNPs-rGO substrate on repeatability and reproducibility study**

Study	Average Raman intensity (a.u.)	SD.	%RSD
Repeatability (n=20)	48755.12	2129.33	4.37
Reproducibility (n=10)	48413.22	952.88	1.99

**Table B.54 Raman intensity of the TiO<sub>2</sub> NTs/AgNPs-rGO and TiO<sub>2</sub> NTs/AgNPs substrates on stability**

Days	TiO <sub>2</sub> NTs/AgNPs-rGO		TiO <sub>2</sub> NTs/AgNPs	
	Average intensity (a.u.) (n=20)	Relative intensity (%)	Average intensity (a.u.) (n=20)	Relative intensity (%)
0	48311.41 ± 1724.72	100.00	47567.71 ± 1861.97	100.00
2	45854.39 ± 1753.54	94.91	33110.79 ± 7881.78	69.61
4	47078.87 ± 903.97	97.45	32081.59 ± 6627.11	67.44
6	48147.03 ± 294.10	99.66	33732.77 ± 3474.48	70.91
8	47731.77 ± 2782.14	98.80	35459.28 ± 7356.92	74.55
10	47339.03 ± 2136.47	97.99	34451.51 ± 5722.58	72.43

**Table B.54 Raman intensity of the TiO<sub>2</sub> NTs/AgNPs-rGO and TiO<sub>2</sub> NTs/AgNPs substrates on stability (continued)**

Days	TiO <sub>2</sub> NTs/AgNPs-rGO		TiO <sub>2</sub> NTs/AgNPs	
	Average intensity (a.u.) (n=20)	Relative intensity (%)	Average intensity (a.u.) (n=20)	Relative intensity (%)
12	48736.40 ± 2391.39	100.88	33948.55 ± 7124.82	71.37
14	47578.80 ± 891.76	98.48	28500.66 ± 8714.87	59.92
16	46489.77 ± 1626.97	96.23	25448.86 ± 7997.41	53.50
18	46691.56 ± 291.64	96.65	23745.12 ± 3302.40	49.92
20	46473.00 ± 1283.63	96.20	20065.11 ± 4147.64	42.18
22	47329.53 ± 2480.63	97.97	21226.41 ± 2038.90	44.62
24	48079.71 ± 1591.22	99.52	19889.65 ± 1808.86	41.81
26	48261.86 ± 2506.55	99.90	22758.77 ± 4433.07	47.84
28	49287.54 ± 2329.03	102.02	20418.67 ± 2790.98	42.92
30	47913.24 ± 2027.50	99.18	21358.19 ± 2826.14	44.90
60	46012.17 ± 4475.31	95.24	-	
90	45605.97 ± 1945.41	94.40	-	

**Table B.55 Raman intensity of the TiO<sub>2</sub> NTs/AgNPs-rGO on recyclability**

Cycles	Average Raman intensity (a.u.)	SD. (n=20)	%RSD	Relative intensity (%)
0	49100.16	2689.19	5.48	100.00
1	48540.57	1964.86	4.05	98.86
2	48100.38	1807.12	3.76	97.96
3	47335.13	2353.80	4.97	96.41

**Table B.56 Raman intensity of the Si wafer, TiO<sub>2</sub> NTs/AgNPs-rGO, and commercial SERS substrates**

Substrate	Average Raman intensity (a.u.)	SD. (n=20)	%RSD
Si wafer	246.38	48.23	19.57
TiO <sub>2</sub> NTs/AgNPs-rGO	48470.81	2156.19	4.44
AtoID™	31076.48	1522.21	4.90
Ocean optics	9304.19	952.63	10.23
Hamamatsu	16022.28	1536.61	9.59

**Table B.57 Raman intensity of the SERS sensor on glyphosate determination**

Concentration (mg/L)	Average Raman intensity (a.u.)	SD. (n=20)	%RSD
0.1	404.11	50.32	12.45
1.0	528.64	102.22	19.33
5.0	765.50	143.94	18.80
10.0	864.72	113.57	13.13
25.0	1399.77	207.18	14.80
50.0	2061.65	250.49	12.15
75.0	2505.00	220.03	8.78
100.0	3483.98	322.97	12.14

**Table B.58 Raman intensity on the detection of background signal**

Number	Raman intensity (a.u.)
1	48.59
2	49.57
3	78.29
4	88.89
5	99.71

**Table B.58 Raman intensity on the detection of background signal (continued)**

Number	Raman intensity (a.u.)
6	106.15
7	106.18
8	56.92
9	36.58
10	101.69
<b>Average <math>\pm</math> SD</b>	<b>77.26 <math>\pm</math> 27.01</b>

**Table B.59 Raman intensity of the TiO<sub>2</sub> NTs/AgNPs-rGO on its selectivity**

Substances	Concentration (mg/L)	Average Raman intensity (a.u.)	Relative Raman signal (%)
Glyphosate	10	825.52 $\pm$ 22.19	100.00
POEA	10	792.90 $\pm$ 20.98	96.05
Glycine	10	813.91 $\pm$ 59.87	98.59
Chlorpyrifos	10	846.80 $\pm$ 15.63	102.58
Paraquat	10	847.10 $\pm$ 71.52	102.61
Carbaryl	10	813.85 $\pm$ 20.73	98.59
Carbendazim	10	866.33 $\pm$ 34.29	104.94
KPO <sub>4</sub>	50	865.43 $\pm$ 20.86	104.83
NaSO <sub>4</sub>	100	829.41 $\pm$ 24.42	100.47
MgSO <sub>4</sub>	100	817.45 $\pm$ 61.55	99.02
CuSO <sub>4</sub>	100	872.90 $\pm$ 53.28	105.74
KNO <sub>3</sub>	100	805.02 $\pm$ 21.24	97.55
NaNO <sub>3</sub>	100	820.42 $\pm$ 20.08	99.38
ZnNO <sub>3</sub>	100	797.44 $\pm$ 30.03	96.60
CaCO <sub>3</sub>	100	856.91 $\pm$ 43.22	103.80
KCl	100	837.01 $\pm$ 28.50	101.39
NaCl	100	864.08 $\pm$ 27.71	104.67
CaCl <sub>2</sub>	100	871.11 $\pm$ 27.20	105.52



**Table B.60 SERS intensity and concentration of glyphosate found in the samples using external calibration method by the TiO<sub>2</sub> NTs/AgNPs-rGO**

<b>Samples</b>	<b>Raman intensity (n=20) (a.u.)</b>	<b>Glyphosate in sample</b>
Spiked water A (0.5 mg/L)	706.61 ± 123.51	0.557 mg/L
	708.23 ± 90.98	0.562 mg/L
	692.20 ± 77.21	0.506 mg/L
Spiked water A (1.0 mg/L)	846.27 ± 166.64	1.043 mg/L
	852.92 ± 92.58	1.066 mg/L
	848.50 ± 147.66	1.051 mg/L
Spiked water B (0.5 mg/L)	706.31 ± 85.81	0.555 mg/L
	694.23 ± 87.75	0.513 mg/L
	689.10 ± 113.42	0.496 mg/L
Spiked water B (1.0 mg/L)	832.82 ± 173.17	0.970 mg/L
	855.84 ± 132.93	0.996 mg/L
	858.24 ± 173.88	1.085 mg/L
Spiked water C (0.5 mg/L)	713.33 ± 64.04	0.580 mg/L
	708.96 ± 137.47	0.564 mg/L
	682.23 ± 102.24	0.472 mg/L
Spiked water C (1.0 mg/L)	857.79 ± 102.86	1.083 mg/L
	810.87 ± 111.60	0.920 mg/L
	816.88 ± 147.29	0.941 mg/L
Soil sample A	627.20 ± 68.93	1.120 mg/kg
	690.48 ± 137.75	2.002 mg/kg
	678.11 ± 112.95	1.830 mg/kg
Soil sample A (2 mg/kg)	801.36 ± 195.97	3.550 mg/kg
	811.94 ± 175.73	3.694 mg/kg
	787.69 ± 116.12	3.352 mg/kg

**Table B.60 SERS intensity and concentration of glyphosate found in the samples using external calibration method by the TiO<sub>2</sub> NTs/AgNPs-rGO (continued)**

Samples	Raman intensity (n=20) (a.u.)	Glyphosate in sample
Soil sample A (4 mg/kg)	944.84 ± 108.78	5.546 mg/kg
	949.16 ± 163.81	5.606 mg/kg
	944.88 ± 187.52	5.545 mg/kg
Soil sample B (2 mg/kg)	709.68 ± 188.16	2.268 mg/kg
	685.65 ± 154.28	1.934 mg/kg
	704.52 ± 132.63	2.197 mg/kg
Soil sample B (4 mg/kg)	830.38 ± 103.07	3.950 mg/kg
	857.25 ± 109.42	4.325 mg/kg
	851.35 ± 117.65	4.243 mg/kg
Soil sample C (2 mg/kg)	704.84 ± 174.25	2.202 mg/kg
	692.89 ± 172.49	2.034 mg/kg
	697.81 ± 128.07	2.104 mg/kg
Soil sample C (4 mg/kg)	828.26 ± 116.72	3.921 mg/kg
	818.89 ± 175.90	3.790 mg/kg
	846.57 ± 178.54	4.176 mg/kg

#### Spiked water sample calculation

For water sample preparation, 50 mL of water samples are extracted and pre-concentrated for 10 times. Then, 5 µL of the samples are dropped onto the surface of SERS substrate. Therefore, the concentration of glyphosate can be calculated as follow.

For example, spiked glyphosate (0.5 mg/L) in water sample A;

From the linear regression of  $y = 28.71x + 546.75$

$$\begin{aligned}
 y &= 28.71x + 546.75 \\
 706.61 &= 28.71x + 546.75 \\
 x &= \frac{706.61 - 546.75}{28.71} = 5.568 \text{ mg/L} \div 10 \text{ dilution factor} = 0.557 \text{ mg/L}
 \end{aligned}$$

Thus, the concentration of glyphosate in the spiked water sample A is 0.557 mg/L.

### Soil sample and spiked soil calculation

For soil samples preparation, 25 g of the collected soils are added to 60 mL of NaOH. After extraction and filtration, the samples are diluted to 100 mL using DI-water and then pre-concentrated for 10-times. Then, 5  $\mu$ L of the samples are dropped onto the surface of SERS substrate.

For example, soil sample A;

From the linear regression of  $y = 28.71x + 546.75$

$$\begin{aligned}
 y &= 28.71x + 546.75 \\
 627.20 &= 28.71x + 546.75 \\
 x &= \frac{627.20 - 546.75}{28.71} = 2.802 \text{ mg/L} \div 10 \text{ dilution factor} = 0.280 \text{ mg/L}
 \end{aligned}$$

Thus, the concentration of glyphosate in the 100 mL-volumetric flasks is 0.28 mg/L.

$$\begin{aligned}
 &\text{In } 1000 \text{ mL} \quad \text{there is glyphosate} \quad 0.28 \text{ mg} \\
 &\text{In } 100 \text{ mL} \quad \text{there is glyphosate} \quad \frac{(0.28 \text{ mg})(100 \text{ mL})}{1000 \text{ mL}} = 0.028 \text{ mg} \\
 &\text{In } 25.0 \text{ g} \quad \text{there is glyphosate} \quad 0.028 \text{ mg} \\
 &\text{In } 1000 \text{ g} \quad \text{there is glyphosate} \quad \frac{(0.028 \text{ mg})(1000 \text{ g})}{25.0 \text{ g}} = 1.12 \text{ mg/kg}
 \end{aligned}$$

Thus, the concentration of glyphosate in the soil sample A is 1.12 mg/kg.



**APPENDIX C**  
**CALCULATION PART**



### C.1 Active surface of GCPE

A diameter of the GCPE is 0.8 cm. Therefore, a radius of GCPE is 0.4 cm.

Surface area of circle =  $\pi r^2$

Thus, the surface area of GCPE is  $3.14 \times 0.4^2 = 0.5 \text{ cm}^2$

### C.2 Amount of IL functionalized on the GCPE surface

For preparation, 5  $\mu\text{L}$  of IL are added to the GNP suspension and the final volume is 500  $\mu\text{L}$ . For modification, 5  $\mu\text{L}$  of GNP-IL are spread on the GCPE surface

Density of IL is 1.198 g/mL

Therefore, the amount of IL is calculated as  $(1.198 \text{ g/mL})(0.005 \text{ mL}) = 0.006 \text{ g}$

$$\begin{aligned} \text{In } 0.5 \text{ mL there are IL } 0.006 \text{ g} \\ 0.005 \text{ mL there are IL} = \frac{(0.006 \text{ g})(0.005 \text{ mL})}{0.5 \text{ mL}} = 0.06 \text{ mg} \end{aligned}$$

Thus, the amount of IL on the electrode surface is  $\frac{0.06 \text{ mg}}{0.5 \text{ cm}^2} = 0.1 \text{ mg.cm}^{-2}$

### C.3 Amount of GNP-IL composites on the sensing surface

For preparation, 1 mg/mL GNP are prepared and then mixed with IL. The final volume of the GNP-IL is 500  $\mu\text{L}$ . For modification, 2  $\mu\text{L}$  of the mixture are dropped onto the sensing area of the GCPE.

In 1 mL there are GNP 1 mg  
Therefore, 0.5 mL there are GNP 1 mg as well

$$\begin{aligned} \text{In } 0.5 \text{ mL there are GNP } 1 \text{ mg} \\ 0.002 \text{ mL there are GNP} = \frac{(1 \text{ mg})(0.002 \text{ mL})}{0.5 \text{ mL}} = 4 \mu\text{g} \end{aligned}$$

Thus, the amount of GNP-IL on the electrode surface is  $\frac{4 \mu\text{g}}{0.5 \text{ cm}^2} = 8 \mu\text{g.cm}^{-2}$

#### C.4 Active surface of SPCE

A radius of SPCE is 0.35 cm.

Surface area of circle =  $\pi r^2$

Thus, the surface area of GCPE is  $3.14 \times 0.35^2 = 0.4 \text{ cm}^2$

#### C.5 Amount of GNP on the SPCE surface

For modification, 0.1 mg of the synthesized GNP-MnO<sub>2</sub> are re-dispersed in 1 mL DI-water. Then, 10  $\mu$ L of the GNP-MnO<sub>2</sub> composites is dropped onto the SPCE.

In 1 mL there are GNP 0.1 mg

$$0.01 \text{ mL there are GNP} = \frac{(0.1 \text{ mg})(0.01 \text{ mL})}{1 \text{ mL}} = 1.0 \mu\text{g}$$

Thus, the amount of GNP on the electrode surface is  $\frac{1.0 \mu\text{g}}{0.4 \text{ cm}^2} = 2.5 \mu\text{g.cm}^{-2}$

#### C.6 Ratio of MnO<sub>2</sub> decorated on the GNP sheet

For preparation, 5 mg of GNP and 1 mg of MnSO<sub>4</sub>.4H<sub>2</sub>O are dispersed in 50 mL DI-water in order to synthesis of GNP-MnO<sub>2</sub> nanocomposites.

MnSO<sub>4</sub>.4H<sub>2</sub>O 223.06 g/mol contain Mn 54.94 g/mol

$$\text{MnSO}_4.4\text{H}_2\text{O} \quad 1 \quad \text{mg} \quad \text{contain} \quad \text{Mn} = \frac{(1 \text{ mg})(54.94 \text{ g/mol})}{223.06 \text{ g/mol}}$$

$$= 0.25 \text{ mg}$$

Therefore, the ratio of GNP:Mn is 5 mg:0.25 mg or 1:0.05 (mg:mg)

#### C.7 Amount of rGO on the SPCE surface

For modification, 0.1 mg of the commercial GO powder are dispersed in 1 mL DI water. Then, 10  $\mu$ L of the GO suspension is dropped onto the SPCE and the rGO film is constructed by electrochemically reduction method.



In 1 mL there are rGO 0.1 mg

$$0.01 \text{ mL there are rGO} = \frac{(0.1 \text{ mg})(0.01 \text{ mL})}{1 \text{ mL}} = 1.0 \mu\text{g}$$

Thus, the amount of rGO on the electrode surface is  $\frac{1.0 \mu\text{g}}{0.4 \text{ cm}^2} = 2.5 \mu\text{g.cm}^{-2}$

### C.8 Amount of AgNPs on the SPCE surface

AgNPs is deposited onto the surface of SPCE/rGO by electrochemically reduction of 1 mM AgNO<sub>3</sub> by using CV method.

Molecular weight of AgNO<sub>3</sub> is 169.87 g/mol.

Therefore, In 1 mol there are AgNO<sub>3</sub> 169.87 g  
1 mmol there are AgNO<sub>3</sub> 0.17 mg

AgNO<sub>3</sub> 169.87 g/mol contain Ag 107.87 g/mol

$$\text{AgNO}_3 \quad 0.17 \text{ mg} \quad \text{contain Ag} = \frac{(0.17 \text{ mg})(107.87 \text{ g/mol})}{169.87 \text{ g/mol}}$$

$$= 0.11 \text{ mg}$$

Thus, the amount of AgNPs on the electrode surface is  $\frac{0.11 \text{ mg}}{0.4 \text{ cm}^2} = 0.2 \text{ mg.cm}^{-2}$

### C.9 Amount of ACP enzyme on the SPCE surface

For biosensor preparation, 5  $\mu\text{L}$  of 5 mg/mL ACP is casted onto the modified electrode by cross-linking with glutaraldehyde.

In 1 mL there are ACP 5 mg

$$0.005 \text{ mL there are ACP} = \frac{(5 \text{ mg})(0.005 \text{ mL})}{1 \text{ mL}} = 0.025 \text{ mg}$$

The ACP obtained from wheat germ (0.5 units/mg).

Therefore, In 1 mg there are ACP 0.5 units

$$\begin{aligned} 0.025 \text{ mg} \quad \text{there are ACP} &= \frac{(0.5 \text{ units})(0.025 \text{ mg})}{1 \text{ mg}} \\ &= 0.0125 \text{ units} \end{aligned}$$

Thus, the amount of ACP on the electrode surface is  $\frac{0.0125 \text{ units}}{0.4 \text{ cm}^2} = 0.03 \text{ units.cm}^{-2}$

**APPENDIX D**  
**PUBLICATIONS AND PRESENTATIONS**



**PUBLICATIONS**

- (1) A. Samphao, P. Butmee, J. Jitcharoen, L. Švorc, G. Raber, K. Kalcher, Flow-injection amperometric determination of glucose using a biosensor based on immobilization of glucose oxidase onto Au seeds decorated on core Fe<sub>3</sub>O<sub>4</sub> nanoparticles, *Talanta* 142 (2015) 35-42.
- (2) P. Butmee, S. Prasertsri, S. Pimmongkol, G. Tumcharern, A. Veseli, E. Mehmeti, K. Kalcher, A. Samphao, A biosensor for the determination of ammonium ion using flow injection amperometric system, *Monatshefte für Chemie* 148 (2017) 635-644.
- (3) A. Samphao, P. Butmee, P. Saejueng, C. Pukahuta, L. Švorc, K. Kalcher, Monitoring of glucose and ethanol during wine fermentation by bioenzymatic biosensor, *Journal of Electroanalytical Chemistry* 816 (2018) 179-188.
- (4) P. Butmee, G. Tumcharern, P. Saejueng, D. Stankovic, A. Ortner, J. Jitcharoen, K. Kalcher, A. Samphao, A direct and sensitive electrochemical sensing platform based on ionic liquid functionalized graphene nanoplatelets for the detection of bisphenol A, *Journal of Electroanalytical Chemistry* 833 (2019) 370-379.
- (5) P. Butmee, G. Tumcharern, G. Thouand, K. Kalcher, A. Samphao, An ultrasensitive immunosensor based on manganese dioxide-graphene nanoplatelets and core shell Fe<sub>3</sub>O<sub>4</sub>@Au nanoparticles for label-free detection of carcinoembryonic antigen, *Bioelectrochemistry* 132 (2020) 107452.

**PETTY PATENT**

Biosensor for ammonium ion detection (1603002077)

**MANUSCRIPTS**

- (1) P. Butmee, J. Mala, C. Damphathik, K. Kunpatee, G. Tumcharern, M. Kerr, E. Mehmeti, G. Raber, K. Kalcher, A. Samphao, A portable selective electrochemical sensor amplified with Fe<sub>3</sub>O<sub>4</sub>@Au-cysteamine-thymine acetic acid as conductive mediator for determination of mercuric ion (Revised)
- (2) P. Butmee, A. Samphao, G. Tumcharern, Reduced graphene oxide on staked dual layer silver nanoparticles-decorated titanium dioxide nanotube arrays as SERS-based sensor for rapid detection of glyphosate herbicide (Manuscript)
- (3) P. Butmee, G. Tumcharern, M.J.D. Thouand, G. Thouand, K. Kalcher, A. Samphao, An enzymatic electrochemical biosensor for glyphosate detection based on acid phosphatase inhibition using screen-printed carbon electrode modified silver nanoparticles decorated reduced graphene oxide (Manuscript)
- (4) P. Butmee, A. Assaf, A. Samphao, G. Tumcharern, M.J.D. Thouand, G. Thouand, Evaluation of glyphosate-based herbicide and its formulation adjustment toxicity on living cells by using Raman spectroscopy (Manuscript)

**ORAL****PRESENTATIONS**

- (1) Congress on Science and Technology of Thailand, Suranaree University of Technology, Nakhon Ratchasima, Thailand (2015) “Determination of mercury in real samples by a biosensor based on flow injection analysis”
- (2) Seoul International Conference on Engineering and Applied Science, Courtyard by Marriott Seoul Times Square, Seoul, South Korea (2016) “A biosensor for the determination of ammonium ion in concentrated latex”

**POSTER****PRESENTATIONS**

- (1) North Eastern Science and Technology Conference, Faculty of Science, Ubon Ratchathani, Thailand (2013) “Glucose amperometric biosensor based on flow injection analysis”
- (2) Pure and Applied Chemistry International Conference (PACCON 2014), Centara Hotel and Convention Centre, Khon Kaen, Thailand (2014) “Fe<sub>3</sub>O<sub>4</sub>/Au nanoparticles for immobilization of glucose oxidase on screen printed carbon electrode based on flow injection analysis for glucose determination”
- (3) Pure and Applied Chemistry International Conference (PACCON 2015), Amari Watergate Hotel, Bangkok, Thailand (2015) “Monitoring of ethanol during wine fermentation by an ethanol biosensor”
- (4) Pure and Applied Chemistry International Conference (PACCON 2016), Bangkok International Trade & Exhibition Centre, Bangkok, Thailand (2016) “A biosensor based on alanine dehydrogenase immobilized on Fe<sub>3</sub>O<sub>4</sub>@Au nanoparticles for the determination of ammonium ion in concentrated latex samples using flow-injection amperometric system”
- (5) The 13<sup>th</sup> Asian Conference on Analytical Sciences, The Empress International Convention Center, Chiang Mai, Thailand (2016) “Monitoring of glucose and ethanol during wine fermentation by a dual enzymatic biosensor”
- (6) The 6<sup>th</sup> International Conference on Bio-Sensing Technology, Renaissance Kuala Lumpur Hotel, Kuala Lumpur, Malaysia (2019) “An ultrasensitive voltammetric and impedimetric immunosensors based on manganese dioxide-graphene nanoplatelets composite and core shell Fe<sub>3</sub>O<sub>4</sub>@Au nanoparticles for the label-free detection of carcinoembryonic antigen”

## CURRICULUM VITAE

<b>NAME</b>	Miss Preeyanut Butmee
<b>BIRTH DATE</b>	15 November 1990
<b>BIRTH PLACE</b>	Sisaket, Thaniland
<b>EDUCATION</b>	2009-2012, B.Sc. (Chemistry), Ubon Ratchathani University 2013-2015, M.Sc. (Analytical Chemistry), Ubon Ratchathani University 2016-2020, Ph.D. (Analytical Chemistry), Ubon Ratchathani University
<b>SCHORLASHIPS</b>	(1) Thailand Graduate Institute of Science and Technology (TGIST), National Science and Technology Development Agency (NSTDA), Thailand (From August 1 <sup>st</sup> 2017 to July 31 <sup>th</sup> 2020) (2) The CNRS GEPEA laboratory, Technological Institute of Nantes University, France (From March 1 <sup>st</sup> to July 31 <sup>th</sup> 2018)
<b>AWARDS</b>	(1) Good poster presentation, “Glucose amperometric biosensor based on flow injection analysis”, North Eastern Science and Technology Conference 2013. (2) Outstanding poster presentation, “Fe <sub>3</sub> O <sub>4</sub> /Au nanoparticles for immobilization of glucose oxidase on screen printed carbon electrode based on flow injection analysis for glucose determination”, PACCON 2014. (3) Outstanding poster presentation, “Monitoring of ethanol during wine fermentation by an ethanol biosensor”, PACCON 2015. (4) Outstanding thesis award, “Development of a biosensor for the determination of ammonium ion in concentrated latex samples”, Ubon Ratchathani University 2016.